

CONTENS

ADDRESS OF PUBLISHER & EDITOR'S OFFICE:

GDAŃSK UNIVERSITY
OF TECHNOLOGY

Faculty of Ocean Engineering
& Ship Technology
G. Narutowicza 11/12
80-233 Gdańsk, POLAND

tel.: +48 58 347 13 66
fax: +48 58 341 13 66

EDITORIAL STAFF:

Jacek Rudnicki
| Editor in Chief
Przemysław Wierzchowski
| Associate Editor
Rafał Szłapczyński
| Associate Editor
Aleksander Kniat
| Editor for international
relations
Kazimierz Kempa
| Technical Editor

Price:
single issue: 25 zł

Prices for abroad
single issue:
- in Europe EURO 15
- overseas USD 20

WEB:

www.bg.pg.gda.pl/pmr/pmr.php

ISSN 1233-2585

- | | |
|----|---|
| 3 | Chih-Li Chen
<i>A SYSTEMATIC APPROACH FOR SOLVING THE GREAT CIRCLE TRACK PROBLEMS BASED ON VECTOR ALGEBRA</i> |
| 14 | Józef Lisowski
<i>THE SENSITIVITY OF STATE DIFFERENTIAL GAME VESSEL TRAFFIC MODEL</i> |
| 19 | Jan P. Michalski
<i>PARAMETRICAL METHOD FOR DETERMINING OPTIMAL SHIP CARRYING CAPACITY AND PERFORMANCE OF HANDLING EQUIPMENT</i> |
| 25 | Ehsan Yari, Hassan Ghassemi
<i>BOUNDARY ELEMENT METHOD APPLIED TO ADDED MASS COEFFICIENT CALCULATION OF THE SKEWED MARINE PROPELLERS</i> |
| 32 | Tomasz Kowalczyk, Jerzy Głuch, Paweł Ziółkowski
<i>ANALYSIS OF POSSIBLE APPLICATION OF HIGH-TEMPERATURE NUCLEAR REACTORS TO CONTEMPORARY LARGE-OUTPUT STEAM POWER PLANTS ON SHIPS</i> |
| 42 | M. I. Lamas, C. G. Rodríguez, J. D. Rodríguez, J. Telmo
<i>NUMERICAL MODEL OF SO₂ SCRUBBING WITH SEAWATER APPLIED TO MARINE ENGINES</i> |
| 48 | JY. Ust, A. Sinan Karakurt, U. Gunes
<i>PERFORMANCE ANALYSIS OF MULTIPURPOSE REFRIGERATION SYSTEM (MRS) ON FISHING VESSEL</i> |
| 57 | Agnieszka Maczyszyn
<i>METHOD OF SUM OF POWER LOSSES AS A WAY FOR DETERMINING THE K_f COEFFICIENTS OF ENERGY LOSSES IN HYDRAULIC MOTOR</i> |
| 64 | Daria FILIPIAK – KOWSZYK, Waldemar KAMIŃSKI
<i>THE APPLICATION OF KALMAN FILTERING TO PREDICT VERTICAL RAIL AXIS DISPLACEMENTS OF THE OVERHEAD CRANE BEING A COMPONENT OF SEAPORT TRANSPORT STRUCTURE</i> |
| 71 | Heba W. Leheta, Ahmed M. H. Elhewy, Helmy A. Younes
<i>ANALYSIS OF FATIGUE CRACK GROWTH IN SHIP STRUCTURAL DETAILS</i> |
| 83 | Henryk Tomaszek, Mariusz Zieja, Mariusz Ważny
<i>A METHOD FOR RELIABILITY ASSESSMENT OF STRUCTURAL COMPONENTS OF AIRCRAFT AND SEA-GOING SHIPS WITH TAKING INTO ACCOUNT A GIVEN FAILURE GENERATION MODEL</i> |
| 91 | Tomasz Dziubich, Julian Szymański, Adam Brzeski, Jan Cychnerski, Waldemar Korłub
<i>DEPTH IMAGES FILTERING IN DISTRIBUTED STREAMING</i> |

Editorial

POLISH MARITIME RESEARCH is a scientific journal of worldwide circulation. The journal appears as a quarterly four times a year. The first issue of it was published in September 1994. Its main aim is to present original, innovative scientific ideas and Research & Development achievements in the field of :

Engineering, Computing & Technology, Mechanical Engineering,

which could find applications in the broad domain of maritime economy. Hence there are published papers which concern methods of the designing, manufacturing and operating processes of such technical objects and devices as : ships, port equipment, ocean engineering units, underwater vehicles and equipment as well as harbour facilities, with accounting for marine environment protection.

The Editors of POLISH MARITIME RESEARCH make also efforts to present problems dealing with education of engineers and scientific and teaching personnel. As a rule, the basic papers are supplemented by information on conferences , important scientific events as well as cooperation in carrying out international scientific research projects.

Scientific Board

Chairman : Prof. JERZY GIRTLEK - Gdańsk University of Technology, Poland

Vice-chairman : Prof. MIROSLAW L. WYSZYŃSKI - University of Birmingham, United Kingdom

Dr POUL ANDERSEN
Technical University of Denmark
Denmark

Dr MEHMET ATLAR
University of Newcastle United
Kingdom

Prof. GÖRAN BARK
Chalmers University of Technology
Sweden

Prof. SERGEY BARSUKOV
Army Institute of Odessa Ukraine

Prof. MUSTAFA BAYHAN
Süleyman Demirel University
Turkey

Prof. VINCENZO CRUPI
University of Messina, Italy

Prof. MAREK DZIDA
Gdańsk University of Technology
Poland

Prof. ODD M. FALTINSEN
Norwegian University of Science
and Technology
Norway

Prof. PATRICK V. FARRELL
University of Wisconsin Madison,
WI
USA

Prof. WOLFGANG FRICKE
Technical University Hamburg-
Harburg Germany

Prof. HASSAN GHASSEMI
Amirkabir University of Technology
Iran

Prof. STANISŁAW GUCMA
Maritime University of Szczecin
Poland

Prof. ANTONI ISKRA
Poznań University of Technology
Poland

Prof. JAN KICIŃSKI
Institute of Fluid-Flow Machinery
of PASci
Poland

Prof. ZBIGNIEW KORCZEWSKI
Gdańsk University of Technology
Poland

Prof. JANUSZ KOZAK
Gdańsk University of Technology
Poland

Prof. JAN KULCZYK
Wrocław University of Technology
Poland

Prof. NICOS LADOMMATOS
University College London United
Kingdom

Prof. JÓZEF LISOWSKI
Gdynia Maritime University Poland

Prof. JERZY MATUSIAK
Helsinki University of Technology
Finland

Prof. EUGEN NEGRUS
University of Bucharest Romania

Prof. YASUHIKO OHTA
Nagoya Institute of Technology
Japan

Dr YOSHIO SATO
National Traffic Safety and
Environment Laboratory
Japan

Prof. KLAUS SCHIER
University of Applied Sciences
Germany

Prof. FREDERICK STERN
University of Iowa, IA, USA

Prof. ILCEV DIMOV STOJCE
Durban University of Technology
South Africa

Prof. JÓZEF SZALA
Bydgoszcz University
of Technology and Agriculture
Poland

Prof. WITALIJ SZCZAGIN
State Technical University of
Kaliningrad, Russia

Prof. BORIS TIKHOMIROV
State Marine University of St.
Petersburg, Russia

Prof. DRACOS VASSALOS
University of Glasgow and
Strathclyde United Kingdom

A SYSTEMATIC APPROACH FOR SOLVING THE GREAT CIRCLE TRACK PROBLEMS BASED ON VECTOR ALGEBRA

Chih-Li Chen, Ph.D.

National Taiwan Ocean University, Taiwan

ABSTRACT

A systematic approach, based on multiple products of the vector algebra (S-VA), is proposed to derive the spherical triangle formulae for solving the great circle track (GCT) problems. Because the mathematical properties of the geometry and algebra are both embedded in the S-VA approach, derivations of the spherical triangle formulae become more understandable and more straightforward as compared with those approaches which use the complex linear combination of a vector basis. In addition, the S-VA approach can handle all given initial conditions for solving the GCT problems simpler, clearer and avoid redundant formulae existing in the conventional approaches. With the technique of transforming the Earth coordinates system of latitudes and longitudes into the Cartesian one and adopting the relative longitude concept, the concise governing equations of the S-VA approach can be easily and directly derived. Owing to the advantage of the S-VA approach, it makes the practical navigator quickly adjust to solve the GCT problems. Based on the S-VA approach, a program namely GCTPro_VA is developed for friendly use of the navigator. Several validation examples are provided to show the S-VA approach is simple and versatile to solve the GCT problems.

Keywords: great circle; vector algebra; multiple products; spherical trigonometry

INTRODUCTION

The great circle arc is the shortest distance between two non-antipodal points on the Earth's surface. Therefore, without considering the wind and tide effects, the most economical route is the great circle track (GCT). As known, a vessel sailing on the GCT in a constantly varying course is impossible and thus, a series of rhumb lines is necessary to be adopted for approximating the GCT in practice [2, 3, 9, 18]. Before doing so, the waypoints must be located. However, to determine the waypoints on the GCT, the navigator has to provide some initial conditions. Theoretically, these given initial conditions include: (1) giving the great circle distances to obtain the latitudes and longitudes of the waypoints (hereafter is called "condition 1"); (2) giving the

longitudes of the waypoints to yield the latitudes (hereafter is called "condition 2"); (3) giving latitudes of the waypoints to reach the longitudes (hereafter is called "condition 3"). Then, locating these obtained waypoints on the Mercator chart or ECDIS (Electronic Chart Display and Information System) for every rhumb line sailing is called the great circle sailings in practical navigation [2, 3, 9, 18]. For dealing with GCT problems under all initial conditions, a systematic approach to tackle the problems is necessary and becomes one of our research motivations.

Spherical trigonometry (ST) has been used for solving every navigational triangle. Since the Napier's rules was proposed by John Napier (1550-1617), the navigator has adopted the rules in conjunction with the spherical triangle formulae to solve

the GCT problems. While using the Napier's rules of the right-angled spherical triangles, one needs to take the vertex as the reference point (RP-V). This method has lasted for several centuries and is adopted in the current international maritime education [2, 3, 9, 12, 14, 18]. In addition, because finding the equator crossing point of the GCT is easier than finding the vertex, a method of taking the equator crossing point as the reference point (RP-E) was proposed [4, 7]. Both the RP-V and RP-E have to decide the reference point in advance when solving the GCT problems; they can be categorized as a kind of indirect methods. In contrast to the indirect methods, some researchers took the departure point as the reference point (RP-F) because such a method can directly obtain the waypoint on the GCT. Due to this advantage, Jofeh [13] used a linear equation of the GCT to represent a straight line on the polar gnomonic chart. According to his method, the waypoints are determined only under given condition 2. Thereafter, the linear combination of a vector basis (VB) to derive the used formula was also proposed [5, 15, 16]. Although the VB was claimed a method of the operation of the vector, it is actually an essence of geometric analysis, which make the derivation of this method hard to understand and results in redundant formulae. In addition, the VB cannot determine the waypoints under all given initial condition. Apart from the VB, a method using multiple products of the vector algebra (VA) appeared lately [4, 6, 7]. A disadvantage of this method is that all given initial conditions cannot be covered when solving the waypoints on the GCT. Therefore, this paper systematically adopts multiple products of the vector algebra (S-VA) to derive the spherical triangle formulae for solving the GCT problems. Advantages of the S-VA approach are that it can handle all given initial conditions more straightforward and avoid redundant formulae existing in the conventional approaches. A comparison of those mentioned methods are listed in Table 1 for convenience.

As compared with the geometric analysis, the dot or cross products of vector algebra are more convenient to describe the relationships between the sides and the angles of the spherical triangle [11, 19]. Because the S-VA approach transforms the Earth coordinates system of the latitude and longitude into the Cartesian one and adopts the relative longitude concept, the derivation of the spherical triangle formulae becomes simple and clear. In addition, the mathematical properties of the geometry and algebra are both embedded in the S-VA approach; therefore, they are adopted for constructing the theoretical background of the current research. Based on the S-VA approach, a program namely GCTPro_VA is developed for the use of the navigator. The GCTPro_VA with a friendly interface offers a quick and practical tool for the choice of three given initial conditions.

Apart from the current section, the theoretical backgrounds are presented in Section 2. Computation procedures including of all the given initial conditions and its numerical program are illustrated in Section 3. Several validated examples and discussions are given in Section 4. Finally, Section 5 draws concrete conclusions after recasting this research work.

THEORETICAL BACKGROUNDS

In the spherical geometry, the spherical triangle is the most concise and simplest form for all the geometrical figures. The fundamental structure of the spherical triangle consists in the relationships between the sides (great circle arcs) and angles (dihedral angles). Among the spherical triangle formulae, the two most important laws are the sine law and side cosine law, which are called the "genetic codes" for developing all the spherical triangle formulae [8].

There are two ways to derive the spherical triangle formulae. One is based on the geometry analysis and the other depends on the vector algebra. Theoretically speaking, the most straightforward and understandable operations are using systematic approach with multiple products of the vector algebra (S-VA) [8, 11, 19]. Since the S-VA implies both the mathematical properties of the geometry and algebra, all the spherical triangle formulae can be easily and directly derived. In this regard, three stages are necessary to derive the used spherical triangle formulae and governing equations with respect to the GCT problems. First, the Earth coordinates system of the latitude and longitude is transformed into the Cartesian coordinates system to yield the vector representation. Then, the S-VA is introduced to derive the used spherical triangle formulae. Finally, aimed at the GCT problems, the concise governing equations are yielded by simplifying the related spherical triangle formulae. All symbols used in this article are listed in NOMENCLATURE.

Tab. 1. A comparison of different methods for solving the GCT problem

Authors	Category	Formulae derivation	Available condition
Holm, 1972	RP-V	ST	2
Jofeh, 1981	RP-F	Linear eqn.	2
Bowditch, 1981; 2002	RP-V	ST	all
Keys, 1983	RP-V	ST	all
Miller et al., 1991	RP-F	VB	1
Chen, 2003	RP-V, RP-E	ST	all
	RP-F	VA (GCEM)	2 and 3
Cutler, 2004	RP-V	ST	all
Chen et al., 2004	RP-V	ST	all
	RP-F	VA (GCEM)	2 and 3
Nastro and Tancredi, 2010	RP-F	VB	1
Chen et al., 2014	RP-E	ST	all
	RP-F	VA (COFI)	1
Chen et al., 2015	RP-F	VB (RT)	1 and 2
Chen, 2016 (the current paper)	RP-F	S-VA	all

COORDINATES TRANSFORMATION

First, the Earth is treated as a unitary sphere for practical navigation. Then, the Earth coordinates system of the latitude and longitude is transformed into the Cartesian coordinates system. As shown in Fig. 1, the vector of any point P on the Earth's surface can be represented by the latitude and the

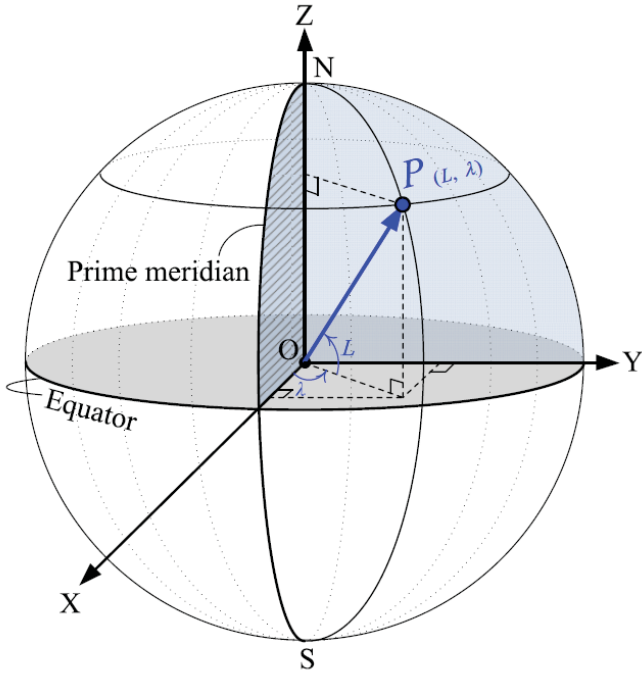


Fig. 1. An illustration of transforming the Earth coordinates system into the Cartesian one

longitude in the Cartesian coordinates system as:

$$\vec{P} = [\cos L \cos \lambda, \cos L \sin \lambda, \sin L], L = \left[-\frac{\pi}{2}, \frac{\pi}{2}\right], \lambda = [0, 2\pi). \quad (1)$$

To avoid an additional judgment of sign convention, the concept of the fixed coordinates system is first considered, that is, the north latitude is treated as a positive value and the south latitude is treated as a negative one. To reduce the number of the variables, the relative longitude concept that replaces the Greenwich meridian by the meridian of the departure point is introduced. As shown in Fig. 2, the unit vectors of the North Pole (N), the departure (F), the destination (T) and the waypoints (X) along the GCT located on the Earth's surface can be expressed as:

$$\vec{N} = [0, 0, 1], \quad (2a)$$

$$\vec{F} = [\cos L_F, 0, \sin L_F], \quad (2b)$$

$$\vec{T} = [\cos L_T \cos DLo, \cos L_T \sin DLo, \sin L_T], \quad (2c)$$

$$\vec{X} = [\cos L_X \cos DLo_{FX}, \cos L_X \sin DLo_{FX}, \sin L_X]. \quad (2d)$$

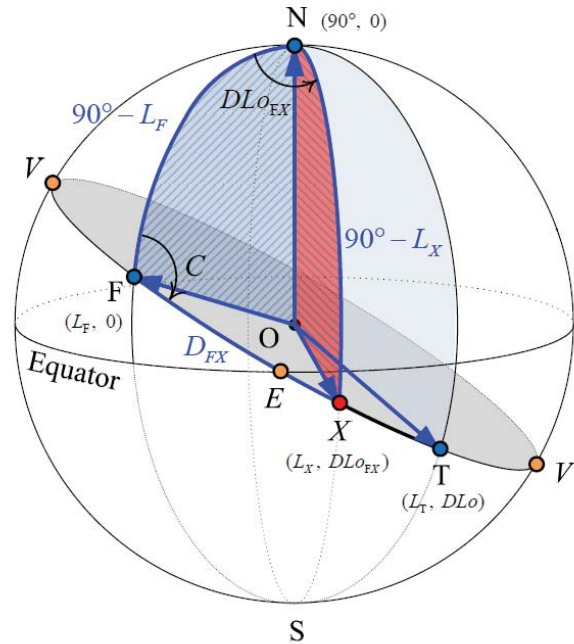


Fig. 2. An illustration of the unit vectors of four points located on the Earth's surface

MULTIPLE PRODUCTS OF VECTOR ALGEBRA

- To obtain a great circle arc (side of spherical triangle), we can adopt the dot and cross product of two vectors. From the viewpoint of geometry, the dot product of two vectors is defined as:

$$\begin{aligned} \vec{N} \cdot \vec{F} &= \vec{F} \cdot \vec{N} = \sin L_F, & \vec{N} \cdot \vec{T} &= \sin L_T, & \vec{F} \cdot \vec{T} &= \cos D, \\ \vec{N} \cdot \vec{X} &= \sin L_X, & \vec{F} \cdot \vec{X} &= \cos D_{FX}. \end{aligned} \quad (3)$$

Similarly, the cross product of two vectors is defined as:

$$\begin{aligned} |\vec{N} \times \vec{F}| &= |\vec{F} \times \vec{N}| = \cos L_F, & |\vec{N} \times \vec{T}| &= \cos L_T, \\ |\vec{F} \times \vec{T}| &= \sin D, \end{aligned} \quad (4)$$

$$|\vec{N} \times \vec{X}| = \cos L_X, \quad |\vec{F} \times \vec{X}| = \sin D_{FX}.$$

- To construct a great circle equation (GCE), we can use the scalar triple products.

A necessary and sufficient condition for the vectors \vec{F} ,

\vec{T} , and \vec{X} to be coplanar, the volume of the parallelepiped form by three vectors must be zero, that is,

$$(\vec{F} \times \vec{T}) \cdot \vec{X} \equiv (\vec{F} \vec{T} \vec{X}) = 0. \quad (5)$$

Let the coefficient vector be:

$$(\vec{F} \times \vec{T}) = [k_1, k_2, k_3],$$

in which the components of the coefficient vector are as follows:

$$k_1 = -\sin L_F \cos L_T \sin DLo, \quad (6a)$$

$$k_2 = \sin L_F \cos L_T \cos DLo - \cos L_F \sin L_T, \quad (6b)$$

$$k_3 = \cos L_F \cos L_T \sin DLo. \quad (6c)$$

Substituting equations (6a), (6b) and (6c) into equation (5) yields the great circle equation (GCE) as [4, 6, 7]:

$$k_1 \cos L_X \cos DLo_{FX} + k_2 \cos L_X \sin DLo_{FX} + k_3 \sin L_X = 0. \quad (7)$$

Equation (7) has two variables, that is L_X , and DLo_{FX} ; therefore, we can rearrange equation (7) to obtain two forms in the following. One is

$$\tan L_X = \frac{k_1 \cos DLo_{FX} + k_2 \sin DLo_{FX}}{-k_3}, \quad (8)$$

which can be used to yield latitudes of the waypoints by giving their longitudes.

When we assume

$$\sin \alpha = \frac{k_1}{\sqrt{k_1^2 + k_2^2}}, \quad \cos \alpha = \frac{k_2}{\sqrt{k_1^2 + k_2^2}},$$

and substituting them into equation (7), the other form can be yielded as:

$$\tan \alpha = \frac{k_1}{k_2}, \quad (9a)$$

$$\sin(DLo_{FX} + \alpha) = \frac{-k_3}{\sqrt{k_1^2 + k_2^2}} \tan L_X. \quad (9b)$$

The above two equations are a set governing equations. They can be used to obtain longitudes of the waypoints by giving their latitudes.

3. To obtain a dihedral angle (angle of spherical triangle), we can adopt the dot and cross products of two normal vectors of two planes. Therefore the sine law, the side cosine law and the four-part formula can be yielded in the following:

1. Derive the sine law of the spherical triangle by using the cross product of two normal vectors of two planes To obtain the dihedral angle (C), we have

$$(\vec{F} \times \vec{N}) \times (\vec{F} \times \vec{X}) = (\cos L_F \sin D_{FX} \sin C) \vec{F} \quad (10a)$$

in which the first row of the above equation is the definition of geometry and the second row is the operation result of vector algebra [11, 19]. Then, from equation (10a), we have

$$\cos L_F \sin D_{FX} \sin C = (\vec{F} \times \vec{N} \times \vec{F}). \quad (10b)$$

Similarly, to obtain the dihedral angle (DLo_{FX}), we have

$$(\vec{N} \times \vec{X}) \times (\vec{N} \times \vec{F}) = (\cos L_X \cos L_F \sin DLo_{FX}) \vec{N} \quad (11a)$$

in which the first row of the above equation is the definition of geometry and the second row is the operation result of vector algebra [11, 19]. Then, we have:

$$\cos L_X \cos L_F \sin DLo_{FX} = (\vec{N} \times \vec{X} \times \vec{F}). \quad (11b)$$

Since the right-hand sides of equations of (10b) and (11b) are equal, we achieve:

$$\sin D_{FX} \sin C = \cos L_X \sin DLo_{FX}, \quad (12)$$

which is the sine law of the spherical triangle.

2. Derive the side cosine law of the spherical triangle by using the dot product of two normal vectors of two planes

To obtain the dihedral angle (C), we have:

$$(\vec{F} \times \vec{N}) \cdot (\vec{F} \times \vec{X}) = \cos L_F \sin D_{FX} \cos C \quad (13a)$$

$$= \begin{vmatrix} (\vec{F} \cdot \vec{F}) & (\vec{F} \cdot \vec{X}) \\ (\vec{N} \cdot \vec{F}) & (\vec{N} \cdot \vec{X}) \end{vmatrix} = \sin L_X - \sin L_F \cos D_{FX},$$

in which the first row of the above equation is the definition of geometry and the second row is the operation result of vector algebra [11, 19]. Then, from equation (13a), we have:

$$\cos L_F \sin D_{FX} \cos C = \sin L_X - \sin L_F \cos D_{FX}. \quad (13b)$$

Similarly, to obtain the dihedral angle (DLo_{FX}), we have:

$$(\vec{N} \times \vec{X}) \cdot (\vec{N} \times \vec{F}) = \cos L_X \cos L_F \cos DLo_{FX} \quad (14a)$$

$$= \begin{vmatrix} (\vec{N} \cdot \vec{N}) & (\vec{N} \cdot \vec{F}) \\ (\vec{X} \cdot \vec{N}) & (\vec{X} \cdot \vec{F}) \end{vmatrix} = \cos D_{FX} - \sin L_F \sin L_X,$$

in which the first row of the above equation is the definition of geometry and the second row is the operation result of vector algebra [11, 19]. Then, we have:

$$\cos L_X \cos L_F \cos DLo_{FX} = \cos D_{FX} - \sin L_F \sin L_X. \quad (14b)$$

It should be noticed that both equation (13b) and equation (14b) are the side cosine laws.

- Derive the four-part formula of the spherical triangle by using a combination of the sine and side cosine laws

Dividing equations (10a) by equation (13a) yields:

$$\begin{aligned} \frac{(\vec{F} \times \vec{N}) \times (\vec{F} \times \vec{X})}{(\vec{F} \times \vec{N}) \cdot (\vec{F} \times \vec{X})} &= \tan C \\ &= \frac{\cos L_F \sin D_{FX} \sin C}{\sin L_X - \sin L_F \cos D_{FX}}. \end{aligned} \quad (15a)$$

From the above equation, we have:

$$\tan C = \frac{\cos L_F \sin D_{FX} \sin C}{\sin L_X - \sin L_F \cos D_{FX}}. \quad (15b)$$

To yield the four-part formula, we have to substitute equations (12) and (14b) into equation (15b) for eliminating D_{FX} . Then, we have the four-part formula as:

$$\cos L_F \tan C \tan L_X = \sin DLo_{FX} + \sin L_F \tan C \cos DLo_{FX}. \quad (16)$$

DERIVATIONS OF THE GOVERNING EQUATIONS

- The great circle distance

There are two ways to yield the great circle distance. One is:

$$\begin{aligned} \vec{F} \cdot \vec{T} &= \cos D \\ &= \cos L_F \cos L_T \cos DLo + \sin L_F \sin L_T. \end{aligned} \quad (17a)$$

The other is to replace \vec{X} by \vec{T} in the equation (14a). Then, we have:

$$\begin{aligned} (\vec{N} \times \vec{T}) \cdot (\vec{N} \times \vec{F}) &= \cos L_T \cos L_F \cos DLo \\ &= \left| \begin{array}{cc} (\vec{N} \cdot \vec{N}) & (\vec{N} \cdot \vec{F}) \\ (\vec{T} \cdot \vec{N}) & (\vec{T} \cdot \vec{F}) \end{array} \right| = \cos D - \sin L_F \sin L_T. \end{aligned} \quad (17b)$$

It is found that equations (17a) and (17b) are the same. Rewriting the equation (17a) yields:

$$\cos D = \sin L_F \sin L_T + \cos L_F \cos L_T \cos DLo. \quad (18)$$

It should be noticed that equation (18) is the governing equation to obtain the great circle distance.

- The great circle initial course angle

There are also two ways to yield the great circle initial course angle. One is to rearrange equation (12), which is the sine law of the spherical triangle. Then, we have:

$$\sin C = \frac{\cos L_T \sin DLo}{\sin D}. \quad (19)$$

The other is to replace \vec{X} by \vec{T} in equation (13a), which is the side cosine law of the spherical triangle. Then, we have:

$$\begin{aligned} (\vec{F} \times \vec{N}) \cdot (\vec{F} \times \vec{T}) &= \cos L_F \sin D \cos C \\ &= \left| \begin{array}{cc} (\vec{F} \cdot \vec{F}) & (\vec{F} \cdot \vec{T}) \\ (\vec{N} \cdot \vec{F}) & (\vec{N} \cdot \vec{T}) \end{array} \right| = \sin L_T - \sin L_F \cos D. \end{aligned} \quad (20a)$$

Either equation (19) or equation (20a) can be used to yield the great circle initial course angle; however, for avoiding an additional sign judgment, we suggest the navigator use equation (20a). Rearranging equation (20a) obtains:

$$\cos C = \frac{\sin L_T - \sin L_F \cos D}{\cos L_F \sin D}. \quad (20b)$$

It should be noticed that equation (20b) is the governing equation to obtain the great circle initial course angle.

- The waypoints on the GCT

Condition 1: Giving the great circle distances to obtain the latitudes and the longitudes of the waypoints on the GCT. Rearranging equations (13b) and (14b), respectively yields:

$$\sin L_X = \sin L_F \cos D_{FX} + \cos L_F \sin D_{FX} \cos C, \quad (21)$$

and

$$\cos DLo_{FX} = \frac{\cos D_{FX} - \sin L_F \sin L_X}{\cos L_F \cos L_X}. \quad (22)$$

It should be noticed that equations (21) and (22) are a set of the governing equations to obtain the latitudes and the longitudes of the waypoints on the GCT under condition 1.

Condition 2: Giving the longitudes of the waypoints to obtain their latitudes

There are two ways to obtain the latitudes of the waypoints by giving the longitudes. Either rearranging equation (16) or substituting equations (18), (19), and (20b) into equation (8) to eliminate DLo yields the same result, which can be expressed as:

$$\tan L_X = \frac{\cos C \sin DLo_{FX} + \sin L_F \sin C \cos DLo_{FX}}{\cos L_F \sin C}. \quad (23a)$$

It is noticed, that equation (23a) is the governing equation to yield latitudes of the waypoints on the GCT under condition 2. However, this equation needs to find the great circle initial course angle (C) in advance. To avoid this unnecessary step, we first rearrange equation (16) to obtain:

$$\tan L_X \cos L_F = \cot C \sin DLo_{FX} + \sin L_F \cos DLo_{FX}. \quad (23b)$$

Then replacing X by T in equation (23b) yields:

$$\tan L_T \cos L_F = \cot C \sin DLo + \sin L_F \cos DLo. \quad (23c)$$

Finally, substituting equation (23c) into equation (23b) can eliminate C and introducing additional formula of trigonometric functions to obtain:

$$\tan L_X = \frac{\tan L_F \sin(\lambda_X - \lambda_T) + \sin L_T \sin(\lambda_X - \lambda_F)}{\sin(\lambda_T - \lambda_F)}. \quad (23d)$$

It is noticed, that equation (23d) is the most concise form of the governing equation (or so called meridian method) to yield latitudes of the waypoints on the GCT under condition 2 [18].

Condition 3: Giving the latitudes of the waypoints to obtain their longitudes

There are also two ways to obtain the longitudes of the waypoints by giving the latitudes. One way is to use a set of governing equations, equations (9a) and (9b), which are derived from the GCE. The other one is yielded from the four-part formula of spherical triangle, that is, equation (16) and derived as follows. First we set

$$\tan \alpha = \sin L_F \tan C, \quad (24a)$$

and then, introduce the additional formula of trigonometric functions into equation (16). Therefore, we have:

$$\sin(DLo_{FX} + \alpha) = (\cos \alpha \cos L_F \tan C) \tan L_X. \quad (24b)$$

It should be noticed, that equations (24a) and (24b) are a set of the most concise form of the governing equations to yield longitudes of the waypoints on the GCT under condition 3.

4. The equator crossing point

The latitude of the equator crossing point must be zero. Substituting it into equation (23) and rearranging it can yield the equation:

$$\tan DLo_{FE} = -\sin L_F \tan C. \quad (25)$$

It should be noticed, that equation (25) is the governing equation to obtain the longitude of the equator crossing point.

5. The vertex

The vertices of a great circle are the points nearest the

poles. Accordingly, let the first derivative of equation (23) be zero and rearrange it, we get equation:

$$\tan DLo_{FV} = \frac{1}{\sin L_F \tan C}. \quad (26a)$$

While using the sine law of the right-angled spherical triangles, we have:

$$\cos L_V = \cos L_F \sin C. \quad (26b)$$

It is noticed that equations (26a) and (26b) are a set of the governing equations to yield the vertex.

COMPUTATION PROCEDURES AND NUMERICAL PROGRAM

As mentioned above, the main task of the GCT problems is to obtain the waypoints on the GCT. These waypoints are then transferred to a Mercator chart or the ECDIS. Then, the course and distance of the rhumb line between two adjacent waypoints are determined by using the spherical Mercator sailing. In this regard, we first introduce all needed formulae used for the spherical Mercator sailing. Thereafter, all the governing equations derived for solving the GCT problems are summarized in computation procedures. Finally, a program GCTPro_VA is developed for navigator friendly use.

THE COURSES AND DISTANCES OF THE RHUMB LINES

Basically, there are two kinds of sailings to obtain the course and distance of the rhumb line between two adjacent waypoints on the GCT. One is the spheroid rhumb line sailing and the other is the spherical Mercator sailing [1, 3, 5, 7, 17, 18]. Since the spherical Mercator sailing meets most of the needs of navigational practice and the distance for a rhumb line on the navigation sphere is within 0.5% of the distance on the rhumb line on the spheroid [10], we adopt the spherical Mercator sailing to yield the course and distance of the rhumb line. For convenience, all needed formulae and related constants in the numerical program are listed as follows [3, 7, 17, 18]:

$$M = a_e \ln \left[\tan \left(45^\circ + \frac{L}{2} \right) \times \left(\frac{1 - e \sin L}{1 + e \sin L} \right)^{\frac{e}{2}} \right], \quad (27)$$

in which nautical miles (nm) [3] $e=0.081819190842622$, for WGS-84 [17]. And then,

$$l = 60' \times (L_{X_{i+1}} - L_{X_i}), \quad dlo = 60' \times (\lambda_{X_{i+1}} - \lambda_{X_i}),$$

$$\Delta M = M_{X_{i+1}} - M_{X_i}, \quad (28)$$

$$\tan cm = \frac{dlo}{\Delta M}, \quad (29)$$

$$dm = \begin{cases} l \sec cm & , cm \neq 90^\circ \\ d \operatorname{locos} L_{X_i} & , cm = 90^\circ \end{cases} \quad (30)$$

CONSTRUCTING COMPUTATION PROCEDURES

To completely illustrate the derived governing equations used in each step of the computation procedures, they are summarized as follows.

Step 1. Calculating the great circle information:

The great circle distance and initial course angle are yielded by using equations (18) and (20b), respectively.

The equator crossing points of the great circle are obtained by using equation (25).

The vertices of the great circle are reached by using equations (26a) and (26b).

Step 2. Calculating the waypoints on the GCT under different given initial conditions:

Condition 1: Giving the great circle distances to obtain the latitudes and the longitudes of the waypoints on the GCT. The latitudes and longitudes of the waypoints are calculated by using equations (21) and (22), respectively.

Condition 2: Giving the longitudes of the waypoints to yield the latitudes. The latitudes of the waypoints are calculated by using equation (23d).

Condition 3: Giving the latitudes of the waypoints to reach the longitudes. The longitudes of the waypoints are calculated by using equations (24a) and (24b).

Step 3. Calculating the course and distance between two adjacent waypoints: The Mercator course and distance of every

rhumb line between two adjacent waypoints are calculated by using equations (27), (28), (29) and (30) of spherical Mercator sailings.

DEVELOPING THE NUMERICAL PROGRAM

To deal with GCT problems under all given initial conditions, a program, namely GCTPro_VA, is developed based on the S-VA approach. In addition, for selecting the reasonable number of the waypoints, a diagram of total Mercator distance versus waypoints number (hereafter is called tMd-n diagram) is provided for the navigator. The GCTPro_VA program is coded in the Visual Basic 6.0 (VB6) with the graphical user interface (GUI) for popular and friendly use of the navigator.

VALIDATED EXAMPLES AND DISCUSSIONS

Example 1. A vessel is proceeding from **San Francisco (USA)** to **Sydney (AUSTRALIA)**. The navigator desires to use great circle sailing from $L37^\circ 47.5'N$, $\lambda 122^\circ 27.8'W$ to $L33^\circ 51.7'S$, $\lambda 151^\circ 12.7'E$ (Bowditch, 1981, pp. 616-618).

Required: Using the GCTPro_VA program to calculate the great circle information and the latitudes and longitudes of the waypoints along the GCT at equal interval of great circle distance, 360 nm (6°) apart from the departure (Condition 1). In addition, the relationships of total Mercator distance and numbers of the waypoints are acquired.

Solution: The GCTPro_VA program is run to solve the great circle information and the waypoints on the GCT under

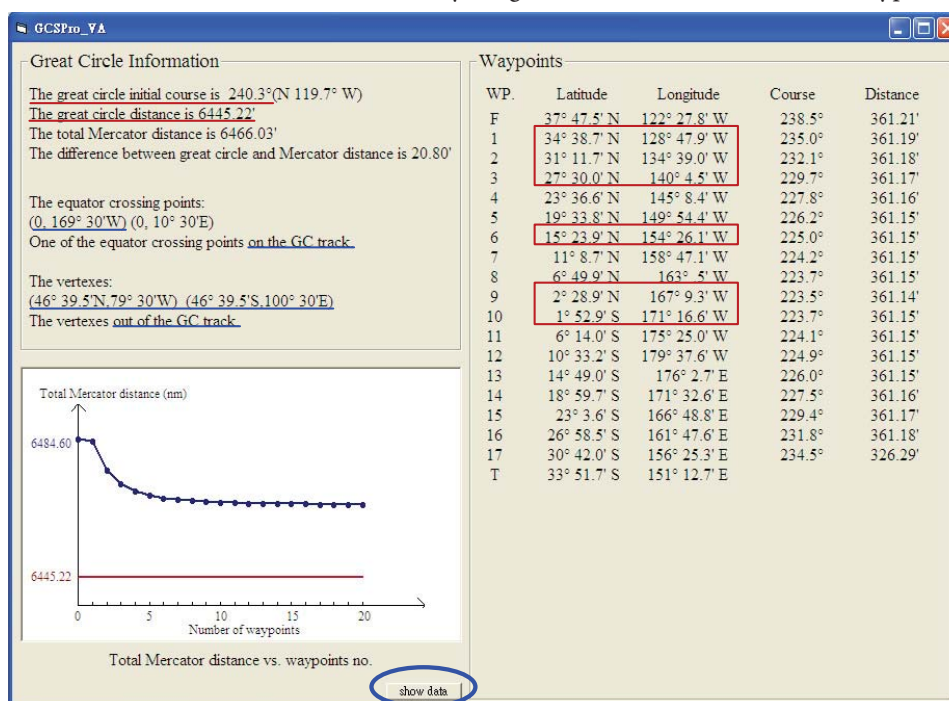


Fig. 3. Results of condition 1 by running the GCTPro_VA program in example 1

condition 1 successfully. Results of the great circle information, the waypoints on the GCT and a tMd-n diagram are all shown in Fig. 3. The comparison of results obtained by the S-VA approach and those by tabular method (Ageton method) [2] is shown in Table 2. In addition, when the button of “show data” in Fig. 3 is clicked, the relationships between the total Mercator distance and numbers of the waypoints on the GCT will be shown in Table 3.

Remark: With respect to the waypoints on the GCT under condition 1, the S-VA approach has been validated by this example. It is noticed that the computerized solution is always more accurate than the tabular method because it is free of rounding errors, which was also reported in Bowditch book [3]. As shown in Table 3 the total Mercator distance of 16 waypoints is nearly equal to that of 8 waypoints and their difference of the distance is less than 1 nm. A reasonable number of waypoints can be considered from this table for the navigator. It is an interesting discovery here.

Example 2. A vessel is proceeding from Sydney (AUSTRALIA) to Balboa (PANAMA). The master desires to use the great circle sailing from $L33^{\circ}51.5'S$, $\lambda151^{\circ}13.0'E$ to $L08^{\circ}53.0'N$, $\lambda079^{\circ}31.0'W$ (Chen et al, 2004, pp. 317-319).

Required:

- Using the GCTPro_VA program to calculate the great circle information and the latitudes and longitudes of the waypoints along the GCT at longitude $170^{\circ}E$ and

Tab. 2. A comparison of results obtained by tabular method and those by the S-VA approach in example 1

Item	Tabular method*	GCTPro_VA
D	6445.5'	6445.22'
C	$240^{\circ}17.5'$	240.3°
V	$L46^{\circ}39.5'S$, $\lambda100^{\circ}29.7'E$	$L46^{\circ}39.5'S$, $\lambda100^{\circ}30.0'E$ $L46^{\circ}39.5'N$, $\lambda79^{\circ}30.0'W$
E	-	$L00^{\circ}00.0'$, $\lambda169^{\circ}30.0'W$ $L00^{\circ}00.0'$, $\lambda010^{\circ}30.0'E$
D_{EX}	6°	$L34^{\circ}39.0'N$, $\lambda128^{\circ}48.3'W$
	12°	$L31^{\circ}12.0'N$, $\lambda134^{\circ}39.3'W$
	18°	$L27^{\circ}30.0'N$, $\lambda140^{\circ}04.3'W$
	36°	$L15^{\circ}24.0'N$, $\lambda154^{\circ}26.3'W$
	54°	$L02^{\circ}29.0'N$, $\lambda167^{\circ}09.3'W$
	60°	$L01^{\circ}52.5'S$, $\lambda171^{\circ}17.3'W$

*Resource : Bowditch, 1981, pp. 616-618 (Ageton method).

Tab. 3. Relationships between waypoints number on the GCT and total Mercator distance (nm) in example 1

waypoints number	total Mercator distance	waypoints number	total Mercator distance
0	6484.60	9	6466.74
1	6483.89	10	6466.56
2	6475.60	11	6466.43
3	6471.67	12	6466.32
4	6469.65	13	6466.24
5	6468.49	14	6466.17
6	6467.77	15	6466.12
7	6467.30	16	6466.07
8	6466.97	17	6466.03

at each 20 degrees of longitude thereafter to longitude $90^{\circ}W$ (Condition 2).

- Using the GCTPro_VA program to calculate the great circle information and the latitudes and longitudes of the waypoints on the GCT at latitude $35^{\circ}S$ and at each 10 degrees of latitude northward to latitude $05^{\circ}N$ (Condition 3).

Solution:

- The GCTPro_VA program is used to solve the great circle information and the waypoints on the GCT under condition 2 successfully. Results of the great circle information, the waypoints on the GCT and a tMd-n diagram are all shown in Fig. 4.
- The GCTPro_VA program is used to solve the great circle information and the waypoints on the GCT under condition 3 successfully. Results of the great circle information, the waypoints on the GCT and a tMd-n diagram are all shown in Fig. 5.

Remark:

1. With respect to the waypoints on the GCT under conditions 2 or 3, the S-VA approach has been validated by this example. A comparison of the results of the GCE method [6] and those of the S-VA approach shows that the proposed approach is as accurate as the GCE method. However, the derived governing equations of the S-VA approach are simpler and clearer than those of the GCE method.

2. The developed GCTPro_VA program has also been verified by examples 1 and 2. It is found, that the GCTPro_VA program shows the advantages of completeness and wide applications for navigator.

CONCLUSIONS

The proposed S-VA approach has systematically derived the spherical triangle formulae for solving the GCT problems and it can handle the waypoints on the GCT

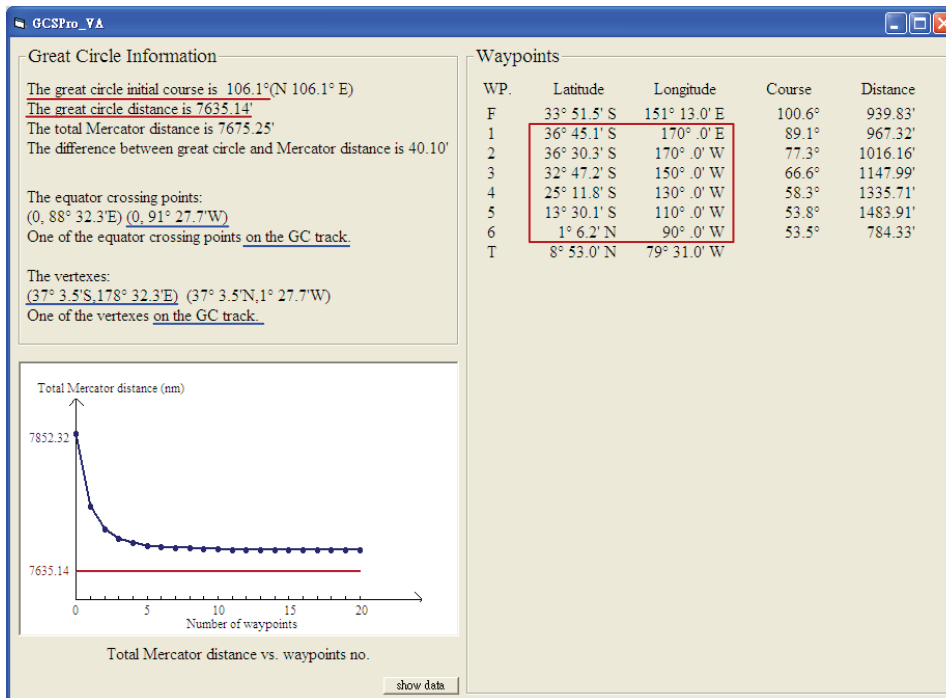


Fig. 4. Results of condition 2 by running the GCTPro_VA program in example 2

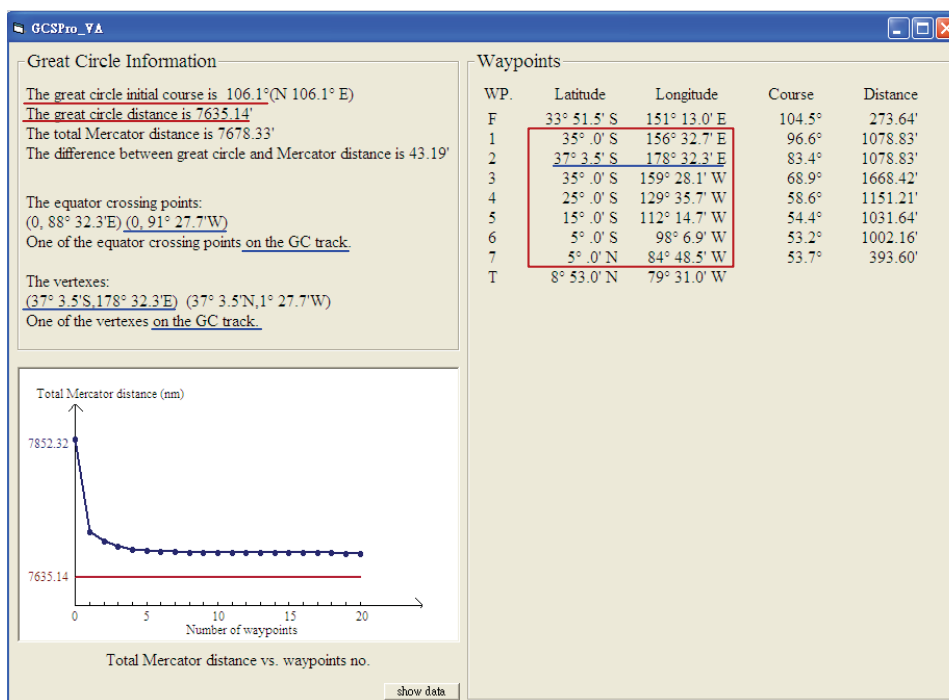


Fig. 5. Results of condition 3 by running the GCTPro_VA program in example 2

under all given initial conditions successfully. Because the mathematical properties of the geometry and algebra are both implied in the S-VA approach, the derivation process becomes more understandable and more straightforward as compared with those of conventional approaches. With the technique of transforming the Earth coordinates system into the Cartesian one and adopting the relative longitude concept, the derived governing equations by using the S-VA approach are simpler and clearer than those by the conventional approaches. Based on the S-VA approach, the GCTPro_VA program has been developed for friendly use of

the navigator. Several benchmark examples are conducted to validate the proposed S-VA approach effectively and to verify the developed GCTPro_VA program successfully.

ACKNOWLEDGEMENTS

The author would like to express his thanks to Professor Jiang-Ren Chang for his valuable suggestions on this paper and Miss Pin-Fang Liu for drawing figures in this paper. In addition, the financial support from National Taiwan Ocean

University under contract number: NTOU-103-001 is highly appreciated.

NOMENCLATURE

N	North pole
S	South pole
F	the departure
T	the destination
X	the waypoints on great circle track
E	the equator crossing point
V	the vertex
L	the latitude
L_F	the latitude of the departure
L_T	the latitude of the destination
L_X	the latitude of the waypoints
L_E	the latitude of the equator crossing point
L_V	the latitude of the vertex
λ	the longitude
λ_F	the longitude of the departure
λ_T	the longitude of the destination
λ_X	the longitude of the waypoints
λ_E	the longitude of the equator crossing point
λ_V	the longitude of the vertex
DLo	the difference of longitude from the departure to the destination
DLo_{FX}	the difference of longitude from the departure to the waypoints; a dihedral angle in Fig. 2
DLo_{FE}	the difference of longitude from the departure to the equator crossing point
DLo_{FV}	the difference of longitude from the departure to the vertex
D	the great circle distance from the departure to the destination
D_{FX}	the great circle distance from the departure to the waypoints
C	the great circle initial course angle from the departure to the destination; a dihedral angle in Fig. 2
M	the meridional parts between the given latitude and the equator
a_e	the equatorial radius of the Earth, $a_e=3437.74677078$ nm
e	the eccentricity of the Earth, $e=0.081819190842622$ from WGS-84
l	the difference of latitude between two adjacent waypoints
dlo	the difference of longitude between two adjacent waypoints
ΔM	the difference of meridional parts between two adjacent waypoints
cm	the course angle in spherical Mercator sailings
dm	the distance in spherical Mercator sailings

REFERENCES

- Bennett, G. G.: Practical Rhumb Line Calculations on the Spheroid. The Journal of Navigation, 49(1), pp. 112-119, 1996.
- Bowditch, N.: American Practical Navigator. Volume 2, DMAH/TC, Washington, 1981.
- Bowditch, N.: The American Practical Navigator. 2002 Bicentennial Edition, National Imagery and Mapping Agency, Maryland, 2002.
- Chen, C. L.: New Computational Approaches for Solving the Great Circle Sailing and Astronomical Vessel Position. Ph.D. Dissertation, Department of Civil Engineering, National Taiwan University, Taipei, Taiwan, 2003.
- Chen, C. L., Hsieh, T. H. and Hsu, T. P.: A Novel Approach to Solve the Great Circle Sailings Based on Rotation Transformation. Journal of Marine Science and Technology, 23(1), pp 13-20, 2015.
- Chen, C. L., Hsu, T. P., and Chang, J. R.: A Novel Approach to Great Circle Sailings: The Great Circle Equation. The Journal of Navigation, 57(2), pp. 311-320, 2004.
- Chen, C. L., Liu, P. F. and Gong, W. T.: A Simple Approach to Great Circle Sailing: The COFI Method. The Journal of Navigation, 67(3), pp. 403-418, 2014.
- Clough-Smith, J. H.: An Introduction to Spherical Trigonometry. Brown, Son & Ferguson, Ltd., Glasgow, 1966.
- Cutler, T. J.: Dutton's Nautical Navigation. Fifteenth Edition, Naval Institute Press, Maryland, 2004.
- Earle, M. A., Sphere to Spheroid Comparison. The Journal of Navigation, 59(3), pp. 491-496, 2006.
- Greenberg, M. D.: Advanced Engineering Mathematics. Second Edition, Prentice-Hall International, Inc., 1998.
- Holm, R. J.: Great Circle Waypoints for Inertial Equipped Aircraft. NAVIGATION, Journal of the Institute of Navigation, 19(2), pp. 191-194, 1972.
- Jofeh, M. L.: The Analysis of Great-circle Tracks. The Journal of Navigation, 34(1), pp. 148-149, 1981.
- Keys, G.: Practical Navigation by Calculator. Stanford Maritime, London, 1983.
- Miller, A. R., Moskowitz, I. S. and Simmen, J.: Traveling on the Curved Earth. NAVIGATION, Journal of the Institute of Navigation, 38(1), pp. 71-78, 1991.
- Nastro, V. and Tancredi, U.: Great Circle Navigation with Vectorial Methods. The Journal of Navigation, 63(3), pp. 557-563, 2010.
- National Imagery and Mapping Agency (NIMA): Department of Defense World Geodetic System 1984: Its definition and relationship with local geodetic systems. Third Edition, Technical Report NIMA TR8350.2, 2000.
- Royal Navy: Admiralty Manual of Navigation: The Principles of Navigation, Volume 1. 10th Edition. The Nautical Institute, London, 2008.
- Spiegel, M. R., Lipschutz, S. and Spellman, D.: Vector analysis and an introduction to Tensor analysis. Second Edition, McGraw-Hill, 2009.

CONTACT WITH THE AUTHOR

Chih-Li Chen, Ph.D.

Merchant Marine Department
National Taiwan Ocean University
2 Pei-Ning Road, Keelung, 20224
TAIWAN

Email: clchen@mail.ntou.edu.tw

THE SENSITIVITY OF STATE DIFFERENTIAL GAME VESSEL TRAFFIC MODEL

Józef Lisowski, Prof.
Gdynia Maritime University, Poland

ABSTRACT

The paper presents the application of the theory of deterministic sensitivity control systems for sensitivity analysis implemented to game control systems of moving objects, such as ships, airplanes and cars. The sensitivity of parametric model of game ship control process in collision situations have been presented. First-order and k-th order sensitivity functions of parametric model of process control are described. The structure of the game ship control system in collision situations and the mathematical model of game control process in the form of state equations, are given. Characteristics of sensitivity functions of the game ship control process model on the basis of computer simulation in Matlab/Simulink software have been presented. In the end, have been given proposals regarding the use of sensitivity analysis to practical synthesis of computer-aided system navigator in potential collision situations.

Keywords: marine transport; safety of navigation, game control, sensitivity analysis

INTRODUCTION

By taking into consideration the form of the quality index the problem of optimal control of the technical processes may be split into three groups for which cost of the process course:

- is a univocal control function,
- depends on the way of control and also on a certain random event of a known statistical description,
- is defined by a choice of the control method and by a certain indefinite factor of an unknown statistical description, respectively.

The last group of the problems refers to game control systems the synthesis of which is performed by using methods of the games theory [1,2,3,13].

The following types of games can be distinguished:

- with regard to the number of players: two-person and n-person,
- with regard to the strategy sets: finite and infinite,
- with regard to the nature of co-operation: non-coalition, co-operative - through the relationships established earlier and coalition ones,
 - with regard to the nature of the prize: zero-sum - closed with a saddle point determined by the optimal pure strategies and those of any sum, e.g.: international trade,
 - with regard to their form of the goal function: matrix, non-continuous and convex,
 - with regard to the nature of conducting the game: in the normal form - one-step static ones and in the extensive

form as multi-step games determined by a sequence of movements executed alternately within the kinematical and dynamical processes, the games in their extensive form are split into: positional, stochastic and differential,

- with regard to the nature of information: with complete and incomplete information,
- with regard to the kind of an opponent: with a thinking opponent and with the nature – the environment performing random movements and not interested in the final result of the game [14].

Generally, may be distinguished three classes of the control problems which may offer possibilities to use games both for the description and synthesis of the optimal control:

- multi-layer hierarchical systems. One of the essential hierarchical languages for the steering systems of various nature and methods of determining optimal control is the theory of games including common interests and the right to the first turn [18];
 - object with no information available from the disturbances operating on such object. In this case we have only the state equations of the object and a set of acceptable steering actions. Such control should be then determined as to ensure the minimal functional, under a condition that the disturbance tends to its maximum; in this case the differential game should be solved with a min- max optimum condition [10,16,17,20,22];
 - object encountering a greater number of the moving objects of different quality index and final goals. An example,

in this case, may be a process of steering a ship in collision situations when encountering a greater number of the moving or non-moving objects (vessels, underwater obstructions, shore line, etc), i.e. a differential game with many participants [8,9,11,12].

This paper presents, as an example, the sensitivity of parametric model of differential game ship control process in collision situations.

DIFFERENTIAL GAME VESSEL TRAFFIC MODEL

The way of steering a ship - which is a multi-dimensional and non-linear dynamic object - depends on the range and accuracy of information on the prevailing navigational situation and on the adopted model of the process. The variety of the models to be adopted directly influences the synthesis of various algorithms supporting the navigator's work, and then on the effects of a safe control of the ship's movement.

As the process of steering the ship in collision situations, when a greater number of objects is encountered, often occurs under the conditions of indefiniteness and conflict, accompanied by an inaccurate co-operation of the objects within the context of COLREG Regulations, then the most adequate model of the process to be adopted is a model of a differential game, in general, of j tracked ships as objects of steering (Fig. 1).

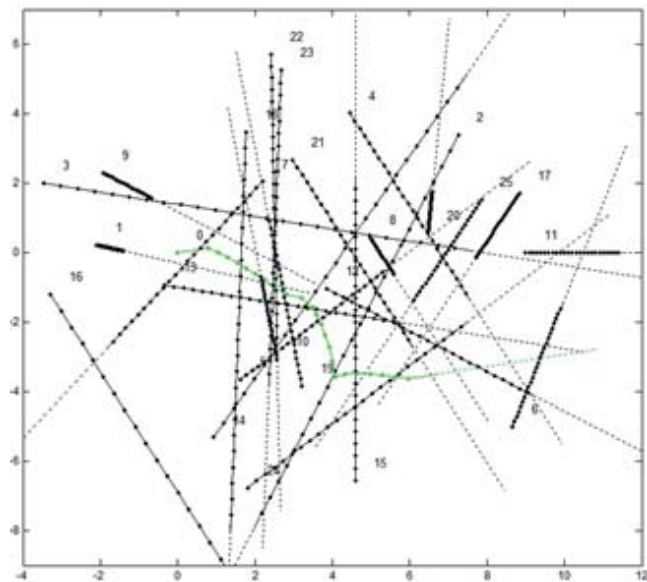


Fig. 1. Situation of relative motion of own ship (green trajectory) and j met ships

The diversity of selection of possible models directly affects the synthesis of the ship's handling algorithms which are afterwards effected by the ship's handling device directly linked to the ARPA anti-collision system and, consequently, determines the effects of the safe and optimal control.

The structure of the game control process model of own ship in collision situations at sea is presented in Fig. 2.

The control process is described by state equations:

$$\dot{x} = f(x, u, t) \quad (1)$$

constraints of state and control:

$$g(x, u, t) \leq 0 \quad (2)$$

and quality control index:

$$I = \int_{t_0}^{t_K} f_o(x, u, t) dt \quad (3)$$

where:

x - state variable,

u - control variable,

t - time.

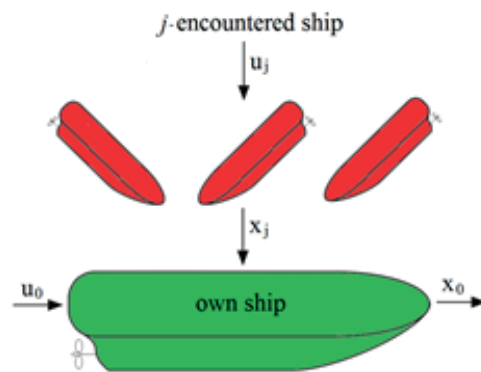


Fig. 2. Game ship control process: u_0 - control of own ship, u_j - control of j -encountered ship, x_0 - state of own ship, x_j - state of j -encountered ship

The current state of the control process is determined by the co-ordinates of the own ship's position and the positions of the encountered objects (Fig. 3):

$$\left. \begin{aligned} x_0 &= (X_0, Y_0) \\ x_j &= (X_j, Y_j) \\ j &= 1, 2, \dots, m \end{aligned} \right\} \quad (4)$$

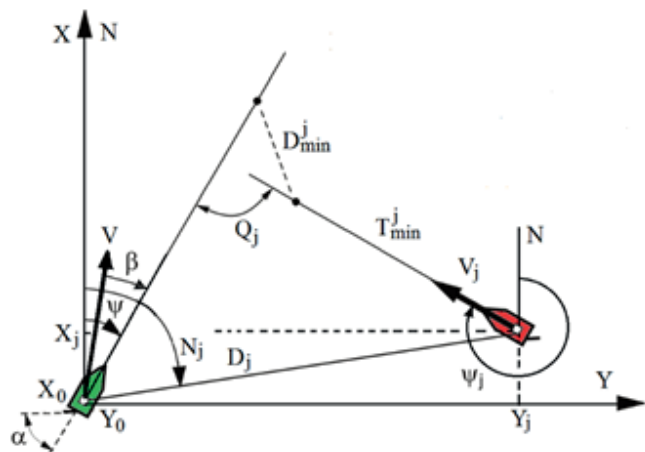


Fig. 3. Situation of relative motion of own ship and j met ship

The system generates its control at the moment t_k on the basis of data received from the ARPA anti-collision system pertaining to the positions of the encountered ships:

$$x(t_k) = \begin{bmatrix} x_0(t_k) \\ x_j(t_k) \end{bmatrix} \quad j = 1, 2, \dots, m \quad k = 1, 2, \dots, K \quad (5)$$

The constraints for the state co-ordinates:

$$\{x_0(t), x_j(t)\} \in P \quad (6)$$

are navigational constraints, while control constraints:

$$u_0 \in U_0, u_j \in U_j \quad j = 1, 2, \dots, m \quad (7)$$

take into consideration: the ship's movement kinematics, recommendations of the COLREG Rules and the condition to maintain a safe passing distance D_s as per relationship:

$$D_{\min}^j = \min D_j(t) \geq D_s \quad (8)$$

where:

D_{\min}^j - minimum approach distance of the own ship to met j-th ship.

By taking into consideration the equations of the own ship hydromechanics and equations of the own ship relative movement to the j-th encountered ship, the state process equations take the following form:

$$\left. \begin{aligned} \dot{x}_1 &= x_2 \\ \dot{x}_2 &= a_1 x_2 x_3 + a_2 x_3 |x_3| x_4 + a_3 x_3 |x_3| u_1 \\ \dot{x}_3 &= a_4 x_3 |x_3| |x_4| x_4 + a_5 x_3 |x_3| x_4^2 + a_6 x_2 x_3 x_4 |x_4| + \\ &\quad a_7 x_2 x_3 x_4 |x_4| + a_8 x_3 |x_3| + a_9 x_5 |x_5| x_6 + a_{10} x_3 |x_3| x_4 u_1 \\ \dot{x}_4 &= a_4 x_3 x_4 + a_5 x_3 x_4 |x_4| + a_6 x_2 x_4 + a_{11} x_2 + a_{10} x_3 u_1 \\ \dot{x}_5 &= a_{12} x_5 + a_{13} u_2 \\ \dot{x}_6 &= a_{14} x_6 + a_{15} u_3 \\ \dot{x}_{6+j} &= -x_3 + x_{7+j} x_2 + x_{9+j} \cos x_{8+j} \\ \dot{x}_{7+j} &= -x_2 x_{6+j} + x_{9+j} \sin x_{8+j} \\ \dot{x}_{8+j} &= a_{15+j} x_{9+j} u_{j1} \\ \dot{x}_{9+j} &= a_{16+j} x_{8+j} |x_{8+j}| + a_{17+j} u_{j2} \end{aligned} \right\} \quad (9)$$

where state variables and control values are represented by:

$x_1 = \psi$ - course of the own ship,
 $x_2 = \dot{\psi}$ - angular turning speed of the own ship,
 $x_3 = V$ - speed of the own ship,
 $x_4 = \beta$ - drift angle of the own ship,
 $x_5 = n$ - rotational speed of the screw propeller of the own ship,
 $x_6 = H$ - pitch of the adjustable propeller of the own ship,
 $x_{6+j} = X_j$ - x coordinate of the j-th ship position,
 $x_{7+j} = Y_j$ - y coordinate of the j-th ship position,

$x_{8+j} = N_j$ - bearing of the j-th ship or Q_j - relative meeting angle,

$x_{9+j} = D_j$ - distance to j-th ship.

$u_1 = \alpha_r$ - reference rudder angle of the own ship,

$u_2 = n_r$ - reference rotational speed of the own ship's screw propeller,

$u_3 = H_r$ - reference pitch of the adjustable propeller of the own ship,

$u_{j1} = \psi_j$ - course of the j-th ship,

$u_{j2} = V_j$ - speed of the j-th ship [5,7,19].

SENSITIVITY DEFINITIONS OF PROCESS MODEL AND OPTIMAL PROCESS CONTROL

By sensitivity of control systems one usually means dependence of their properties on parameters' variation. Sensitivity theory became an independent scientific branch of cybernetics and control theory in the 1960s. This was connected in major part with quick development of self-tuning systems that were constructed for effective operation under parametric disturbances. Lately, sensitivity theory methods were widely used for solving various theoretical and applied problems with analysis and synthesis, identification, adjustment, monitoring, testing, tolerance distribution [4,6].

The same distinction is made between the sensitivity of the model control process for changing its parameters and process optimal control sensitivity to changes in its parameters and disturbance influence [15,21].

Previous papers dealt with sensitivity of deterministic systems, but not with game systems. In sea, land and air transport, processes regarding both own object and many encountered objects, occur.

Control of such processes, due to the high proportion of human subjectivity in the decision-making manoeuvre, often takes form of the control of game character.

The simplest method of sensitivity analysis consists in numerical investigation of system parametric model over the whole range of variation of the determining set of parameters.

The main investigation method in sensitivity theory consists in using so called sensitivity functions.

Let a_1, \dots, a_m be a set of parameters constituting a complete set a .

Moreover, let be assumed a function of state variables $F[x_i(t, a)]$ ($i=1, \dots, n$).

The following partial derivative:

$$s_a^{pm} = \frac{\partial F[x(t, a)]}{\partial a} \quad (10)$$

is called first-order sensitivity function of the parametric process model s_a^{pm} .

In automatic control literature first-order sensitivity function is often called simply "sensitivity function".

Theoretically, we can also consider features of the sensitivity functions of k-th order of the parametric model $s_{k,a}^{pm}$ in the

following form:

$$s_{k,a}^{pm} = \frac{\partial^k F[x(t, a)]}{\partial a_1^{k_1} \dots \partial a_m^{k_m}} \quad (11)$$

$$k_1 + \dots + k_m = k$$

DETERMINATION OF SENSITIVITY FUNCTION OF THE DIFFERENTIAL GAME VESSEL TRAFFIC MODEL

As a function of state process variables $F[x(t,a)]$ the risk of collision r_j is assumed in the following form:

$$r_j(x) = \left[w_1 \left(\frac{D_{min}^j}{D_s} \right)^2 + w_2 \left(\frac{T_{min}^j}{T_s} \right)^2 + w_3 \left(\frac{D_j}{D_s} \right)^2 \right]^{\frac{1}{2}} \quad (12)$$

where:

w_1, w_2, w_3 – weight coefficients depending on the visibility at sea and dynamic length and breadth of the met j -th ship (Fig. 4).

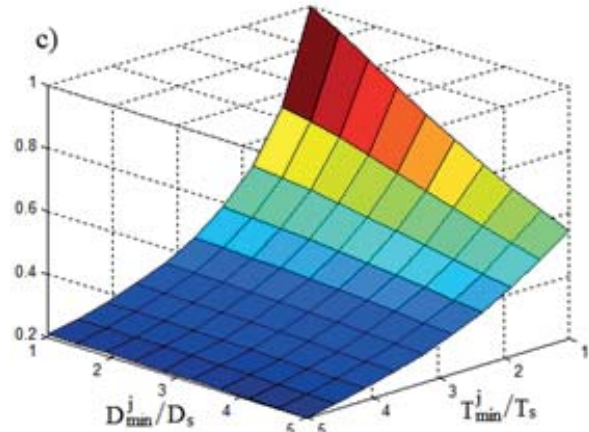
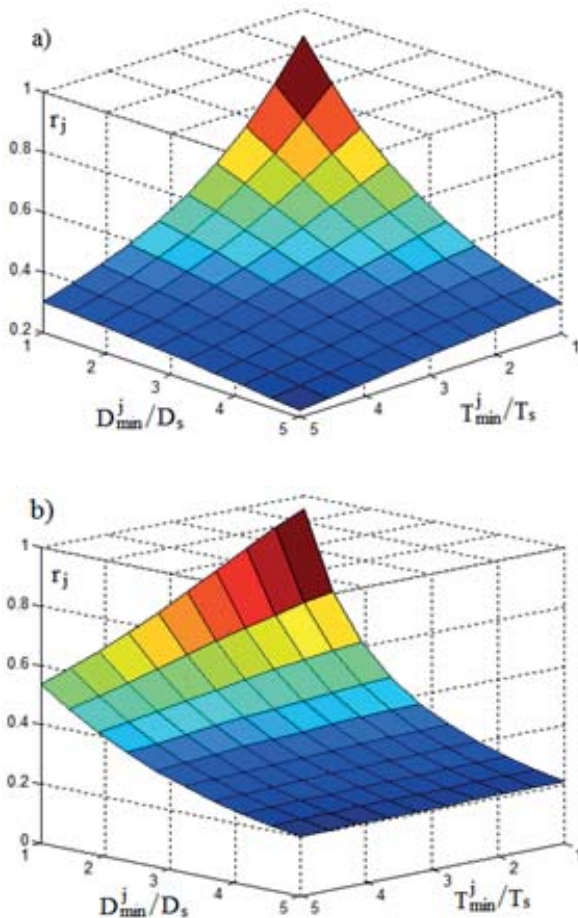


Fig. 4. Examples of risk collision function r_j : a) $w_1=w_2=w_3=0,4$ b) $w_1=0,9; w_2=0,1; w_3=0,1$ c) $w_1=0,1; w_2=0,9; w_3=0$

The sensitivity function according to (10) can be represented as:

$$s_{a_i}^{pm} = \frac{\partial F[x(t, a)]}{\partial a_i} = \frac{\partial r_j[x(t, a_i)]}{\partial a_i} = s_r^i \quad (13)$$

As a measure of safe control process model sensitivity to changes of process parameters, is taken a relative change of risk collision r_j caused by deviation of the coefficient a_i in state equations by ∂a_i .

The coefficients of state equations of model process have been varied within $\pm 10\%$ from their rated value a_i and each time the anti-collision manoeuvre was simulated in Matlab/Simulink software, then relative change of risk collision was calculated by using the formula (13).

As a result of computer simulation investigations the characteristics of sensitivity functions s_r^i at $w_1 = w_2 = w_3 = 1$ weight coefficients (Fig. 5), were obtained.

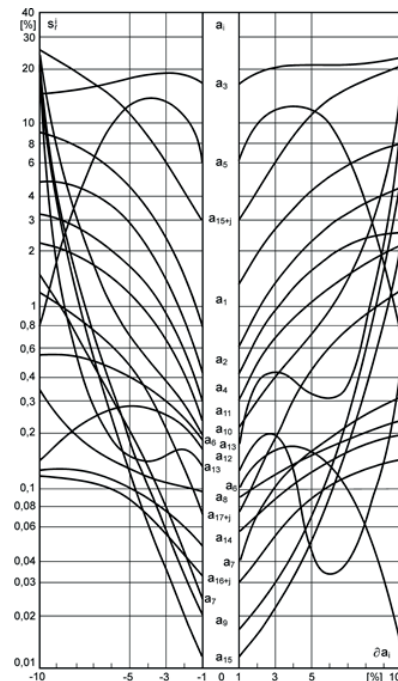


Fig. 5. Sensitivity functions of the risk collision to the changes in coefficients of state equations of process model of situation motion of own ship and j -th met ship

CONCLUSIONS

The model process sensitivity to changes of individual coefficients of the state equations varies from 0,01% to 25%.

The highest sensitivity is shown by the coefficients: a_1 , a_3 , a_5 and a_{15+j} , the lowest one by the coefficients: a_7 , a_9 , a_{15} and a_{16+j} .

The highest changes of sensitivity, so called second-order sensitivity, have occurred for the coefficients: a_7 , a_9 , a_{10} , a_{13} and a_{15} .

The sensitivity functions obtained as a result of computer simulation investigations define the requirements regarding range and accuracy of identification of ship's kinematics and dynamics for the model useful for the safe control system synthesis.

The future investigations should be aimed at obtaining further simplification of the process model by taking into account their sensitivity functions.

BIBLIOGRAPHY

1. Astrom K.J.: Model uncertainty and robust control. Lecture notes on iterative identification and control design. Lund Institute of Technology, Sweden, 2000, pp. 63-100.
2. Cruz J.B.: Feedback systems. Mc Graw-Hill Book Company, New York, 1972.
3. Dorf R.C. and Bishop R.H.: Modern control systems. Addison-Wesley, California, 1998.
4. Eslami M.: Theory of sensitivity in dynamic systems. Springer-Verlag, Berlin, 1994.
5. Fossen T.I.: Marine craft hydrodynamics and motion control. Wiley, Trondheim, 2011.
6. Fujarewicz K.: Structural sensitivity analysis of systems with time delay (in Polish), XVIII Krajowa Konferencja Procesów Dyskretnych (18th Domestic Conference on Discrete Systems), Zakopane, 2014.
7. Gierusz W. and Lebkowski A.: The research ship "Gdynia". Polish Maritime Research, Vol. 19, No. 74, 2012, pp. 11-18.
8. Isaacs R.: Differential games. John Wiley and Sons, New York, 1965.
9. Lazarowska A.: Safe ship control method with the use of ant colony optimization. Solid State Phenomena, Vol. 210, 2014, pp. 95-101.
10. Miller A., Rybczak M.: Model predictive control algorithm verification with the use of real time xPC target platform. Joint Proceedings, No. 84, 2014, pp. 73-84.
11. Mohamed-Seghir M.: The branch-and-bound method, genetic algorithm, and dynamic programming to determine a safe ship trajectory in fuzzy environment. 18th International Conference on Knowledge Based and Intelligent Information and Engineering Systems. Procedia Computer Science, No. 35, 2014, pp. 634-643.
12. Nisan N., Roughgarden T., Tardos E., Vazirani V.V.: Algorithmic game theory. Cambridge University Press, New York, 2007, pp. 717-733.
13. Nise N.S.: Control systems engineering. Wiley, California, 2015.
14. Osborne M.J.: An introduction to game theory. Oxford University Press, New York, 2004.
15. Rosenwasser E. and Yusupov R.: Sensitivity of automatic control systems. CRC Press, Boca Raton, 2000.
16. Rudnicki J.: Application issues of the semi-Markov reliability model. Polish Maritime Research, Vol. 22, No. 1, pp. 55-64.
17. Sanchez-Pena R.S. and Sznaier M.: Robust systems theory and applications. Wiley, New York, 1998.
18. Skogestad S. and Postlethwaite I.: Multivariable feedback control. Wiley, Chichester, 2005.
19. Szlupczynski R.: Evolutionary sets of safe ship trajectories with speed reduction manoeuvres within traffic separation schemes. Polish Maritime Research, Vol. 81, No. 1, 2014, pp. 20-27.
20. Tomera M.: Dynamic positioning system for a ship on harbour manoeuvring with different observers. Experimental results. Polish Maritime Research, Vol. 83, No. 3, 2014, pp. 13-21.
21. Wierzbicki A.: Models and sensitivity of control systems. Wydawnictwa Naukowo-Techniczne, Warszawa, 1977.
22. Zwierzewicz Z.: The design of ship autopilot by applying observer – based feedback linearization. Polish Maritime Research, Vol. 22, No. 1, pp. 16-21.

CONTACT WITH THE AUTHOR

Józef Lisowski
Gdynia Maritime University
83 Morska Str.
81-225 Gdynia
POLAND

PARAMETRICAL METHOD FOR DETERMINING OPTIMAL SHIP CARRYING CAPACITY AND PERFORMANCE OF HANDLING EQUIPMENT

Jan P. Michalski, Assoc. Prof.
Gdańsk University of Technology, Poland

ABSTRACT

The paper presents a method of evaluating the optimal value of the cargo ships deadweight and the coupled optimal value of cargo handling capacity. The method may be useful at the stage of establishing the main owners requirements concerning the ship design parameters as well as for choosing a proper second hand ship for a given transportation task. The deadweight and the capacity are determined on the basis of a selected economic measure of the transport effectiveness of ship – the Required Freight Rate. The mathematical model of the problem is of a deterministic character and the simplifying assumptions are justified for ships operating in the liner trade. The assumptions are so selected that solution of the problem is obtained in analytical closed form. The presented method can be useful for application in the preliminary ship design or in the simulation of pre-investment transportation task studies.

Keywords: ship design; deadweight and cargo handling optimization; required freight rate

INTRODUCTION

Methodology of engineering design with extreme of selected function includes both a general formulation of the problem, eg. [1], [2], as well as considerations relating to the selected technical objects, such as ships [3] ÷ [8]. The area of research in this field are aspects such as criterial measurement assessment values of the ship, defining areas of feasible solutions or algorithms for optimal solutions. The ship-owner - investor making an investment decision - ordering the construction of the ship, or buying a ship - expects an optimal object in the sense important for him. Determining the parameters of such a ship, guided only by intuition and experience does not always lead to the correct choice, as aptness depends on future market conditions in shipping (prices, costs, inflation) [9], which forecasts are subject to uncertainty.

To make the right investment decisions calculation methods to simulate future market conditions and the projected effects of technical and economic can be helpful. In the case of cargo ships such issue can be described by a mathematical model, and the simulated results may provide grounds for making an investment decision. As an example, the method can be used [10] ÷ [13] for a preliminary ship design parameters optimal in the sense of, respectively, minimizing the cost of construction of the hull, fuel consumption, or the lowest freight rate providing the required return on investment.

Parametric studies done with the method described in [12] indicate a significant correlation of optimal carrying capacity of the ship from the efficiency of reloading equipment, on which depends the time the ship is in port intended for loading and unloading. The method presented in the article allows to investigate the relationship between the optimum load capacity of the ship and optimum performance of handling equipment - making the cost of handling dependant of the performance of the handling, and thus from the time of handling, which express the accepted method of analytical relationships. The approach is a generalization of the method described in [12], where the optimum load capacity of the vessel, minimizing the required rate of freight RFR (Required Freight Rate), were determined by arbitrarily ingested handling performance Q and the assumed rate of W_j for handling a cargo unit.

The presented method extends the range of optimization parameters of the designed ship; has both cognitive value, as illustrated by the results presented preliminary parametric studies and the resulting general conclusions and utilitarian value, which is reflected in the attached solution design task example.

STATEMENT OF THE PROBLEM AND OBJECTIVES

The subject of the research is to develop a mathematical model of the method for determining the capacity P_n of cargo

ships and productivity Q of handling equipment - optimal in terms of minimizing the required freight rate RFR for the transport of cargo. It is assumed that both the handling and the unit cost of handling depend on the performance of the Q handling equipment. The relationship $W_j = W_j(Q)$ means a fee for handling unit load with devices of Q capacity.

The issue is described by the collection of the following relationship:

$$RFR = RFR(Pn, Q, \bar{x}) \quad (1)$$

$$\begin{cases} \frac{\partial RFR(Pn, Q, W_j(Q), \bar{x})}{\partial Pn} = 0 \longrightarrow Pn_{opt} = f(W_j(Q), \bar{x}) \\ \frac{\partial RFR(Pn, Q, W_j(Q), \bar{x})}{\partial Q} = 0 \longrightarrow Q_{opt} = f(W_j(Q), \bar{x}) \end{cases} \quad (2)$$

Accepted labels of vector method parameters \bar{x} have the following interpretation:

- Pn – dead-weight tonnage;
- Q – performance of handling equipment;
- W_j – unit cost of loading and unloading;
- \bar{x} – vector of other parameters describing the issue considered;
- v – operational speed;
- R – the length of the cruise route;
- C_j – the unit cost of fuel;
- C_A – Admiralty factor;
- C_H – the coefficient of cost to performance handling proportionality;
- G_j – unit fuel consumption;
- T_M – time route in one cruise;
- T_Q – total time of loading and unloading in one cruise;
- T_O – waiting time on the roadster and in the port;
- Z – weight of supplies;
- Z_H – the number of days of operation of the ship during the year;
- A – the rate of annual depreciation;
- i – average annual rate of inflation;
- m – the number of years of the ship operation;
- n – number of voyages per year;
- r – required rate of return of investment;
- t – tax rate;
- ε – the average capacity utilization rate of the ship;
- λ – the average rate of carrying capacity utilization of the ship;
- η – ship displacements utilization factor;
- μ – ratio of annual maintenance costs.

MATHEMATICAL MODEL OF THE ISSUE

As far as criterial measurement for evaluating the values of the designed ship, expressing its economic and technical effectiveness as in [3] ÷ [6] or in [9] ÷ [12], the minimum required rate of freight RFR has been adopted. The rate of RFR is the lowest rate of freight ensuring a fixed rate of return on investment, at incurred capital costs and operating and other parameters of the problem.

The adoption of the minimum rate of RFR as a measure of evaluation criterion values of the ship is justified by the fact that the future of real market conditions and freight rates, the highest yield is obtained with the smallest ship of the required freight rate [3], [5], [8]. If the future actual freight rates prove to be higher than the minimum freight rate RFR, the actual rate of return will be higher than the rate assumed. When future freight rates are lower than the rate of RFR, then the investment will not provide the assumed profitability.

It was assumed that the cost of construction (or purchase) of a cargo ship with a fixed speed depends mainly on the capacity Pn and grows slower than a linear function [8], [12]; therefore the cost of investment J can be approximated by a simplification of equation:

$$J = K_J \cdot Pn^{2/3} \quad (3)$$

where the proportionality coefficient K_J is determined on the basis of price J_o and capacity Pn_o of the ship like:

$$K_J = J_o \cdot Pn_o^{-2/3} \quad (4)$$

Annual operating expenses of a ship AOC (Annual Operating Cost), which depend on the capacity of the ship, relate mainly to the cost of fuel consumed and the cost of cargo handling operations. The average annual cost of lubricating oil and repair factor expressed as $\mu > 1$ take into account the increasing cost of fuel. Associated with the drive annual operating costs AOC of the vessel making during the year n cruises, with the time of the route T_M , are:

$$AOC = n \cdot T_M \cdot \mu \cdot C_j \cdot G_j \cdot Ne \quad (5)$$

Expressing propulsion power Ne with admiralty equation, where D is the displacement of the ship, and C_A is the ration of the Admiralty, a relationship is obtained:

$$AOC = \mu \cdot n \cdot T_M \cdot C_j \cdot G_j \cdot \frac{D^{2/3} \cdot v^3}{C_A} = \mu \cdot n \cdot T_M \cdot C_j \cdot G_j \cdot \left[\left(\frac{\varepsilon \cdot \lambda \cdot Pn}{\eta} \right)^{2/3} \cdot \frac{v^3}{C_A} \right] = K_C \cdot n \cdot Pn^{2/3} \quad (6)$$

presuming designation:

$$K_C = \frac{\mu \cdot C_j \cdot G_j \cdot v^2 \cdot R}{C_A} \cdot \left(\frac{\varepsilon \cdot \lambda}{\eta} \right)^{2/3} \quad (7)$$

Capacity utilization rates and displacements are defined by the relationship:

$$\lambda = \frac{Pn - Z}{Pn} = const \quad \eta = \frac{Pn}{D} = const \quad (8)$$

where Z is the mass of supplies (fuel) consumed in one cruise.

Loading and unloading time has a significant impact on the efficiency of maritime transport. The size of income for freight depends on the quantity of goods carried - increases with: load capacity and speed of the ship, shortening time handling thanks to load handling devices of increasing productivity, for which the fee is charged adequately. It is assumed that the unit

cost W_j for handling unit load is directly proportional to the efficiency of the Q handling equipment, and the performance of ballast system provides secure vessel reloading.

The value of empirically specific proportionality factor $C_H = W_j/Q$ depends on local market conditions in the ports of the considered shipping line.

The costs of handling by port facilities (loading and unloading) AHC (Annual Handling Cost) depends on the weight of the load, the number of trips a year n, and the unit charge W_p , dependent on performance Q:

$$W_j = C_H \cdot Q \quad (9)$$

Under this assumption the annual cost of handling is:

$$AHC = n \cdot (2 \cdot \varepsilon \cdot \lambda \cdot Pn) \cdot W_j = 2 \cdot \varepsilon \cdot \lambda \cdot n \cdot C_H \cdot Q \cdot Pn = Kh \cdot n \cdot Q \cdot Pn \quad (10)$$

where the factor Kh means:

$$Kh = 2 \cdot \varepsilon \cdot \lambda \cdot C_H \quad (11)$$

The time of one cruise T consists of a rout time T_M , waiting time on the roadstead and in the port T_o , and from the time of loading and unloading T_Q , the total capacity of handling equipment is Q:

$$T = T_M + T_o + T_Q = \frac{R}{v} + T_o + 2 \cdot \frac{\varepsilon \cdot \lambda \cdot Pn}{Q} \quad (12)$$

The number of cruises n made during the year by the ship depends on the time Z_H of operation of the vessel during the year and one cruise time T on the route with a range of R:

$$n = \frac{Z_H}{T} = \frac{Z_H}{\frac{R}{v} + T_o + 2 \cdot \frac{\varepsilon \cdot \lambda \cdot Pn}{Q}} = \frac{Kq \cdot Q}{Kr \cdot Q + Kp \cdot Pn} \quad (13)$$

Adopted auxiliary variables mean:

$$Kq = Z_H \cdot v \quad Kr = R + T_o \cdot v \quad Kp = 2 \cdot \varepsilon \cdot \lambda \cdot v \quad (14)$$

The annual capacity of the vessel (ACC Annual Cargo Capacity) is:

$$ACC = n \cdot \varepsilon \cdot \lambda \cdot Pn \quad (15)$$

After taking into account the depreciation of the ship A and a rate of inflation i and tax and interest rate t, discounted balance of the financial cost of the investment and ongoing m years of operation of the ship with an initial investment cost J is expressed by the relationship:

$$\frac{AAC}{CRFT(r, m, i, t)} = J + \frac{AOC + AHC + A}{CRFT(r, m, i, t)} \quad (16)$$

The coefficient of return of capital after tax CRFT (Capital Recovery Factor after Tax) is defined by the relationship:

$$CRFT(r, m, i, t) = \frac{(r + i + r \cdot i)}{1 - (1 + r + i + r \cdot i)^{-m} \cdot (1 - t)} \quad (17)$$

The annual allocations of linear depreciation loss of value of the vessel are:

$$A = \frac{J}{m} = \frac{K_J \cdot Pn^{2/3}}{m} \quad (18)$$

The discounted annual costs AAC (Annual Average Costs) are:

$$AAC(Pn, Q) = J(Pn) \cdot CRFT(r, m, i, t) + AOC(Pn) + AHC(Pn, Q, W_j) + A(Pn, m) \quad (19)$$

OPTIMAL CAPACITY AND PERFORMANCE OF HANDLING EQUIPMENT

Freight rate bringing income to cover costs within m years of operation of the ship, at the required rate of return of investment r, t tax rate, defines the minimum wage requirement RFR. The rate is the ratio of annual income for freight AAC to the annual capacity of the ship ACC:

$$RFR(Pn, Q, \bar{x}) = \frac{AAC}{ACC} = \frac{J \cdot CRFT + AOC + AHC + A}{ACC} = \frac{Pn^{-1/3}}{\varepsilon \cdot \lambda} \left(\frac{K_J \cdot (CRFT + m^{-1}) \cdot (Kr \cdot Q + Kp \cdot Pn)}{Kq \cdot Q} + Kc \right) + \frac{Kh \cdot Q}{\varepsilon \cdot \lambda} \quad (20)$$

The stationary point of function RFR - defined from the necessary condition of the existence of extreme - is the solution of equations in relation to its unknowns Q and PN:

$$\frac{\partial RFR(Pn, Q, W_j(Q), \bar{x})}{\partial Q} = \frac{\partial}{\partial Q} \left[\frac{Pn^{-1/3}}{\varepsilon \cdot \lambda} \left(\frac{K_J \cdot (CRFT + m^{-1}) \cdot (Kr \cdot Q + Kp \cdot Pn)}{Z_H \cdot v \cdot Q} + Kc \right) + 2 \cdot C_H \cdot Q \right] = \frac{\partial}{\partial Q} \left(\frac{2 \cdot Pn^{2/3} \cdot K_J \cdot (CRFT + m^{-1})}{Z_H \cdot Q} + 2 \cdot C_H \cdot Q \right) = \frac{2 \cdot Pn^{2/3} \cdot K_J \cdot (CRFT + m^{-1})}{Z_H \cdot Q^2} + 2 \cdot C_H = 0 \quad (21)$$

$$\frac{\partial RFR(Pn, Q, W_j(Q), \bar{x})}{\partial Pn} = \frac{\partial}{\partial Pn} \left[\frac{Pn^{-1/3}}{\varepsilon \cdot \lambda} \left(\frac{K_J \cdot (CRFT + m^{-1}) \cdot (Kr \cdot Q + Kp \cdot Pn)}{Z_H \cdot v \cdot Q} + Kc \right) + 2 \cdot C_H \cdot Q \right] = \frac{-1 \cdot Pn^{-4/3}}{3 \cdot \varepsilon \cdot \lambda} \left(\frac{K_J \cdot (CRFT + m^{-1}) \cdot (Kr \cdot Q + Kp \cdot Pn)}{Kq \cdot Q} + Kc \right) + \frac{Pn^{-1/3}}{\varepsilon \cdot \lambda} \frac{K_J \cdot (CRFT + m^{-1}) \cdot Kp}{Kq \cdot Q} = 0 \quad (22)$$

After transformation and organizing expressions, the determined unknowns represent the optimal values that can be expressed explicite by method parameters:

$$Pn_{opt} = \left(\frac{K_J \cdot CRFT \cdot (1 + m^{-1})}{Z_H \cdot C_H} \right)^{3/4} \cdot \left[\frac{1}{4 \cdot \varepsilon \cdot \lambda \cdot v} \left(R + T_o \cdot v + \frac{\mu \cdot C_J \cdot G_J \cdot v^3 \cdot R \cdot (\varepsilon \cdot \lambda)^{2/3} \cdot Z_H}{K_J \cdot C_A \cdot \eta^{2/3} \cdot CRFT \cdot (1 + m^{-1})} \right) \right]^{7/2} \quad (23)$$

$$Q_{opt} = \left(\frac{K_J \cdot CRFT \cdot (1 + m^{-1})}{Z_H \cdot C_H} \right)^{3/4} \cdot \left[\frac{1}{4 \cdot \varepsilon \cdot \lambda \cdot v} \left(R + T_o \cdot v + \frac{\mu \cdot C_J \cdot G_J \cdot v^3 \cdot R \cdot (\varepsilon \cdot \lambda)^{2/3} \cdot Z_H}{K_J \cdot C_A \cdot \eta^{2/3} \cdot CRFT \cdot (1 + m^{-1})} \right) \right]^{7/2} \quad (24)$$

EXAMPLE OF METHOD APPLICATION

Selected application results of the method illustrate its applicability in relation to the tasks of design and investment - determining the optimum capacity of the designed ship Pn_{opt} and coupled to the efficiency of handling equipment Q_{opt} (binding the cost with handling time) - as to minimize the rate of freight RFR, and in particular concern:

- Identification of significant parameters of the model;
- And example of a solution to a design task;
- Parametric studies of relationship RFR, Pn_{opt} and Q_{opt} to the length of the line R and the value factor C_H .

Technical and economic parameters of the model adopted in the presented results are given in the table describing the design task.

1. The essential method parameters.

Tests of parametric sensitivity of the model to change of its parameters performed show that a significant impact on the value determined parameters Pn_{opt} and Q_{opt} , as well as to minimize the rate of freight RFR has the length of the route voyage R and the time TQ and unit cost of handling W_j , which depend on the efficiency of handling Q determined by coefficient of proportionality C_H . The model shows a lower sensitivity to both change in the ship's speed v, and the change in the price of fuel C_f .

This result stems from a significant relationship of cruise route time (bringing freight income), dependent on the length of the cruise route, until handling (non-profit stop of the ship), which depends on the capacity of handling equipment and vessel capacity.

2. An example of a solution to the design task.

One should appoint an optimum load-bearing capacity of the ship, optimum performance of handling equipment, and the minimum rate of the projected freight ship, with service speed $v = 18$ kn, intended for line Gdańsk-Rio de Janeiro of route length of $R = 5930$ NM, accepting the empirical factor $C_H = \frac{W_j [S/t]}{Q [t/h]} = 0,15 \frac{[S/t]}{[t/h]}$. The values of other parameters of the tasks are contained in the table Tab. 1.

3. Selected parametric study.

The results of research on the impact of the coefficient C_H expressing the proportionality of the cost-efficiency of handling, for example, a ship with a given velocity $v = 15$ kn, the length of the shipping line, respectively $R1 = 2000$ NM and $R2 = 5000$ NM, and other parameters, such as in the example design task are presented. The results are shown on graphs in Fig. 1, which illustrate the characteristics and performance of the optimum load handling equipment when changing the proportionality factor handling cost performance to (time) handling.

4. Prospects for implementation of further research.

Multi-dimensional vector of technical and economic parameters of the method allows to conduct parametric studies that may be of interest both in the design of ship-owners investment, as well as in solving ships design issues.

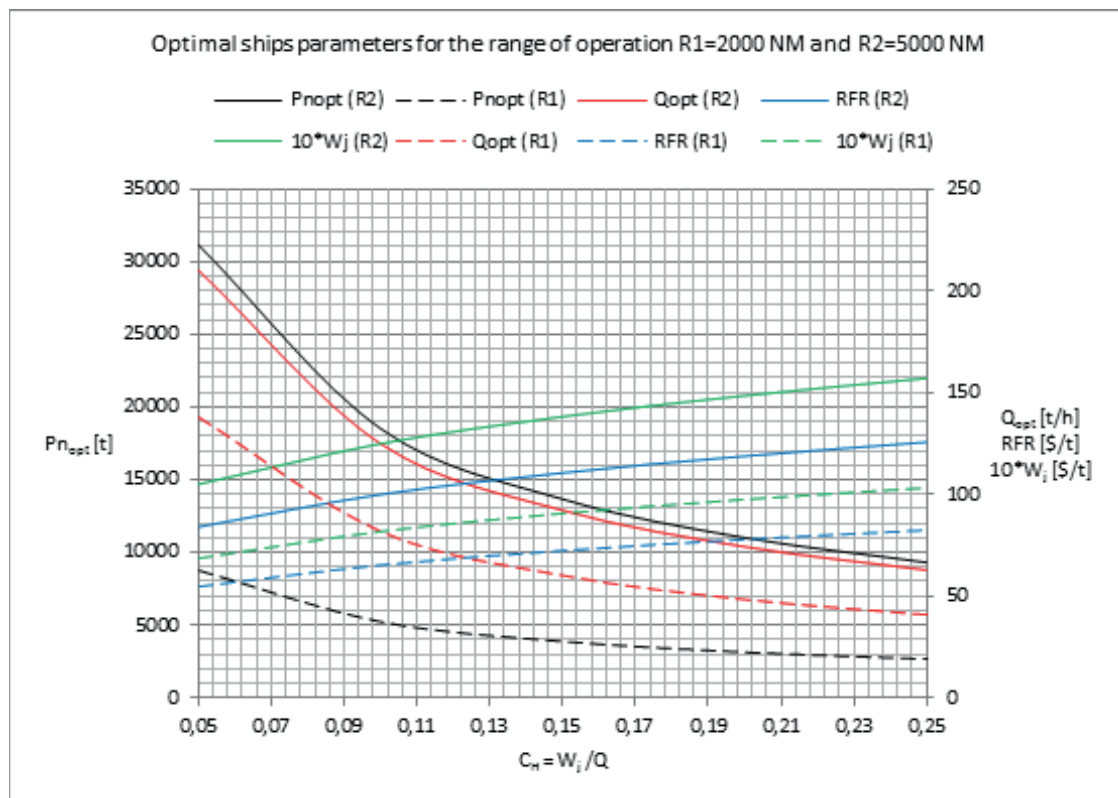


Fig. 1. Example of parametric studies of impact and range of operation on optimal ship's deadweight and required freight rate

Tab. 1. Example of the use of the presented method to optimize the parameters of a ship on the line Gdańsk-Rio de Janeiro

Example design task			
<i>shipowner assumptions</i>	<i>Symbol</i>	<i>Value</i>	<i>U.Measure</i>
The speed of the ship	v	18,00	[kn]
The length of the cruise route	Ra	5930	[NM]
The average annual inflation rate	i	0,03	[-]
The number of days of operation of the ship in the year	Zd	340	[day]
The number of hours of operation of the vessel in the year	Zh	8160	[hours]
The required net rate of return	r	0,09	[-]
Tax rate	t	0,19	[-]
The number of years of operation of the ship	m	20	[years]
Unit fuel consumption	Gj	160	[g/kWh]
Current fuel price LSMGO	Cj	600	[\$/t]
Stopover on the roadstead and in the port	To	1	[day/voyage]
Stopover on the roadstead and in the port	Toh	24	[h/voyage]
Coefficient of price for handling efficiency	CH	0,15	[\$/t]*[t/h] ⁻¹
<i>Parameters of a similar ship</i>	<i>Symbol</i>	<i>Value</i>	<i>U.Measure</i>
Carrying capacity of a similar ship	Pp	10532	[t]
The speed of a similar ship	vp	16,5	[kn]
Displacement of a similar ship	D	14946	[t]
Power of a similar vessel	Ne	5741	[kW]
Coefficient of Admiralty formula	Ca	475	[*]
Price of a similar ship	J	40 000 000	[\$]
Utilization factor of displacement	Eta	0,705	[-]
<i>Determined auxiliary parameters</i>	<i>Symbol</i>	<i>Value</i>	<i>U.Measure</i>
Capacity utilization factor	lamb	0,9	[-]
Factor of ship capacity utilization,	eps	0,9	[-]
Factor of the cost of service	mi	1,1	[-]
Factor of the cost of purchase of the ship	Kj	83 250	[*]
Factor of operating costs	Kc	469	[*]
Factor of handling costs	Kh	0,24	[*]
the cost factor kq	Kq	146 880	[*]
the cost factor kp	Kp	29	[*]
the cost factor kr	Kr	6 362	[*]
Factor of return of capital	CRF	0,136	[-]
Tax correction CRF	CRFT	0,168	[-]
<i>Designated technical parameters of the ship</i>	<i>Symbol</i>	<i>Value</i>	<i>U.Measure</i>
Optimal dead-weight tonnage	Pn_{opt}	17 369	[t]
Optimal handling performance	Q_{opt}	99,7	[t/h]
The minimum freight rate	RFR_{min}	119,69	[\$/t]
The unit rate for handling	W_j	14,96	[\$/t]
The current capacity of the vessel	ML	14069	[t]
The current buoyancy of the ship	Displ	19965	[t]
Explanatory power of the engine	Power	9040	[kW]
Catalogue engine power	P	10404	[kW]
A time of 1 cruise	Tr	636	[h]
time of the route	Tm	329	[h]
Time of loading and unloading	Tq	282	[h]
Number of trips per year	LRR	13	[-]
Fuel consumption in 1 cruise	ZPR	477	[t]
Design displacement of the ship	Dpr	24648	[t]
<i>Designated economic parameters of the ship</i>	<i>Symbol</i>	<i>Value</i>	<i>U.Measure</i>
Invest Cost	Price	55 833 579	[\$]
Annual Cargo Capacity	ACC	180 631	[t]
Annual Cargo Freight	ACF	21 619 473	[\$]
Annual Fuel Cost	AFC	4 038 010	[\$]
Amortization	A	2 791 679	[\$]
Annual Cargo Handling Cost	AHC	5 404 868	[\$]
Annual Operating Cost	AOC	12 234 557	[\$]
Average Annual Cost	AAC	21 619 473	[\$]

BIBLIOGRAPHY

1. Gasparski G. (red.): Metodologia projektowania inżynierskiego. Państwowe Wydawnictwo Naukowe. Warszawa 1973.
2. Bąbiński C.: Elementy nauki o projektowaniu. Warszawa: Wydawnictwa Naukowo-Techniczne 1969.
3. Sójka Z.: Statek Optymalny, Wydawnictwo Morskie, Gdynia 1964.
4. Schneekluth H.: Ship Design for Efficiency and Economy, Butterworth & Co. Ltd., 1987.
5. Benford H.: Principles of Engineering Economy in Ship Design, Transactions SNAME, 1963.
6. Benford H.: Fundamentals of ship design economics. The University of Michigan. Ann Arbor, 1965.
7. Benford H.: Measures of Merit for Ship Design. The University of Michigan. Ann Arbor, 1968.
8. Buczkowski L.: Kryteria oceny projektu na przykładzie okrętów. Konferencja Metodologii Projektowania, PAN, Warszawa 1973.
9. Perycz E., Sójka Z.: Inwestycje w żegludze morskiej. Wydawnictwo Morskie. Gdańsk 1981.
10. Cotta P.S.: Hull Cost as a Factor in Selecting Ship Speed. Report 091. The University of Michigan, 1970.
11. Michalski J.P.: A method of choosing the service speed of liner trade ships at the stage of establishing owners requirements. Marine Technology Transactions Technika Morska, Polish Academy of Sciences, vol. 10, 1999.
12. Michalski J.P.: Parametric method for evaluating optimal ship deadweight. Polish Maritime Research. 2 (82) 2014.
13. Michalski J.P.: Optimization of Inland Vessels' Route Speed. Marine Technology Transactions Technika Morska. Polish Academy of Science. Vol. 15. 2004.

CONTACT WITH THE AUTHOR

JAN P. MICHALSKI

Faculty of Ocean Engineering and Ship Technology
Gdansk University of Technology
Narutowicza 11/12 Str.
80-233 Gdańsk
POLAND

BOUNDARY ELEMENT METHOD APPLIED TO ADDED MASS COEFFICIENT CALCULATION OF THE SKEWED MARINE PROPELLERS

Ehsan Yari, Ph. D.

Hassan Ghassemi, Prof.

Amirkabir University of Technology, Iran

ABSTRACT

The paper mainly aims to study computation of added mass coefficients for marine propellers. A three-dimensional boundary element method (BEM) is developed to predict the propeller added mass and moment of inertia coefficients. Actually, only few experimental data sets are available as the validation reference. Here the method is validated with experimental measurements of the B-series marine propeller. The behavior of the added mass coefficients predicted based on variation of geometric and flow parameters of the propeller is calculated and analyzed. BEM is more accurate in obtaining added mass coefficients than other fast numerical methods. All added mass coefficients are nondimensionalized by fluid density, propeller diameter, and rotational velocity. The obtained results reveal that the diameter, expanded area ratio, and thickness have dominant influence on the increase of the added mass coefficients.

Keywords: Added mass coefficient, Boundary element method, Skew marine propeller

INTRODUCTION

In order to calculate the critical speed of a propeller shaft, it is necessary to know accurate values for the marine propeller added mass and added moment of inertia. In the case of a controllable pitch propeller, the values of the added mass and added moment of inertia are changed by varying the pitch angle, nondimensionalized by the mass and moment of inertia of the displaced fluid, respectively. It can be noted that the added moment of inertia is greatly influenced by the pitch angle. Calculating the added mass coefficient is difficult, especially for bodies of complex shapes. Generally, the added mass coefficient is a second order tensor that depends on the fluid acceleration vector through which the force vector on the body is obtained.

There are several publications discussing the added mass coefficients for marine propellers. Burrill and Robson (1962) conducted experiments to study the added mass of a series propeller [1]. Sahin et al. (1993) introduced the concept of added mass that generalized moving a desired object in different flow regimes [2]. Vernon et al. (1988) considered a surface panel method for calculation of added mass matrices, [3], an approach which is relatively close to the present study. Added mass estimations for a multi-component deeply submerged vehicle were studied by Watt [4]. Bermudez et al [5] investigated fluid-solid vibrations using finite element solution to derive the added mass formulation. Perrault et

al. (2003) presented sensitivity of a typical AUV response to changes of hydrodynamic parameters. That analysis was performed using an axisymmetric computer model. The sensitivity of the added mass coefficients of a typical autonomous underwater vehicle (AUV) was presented as a response to changes of geometric parameters [6-7]. Koo and Lee (2003) developed a FAMD code to calculate the fluid added mass and damping of arbitrary structures submerged in confined viscous fluid [8]. Li et al. (2005) studied numerically the fluid flow and the added mass induced by vibration of a structure using the singularity distribution method in which axial and rotational motion of the structure was taken into account [9]. Wakaba & Balachandar considered numerical simulations of the flow around a rigid sphere subjected to sudden acceleration (or deceleration) in a relative velocity [10]. Jianjun Long et al. reported estimation of the added mass and drag coefficient for a small remotely operated vehicle [11]. Chan & Kang indicated that the drag and added mass coefficients are essential parameters in determining dynamic behavior of a submerged vessel [12]. The added mass coefficients of the Darpa Suboff submarine were calculated by means of the FMBEM [13]. Naveed Raza et al. determined the added mass by simulating the flow about a standard ellipsoid using a commercial CFD code [14]. Recently, a 3-D boundary element method was used by Gaschler and Abdel-Maksoud (2014) to compute the added mass coefficients for a marine propeller under cavitating condition [15].

In the present study, the boundary element method has been extended to enable calculation of the added mass matrix of skewed marine propellers. Then, appropriate grids generated on the geometry of marine propeller (blade, hub and boss) are investigated in order to provide correct results of added mass matrix coefficients. Finally, the added mass coefficients of a skewed marine propeller are presented as polynomial functions of selected geometric parameters.

GOVERNING EQUATIONS

Hydrodynamic forces and moments are determined by fluid inertia and viscous properties, according to the motion of a body in real incompressible fluid. Definitely, the other forces and moments can be calculated by obtaining either inertia or viscous terms. Since the fluid can be assumed inviscid, the inertia forces and moments can be calculated using this estimation. With the aid of this method, the forces and moments of inertia can be introduced as body added mass terms.

Let us consider the closed area Ω , the boundary S , and the unit vector \bar{n} normal to S (Fig. 1). The boundary S is composed of the wetted surface S_B of the body, the wake surface S_W , and the external control surface S_∞ encircling the surface areas S_B and S_W .

Ω encounters the upstream flow of uniform velocity \bar{V}_I . The flow is assumed incompressible, inviscid and irrotational.

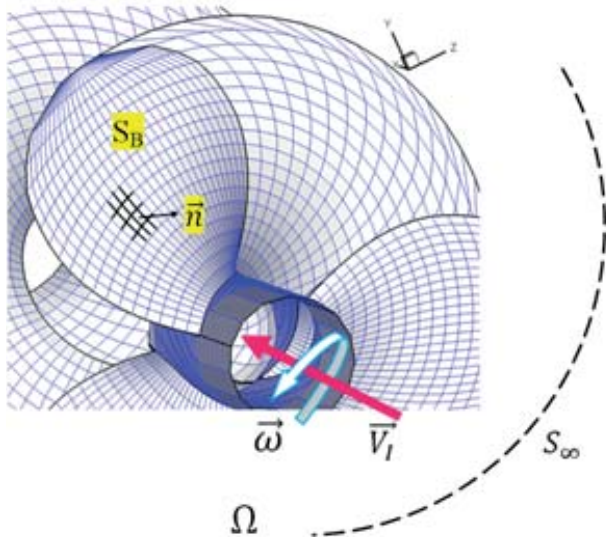


Fig. 1. Three-dimensional propeller

With the above assumptions, the flow field around the body can be identified using the perturbation velocity potential ϕ which satisfies the Laplace equation:

$$\nabla^2 \phi = 0 \quad (1)$$

To solve the problem, the boundary conditions are considered as follows:

BOUNDARY CONDITIONS

Based on the kinematic boundary condition, the flow velocity normal to the body surface is equal to zero.

$$\frac{\partial \Phi}{\partial n} = 0 \quad \text{yields} \quad \frac{\partial \phi}{\partial n} = -V_I \cdot \mathbf{n} \quad (2)$$

where \mathbf{n} , is the unit vector normal to the outside of the boundary. Considering the unit potential kinematics of the boundary condition, the vector is changed as follows:

$$\frac{\partial \phi_j}{\partial n} \Big|_{j=1 \rightarrow 6} = \begin{cases} \mathbf{n}_i \Big|_{i=1 \rightarrow 3}^{j=1 \rightarrow 3} \\ (\mathbf{r} \times \mathbf{n}_i) \Big|_{i=1 \rightarrow 3}^{j=4 \rightarrow 6} \end{cases} \quad (3)$$

where, \mathbf{r} is the vertical distance from the fixed origin point [16].

At the boundary surface at infinity S_∞ , the perturbation velocity due to the body surface tends to zero.

$$x \rightarrow \infty \Rightarrow \nabla \phi \rightarrow 0 \quad (4)$$

WAKE BOUNDARY CONDITIONS

Based on these conditions, there is no flow velocity jump on the wake vortex, however there is a velocity jump of the potential on the surface which equals the circulation Γ around the fin. The mathematical relations between flow velocity and potential are expressed as follows:

$$\begin{cases} (\Delta \phi)_{S_W} = p^B - p^F = -\Gamma \\ (\Delta \frac{\partial \phi}{\partial n})_{S_W} = (\frac{\partial \phi}{\partial n})^B - (\frac{\partial \phi}{\partial n})^F = 0 \end{cases} \quad (5)$$

where B and F represent the back and face side of the propeller, respectively [17].

KUTTA CONDITION

Hess and Smith showed that the flow passing along a thin and non lifting body can be described by distribution of source singularities. But to describe the flow passing along a lifting body, modeled by circulation distribution on the surface, a boundary condition for the trailing edge of the body, expressing that the velocity at the trailing edge should be limited and unique, is to added [18].

$$|\nabla \phi| < 0$$

ADDED MASS FORMULATION

The added mass and added moment coefficients can be formulated using the force point of view and the kinetic

energy theory. The added mass formulation is given by Eq (7). According to this equation, the added mass and added moment coefficients are only functions of body geometry.

$$\lambda_{ik} = -\rho \int_S \frac{\partial \phi_i}{\partial n} \phi_k dS \quad (7)$$

λ_{ik} is called the added mass of the body. The added mass matrix flowchart of the propeller for which the solving process will be continued until the results are converged to an accurate point is shown in Figure 2. [19]

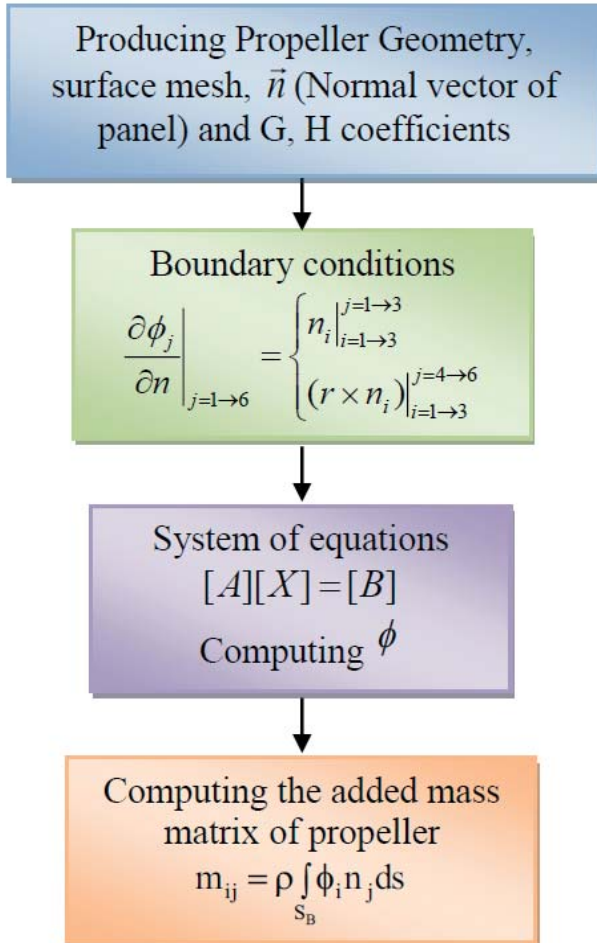


Fig. 2. Flowchart of the added mass matrix of the propeller

BOUNDARY INTEGRAL EQUATION

Using Green's theory, the general solution to the Laplace equation for each point P can be expressed as the following integral equation:

$$2\pi\phi_p = \iint_{S_B} [\phi_q \frac{\partial}{\partial n_q} (\frac{1}{R_{p,q}})] - \frac{\partial \phi}{\partial n_q} (\frac{1}{R_{p,q}})] dS + \iint_{S_W} [\Delta\phi_q \frac{\partial}{\partial n_q} (\frac{1}{R_{p,q}})] dS \quad (8)$$

where the subscripts p, q correspond to the control and variable points in the integration, respectively. In the above

equation, $\partial\phi/\partial n$ is determined using the boundary condition of Eq. (3). $1/R(p,q)$ is the distance between p and q, so the only remaining unknown for solving Eq. (8) is ϕ .

DISCRETIZATION OF EQUATIONS

In order to solve Eq. (8), the equations are discretized and the body boundary surface is meshed with tetragonal elements. Fractional equations lead to a linear system of algebraic equations for ϕ and i, as follows:

$$2\pi\phi_i = \sum_{j=1}^N D_{ij} (\phi_j) + \sum_{j=1}^{N_R} \sum_{l=1}^{N_W} W_{ijl} (\Delta\phi)_i + \sum_{j=1}^N S_{ij} \left(\frac{\partial \phi}{\partial n} \right)_j \quad i = 1, 2, \dots, N_{total} \quad (9)$$

where D_{ij} , S_{ij} and W_{ijl} are the dipole and source coefficients for the j-th element that acts on the arithmetic point i. These dipole and source coefficients are defined as follows:

$$D_{ij} = \sum_{k=1}^k \left[\iint_{S_B} \left[\frac{\partial}{\partial n_j} \left(\frac{1}{R_{ij}} \right) dS_j \right]_k \right] \text{ on } S_B$$

$$W_{ijl} = \sum_{k=1}^k \left[\iint_{S_W} \left[\frac{\partial}{\partial n_j} \left(\frac{1}{R_{ij}} \right) dS_j \right]_k \right] \text{ on } S_W \quad (10)$$

$$S_{ij} = \sum_{k=1}^k \left[\iint_{S_B} \left[\left(\frac{1}{R_{ij}} \right) dS_j \right]_k \right] \text{ on } S_B$$

To obtain these coefficients, numerical solution of the integrals is employed. For this purpose the following matrix equation is formed and then solved using the Gauss - Seidel method, leading to ϕ_j values [20].

$$[D][\phi] = [S] + [W][\Delta\phi] \quad (11)$$

where [D] = dipole potential matrix, [S] = source potential matrix, and [W] = dipole potential matrix (Wake).

For lifting and non-lifting bodies, the use of the above computational method only differs by application, or not, of the Kutta boundary condition. The results are obtained directly regarding the kinematic boundary condition.

Although the Kutta condition is considered to analyze the propeller, the course of obtaining the results reveals no significant difference, as compared to cases without considering the Kutta condition. Therefore, regarding this remark, only D and S matrixes in equation 11 need to be determined.

$$D_{ij} = \sum_{k=1}^k \left[\iint_{S_B} \left[\frac{\partial}{\partial n_j} \left(\frac{1}{R_{ij}} \right) dS_j \right]_k \right] \text{ on } S_B$$

$$S_{ij} = \sum_{k=1}^k \left[\iint_{S_B} \left[\left(\frac{1}{R_{ij}} \right) dS_j \right]_k \right] \text{ on } S_B \quad (12)$$

After extracting D and S, the integrals in Eq. (12), being in fact the same as general terms in Eq. (8), take the form:

$$\int_{S_B} \left[\frac{1}{R} \frac{\partial \phi}{\partial n} \right] dS = \sum_{\substack{k=1 \\ k \neq i}}^N \left[\frac{1}{R} \frac{\partial \phi_j}{\partial n} \right]_{j=1 \rightarrow 6} \delta S_k \quad (13)$$

$$\int_{S_B} \left[\phi \frac{\partial}{\partial n} \left(\frac{1}{R} \right) \right] dS = \sum_{\substack{k=1 \\ k \neq i}}^N \left[\frac{\partial}{\partial n} \left(\frac{1}{R} \right) \right] \delta S_k + 2\pi \phi_{i=k}$$

If the above integrals (Eq.13) are formulated based on matrix equations, the following relation is derived:

$$[A_{ik}][\phi_k]=[B_i] \quad (14)$$

So that $i = K$ and $A_{ik} = 2\pi$

The added mass matrix values obtained by solving the matrix equations for all six potential unit functions can be defined as follows:

$$\lambda_{ik} = -\rho \int_{S_B} \phi_i n_k dS_B$$

If the above equation is written in the matrix form, which is the general form of the added mass matrix, the following matrix is introduced [14].

$$\text{Added Mass Matrix} = \begin{bmatrix} \sum_{i=1}^N \phi_1^i n_1^i \delta S_i & \dots & \sum_{i=1}^N \phi_1^i (r \times n)_3^i \delta S_i \\ \vdots & \ddots & \vdots \\ \sum_{i=1}^N \phi_6^i n_1^i \delta S_i & \dots & \sum_{i=1}^N \phi_6^i (r \times n)_3^i \delta S_i \end{bmatrix}$$

ADDED MASS OF B-SERIES PROPELLER

In this section the added mass coefficients for a standard propeller are studied. The dimensions of the B-Series propeller selected for this study are given in Table 1.

Tab. 1. Main dimensions of the propeller

Propeller Type	B-series
Diameter [m]	1
Pitch Ratio	0.8
Expanded Area Ratio	0.6
Number of Blades	4
Rake Distribution	0.0
Skew Distribution (deg.)	17.7
Hub Ratio	0.2
Rotation	R.H
Total Surface Element	6900

Since the added mass coefficients of the B-Series propeller are available [21], this part of analysis aims at validating the results computed by the boundary element code. The mesh independency of the numerical results was investigated, showing very small error in comparison with the existing

data. The added mass matrix obtained from the numerical analysis for the B-series propeller is shown in Table 2.

Tab. 2. Matrix of Added Mass coefficients per density for B-series propeller ($\times 10^3$)

664.9	-0.2	0.1	-86	0	0
-0.2	89.8	94.9	0	40.4	3.5
0.1	94.9	89.7	0	-3.5	40.4
-86	0	0	11	0	0
0	40.4	-3.5	0	29.3	0
0	3.5	40.4	0	0	29.4

In Fig. 3, the grid independency is evaluated for coefficients M11 and M44. As it can be seen, at 6900 surface elements the coefficient variations tend to zero.

Afterwards, the data obtained from the present study were validated by comparing with the experimental data [21], see Tab. 3. According to these results, for all three coefficients the maximum error percentage is of the order of 3.7%.

Comparing the results of the numerical boundary element based analysis with the experimental data [21] for added mass coefficients of B-series propeller reveals good conformity between the numerical and experimental data.

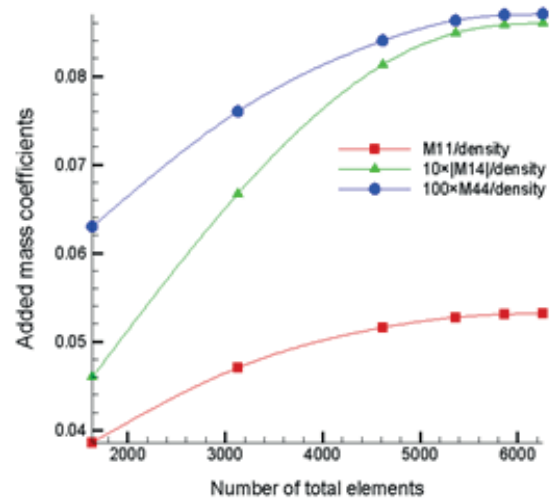


Fig. 3. Mesh independency study for M_{11} and M_{44}

Tab. 3. Comparing numerical and experimental results for B-series propeller

	M_{11}	M_{14}	M_{44}
Exp	0.06906	-0.00878	0.00111
Num	0.06649	-0.00860	0.00110
Difference	0.00257	-0.00018	0.00001
% Error	3.721402	2.050114	0.900901

COMPUTING THE ADDED MASS MATRIX FOR THE BENCHMARK PROPELLER

According to the data and results obtained for the added mass matrix of the B-series propeller it can be found that there is a good accuracy between the experimental data [21] and the numerical solution. This section discusses computing the added mass matrix for a high skew propeller (HSP-4 Blades). Since the added mass matrix is only a function of the body geometry, the object of the study was the effects of changing geometrical parameters of the propeller. Firstly, the existing geometrical data of the propeller, based on the standards, were used to model the propeller geometry with very high accuracy. Then, the propeller surface and the hub were analyzed with respect to flow conditions. The propeller analysis was performed for different numbers of surface elements to arrive at the most appropriate variant for which the obtained answers did not depend on the number of elements.

Grid generation on the marine propeller is one of most important topics in extracting the accurate added mass coefficient matrix using the boundary element method. Since the propeller has the same number of zones as the number of blades, the grid generated on each of these four sections is to be similar. It is noteworthy, however, that using a pave mesh on the propeller and especially on the hub may lead to incorrect results.

As it is shown in Figure 4, the grid was generated on the blades, hub, and boss, taking into account the above mentioned remarks.

Thereafter, the added mass matrix was derived for three cases: only blades, blades and middle hub, and finally complete geometry of the propeller. The effect of each geometric element was evaluated based on the obtained data.

According to the numerical results, each increase of the added mass coefficient rate amounted to less than one percent, regarding the middle hub with blades. When the boss was taken into account, the added mass coefficient rate increased significantly, by about at least 5 to 6 percent.

Thus, the geometric design of the boss has an important role in propeller design. In particular for high diameter propellers, optimizing the boss geometry is essential.

Tab. 4. Added mass matrix for HSP-4 blade propeller in three conditions

$$\begin{bmatrix} 50.17 & 0.00 & 0.00 & -6.64 & 0.00 & 0.00 \\ 0.00 & 68.10 & -11.36 & 0.02 & 2.05 & -5.46 \\ 0.00 & -11.36 & 73.93 & -0.01 & 6.87 & 3.91 \\ -6.64 & 0.02 & -0.01 & 7.55 & 0.00 & 0.00 \\ 0.00 & 2.05 & 6.87 & 0.00 & 9.54 & 0.11 \\ 0.00 & -5.46 & 3.91 & 0.00 & 0.11 & 9.29 \end{bmatrix}$$

Since the data compared to the main diameter are symmetrical and some coefficients have zero with accuracy of up to 5 decimal points, this testifies to high precision of the reported calculations (Tab. 4). The geometric and flow data of the high skew four-blade propeller are given in Tab. 5.

Tab. 5. Geometric and flow data of HSP-4 blade Propeller

Parameter	Value
Type	FPP
No. of Blades, Z	4
Skew at $r/R=0.7$	41.62 deg
Hub Ratio, H/D	0.20
Pitch Ratio, P/D	0.80
Expanded Area Ratio	0.60
Advance Ratio, J	0.50
Diameter, D (m)	2

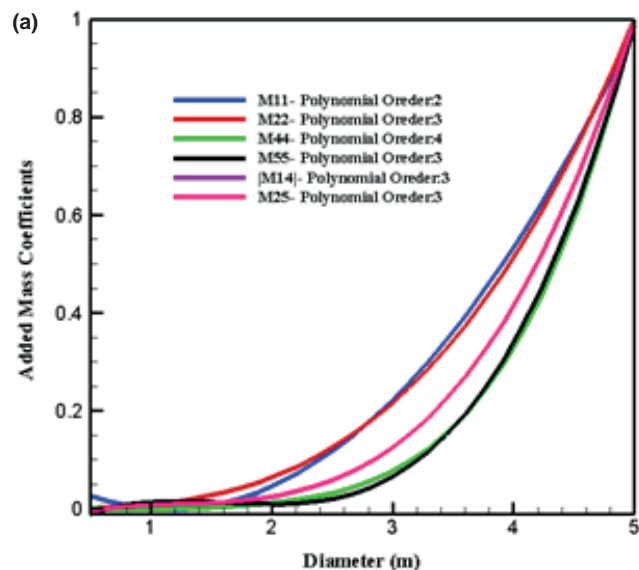
PARAMETERS AFFECTING THE ADDED MASS OF THE SKEWED PROPELLER

Since the added mass coefficient is only a function of propeller geometry, its changes have been studied based on the sensitivity to geometrical parameters.

Figure 4-a shows the calculated variations of predominant added mass matrix coefficients as the propeller diameter increases. As can be seen, for most coefficients these variations have the form of the polynomial of the order of 3. Only the coefficients M_{44} and M_{11} form the polynomials of the order of 2 and 4, respectively. These changes are quite noticeable in the case of M_{11} and the 2-order polynomial, while M_{44} can also be considered as the approximation by the 3-order polynomial. Consequently, it can be concluded that changes of most general mass matrix coefficients have the form of the 3-order polynomial as the propeller diameter increases.

Figure 4-b shows changes of the added mass matrix coefficients in response to changes of the expanded area ratio of the propeller. According to the obtained results, it can be found that the changes of all moment and added mass coefficients are of the order of 2 as the expanded area ratio of the propeller increases.

Figure 5-c shows changes of the added mass coefficients as functions of the maximum thickness of the propeller profile section. For all diagonal coefficients this relation is linear, while for other coefficients it has the form on a 3-order polynomial.



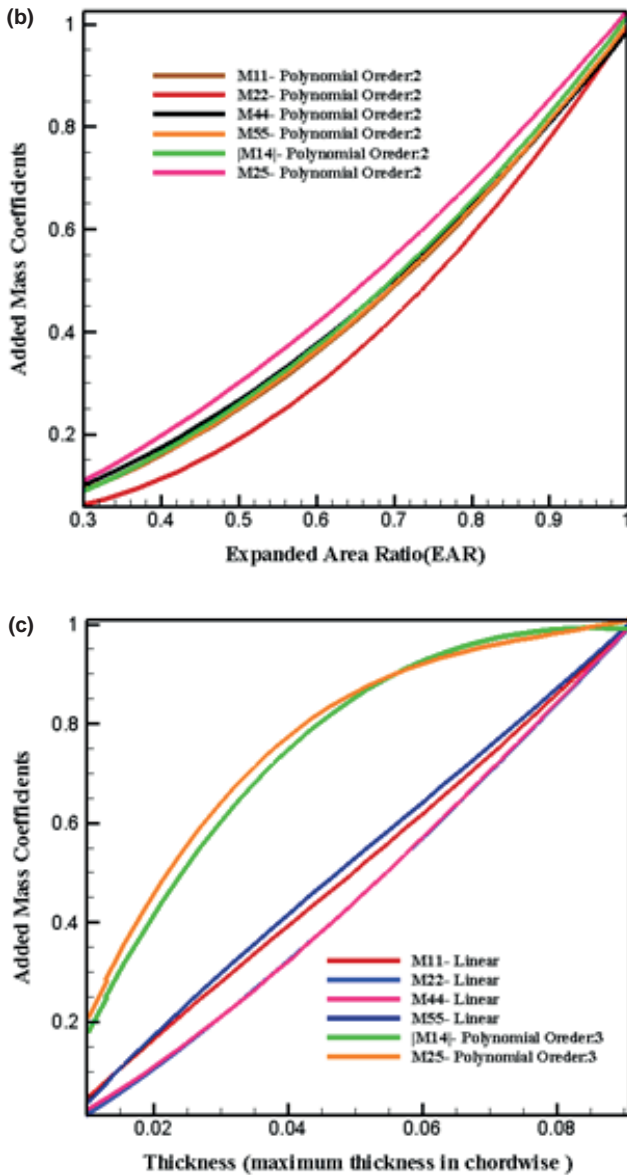


Fig. 4. Changes of the added mass coefficients as functions of geometrics parameters of the propeller

CONCLUSIONS

All coefficients cannot be derived using the reference formulation. However, they can be obtained with appropriate accuracy using the present study. As mentioned in the article, the added mass matrix of the B-series propeller was extracted and the results were validated with the available data.

The largest obtained error, compared to the experimental data, was about 3.7 percent, which is a very small amount, and for other coefficients the error rate was even fairly smaller.

Therefore, all the added mass and added moment coefficients can be calculated with good accuracy using the present study and taking into account the earlier mentioned remarks about propeller geometry generation.

Afterwards, the added mass matrix for a benchmark skewed propeller in various geometrical data was computed. According to the obtained results, changes of the added

mass coefficients of the propeller caused by varying geometrical parameters such as diameter, expanded area ratio, and thickness, had the form of polynomial function of cubic, quadratic, and linear and quadratic order (3-2-1-2), respectively.

REFERENCES

1. Burrill, L. C., Robson, W.: Virtual mass and moment of inertia of propellers. *Trans. North East Coast Institution of Engineers and Shipbuilders* 78, 325-360, 1962.
2. Sahin I, Crane JW and Waston KP: Added mass coefficients for submerged bodies by a low-order panel method. *J Fluids Eng* 1993; 115:452-7.
3. Sahin I, Crane JW, Waston KP: Application of a panel method to hydrodynamics of underwater vehicles. *Ocean Eng* 1997; 24(6):501-12.
4. George D. Watt: Estimates for the added mass of a multi-component, deeply submerged vehicle. *Defense Research Establishment Atlantic (Report)*, October 1988.
5. Bermudez Alfredo, Rodr'iguez Rodolfo, Santa Marina Duarte: A finite element solution of an added mass formulation for coupled fluid-solid vibrations. *Numer. Math.* (2000) 87: 201-227
6. Perrault Doug, Bose Neil, O'Young Siu, Williams D. Christopher: Sensitivity of AUV response to variations in hydrodynamic parameters. *Ocean Engineering* 30 (2003) 779-811.
7. Perrault Doug, Bose Neil, O'Young Siu, and Williams D. Christopher: Sensitivity of AUV added mass coefficients to variations in hull and control plane geometry. *Ocean Engineering* 30 (2003) 645-671.
8. Gyeong-Hoi Koo, Jae-Han Lee: Development of FAMD Code to Calculate the Fluid Added Mass and Damping of Arbitrary Structures Submerged in Confined Viscous Fluid. *KSME International Journal*, Vol. 17 No. 3, pp. 457-466~ 2003.
9. Su Li, Li Shu-Juan, and Tan Guo-an: Numerical analysis of Fluid Flow and Added Mass Induced by Vibration of Structure. *Applied Mathematics and Mechanics*, Vol. 26, No 2, Feb 2005.
10. Wakaba L. · S. Balachandar: On the added mass force at finite Reynolds and acceleration numbers. *Theor Comput Fluid Dyn.* (2007) 21: 147-153.
11. Jianjun Long, Baihai Wu, Jinping Wu, Tibing Xiao and Lili Wang: Estimation of Added Mass and Drag Coefficient for a Small Remotely Operated Vehicle. *Proceedings of the 2008 IEEE International Conference on Information and*

Automation June 20 -23, 2008, Zhangjiajie, China.

12. Wai Leung Chan and Taesam Kang: Simultaneous Determination of Drag Coefficient and Added Mass. IEEE Journal of Oceanic Engineering, Vol. 36, No. 3, July 2011.
13. Zhiliang Lin, Shijun Liao: Calculation of added mass coefficients of 3D complicated underwater bodies by FMBEM “Commun Nonlinear Sci Numer Simulat 16 (2011) 187–194.
14. Naveed Raza, Imran Mehmood, Hafiz Rafiuddin and Mohammad Rafique: Numerical Simulation of Added Mass Determination of Standard Ellipsoids. Proceedings of 2012 9th International Bhurban Conference on Applied Sciences & Technology (IBCAST).
15. Gaschler, M., Abdel-Maksoud, M.: Computation of hydrodynamic mass and damping coefficients for a cavitating marine propeller flow using a panel method. Journal of Fluids and Structures 49, 574-593, 2014.
16. Olivier Saout: Computation of Hydrodynamic Coefficients and Determination of Dynamic Stability Characteristics of an Underwater Vehicle Including Free Surface Effects. Ms Thesis, Florida Atlantic University, May 2003.
17. Kinnas S.A. and Hsin C.Y: Boundary Element Method for the Analysis of the Unsteady Flow around Extreme Propeller Geometry. AIAA, Journal, 30 (3), 1992.
18. Hess J T, Smith A M: Calculation of non-lifting potential flow about arbitrary three-dimensional bodies. Journal of Ship Research,8(2),1964.
19. Ghassemi H, Yari E.: The Added Mass Coefficient computation of sphere, ellipsoid and marine propellers using Boundary Element Method. Polish Maritime Research 1(68) 2011 Vol 18; pp. 17-26.
20. Morino L and Kuo C.C: Subsonic Potential Aerodynamics for Complex Configuration: A general Theory. AIAA Journal, 12 (2), 191-197, 1974.
21. Alexandr I. Korotkin: Added mass of ship structure. Fluid mechanics and its applications, Volume 88, 2009.

CONTACT WITH THE AUTHORS

Ehsan Yari

Faculty of Maritime Engineering
Amirkabir University of Technology
Hafez Ave., Tehran,
IRAN

E-mail: ehsanyari_mechanical@yahoo.com

Hassan Ghassemi

Faculty of Maritime Engineering,
Amirkabir University of Technology
Hafez Ave., Tehran,
IRAN

E-mail: gasemi@aut.ac.ir

ANALYSIS OF POSSIBLE APPLICATION OF HIGH-TEMPERATURE NUCLEAR REACTORS TO CONTEMPORARY LARGE-OUTPUT STEAM POWER PLANTS ON SHIPS

T. Kowalczyk, M.Sc.^a

J. Głuch, Prof.^b

P. Ziółkowski, M.Sc.^a

^a Institute of Fluid Flow Machinery, Polish Academy of Sciences, Poland

^b Gdańsk University of Technology, Poland

ABSTRACT

This paper is aimed at analysis of possible application of helium to cooling high-temperature nuclear reactor to be used for generating steam in contemporary ship steam-turbine power plants of a large output with taking into account in particular variable operational parameters. In the first part of the paper types of contemporary ship power plants are presented. Features of today applied PWR reactors and proposed HTR reactors are discussed. Next, issues of load variability of the ship nuclear power plants, features of the proposed thermal cycles and results of their thermodynamic calculations in variable operational conditions, are presented.

Keywords: ship power plants, steam turbines, nuclear reactors, PWR, HTR, variable operational conditions

INTRODUCTION

Structure of contemporary world economy demands to make use of developed transport by sea. Therefore is today observed an increasing number of orders for carrying goods by sea as well as increasing average load carrying ability of containerships, bulk carriers and tankers [1]. The changes determine development of ship power plants, aimed at moderating detrimental impact on the environment, improving energy conversion efficiency as well as economic indices [24]. The aims can be reached by applying balanced energy conversion which becomes more and more popular both in the case of conventional fuels and alternative ones [2]. As far as sea transport has been concerned this means perfecting the combustion engine power plants and combined systems [3,11,12], improving operational parameters of gas turbines [13] and steam thermal cycles [8], developing novel systems based on fuel cells - SOFC [14] as well as making use of nuclear energy [15]. Special attention should be paid to HTR nuclear reactors. This is a prospective, fast developing solution both for power industry and sea transport [4,16,19,21].

This work is aimed at making analysis of possible profits, in thermodynamic and operational aspects, resulting from application of HTR reactors into ship nuclear power plants of a large output with taking into account load variability, in particular. For this reason calculations of selected power plant parameters in function of changes in generated effective power have been conducted for two selected thermal cycles of ship steam power plants.

TYPES OF PRESENTLY USED SHIP POWER PLANTS

Contemporary ship power plants of a large output are usually fitted with two-stroke low-speed diesel engines. Engines of the type, i.e. internal-combustion ones, are characterized by a high efficiency of the order of 51% [3,11,12]. Their huge popularity in shipbuilding results from economic conditions, namely, relatively low investment cost, low specific fuel combustion, possible charging with cheap heavy fuel oil. Moreover the engines under consideration

are of favourable external characteristics and low rotational speeds. In the case of the largest merchant ships it is possible to couple directly together screw propeller and engine shaft omitting this way any reduction gear. This is reached in expense of ship's manoeuvrability. Piston engines have also some disadvantages such as large mass of power plant, generation of nuisance vibration, long start-up period as well as emission of gas black and sulphur oxides in case of heavy oil charging. Aspects of emission of noxious substances negatively influence profitability of low-speed engines as regulations limiting exhaust gas emission level become more and more restrictive [3,11,12,14].

Gas and steam turbine engines are applied in shipbuilding less often. Turbine engines are characteristic of a high ratio of power output to mass of power plant, generation of high frequency vibrations (in contrast to piston engines, there occur no nuisance vibration but high frequency noise difficult to be damped) [3,11]. Additionally, gas turbines can be very fast started hence ship can reach full serviceability much faster [2,11], as well as no "running-in" period is necessary [9]. And, as far as boilers producing steam for steam turbines are concerned they are capable of burning various fuels. Additionally, in the case of steam power plants pumps and compressors can be directly fed with steam, that makes mass of auxiliary devices lower [9,12,13]. Among drawbacks of both the types of turbine engines, can be numbered a greater specific fuel combustion (compared to diesel engines), high rotational speeds, that makes application of reduction gear necessary [9,10,13]. The above mentioned features resulted in that gas turbines have found their application first of all to combat vessels and fast passenger boats, whereas steam power plants – to the largest cargo ships, gas tankers and ships of nuclear propulsion [13]. The last particular case dealing with ship large-output steam power plants is discussed below.

SHIP NUCLEAR POWER PLANTS

Contemporary ship nuclear power plants are used only on naval ships and for propulsion of Russian icebreakers of Arktika and Taimyr class [4,22]. It provides a tactical advantage over ships propelled by combustion engines. Nuclear submarines – from technical point of view – have practically unlimited combating range and submerge time. Aircraft carriers consume vast amount of energy for servicing airplanes and crews of even 6000 persons in number, they are almost self-sufficient "towns", and Russian icebreakers keep free way through Northern Path and riverways of Russian tundra [20,23].

Lack of application of nuclear energy to merchant fleet results from a low profitability of contemporary ships fitted with nuclear propulsion, compared to conventionally propelled ones. It is connected first of all with high investment and operational costs. Crew of nuclear ship is even two times greater in number and must be highly skilled [4,20].

Moreover, nuclear energy industry is often confronted with social resistance in spite of its high level of safety. This is caused by the fact that consequences of possible failures or disasters lead to long-lasting and serious hazards for people

and the environment. However it should be stressed that the social resistance presently weakens and this is only nuclear energy which makes it possible to have reliable source of energy after running low conventional fuels [20,21,23].

PWR REACTORS

In present, PWR reactors are mainly applied to ship nuclear power plants [4,23]. Such solution is advantageous from point of view of economic investment planning. They are moderated, water-cooled reactors and their low values of operational temperature do not require use of heat-resistant materials. The reactors are of a high core power density owing to which core volume does not exceed 1 m³ also in ship applicable solutions [4,22]. However the high power density is not advantageous from the safety side because in case of a cooling system breakdown a violent evaporation of cooling water, fracture of reactor vessel and core melt-down, may happen. Among other drawbacks of PMR reactors may be numbered the fuel reloading operation which usually is associated with disassembling the whole reactor. The fuel reloading operation is carried out every 5th or 10th year on average, that is connected with long-lasting overhauls resulting from several month long periods of reactor's cooling-down and – usually – with the necessity of cutting openings in ship sides. Moreover nuclear power plants are characterized by a large mass of reactor (thickness of reactor vessel walls reaches even 200 mm because of high safety margin necessary due to contaminated water pressure up to 16 MPa at 350 °C temperature) [4,17]. At so low parameters of reactor's cooling agent, power plants based on PWR reactors achieve low values of live steam parameters in steam cycle, which usually do not exceed 300 °C and 4 MPa. It leads to obtaining a low value of thermodynamic efficiency not greater than 35%. Live steam in the cycles fed by water-cooled reactors is saturated steam or overheated one in the range of 50K [4,23]. It results in the necessity of applying additional solutions to dewater expanding steam. The above mentioned drawbacks make that PWR reactors can be successfully substituted by HTR reactors (described below).

HTR REACTORS

HTR reactors (i.e. High Temperature Reactors) or VHTR ones (i.e. Very High Temperature Reactors) belong to a broad group of HTGR reactors (i.e. High Temperature Gas Reactors) whose first types were built as early as in the 1970s [4,23]. Their technology has been proved but not implemented mainly due to the then economic conditions. But, as it was already mentioned, today the technology is under intensive development [5].

The HTR reactors are equipped with a pebble bed reactor (i.e. Pebble Bed Reactor). Such reactor has form of a cylinder filled with TRISO fuel in the form of graphite balls. TRISO (i.e. TRiple coated ISOtropic fuel) is combined with fissile material particles of 0,5 mm diameter. It is usually uranium oxide of a low degree of enrichment (about 10%) with an addition of radiothorium. The fuel particles are closed in three ceramic shells of total diameter of 0,92 mm. The protection

shells maintain their structure and tightness up to 2000 °C temperature [5]. TRISO particles are uniformly arranged within a graphite ball of 60 mm in diameter. In the case of such fuel parameters the reactor in question is filled up to 1/3 of its volume with graphite balls which serve as a moderator.

The application of the pebble bed reactor is associated with many advantages, a.o. possible supplying with fuel of various compositions and enrichment degree (diversification of supply), very high level of fuel burn-up up to 100 000 MWd/t (for PWR reactors - abt. 45 000 MWd/t), that results from second fuel charging (one ball leaves the reactor every 30 s and is loaded again into it 15 times on average) [5]. This is made possible due to very easy procedure of reloading the fuel, which does not even require to shut-down the reactor. Moreover, in the case of a failure the reactor can be unloaded under gravity force only, and the fuel does not suffer any damage and can be loaded again into the reactor. In the case of loss of tightness of reactor's vessel a cooling agent leakage does not endanger people and the environment because helium, i.e. reactor cooling agent, does not undergo radioactive activation and gaseous products of fission maintain kept closed within fuel balls. Walls of the reactor may be only 50 mm thick because of a low pressure inside [4].

In gaseous reactors it is possible to make use of the hot reactor - cooling gas directly in Joule-Brayton cycle or gas-steam cycles. In case of such solution, in order to limit dimensions of ship power plant (especially its heat exchanger), it is advised to use helium as a cooling agent because its specific heat amounts as much as $5,193 \frac{kJ}{kg \cdot K}$. As an alternative is used inexpensive carbon dioxide of specific heat equal to $1,292 \frac{kJ}{kg \cdot K}$. Helium is an expensive perfect gas which, because of a small size of its particles and low viscosity, makes keeping

tightness of pressure installation troublesome, but, as it has been proved, use of it in steam generators multifold lowers their dimensions compared to steam boilers. Dimensions of such generators will be also advantageous compared to application of other gases (e.g. CO₂), and their live steam parameters – much more higher than in the case of application of water. Moreover, a smaller mass flux of the cooling agent makes it possible to significantly reduce demand of power necessary to drive fans of reactor- cooling loop [7].

The use of HTR reactor- cooling gas to feed a steam generator makes it possible to reach supercritical parameters of steam cycle and to achieve this way high heat energy conversion efficiency. In the case of contemporary ship power plants their live steam parameters are as follows: 10 MPa and 535 °C. It results in extensive “piling-up” temperature in steam generator that additionally improves heat exchange parameters and allows to decrease dimensions of the generator. Moreover, water present in steam cycle is not subjected to radioactive exposure [16,19].

VARIABLE OPERATIONAL CONDITIONS

The necessity of operation under distinctly variable conditions is very characteristic for ship power plants. For stabilizing rotational speed of propulsion turbines an electric reduction gear may be applied. In consequence, additional losses are introduced as a result of electric energy conversion, but the efficiency characteristics in function of changes in rotational speed of screw propeller, are improved. Moreover, it makes application of back running unnecessary, and possible application of azimuth propellers may provide excellent manoeuvrability to ship. In this case schematic ship power plant diagram resembles that of stationary small-output power plants [20,21,23].

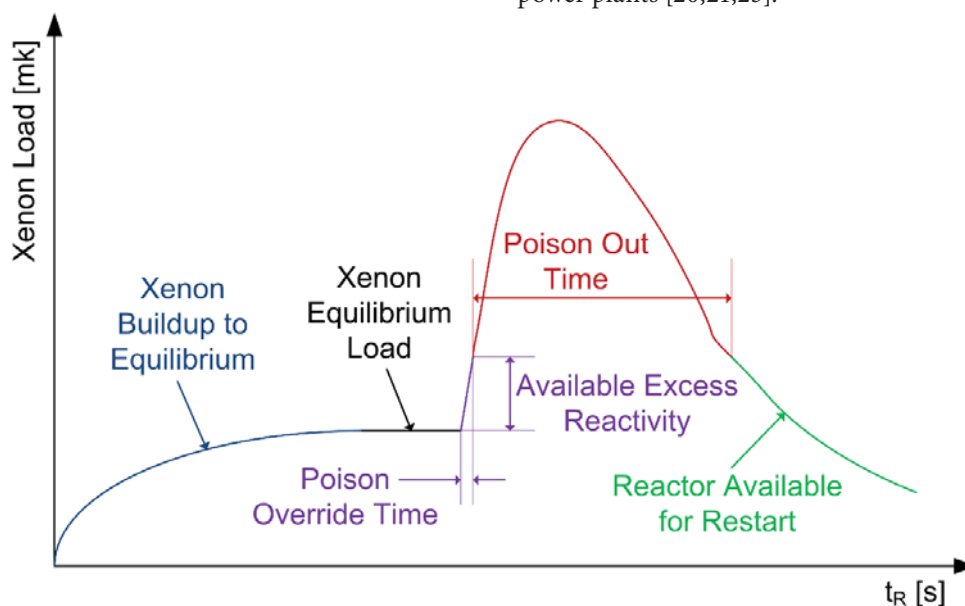


Fig.1. Simplified characteristics of reactivity losses as a result of Xe-135 poisoning during start-ups and power reduction [6]

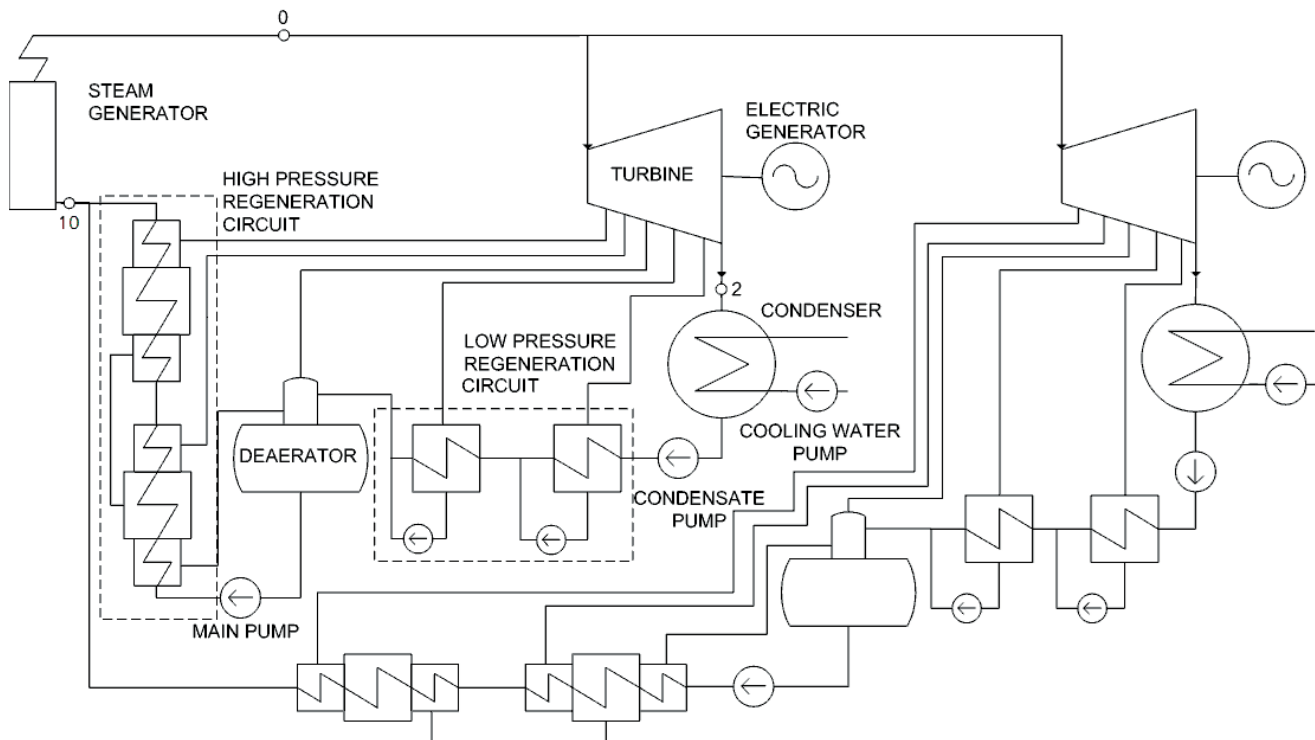


Fig. 2. Schematic thermodynamic diagram of the "twin" system of ship power plant

Another way to optimize parameters of ship power plants under variable operating conditions, which however interferes also cycle parameters, is application of control of rate of steam turbine condenser. It leads to some savings in amount of energy necessary to drive cooling - water pump and to prevention against condensate overcooling [8].

Amount of power generated in ship steam turbine is usually controlled by means of throttle governing. This is not a control desirable from the economic point of view as it introduces losses resulting from steam throttling. However it makes it possible to control turbine output in a broad range without changes in temperature distribution within turbine casing and steam extractions. Such control allows to conduct manoeuvres of the ship. However for the output control in longer time intervals, e.g. for keeping a given speed of a ship, slipping control is used. It consists in decreasing heat power of steam boiler by changing flux of energy delivered with fuel. And, in the case of water -cooled reactors such control is executed by tentative moderating the fission reaction by means of control rods or introduction of neutron absorbers in the form of boric acid into fuel - cooling water. However it leads to drop of fuel temperature and rise of Xe-135 concentration (xenon isotope). This is the so-called xenon poisoning phenomenon whose run is illustrated in Fig. 1 [6].

During rated power operation, xenon isotopes are burned out in the same quantity as that produced, hence their amount, expressed in the reactivity units mk , reaches an appropriate level (Xenon Equilibrium Load). When Xe-135 concentration, as a result of output control process, causes Available Excess Reactivity to be exceeded, then fission chain reaction will start to extinct (Poison Out Time). To develop again the fission reaction is possible only if Xe-135 excessive amount is converted into other isotopes a smaller

cross-section capable of absorbing neutrons generated during radioactive half-life period (Reactor Available for Restart). The radioactive half-life for Xe-135 is equal to 9,1 h [6,17].

HTR reactors are of a low core power density, namely on the level below 10 MW/m^3 . The feature, in association with negative reactivity, makes that at lowering power plant load heat flux absorbed from the reactor becomes also lower, fuel temperature rises and generated power drops. It was proved experimentally that in the case of full switching-off the cooling circulation loop, fuel balls reach their maximum temperature limited to $1600 \text{ }^\circ\text{C}$, and fission reaction then starts to decay [5]. Heat energy generated during the entire process is absorbed by reactor walls and transferred to the atmosphere by natural circulation of air. Therefore there is no danger of melting the reactor core or protective barrier. Coolant pressure does not provide any risk of fracture to reactor's vessel. This mode of control has also two advantages: it protects reactor against xenon poisoning, and at a partial load live steam temperature can be kept on a constant level.

Therefore it should be unambiguously stated that HTR reactors ensure in every respect better operational parameters under variable operation conditions than PWR reactors.

CONDITIONS OF ANALYSIS

Design parameters of ship power plants are chosen in compliance with mission of a ship, its service speed, manoeuvrability and own demands of the ship such as: energy supply to refrigeration plant, living accommodations and objects for passenger needs. For the reasons two steam-turbine cycles were taken into account in analyzing possible use of HTR reactors in ship steam power plants. First of them

Tab.1 Steam parameters in characteristic points of the proposed steam cycles [20].

Parameter	Symbol	Unit	Cycle with inter-stage overhear	“Twin” cycle
Temperature of live steam	t_0	°C	535	535
Pressure of live steam	p_0	[bar]	100	100
Temperature of steam from interstage overhear	t_0'	°C	535	-
Pressure of steam from inter-stage overhear	p_0'	[bar]	18	-
Pressure in condenser	p_2	[bar]	0,05	0,05
Number of regenerative exchangers	-	-	5	4

(called further “twin” system or cycle) is consisted of two identical, independent turbine sets fitted with a supply - water regenerative pre-heater (circuit). Schematic thermodynamic diagram of the system is presented in Fig. 2.

The other cycle consists a turbine set with interstage overhear and supply - water regenerative pre-heater. Schematic thermodynamic diagram of the cycle is presented in Fig. 3. The basic difference between the cycles in question is the distribution of power between propulsion turbines. Namely, in the “twin” system it is possible to reach full thermodynamic efficiency both under rated load and that equal to a half of the rated output. This is achieved at the expense of maximum thermodynamic efficiency which is higher in the case of application of interstage overhear.

Tab. 1. shows parameters of live steam, overhear and condenser. For both the cycles temperatures and pressures of the upper and lower heat source have been selected on the same level.

The cycle with interstage overhear has one regenerative exchanger more however it maintains the same heat exchange area for both the power plants. This ensures similar dimensions and masses for both the proposed power plants and makes more exact comparing them possible. Own demands of the power plants are the following: to drive the condensate and water - supply pumps and reactor - cooling helium fans.

The above discussed solutions are advantageous because in case of a failure of one of the turbine sets it is still possible to reach a partial output. In the case of the „twin” cycle it

is possible to switch off one of the turbine sets by means of a quick-closing valve whose main function is to protect turbine against racing over a permissible rotational speed. In the case of the cycle with interstage overhear it is possible to keep in operation either its high-pressure or low-pressure turbine with the use of reducing-cooling stations which adjust steam parameters to demands of the low-pressure turbine or condenser.

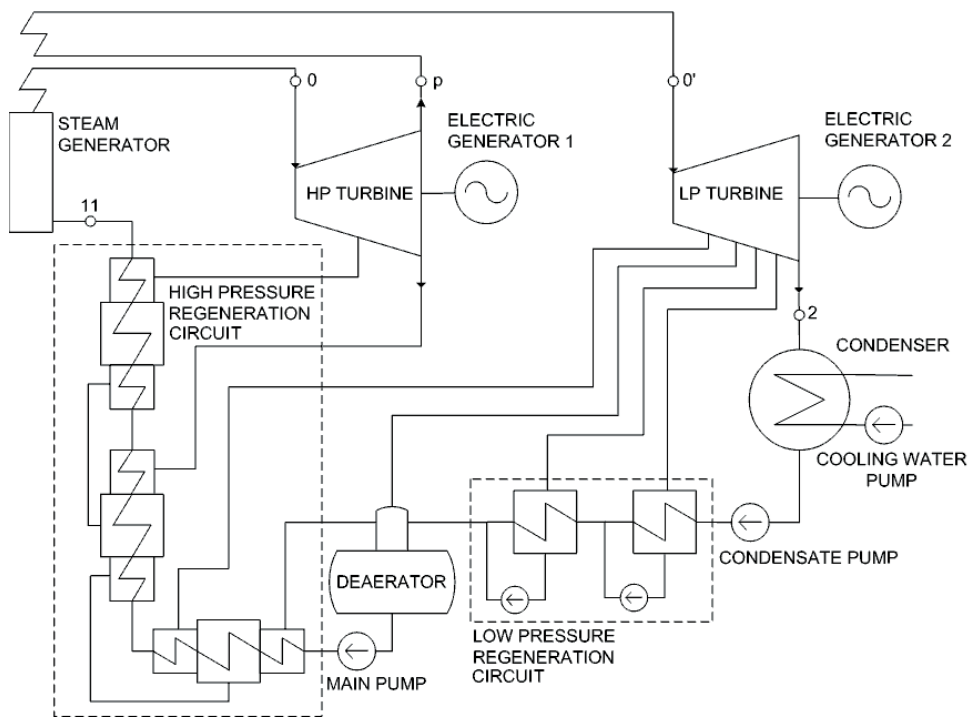


Fig. 3. Schematic thermodynamic diagram of the cycle of power plant with interstage steam overhear

MATHEMATICAL MODEL

Steam parameters in the characteristic points of the thermal cycles in question in variable operational conditions were determined by using Flügl equation which describes steam flow capacity of a turbine [8]:

$$\frac{m_i}{m_{i0}} = \frac{p_i}{p_{i0}} \sqrt{\frac{t_{i0}}{t_i}} \sqrt{\frac{1 - \left(\frac{p_{i+1}}{p_i}\right)^2}{1 - \left(\frac{p_{i+10}}{p_{i0}}\right)^2}} \quad (1)$$

where „0” stands for a value in the state of rated load, and „i” - steam flux flowing behind i-th extraction point.

As intermediate pressure values rise or drop simultaneously the expression which describes the pressure ratio can be simplified according to (2) and neglected in Eq. (1) (behind the last stage of the turbine where p_{i+1} is equal to the pressure p_2 in the condenser).

$$\frac{1 - \left(\frac{p_{i+1}}{p_i}\right)^2}{1 - \left(\frac{p_{i+10}}{p_{i0}}\right)^2} \approx 1 \quad (2)$$

Eq. (1) obtains then the simplified form as follows :

$$\frac{\dot{m}_i}{\dot{m}_{i0}} \approx \frac{p_i}{p_{i0}} \sqrt{\frac{t_{i0}}{t_i}} \quad (3)$$

Further calculations consist in performing subsequent iterations. In the first approximation it is assumed that change in steam mass flux in a given group of stages is the same as change in steam flux into turbine inlet.

$$\frac{\dot{m}'_i}{\dot{m}'_{i0}} = \frac{\dot{m}}{\dot{m}_0} \quad (4)$$

In the current stage of calculations pressure in all extraction points changes proportionally to steam mass flux into turbine inlet , that is expressed as follows :

$$\frac{p'_i}{p'_{i0}} = \frac{p'}{p_0} = \frac{\dot{m}}{\dot{m}_0} \sqrt{\frac{t_1}{t_{10}}} \quad (5)$$

Knowing value of the pressure p'_i in subsequent extraction points one can determine, for a given load, a more exact value of steam mass flux flowing through the turbine in a considered state , by executing again thermodynamic calculations of the thermal cycle.

Net electric efficiency of the power plant is defined by the expression:

$$\eta_{netto} = \frac{N_{netto}}{\dot{Q}_{SG}} \quad (6)$$

Where, for the “twin” cycle, the net efficiency is defined by Eq. (7), and for that with inter-stage overhear – by Eq. (8).

$$\eta_{netto} = \frac{N_G - N_{OC}}{\dot{m}_0(i_1 - i_{10})} \quad (7)$$

$$\eta_{netto} = \frac{N_G - N_{OC}}{\dot{m}_0(i_0 - i_{11}) + \dot{m}_{0r}(i_{0r} - i_p)} \quad (8)$$

For the conducted analyses the following was additionally assumed:

- the generator efficiency characteristics – on the basis of the data for TGH-30 synchronous hydrogen-cooled generator (within the range of 0,95 ÷ 0,98 for the considered load changes) [10];
- the rated internal efficiency of the turbines was selected according to [9] as follows:
 - a. 0,87 - for the high pressure (HP) part of the cycle with interstage steam overhear;
 - b. 0,92 - for the low pressure (LP) part of the cycle with interstage steam overhear;
 - c. 0,90 - for the turbine of the twin cycle.

The internal efficiency of turbines, at partial loads, is dependent on value of steam mass flux flowing through turbine, which was discussed in detail in [20].

- constant value of mechanical efficiency at a given rotational speed , equal to 0,99, according to [9];
- constant value of efficiency of supply water, condensate and condenser cooling water pumps, equal to 0,85;
- constant values of efficiency of asynchronous motors (dependent on rated power) in case of driving:
 - a. supply water pump, equal to 0,95
 - b. condensate pump, equal to 0,88
 - c. condenser cooling water pump, equal to 0,95
- constant efficiency value of helium fan, equal to 0,8, and of asynchronous motor driving the fan, equal to 0,95;
- losses in regenerative heat exchangers were neglected, was assumed equal to 1,00.

Some analytical models of steam cycle of ship nuclear power plants can be found in [16,18], however they simplify much more cycle schemes and do not take into account e.g. the principle of steam flow capacity.

RESULTS OF ANALYSIS OF POWER PLANT OPERATION

On the basis of the taken model and assumptions, were determined characteristics of change in selected parameters of power plant under variable operational conditions for the selected output of the turbines, equal to 50 MW, measured on their shafts.

The obtained results of changes in the generator efficiency η_G , net electric efficiency η_{netto} , average mechanical efficiency of HP and LP part of the turbine, η_T , as well as the relative steam flux \dot{m}_x/\dot{m}_0 , all in function of change in the power plant load N_x/N_0 for the cycle with interstage overhear, are presented in Fig. 4.

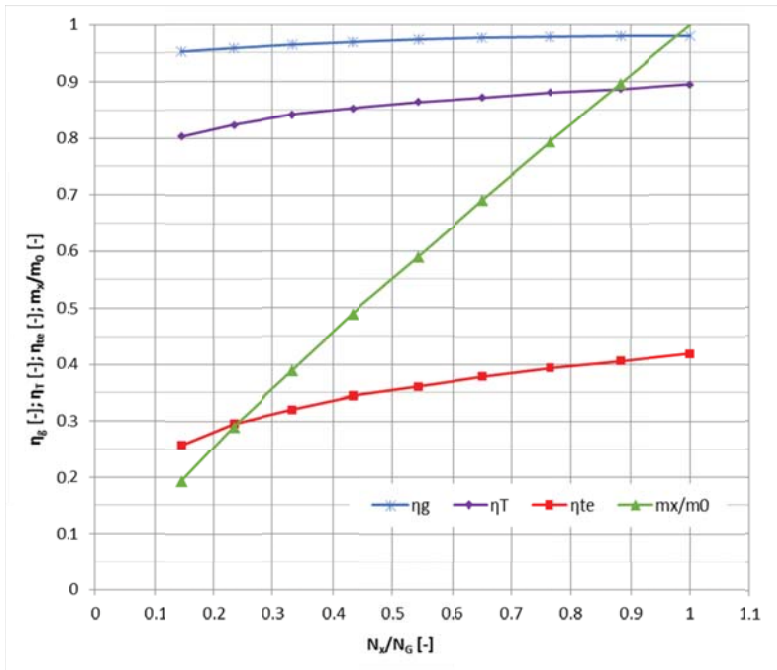


Fig. 4. Changes in the generator efficiency η_G , net electric efficiency η_{net} , average mechanical efficiency of HP and LP part of the turbine, η_T , as well as the relative steam flux m_x/m_0 , all in function of change in the power plant load N_x/N_G for the cycle with interstage overheating

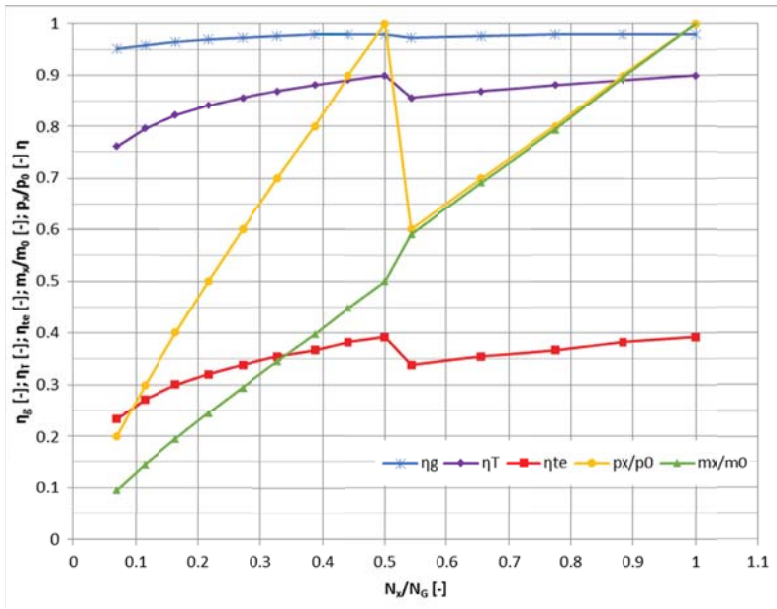


Fig.5 Changes in the generator efficiency η_G , net electric efficiency η_{net} , average mechanical efficiency of the turbines, η_T , the relative steam flux m_x/m_0 and the relative turbine inlet pressure in function of changes in the power plant load N_x/N_G for the 'twin' cycle

And, the calculation results for the "twin" cycle are given in Fig. 5. The diagram additionally contains the relative average pressure at turbine inlet in function of changes in power plant

load. In case of the cycle with interstage overheating, the parameter practically agrees with the relative steam mass flux m_x/m_0 and for this reason it was omitted in Fig. 4.

The rated parameters of the analyzed power plants are presented in Tab. 2. On the basis of the data given in the diagrams of Fig. 4 and 5 as well as Tab. 2 it may be stated that the application of interstage steam overheating improves thermodynamic efficiency of thermal cycle of steam power plants, whereas the multiplication of turbine sets improves energy conversion efficiency in case of partial load. It should be stressed that the thing is the long-lasting partial load but not manoeuvring conditions.

FINAL CONCLUSIONS

As results from the performed literature review and calculations, the today used steam cycles in ship power plants could effectively interact with HTR reactors. The application of HTR reactors would improve this way energy conversion efficiency of ship nuclear power plants compared to the presently used PWR reactors, without introduction any significant changes in today implemented solutions of steam cycles.

The performed analyses of thermodynamic cycles of a power plant fitted with two-case steam turbine and interstage overheating as well as of two identical single-case turbines of cycle without overheating have demonstrated differences, at the same shaft power, both in net electric power quantity developed by the power plant and in its efficiency values under partial loads.

The analysis of the efficiency characteristics presented in Fig. 4 and 5 and the data given in Tab. 1 and 2 leads to the conclusions that single-case steam turbines operating under a simple thermodynamic cycle, doubled or multiplied in ship power plant, are able to ensure a higher energy conversion efficiency of power plant at partial loads. Such situations most often occur in case of passenger cruisers and other large passenger ships which consume vast amounts of energy even during mooring operations in ports. Such power plants may be also so designed as to deliver, from an additional turbine set, a peak power necessary e.g. during manoeuvres or to ensure reaching the same ship speed both in favourable and harsh weather conditions without any impact on thermodynamic efficiency of the power plant in rated operational conditions. Moreover, in this case a main propulsion electric reduction gear finds especially its application as it ensures a flexible electric power distribution as well as possible use of azimuth propellers which can provide excellent ship manoeuvrability.

Tab. 2 Selected parameters of power plants under rated operational conditions at the same output of steam generator

Parameter	Symbol	Unit	Cycle with interstage overheat	“Twin” cycle
Output of steam generator (reactor)	\dot{Q}_{SG}	MWt	112,40	120,41
Net electric output of power plant	N_{netto}	MWe	47,21	46,96
Live steam mass flux	m_0	$\frac{kg}{s}$	38,31	44,67
Overheated steam mass flux	m_{ov}	$\frac{kg}{s}$	33,14	-
Heat exchange surface area	F_w	m^2	3022,75	3022,75
Net electric efficiency of power plant	η_{netto}	-	0,42	0,39

And, more complex ship power plants composed of two-case steam turbine and interstage overheat, show higher efficiency values under rated loads. As far as the presently possible application of nuclear energy to merchant ships are considered, the greatest chance is connected with the largest cargo ships operating on inter-continental routes. Therefore these are the considered power plants showing higher efficiency values under rated loads which have the greatest chance to be introduced in practice. Moreover, the highly efficient thermodynamic cycles in association with nuclear energy sources make it possible to resign from using economic speeds, that offers additional advantages to ship owners. Without a doubt, the analysis of the data presented in this paper constitutes a valuable source of information for preliminary analyses and choice of parameters for ship power plants based on nuclear energy.

The idea of application of high-temperature, graphite-moderated, helium - cooled nuclear reactors eliminates operational disadvantages of contemporary ship nuclear power plants by increasing their parameters over those of contemporary conventional steam power plants. Application of HTR reactors improves hence profitability of ship nuclear power plants compared to today used PWR reactors, increases their safety and lowers hazards to the environment. All the features make that application of HTR reactors could lead to more common use of nuclear energy in merchant shipbuilding.

NOMENCLATURE

- N_{netto} – net electric output of power plant [MWe]
 \dot{Q}_{SG} – heat flux transferred to supply water in steam generator [MWth]
 N_G – total electric power measured at terminals of turbine - set generators [MWe]
 N_x – a given power plant output measured at terminals of turbine - set generators [MWe]
 N_{OC} – total power for own demands of power plant to drive water pump and helium fan [MWe]
 F_w – heat exchange surface area of regenerative exchangers
 \dot{m}_0 – live steam flux at outlet from steam generator [$\frac{kg}{s}$]
 \dot{m}_{ov} – live steam flux for interstage overheat [$\frac{kg}{s}$]
 i_1 – live steam enthalpy at outlet from steam generator in case of the „twin” cycle [$\frac{J}{kg \cdot K}$]
 i_{10} – enthalpy of supply water for steam generator in case of the „twin” cycle [$\frac{J}{kg \cdot K}$]
 i_p – enthalpy of steam at outlet from high-pressure turbine casing, used for interstage overheat [$\frac{J}{kg \cdot K}$]
 i_{11} – enthalpy of supply water for steam generators in case of the cycle with interstage overheat [$\frac{J}{kg \cdot K}$]
 η_{netto} – net electric efficiency of power plant
 η_g – electric generator efficiency
 η_T – average mechanical efficiency of turbine
 m_x/m_0 – relative live steam mass flux at inlet to turbine
 p_x/p_0 – relative live steam pressure at inlet to turbine
 γ_i – relative steam flux

BIBLIOGRAPHY

1. PortalMorski.pl : *Sea traffic statistical data* (in Polish), <http://www.portalmorski.pl/info/statystyki> 14.02.2014.
2. Badur J.: *Modelling of balanced combustion in gas turbines* (in Polish), Publ. IMP PAN, Gdańsk, 2003
3. Dzida M., Mucharski J.: *On the possible increasing of efficiency of ship power plant with the system combined of marine diesel engine, gas turbine and steam turbine in case of main engine cooperation with the gas turbine fed in parallel and the steam turbine*, Polish Maritime Research, No. 2 (60), 2009 , Vol. 16 p.40÷44
4. Jezierski G: *Nuclear energy yesterday and to tomorrow* (in Polish), Scientific Technical Publishing House (Wydawnictwo Naukowo-Techniczne), Warsaw 2005
5. Department of Nuclear Science and Engineering, MIT: *Modular Pebble Bed Reactor*, <http://web.mit.edu/pebble-bed/>14.02.2014
6. Kubowski J.: *Problems of interaction between nuclear power plants and electric power network* (in Polish), Elektroenergetyka, No. 4 (670), 2010, pp.218÷221
7. Przybylski M., Głuch J.: *Selected design and construction aspects of supercritical steam generators for high temperature reactors*. Archives of Energetics, No 2 Vol. 42, 2012, pp.113÷120
8. Błaszczuk A., Głuch J., Gardzielewicz A.: *Operating and economic conditions of cooling water control for marine steam turbine condenser*, Polish Maritime Research, No. 3 (70), Vol. 18, 2011, pp.48÷54
9. Perycz S.: *Gas and steam turbines* (in Polish), Publishing House of Gdansk University of Technology (Wydawnictwo Politechniki Gdańskiej), Gdańsk 1988
10. Stein Z.: *Electric engines and drives* (in Polish), School and Pedagogical Publishers (Wydawnictwo Szkolne i Pedagogiczne), Warszawa 1985
11. Dzida M.: *On the possible increasing of efficiency of ship power plant with the system combined of marine diesel engine, gas turbine and steam turbine, at the main engine - steam turbine mode of cooperation*, Polish Maritime Research, No.1 (59), 2009, Vol. 16, pp. 47÷52
12. Dzida M., Giltler J., Dzida S.: *On the possible increasing of efficiency of ship power plant with the system combined of marine diesel engine, gas turbine and steam turbine in case of main engine cooperation with the gas turbine fed in series and the steam turbine*, Polish Maritime Research, No. 3 (61), 2009 Vol. 16, pp. 26÷31
13. Hagling F.: *Variable geometry gas turbines for improving the part-load performance of marine combined cycles - Combined cycle performance*, Applied Thermal Engineering, No. 31, 2011, pp.467 ÷ 476
14. Welaya Y., Mosleh M., Ammar N.: *Energy analysis of a combined solid oxide fuel cell with a steam turbine power plant for marine applications*, J. Marine Sci. Appl., No. 12, 2013, pp.473÷483
15. Nisan S., Rouyer J., Marcetteau P., Duflo D.: *SEMER: A simple code for the economic evaluation of nuclear and fossil energy-based power production systems*, Nuclear Engineering and Design, No. 221, 2003, pp.301÷313
16. Geschwindt J., Lommers L., Southworth F., Shahrokhi F.: *Performance and optimization of an HTR cogeneration system*, Nuclear Engineering and Design, No. 251, 2012, pp.297÷300
17. Teichela H., Pouget-Abadie X.: *How the European Pressurized Water Reactor fulfils the utility requirements*, Nuclear Engineering and Design, No. 187, 1999 , pp. 9÷13
18. Asiedu-Boateng P., Akaho E., Nyarkob B., Yamoah S.: *Modeling and simulation of cogeneration nuclear power plant for seawater desalination*, Nuclear Engineering and Design, No. 242, 2012, pp.143÷147
19. Lommers L., Shahrokhi F., Mayer III J., Southworth F.: *AREVA HTR concept for near-term deployment*, Nuclear Engineering and Design, No. 251, 2012, pp.292÷296
20. Kowalczyk T.: *Power engineering analysis of possible application of a ship steam power plant of 50MW output , equipped with a steam generator heated by helium agent cooling a high temperature nuclear reactor* (in Polish), M.Sc. thesis , Gdańsk University of Technology, Gdańsk 2012
21. Smith C.: *The energy challenge*, Appl. Petrochem Res, No. 2, 2012, pp.3÷6
22. Sarkisov A., Vysotskii V., Bilashenko V., Barinov N., Kiselev A., Markarov V., Kulakov I., Lepekhin A., Petrunin V., Pichugin A., Krysov S.: *Expected radiological and radio-ecological consequences of operating floating nuclear heat and power plants*, Atomic Energy, Vol. 104, No. 3, 2008, pp. 237÷249.
23. Hirdaris S., Cheng Y., Shallcross P., Bonafoux J., Carlson D., Prince B., Sarris G.: *Considerations on the potential use of Nuclear Small Modular Reactor (SMR) technology for merchant marine propulsion*, Ocean Engineering, No. 79, 2014, pp.101÷130

24. Staliński J., Szewalski R.: *Analysis of impact of changes in technical-economic indices of ship power plants onto calculation results of economic profitability of ships* (in Polish), Acta Technica Gedanensia No. 1, 1963, Gdańsk 1963.

CONTACT WITH THE AUTHOR

Tomasz Kowalczyk, M. Sc.
Paweł Ziółkowski, M. Sc.

Energy Conversion Department, Institute of Fluid Flow
Machinery , Polish Academy of Sciences
ul. Fiszer 14
80-231 Gdańsk

e-mail: tomek.kowalczyk@imp.gda.pl
pawel.ziolkowski@imp.gda.pl

Jerzy Głuch, Prof.

Department of Automatics and Turbine Propulsion,
Faculty of Ocean Engineering and Ship Technology
Gdańsk University of Technology
11/12 Narutowicza St.
80 - 233 Gdańsk

POLAND

NUMERICAL MODEL OF SO₂ SCRUBBING WITH SEAWATER APPLIED TO MARINE ENGINES

M. I. Lamas^a

C. G. Rodríguez^a

J. D. Rodríguez^a

J. Telmo^b

^a University of Coruña, Spain

^b University of Santiago de Compostela, Spain

ABSTRACT

The present paper proposes a CFD model to study sulphur dioxide (SO₂) absorption in seawater. The focus is on the treatment of marine diesel engine exhaust gas. Both seawater and distilled water were compared to analyze the effect of seawater alkalinity. The results indicate that seawater is more appropriate than distilled water due to its alkalinity, obtaining almost 100% cleaning efficiency for the conditions analyzed. This SO₂ reduction meets the limits of SO_x emission control areas (SECA) when operating on heavy fuel oil. These numerical simulations were satisfactory validated with experimental tests. Such data are essential in designing seawater scrubbers and judging the operating cost of seawater scrubbing compared to alternative fuels.

Keywords: Sulphur dioxide, SO₂, scrubbers, CFD

INTRODUCTION

Most medium and large marine engines operate on heavy fuel oil. This is a cheap combustible but contains an important quantity of pollutant substances, especially sulphur. Oxidation of the sulphur in the fuel forms sulphur oxides (SO_x) in the exhaust gas, which constitute the major source of acid rain. In order to prevent SO_x formation, IMO Annex VI of MARPOL 73/78, Regulations for the Prevention of Air Pollution from Ships, which was ratified and entered into force from 2005, regulates the SO_x emissions by setting a maximum limiting value on the fuel sulphur content. This limit has been progressively reduced, from 4.5% to 3.5% from January 1st 2012 and from 3.5 to 0.5% w/w from January 1st 2020. Besides, there are sulphur emission control areas (SECA) with more stringent requirements. So far, using low sulphur content fuels was preferred to scrubbing applications. Nevertheless, exhaust gas cleaning/after-treatment systems have become a promising alternative due to these stricter

emission limits and the high price of alternative fuels [1].

Regarding exhaust gas cleaning/after-treatment systems, there are many alkali absorbents such as urea, NaOH, limestone slurry, NaCl, etc. Seawater is a promising solution for marine applications. The main advantages of seawater are the availability and the fact that the acidified effluent can be discharged directly into the sea after a simple neutralization process.

There are some reports about seawater scrubbers available in the literature. For instance, Zhang et al. [2], Oikawa et al. [3] and Williams [4] analyzed seawater wet scrubbers used in power plants. Sun et al. [5] focused on a membrane contactor scrubber and showed that the mass transfer coefficient in seawater is about twice of the NaOH solution with pH 8.35. Darake et al. [6] carried out an experimental study and mathematical modelling of SO₂ removal by seawater in a packed-bed tower. Caiazza et al. [7] analyzed a seawater spray scrubber operating under marine diesel exhaust conditions and compared seawater and distilled water in order to

elucidate the effect of seawater. Andreassen and Mayer [8] formulated a model to analyze seawater scrubbing, focused on marine engine applications, and concluded that a seawater scrubber is a promising option to low sulphur fuels. Sukheon and Nishida [9] analyzed the effect of seawater under SO_x , particulate matter, CO_2 and NO_x .

In order to expand this literature about seawater scrubbers, the purpose of this paper is to develop a numerical model to analyze SO_2 absorption by seawater. A moving water droplet immersed in a gas medium was analyzed. Both liquid and gas phases were included in the model. The proposed CFD model takes in consideration the fluid motion inside and outside the droplet, heat transfer, chemical reactions and mass diffusion. In order to validate the numerical results with experimental ones, the single droplet model was implemented into a complete spray model.

COMPUTATION OF SO_2 ABSORPTION

PHYSICAL AND CHEMICAL DESCRIPTION OF THE PROBLEM

A schematic representation of a seawater scrubber is indicated in Fig. 1. A spray of falling-down droplets encounters a counter-current exhaust gas flow which contains SO_x and other pollutants. Each droplet is exposed to the exhaust gas, and the viscosity between the gas and droplet induce a shear stress. This drag force promotes a vortex motion in the interior of the droplet, indicated in the figure. The droplet velocity tends to decay in the course of movement due to the drag effect. Soon after the gas is in touch with the droplet, a concentration gradient is induced in the interface and SO_2 is transported into the water by mass diffusion. At the same time, chemical dissociation reactions take place.

The model proposed in the present paper analyzes the amount of SO_2 absorbed by a single droplet, with given initial velocity and diameter, falling counter flow with respect to

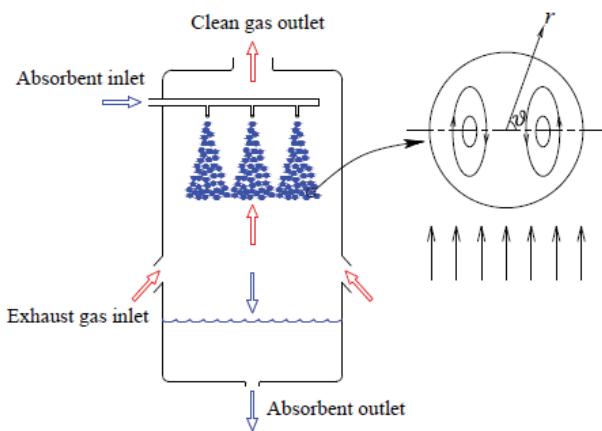


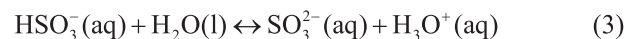
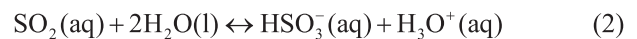
Fig. 1. Schematic representation of the problem

the exhaust gas stream coming from a typical marine engine burning heavy fuel oil. The following assumptions were adopted in order to simplify the problem:

- Axisymmetric flow on both phases.
- The shape of the droplet remains spherical due to surface tension and viscous forces.
- The fluids are Newtonian.
- The flow fields are laminar due to its low Reynolds numbers.
- Phase equilibrium, Henry's law, prevails at the interface.
- Mass diffusion follows Fick's law.

While the average salinity depends on the regional location, the relative amounts of the constituents of seawater are more or less invariant. Many alkaline species are presented in seawater, such as HCO_3^- , CO_3^{2-} , OH^- , HPO_4^{2-} , etc. Between them, the main contribution to alkalinity is by far the bicarbonate ion HCO_3^- . Typical alkaline concentrations are $2400 \mu\text{mol/kg}$ of H_2O [8, 10, 11].

Inside the droplet, the following reactions take place [8]:



Reaction (1) is the dissolution of gaseous SO_2 in water at the liquid-gas interphase, governed by Henry's law:

$$[\text{SO}_2(\text{aq})] = p_{\text{SO}_2} k_H \quad (6)$$

where p_{SO_2} is the partial pressure of SO_2 , $[\text{SO}_2(\text{aq})]$ is the concentration of SO_2 in the solution and k_H is Henry's constant, expressed as:

$$k_H = k_H^0 e^{\frac{-\Delta H_{\text{soln}}}{R} \left(\frac{1}{T} - \frac{1}{T^0} \right)} \quad (7)$$

where k_H^0 is the Henry's constant at the reference state, ΔH_{soln} is the enthalpy of solution, T is the temperature and T^0 is the reference state temperature (298.15 K). A value of $k_H^0 = 1.2 \text{ mol}/(\text{kg atm})$ and the slope $-\Delta H_{\text{soln}}/R = 2850 \text{ K}$ were employed, Sander [12].

Reaction (2) is the reaction between dissolved SO_2 and water, producing bisulfite. Reaction (3) is the dissociation of bisulfite to sulfite. Reaction (4) is the neutralization of formed bisulfite with the seawater alkalinity. Reactions (2-4) are so fast to assume equilibrium, Andreassen and Mayer [8].

Reaction (5) is the dissolution of CO_2 at the liquid-gas interphase, also governed by Henry's law. A value of $k_H^0 = 0.034 \text{ mol}/(\text{kg atm})$ and $-\Delta H_{\text{soln}}/R = 2400 \text{ K}$ were employed, Sander [12].

GOVERNING EQUATIONS

As mentioned previously, the fluid motion inside and outside a droplet, heat transfer, chemical reactions and mass diffusion were analyzed. The governing equations consist of the continuity, momentum, energy and species for both liquid and gas phases, Table 1.

Tab. 1. Governing equations

Gas phase	Continuity	$\nabla \cdot \bar{u}_g = 0$
	Momentum	$\frac{\partial(\rho_g \bar{u}_g)}{\partial t} = -\nabla \cdot (\rho_g \bar{u}_g \bar{u}_g) - \nabla p_g - \nabla \cdot \bar{\tau}_g$
	Energy	$\frac{\partial(\rho_g c_{pg} T)}{\partial t} + \nabla \cdot (\rho_g \bar{u}_g c_{pg} T) = \nabla \cdot (k_g \nabla T)$
	Species	$\frac{\partial C_i}{\partial t} = -\nabla \cdot (C_i \bar{u}_g) - D_g \nabla^2 C_i + R_i$
Liquid phase	Continuity	$\nabla \cdot \bar{u}_l = 0$
	Momentum	$\frac{\partial(\rho_l \bar{u}_l)}{\partial t} = -\nabla \cdot (\rho_l \bar{u}_l \bar{u}_l) - \nabla p_l - \nabla \cdot \bar{\tau}_l$
	Energy	$\frac{\partial(\rho_l c_{pl} T)}{\partial t} + \nabla \cdot (\rho_l \bar{u}_l c_{pl} T) = \nabla \cdot (k_l \nabla T)$
	Species	-

In the equations above, the subscript i shown in the species equations represents SO_2 , HSO_3^- , H_3O^+ , SO_3^{2-} , HCO_3^- or CO_2 . C is the concentration, D the mass diffusivity, c_p the specific heat, and R a source which models the chemical reactions.

A reference frame which moves with the droplet was employed. A free-stream velocity was imposed as inlet boundary condition. The drag force decelerates the relative velocity between the droplet and gas, and this was implemented in the numerical model adjusting the free-stream velocity at each time step. The deceleration is given by:

$$\frac{du_\infty(t)}{dt} = \frac{F_{drag}}{\rho_l \pi D^3 / 6} + g \quad (8)$$

where u_∞ is the free-stream velocity, F_{drag} the drag force, ρ_l the seawater density, ρ_g the gas density and D the droplet diameter.

The free-stream velocity after a time step Δt is given by:

$$u_\infty(t + \Delta t) = u_\infty(t) + \Delta t \frac{du_\infty(t)}{dt} \quad (9)$$

Heat transfer between the droplet and gas was considered. Inside the droplet, the energy equation was solved until the evaporation temperature was reached. From this temperature, the computational grid was regenerated at every time step to account for droplet diameter reduction due to evaporation. The rate of change of the droplet mass, which is equivalent to the rate of evaporated mass, is obtained from a heat balance:

$$hA(T_e - T_g) = \frac{dm}{dt} h_{fg} \quad (10)$$

where T_e is the evaporation temperature, T_g the gas temperature, h_{fg} the latent heat of evaporation, A the surface and h the heat transfer coefficient, given by the Ranz-Marshall equation [13]:

$$\frac{hD}{k} = 2 + 0.6 \text{Re}^{1/2} \text{Pr}^{1/3} \quad (11)$$

where D is the droplet diameter, k the thermal conductivity, Re the Reynolds number and Pr the Prandtl number.

As initial conditions, zero velocity was imposed to the liquid phase and free-stream velocity to the gas phase. The free-stream velocity was also imposed as boundary condition. A zero SO_2 concentration was imposed to the liquid phase. Regarding the gas phase, initial SO_2 concentrations between 500 and 1000 ppm were studied, corresponding to typical values for exhaust gas from marine engines operating on fuel oil [14, 15].

CFD MODEL

The computational mesh is indicated in Fig. 2. The grid size is uniform in the tangential direction, with $\Delta\theta = 4^\circ$. In the radial direction the mesh is finer inside the droplet and near the interface. The domain size was 15 droplet radii from the droplet center. Several tests were performed in order to determine the adequate extent of the domain in such a way as to eliminate any potential effects of the outer boundaries on the flow close to the droplet. As mentioned previously, this grid was regenerated at every time step to account for the droplet reduction.

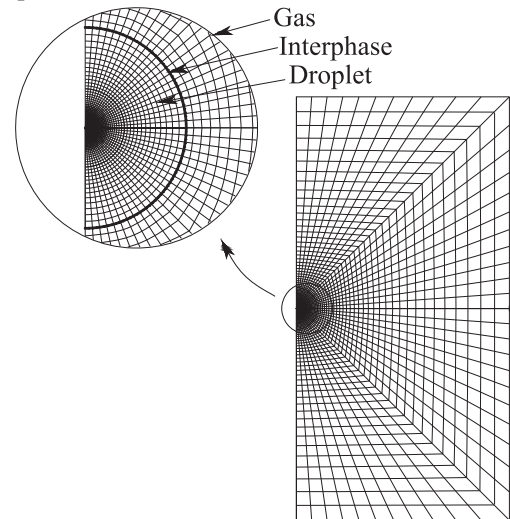


Figure 2. Computational mesh.

The problem was simulated using the open software OpenFOAM (Open Field Operation and Manipulation).

This software was chosen because it allows total manipulation of the code. A new OpenFOAM solver was developed for the presented study. C++ programming language was employed to write this new solver.

OpenFOAM is based on the finite volume method. The pressure-velocity coupling was treated using the PISO (Pressure Implicit Splitting of Operators) procedure. The equations were discretized by the QUICK interpolation and the temporal treatment was solved by an implicit method. The solution was checked for refinement sensibility on both mesh size and time step.

RESULTS

Fig. 3 shows the velocity field for 600 ppm SO_2 concentration (i.e., 0.00133 kg/kg of H_2O), alkaline concentration 2400 $\mu\text{mol/kg}$ of H_2O (i.e., 0.000146 kg/kg of H_2O), free stream velocity 2 m/s and initial droplet of 1 mm diameter. As can be seen, a vortex is created inside the droplet. Figs. 4 and 5 indicate the mass fraction of HCO_3^- and SO_2 respectively, for 0.5 and 1 s. These figures indicate that SO_2 is initially at the droplet surface and then the internal vortex transports SO_2 to the core of the droplet. HCO_3^- is consumed first at the interphase and then at the core of the droplet.

EXPERIMENTAL VALIDATION

The accuracy of CFD models applied to marine engines was previously validated in simulations of the scavenging process [16-17], combustion [19] and NO_x reduction methods [19-21]. Nevertheless, it is important to check the accuracy of the CFD model proposed in the present paper, i.e., SO_x reduction. To this end, the results were compared with experimental tests obtained by Caiazza et al. [7].

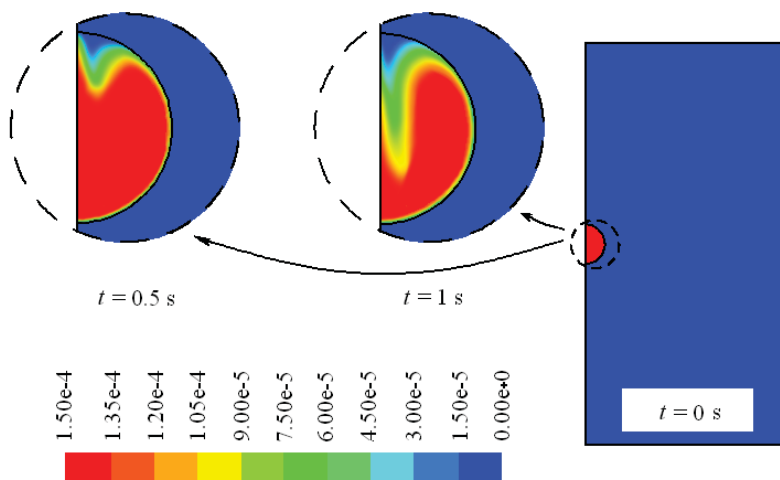


Figure 4. Mass fraction of HCO_3^- .

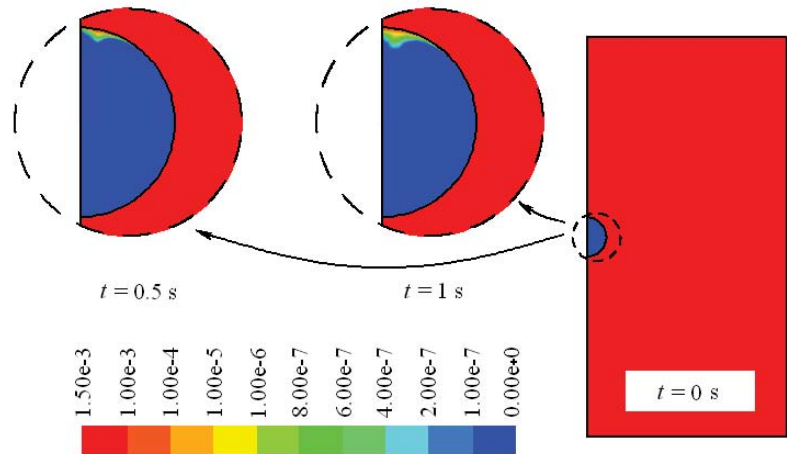


Figure 5. Mass fraction of SO_2 .

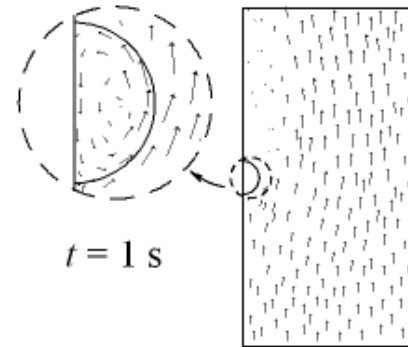


Figure 3. Velocity field, \rightarrow 2 m/s.

These authors analyzed a seawater spray scrubber which can be numerically reproduced since the liquid flow is composed by a set of independent droplets. In their experimental setup, Caiazza et al. [7] employed a compressor to blow air and a heater to reach 250 °C. A stream of air with SO_2 was employed and water was injected countercurrent in a 180 mm diameter and 1880 mm height tube. The SO_2 capture efficiency was calculated by comparing the outlet SO_2 concentration to the inlet SO_2 concentration. A fast camera was employed to measure the droplet diameter. In the experimental tests, a fixed gas flow rate of 40 m^3/h was employed. Three different inlet SO_2 concentration levels were tested, 500, 700 and 900 ppm. The water flow rate was varied in the range 0.06-0.4 m^3/h corresponding to liquid-to-gas ratios in the range of 1-10 $\times 10^{-3}$, common in the marine field [14-15]. Both water and seawater were compared.

Fig. 6 indicates the desulfurization results obtained with distilled water. The desulfurization efficiency increases with the liquid flow rate. As can be seen, numerical results indicate a lower desulfurization efficiency than experimental setups. As original distilled water had negligible alkalinity, after pouring and mixing in the tank

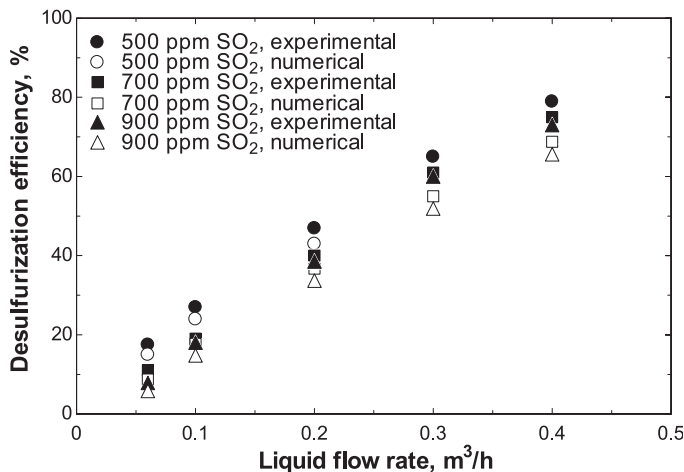


Fig. 6. Numerical and experimental desulfurization efficiency results. Distilled water. Gas flow rate 40 m³/h

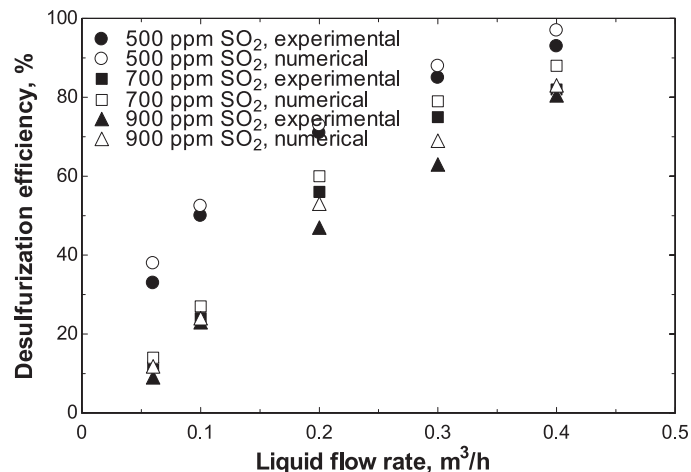


Fig. 7. Numerical and experimental desulfurization efficiency results. Seawater. Gas flow rate 40 m³/h

this water contaminates with seawater residue in the tank and/or in the lines left from previous experiments, Caiazza et al. [7].

Fig. 7 illustrates the desulfurization results obtained with seawater under the same conditions. As expected, seawater is more efficient than distilled water due to the alkalinity. Fig. 8 illustrates the desulfurization results for seawater under 60 m³/h gas flow rate.

Fig. 9 illustrates a summary where all the data are represented in a parity plot. A satisfactory concordance was obtained.

CONCLUSIONS

A numerical investigation was developed on SO₂ capture by means of seawater. The internal circulation, droplet deceleration, evaporation, mass and heat exchange were modeled. The transport equations were solved for both liquid and gas phases on a non uniform computational grid, which was regenerated at every time step to account for droplet diameter reduction.

The numerical results were compared with experimental tests, giving a satisfactory correspondence. This model is very

useful when designing new models of seawater scrubbers.

Almost 100% of SO₂ capture efficiencies were obtained, which indicates that SO₂ scrubbing by seawater is a promising solution for marine applications. It allows to use heavy fuel oil instead of expensive low sulphur fuels such as Marine Diesel Oil or Marine Gas Oil.

ACKNOWLEDGEMENTS

The authors would like to express their gratitude to "Talleres Pineiro, S.L.", sale and repair of marine engines.

REFERENCES

1. Lamas, M.I.; Rodríguez, C.G.; Telmo, J.; Rodríguez, J.D. Numerical analysis of emissions from marine engines using alternative fuels. Submitted to Polish Maritime Research.
2. Zhang, D.N.; Chen, Q.Z.; Zhao, Y.X.; Maeda, Y.; Tsujino, Y. Stack gas desulfurization by seawater in Shanghai. Water, Air & Soil Pollution, vol. 130, pp. 271-276, 2001.
3. Oikawa, K.; Yongsiri, C.; Takeda, K.; Harimoto, T.

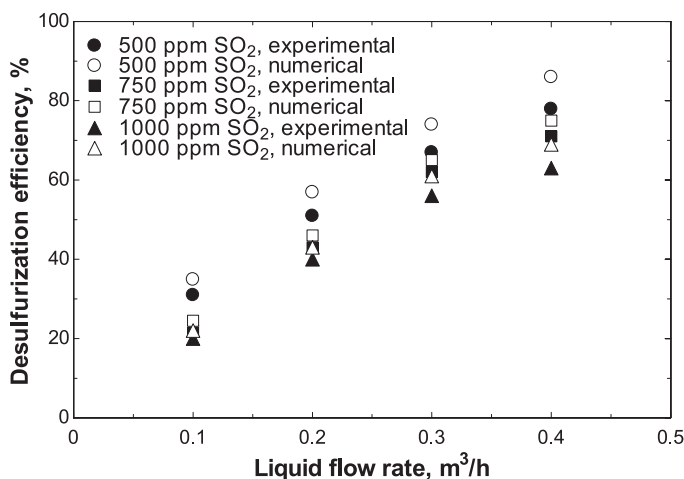


Fig. 8. Numerical and experimental desulfurization efficiency results. Seawater. Gas flow rate 60 m³/h

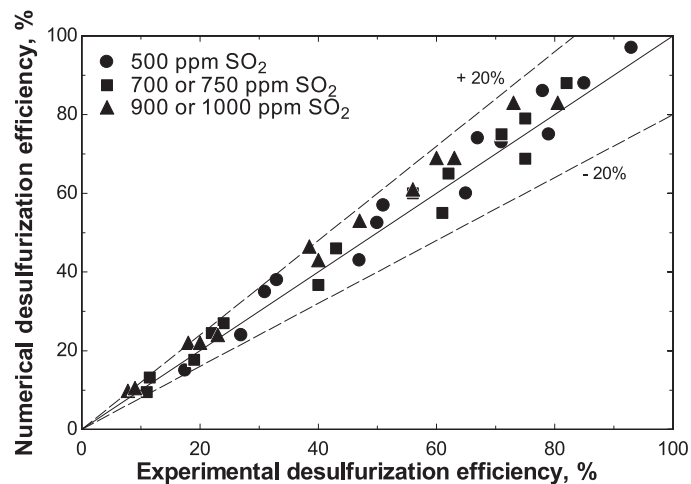


Fig. 9. Comparison between numerical and experimental results

- Environmental Progress, vol. 22, pp. 67-73, 2003.
4. Williams, P.J. Use of seawater as makeup water for wet flue gas desulfurization systems. EPRI-DOE-EPA Combined Utility Air Pollution Control Symposium, August 16-20. Atlanta, Georgia, USA, 1999.
 5. Sun, X.; Meng, F.; Yang, F. Application of seawater to enhance SO₂ removal from simulated flue gas through hollow fiber membrane contactor. *Journal of Membrane Science*, vol. 312, pp. 6-14, 2008.
 6. Darake, S.; Rahimi, A.; Hatamipour, M.S.; Hamzeloui, P. SO₂ removal by seawater in a packed-bed tower: experimental study and mathematical modelling. *Separation Science and Technology*, vol. 49, pp. 988-998, 2014.
 7. Caiazzo, G.; Langella, G.; Miccio, F.; Scala, F. An experimental investigation on seawater SO₂ scrubbing for marine application. *Environmental Progress & Sustainable Energy*, vol. 32, pp. 1179-1186, 2013.
 8. Andreasen, A.; Mayer, S. Use of seawater scrubbing for SO₂ removal from marine engine exhaust gas. *Energy & Fuels*, vol. 21, pp. 3274-3279, 2007.
 9. Sukheon, A.; Nishida, O. New application of seawater and electrolyze seawater in air pollution control of marine diesel engine. *JMSE International Journal, Series B: Fluids and Thermal Engineering*, vol. 46, pp. 206-213, 2003.
 10. Sverdrup, H. U.; Johnson, M. W.; Fleming, R. H. *The Oceans Their Physics, Chemistry, and General Biology*; Prentice-Hall: New York, 1942.
 11. Dickson, A. G.; Goyet, C., Eds.; *Handbook of Methods for the Analysis of the various Parameters of the Carbon Dioxide System in Sea Water, Version 2*, ORNL/CDIAC-74; U.S. Department of Energy: Washington, DC, 1994.
 12. Sander, R. Henry's Law Constants. In *NIST Chemistry Webbook*; NIST Standard Reference Database Number 69; Linstrom P. J., Mallard W. G., Eds.; National Institute of Standards and Technology: Gaithersburg, MD, 2005.
 13. Ranz, W.E.; Marshall, W.R. Evaporation from drops, *Chemical Engineering Progress*, vol. 48, pp. 141-146, 1952.
 14. Kuiken, K. (2008): *Diesel engines for ship propulsion and power plants from 0 to 100000 kW*. 1st Edition. The Netherlands: Target Global Energy Training.
 15. Woodyard, D. *Pounder's marine diesel engines and gas turbines*. 9th Edition. Oxford. Elsevier, 2009.
 16. Lamas, M.I.; Rodríguez, C.G. CFD analysis of the scavenging process in the MAN B&W 7S50MC two-stroke diesel marine engine. *Journal of Ship Research*, vol. 56(3), pp. 154-161, 2012.
 17. Lamas, M.I.; Rodríguez, C.G.; Rebollido, J.M. Numerical model to study the valve overlap period in the Wärtsilä 6L46 four-stroke marine engine. *Polish Maritime Research*, vol.18, pp. 31-37, 2012.
 18. Lamas, M.I.; Rodríguez, C.G.; Rodríguez, J.D.; Telmo, J. Numerical analysis of several port configurations in the Fairbanks-Morse 38D8-1/8 opposed piston marine engine. *Brodogradnja*, vol. 66, no. 1, pp. 1-11, 2015.
 19. Lamas, M.I.; Rodríguez, C.G. Numerical model to study the combustion process and emissions in the Wärtsilä 6L 46 four-stroke marine engine. *Polish Maritime Research*, vol. 20, pp. 61-66, 2013.
 20. Lamas, M.I.; Rodríguez, C.G.; Aas, H.P. Computational fluid dynamics analysis of NO_x and other pollutants in the MAN B&W 7S50MC marine engine and effect of EGR and water addition. *International Journal of Maritime Engineering*, vol. 155, Part A2, pp. A81-A88, 2013.
 21. Lamas, M.I.; Rodríguez, C.G.; Rodríguez, J.D.; Telmo, J. Internal modifications to reduce pollutant emissions from marine engines. A numerical approach. *Journal of Naval Architecture and Marine Engineering*, vol. 5(4), pp. 493-501, 2013.
 22. Lamas, M.I.; Rodríguez, C.G.; Rodríguez, J.D.; Telmo, J. Computational fluid dynamics of NO_x reduction by ammonia injection in the MAN B&W 7S50MC marine engine. *International Journal of Maritime Engineering*, vol. 156, Part A3, pp. A213-A220, 2014.

CONTACT WITH THE AUTHOR

M.I. Lamas

Escuela Politécnica Superior
C/Mendizábal s/n. 15403Ferrol
A Coruña.

e-mail: isbellamas@udc.es

SPAIN

PERFORMANCE ANALYSIS OF MULTIPURPOSE REFRIGERATION SYSTEM (MRS) ON FISHING VESSEL

Y. Ust,
A. Sinan Karakurt,
U. Gunes,
Yildiz Technical University, Turkey

ABSTRACT

The use of efficient refrigerator/freezers helps considerably to reduce the amount of the emitted greenhouse gas. A two-circuit refrigerator-freezer cycle (RF) reveals a higher energy saving potential than a conventional cycle with a single loop of serial evaporators, owing to pressure drop in each evaporator during refrigeration operation and low compression ratio. Therefore, several industrial applications and fish storage systems have been utilized by using multipurpose refrigeration cycle. That is why a theoretical performance analysis based on the exergetic performance coefficient, coefficient of performance (COP), exergy efficiency and exergy destruction ratio criteria, has been carried out for a multipurpose refrigeration system by using different refrigerants in serial and parallel operation conditions. The exergetic performance coefficient criterion is defined as the ratio of exergy output to the total exergy destruction rate (or loss rate of availability). According to the results of the study, the refrigerant R32 shows the best performance in terms of exergetic performance coefficient, COP, exergy efficiency, and exergy destruction ratio from among the other refrigerants (R1234yf, R1234ze, R404A, R407C, R410A, R143A and R502). The effects of the condenser, freezer-evaporator and refrigerator-evaporator temperatures on the exergetic performance coefficient, COP, exergy efficiency and exergy destruction ratios have been fully analyzed for the refrigerant R32.

Keywords: refrigeration cycles; exergy analysis; exergetic performance coefficient; COP; exergy efficiency;

INTRODUCTION

Fish is a highly perishable food product because of bacterial and enzymatic activities. Refrigeration reduces these activities and delays spoilage at lower and appropriate temperatures, so fish preservation starts on the vessel as soon as the fish is caught. Conventional refrigeration consisting in pre-cooling with seawater is a low cost refrigeration method but it needs much time and causes to produce relatively high bacterial activities. To prevent that disadvantage, pre-cooling of up to 0 °C done by a multipurpose refrigeration system is proposed [1].

A single vapor-compression cycle that runs at the freezer evaporating saturation temperature supplies both refrigeration and freezer compartments for industrial goods. Even though there are some advantages in space and investment cost when utilizing a single refrigeration cycle, the major reason for the decrease in the overall refrigerator performance originates from lower coefficient of performance (COP) of refrigeration at the freezer temperature, compared to that performed in refrigeration evaporator conditions. Accordingly, the use of two separate cycles to fulfill respective cooling loads for

the freezer and the refrigeration compartment results in certain energy savings. Gan, et al. [2] have indicated that the magnitude of the cooling provided to fulfill the refrigeration compartment load triggers large amplification in system performance. The amount of energy savings depends on relative compartment loads. A larger increase in system performance is expected if the majority of cooling is provided to fulfill the refrigeration compartment load.

The advantages in energy saving potential and relative humidity of refrigeration compartments raise the preferability of the two-circuit cycle. Three types of the two-circuit cycle have generally been used as a dual loop cycle with two compressors, a bypass two-circuit cycle, and a two-circuit cycle with parallel evaporators. The investment cost of the dual loop cycle is higher than that of other two circuit cycles (bypass two-circuit cycle and parallel cycle) due to the fact that every cycle has its own compressor, condenser, capillary tube, and evaporator. Yoon et al. [3] have indicated in their experimental study that individual optimization of each loop of a dual loop cycle diminishes energy consumption of the RF compartment. Ding et al [4] have simulated a two-circuit refrigerator-freezer cycle and its application.

For the bypass two-circuit cycle, there is extremely large temperature difference between the refrigerant and the air in the R-evaporator, due to high compression ratio in the refrigerator operation and large irreversible losses. On the other hand, the employment of a single compressor reduces the initial cost for this cycle. An extra path makes the design and the characteristics of the bypass two-circuit cycle more complicated, as compared to those of the two-evaporator in series cycle and the dual-loop system. In the second part of their study Lu et al. [5] have validated their results with experimental data, and found them compatible. Lavanis et al. [6] and Won et al. [7] have illustrated that the dual loop cycle with a number of smaller compressors and reduced load on each compressor may produce lower efficiency, as a big compressor is more efficient than a small one [3]. Yoon et al. [8] have optimized the dual-loop system based on theoretical analysis and experimental study. Their study pointed out that lowering the compression ratio means a higher energy saving potential of the dual-loop cycle, because of higher evaporating temperature in the refrigerator operation. Bare et al. [9] have indicated that a dual-loop cycle with R-12 has an advantage of 19% energy saving over the common refrigeration cycle. Also Bare [10] has indicated that the dual-cycle system with refrigerants R142b R152a has a 23% improvement in overall COP, while the distribution of compartment loads is balanced between the freezer and the fresh food compartments.

The two-circuit cycle with parallel evaporators (called the parallel cycle) for a refrigerator-freezer (RF) eliminates the major drawback of the above mentioned cycles [9]. This significant advantage of the parallel cycle attracts attention of many industrial appliance manufacturers. Yoon et al [11] have studied experimentally the performance of the domestic refrigerator-freezer system and their results indicated higher energy saving potential of the parallel cycle, due to low compression ratio, as the main feature, in combination with high evaporating temperature and low pressure drop in the evaporator during refrigerator operation. Kim et al. [12] and Lavanis et al. [6] have indicated that the parallel cycle has higher efficiency by 2.3~8.5% than the two-evaporator cycle in series (serial cycle). On the other hand, Lavanis et al. [6] and Yoon et al. [3] have shown that the refrigerant recovery operation is needed to make adequate flow in the refrigerator operation, which is a source of additional energy consumption, to provide sufficient amount of refrigerant.

Wang and Wang [13] have compared single-stage compression with two-stage compression in the refrigeration cycle. The obtained results show that the COPs of the serial two-stage compression and parallel two-stage compression systems are higher by 2.1% and 11.6%, respectively, than that of the single stage cycle. Also, the COP of the parallel two-stage system is higher by 9.7% than that of the serial two-stage system.

Wang and Yu [14] have presented an experimental study on a novel ejector enhanced refrigeration cycle used in the domestic refrigerator-freezer. They compared the ejector pressure lift ratio and the energy consumption under different combinations of design parameters. Yang et al. [15] have made a parametric analysis of the two-circuit cycle with evaporating

subcooler to obtain the highest COP in domestic refrigerator-freezer systems. Lu and Ding [16] have analyzed two circuit cycles with respect to a new control strategy which based on temperature and time-sharing running combination. Their analyses showed that the refrigerator-freezer cycle with parallel evaporators is more efficient than single-loop and bypass two circuit cycle refrigerator-freezer units.

An "on-off" controlled household refrigerator and freezer system was modeled by Hermes and Melo [17] to simulate transient behavior. It was also experimentally analyzed by Hermes et al. [18] in order to predict energy consumption in steady state conditions. A comparative analysis of different configurations of domestic refrigerators (of top, bottom and side mounted freezer types) was numerically simulated using computational fluid dynamics approach by Esmail and Mokheimer [19]. Sand et al. [20] have presented a numerical and experimental study which compared the basic refrigeration cycle with two evaporator refrigeration systems using different refrigerants and refrigeration cycles. Wisek [21] and Wisek et al. [22] have carried out an experimental study using phase change material concept for a sequential dual evaporator refrigeration system in refrigeration and freezing applications in order to optimize energy consumption and performance parameters. A semi-empirical modeling approach to the household refrigerator model was employed to assess the effect of various system parameters on refrigerator's performance and predicted performance criteria values, compared with experimental data [23].

The exergetic performance coefficient (EPC) is defined as the ratio of exergy output to the total exergy destruction rate. Ust and Karakurt [24] have analyzed the cascade refrigeration system with different refrigerants using the EPC criterion. Their analyses showed that the best EPC rate of the component were obtained for the cascade condenser low-temperature cycle expansion valve, then for the high-temperature cycle expansion valve, the high temperature cycle evaporator, and finally for the low temperature cycle compressor.

The objective of this study is to investigate the theoretical performance of MRS in terms of COP, EPC, exergy efficiency, and exergy destruction ratio. In order to carry out this aim, MRS was first thermodynamically modeled based on mass, energy and exergy balance equations. Using this model, different refrigerants were investigated to find the best refrigerant yielding the highest COP, EPC and exergy efficiency for MRS. Finally, for the selected refrigerant the effects of important parameters, such as condenser temperature and evaporator temperatures, on the performance of the MRS were determined through a parametric study.

THERMODYNAMIC ANALYSIS OF MULTIPURPOSE REFRIGERATOR SYSTEM

TWO-CIRCUIT CYCLE WITH SERIAL EVAPORATOR SYSTEM

The cycle includes two separate evaporators (R-evaporator and F-evaporator), a condenser, a compressor, three expansion

valves and a three-way valve. The schematic diagram of the irreversible two stage multipurpose refrigerator model and its T-s diagram are given in Fig. 1 a-b. The cycle operates between two heat sources of temperature T_R and T_F and a heat sink of temperature T_0 [25]. The refrigerant flowing into the compressor (state 1) is the saturated vapor and is compressed to the condenser pressure in the vapor-compression refrigeration cycle (state 2). The temperature of the refrigerant rises during this isentropic compression above the ambient temperature. Then the refrigerant flows into the condenser, where it becomes the superheated liquid (state 3). The saturated liquid refrigerant coming from the condenser goes to Expansion valve 1 which is throttled to the R-evaporator pressure (state 4). After that the refrigerant goes to F- evaporator. After heat rejection to the environment, the leaving refrigerant becomes wet vapor (state 6). The initial temperature of the refrigerant in both refrigerators is at the level of those in the refrigerated spaces and decreases below them during these processes. The refrigerant part from the F-evaporator becomes the saturated vapor (state 1) and reenters the compressor, thus finalizing the cycle.

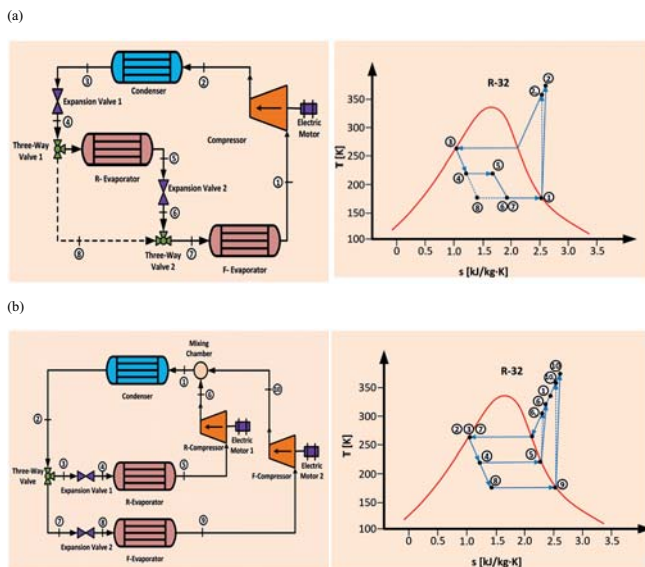


Fig. 1. Schematic diagrams of irreversible MRS and its T-s diagrams.

Two-circuit cycle with parallel evaporators system

This cycle has almost the same equipment as the bypass two-circuit cycle system. Additionally, the parallel cycle has a three-way valve, two separate compressors (R-compressor and F-compressor) and a mixing chamber. The basic difference in operation of the parallel cycle is that the refrigerant leaving R-evaporator does not go to F-evaporator. R-evaporator and F-evaporator are separate cycles. The saturated liquid refrigerant (state 2) goes to the three-way valve, then (states 3 and 7) is throttled to the R-evaporator and F-evaporator pressures by the expansion valve 1 (state 4) and expansion valve 2 (state 8). Heat rejection in R-evaporator and F-evaporator makes the refrigerant become the saturated vapor (state 5 and 9). Then the refrigerant from F-evaporator goes to F-compressor and that from R-evaporator goes to

R-compressor. After the compression process, (states 6 and 10) the both refrigerants mix together (state 1) and the cycle finishes.

The rate of heat flow from the heat source to the evaporator \dot{Q}_{Evap} , the rate of heat transfer from the multipurpose condenser, and the rate of heat flow from the condenser to the heat sink \dot{Q}_{Con} can be written separately as:

$$\dot{Q}_{Evap,R} = \dot{m}_1 (h_5 - h_4) = \dot{m}_f C_{p,f} (T_f - T_{Evap,R}) \quad (1)$$

$$\dot{Q}_{Evap,F} = \dot{m}_2 (h_1 - h_6) = \dot{m}_f C_{p,f} (T_{Evap,R} - T_{Evap,F}) + \dot{m}_f L_f \quad (2)$$

$$\dot{Q}_{Con} = \dot{m} (h_2 - h_3) \quad (3)$$

where \dot{m} is the mass flow rate of the refrigerant ($\dot{m}_1 = \dot{m}_2 = \dot{m}$ for MRS_s and $\dot{m}_1 + \dot{m}_2 = \dot{m}$ for MRS_p) and h denotes the enthalpy. The electrical power input for the compressor is given as:

$$\dot{W}_{Com} = \frac{\dot{m} (h_2 - h_1)}{\eta_m \eta_{em}} \quad (4)$$

The coefficient of performance (COP) is used as a major performance criterion in general performance analyses of refrigeration systems. The coefficient of performance gives the information about the necessary electrical power input to produce certain magnitude of cooling load. The first law of thermodynamics says that the coefficient of performance is specified as the ratio of cooling load to the electrical power input for the multipurpose refrigeration cycle and is given as below:

$$\dot{Q}_L = \dot{Q}_{Evap,R} + \dot{Q}_{Evap,F} \quad (5)$$

$$COP = \frac{\dot{Q}_L}{\dot{W}_{Com}} \quad (6)$$

EXERGY DESTRUCTION RATE IN SYSTEM COMPONENTS

Exergy analysis of the process is an additive to energy analysis. It is used to appreciate work potentials of input and output materials and heat streams, and to determine locations and amounts of irreversibility losses. The exergetic analysis gives significant information about irreversibility distribution among plant's components, specifying which component weighs more on the overall plant inefficiency. In this study, only physical exergy in the system is taken into account, while alterations of kinetic, potential, and chemical exergy are neglected. Physical exergy transformation is provided from thermal and mechanical processes. These equations can be denoted on the basis of their definitions as [26]:

$$\dot{E}_x^{PH} = \dot{m}_i [(h_i - h_0) - T_0 (s_i - s_0)] \quad (7)$$

where \dot{m} is the mass flow rate, s is the specific entropy in conditions specified for the species, and the subscript 0 shows ambient conditions. The general exergy balance can be denoted in the rate form as:

$$\dot{E}_{X, in} = \dot{E}_{X, out} + \dot{E}_{XD} \quad (8)$$

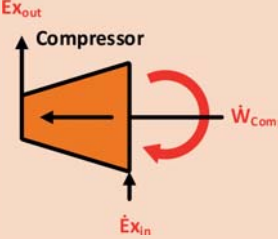
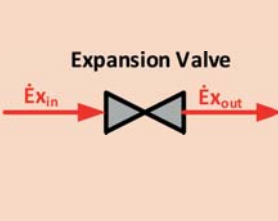
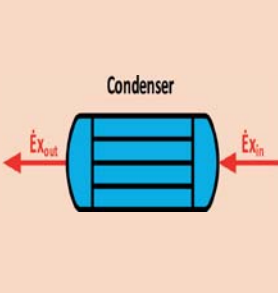
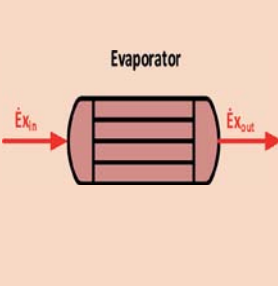
For the control volume of any component of the continual steady state process, the general equation of exergy destruction rate arising from the exergy balance is

$$\dot{E}_{XD,i} = \sum \left[\dot{Q} \left(1 - \frac{T_0}{T} \right) \right]_{in} - \sum \left[\dot{Q} \left(1 - \frac{T_0}{T} \right) \right]_{out} + \sum [(\dot{W})_{in} - (\dot{W})_{out}] + \sum [(\dot{E}_x)_{in} - (\dot{E}_x)_{out}] \quad (9)$$

where $\dot{E}_{XD,i}$, symbolizes the rate of exergy destruction existing in process components. The first and second terms on the right-hand side of the above equation represent exergy rate transfers by heat and work, separately. \dot{Q} symbolizes the heat transfer rate across the boundary of the system at constant temperature T . \dot{E}_x is the exergy rate transfer by mass of each substance flow crossing the system boundary.

By regarding Eq. (8), the rates of exergy destruction acquired for each component of MRS are given in Table-1.

Tab. 1. $\dot{E}_{XD,Evap}$, EPC, ϵ , γ for each component

 <p>Compressor</p>	$\dot{E}_{XD,Com} = \dot{E}_{x,in} - \dot{E}_{x,out} + \dot{W}_{Com}$ $EPC_{Com} = \frac{\dot{E}_{x,out}}{\dot{E}_{x,in} - \dot{E}_{x,out} + \dot{W}_{Com}}$ $\epsilon_{Com} = \frac{\dot{E}_{x,out}}{\dot{E}_{x,in} + \dot{W}_{Com}}$ $\gamma_{Com} = \frac{\dot{E}_{XD,Com}}{\dot{E}_{XD,Tot}}$
 <p>Expansion Valve</p>	$\dot{E}_{XD,Ev} = \dot{E}_{x,in} - \dot{E}_{x,out} $ $EPC_{Ev} = \frac{\dot{E}_{x,out}}{ \dot{E}_{x,in} - \dot{E}_{x,out} }$ $\epsilon_{Ev} = \frac{\dot{E}_{in}}{\dot{E}_{x,out}}$ $\gamma_{Ev} = \frac{\dot{E}_{XD,Ev}}{\dot{E}_{XD,Tot}}$
 <p>Condenser</p>	$\dot{E}_{x,Con} = \left[\dot{Q}_{Con} \left(\frac{T_m - T_0}{T_m} \right) \right]$ $\dot{E}_{XD,Con} = \dot{E}_{x,in} - \dot{E}_{x,out} - \dot{E}_{x,Con}$ $EPC_{Con} = \frac{\dot{E}_{x,out} + \dot{E}_{x,Con}}{\dot{E}_{XD,Con}}$ $\epsilon_{Con} = \frac{\dot{E}_{x,out} + \dot{E}_{x,Con}}{\dot{E}_{x,in}}$ $\gamma_{Con} = \frac{\dot{E}_{XD,Con}}{\dot{E}_{XD,Tot}}$
 <p>Evaporator</p>	$\dot{E}_{x,Evap} = \left[\dot{Q}_{Evap} \left(\frac{T_0}{T_k} \right) \right], (k = F \text{ or } R)$ $\dot{E}_{XD,Evap} = \dot{E}_{x,in} - \dot{E}_{x,out} - \dot{E}_{x,Evap}$ $EPC_{Evap} = \frac{\dot{E}_{x,out} + \dot{E}_{x,Evap}}{\dot{E}_{XD,Con}}$ $\epsilon_{Evap} = \frac{\dot{E}_{x,out} + \dot{E}_{x,Evap}}{\dot{E}_{x,in}}$ $\gamma_{Evap} = \frac{\dot{E}_{XD,Comp}}{\dot{E}_{XD,Tot}}$

Here $\dot{E}_{x, \dot{Q}_{Con}}$, $\dot{E}_{x, \dot{Q}_{Evap,R}}$ and $\dot{E}_{x, \dot{Q}_{Evap,F}}$ are the thermal exergy rates related with \dot{Q}_{Con} , $\dot{Q}_{Evap,R}$ and $\dot{Q}_{Evap,F}$ which can be stated separately. The refrigerated space temperature (T_R), the frozen space temperature (T_F) and the mean temperature (T_m) are defined as:

$$T_R = T_{Evap,R} + \Delta T \quad (10)$$

$$T_F = T_{Evap,F} + \Delta T \quad (11)$$

$$T_m = \left(\frac{h_{in} - h_{out}}{s_{in} - s_{out}} \right)_{Con} \quad (12)$$

EXERGETIC PERFORMANCE COEFFICIENT

Getting the information about exergy destructions in MRS requires adopting another performance criterion. Here, the performance criterion bearing the name of exergetic performance coefficient (EPC), previously proposed by Ust [27], is used. The EPC objective function for MRS is defined as the ratio of exergy output to overall exergy destruction. EPC is defined as:

$$EPC_i = \frac{\dot{E}_{X,out,i}}{\dot{E}_{XD,i}} = \frac{\dot{E}_{X,in,i}}{\dot{E}_{XD,i}} - 1 \quad (13)$$

$$EPC_{Tot} = \frac{\dot{E}_{X,out}}{\dot{E}_{XD,Tot}} = \frac{\dot{E}_{x,Evap,F} + \dot{E}_{x,Evap,R}}{\dot{E}_{XD,Tot}} \quad (14)$$

EXERGY EFFICIENCY

The exergy efficiency is the ratio of the exergy leaving the system to that going into the system. It can also be defined as the amount of fuel exergy provided to the system that is found in the product exergy [28].

$$\epsilon_i = \frac{E_{X,i,out}}{E_{X,i,in}} \quad (15)$$

For MRS, the exergy input is equal to the input of electric power for the compressors,

$$E_{X,in} = \sum \dot{W}_{Com} \quad (16)$$

$$\epsilon_{tot} = \frac{E_{x,out}}{E_{x,in}} \quad (17)$$

EXERGY DESTRUCTION RATIO

The values of exergy destruction rates provide a thermodynamic measure of system inefficiencies. The exergy destruction ratio is defined as the exergy destruction rate of the component to the total exergy destruction rate [28]

$$y_i = \frac{\dot{E}_{XD,i}}{\dot{E}_{XD,Tot}} \quad (18)$$

EPC, ϵ and y for all system components are specified in Table 1.

RESULTS AND DISCUSSION

In order to illustrate the results of the analysis of exergetic performance coefficient (EPC), coefficient of performance (COP), exergy efficiency (ϵ), and exergy destruction ratio (y) for the serial and parallel multipurpose refrigerator (MRS) system, selected numerical results are presented and discussed. The parameters selected for the base case model of MRS system simulation are given in Table 2.

Tab. 2. Basic parameters for MRSP simulation

Parameters	Units	Values
Ambient temperature (T_0)	(K)	298
Ambient pressure (P_0)	(kPa)	101.325
Freezer evaporator temperature ($T_{Evap,F}$)	(K)	233.15
Refrigerator evaporator temperature ($T_{Evap,R}$)	(K)	273.15
Condenser temperature (T_{Con})	(K)	313.15
Fish & seawater temperature	(K)	288.15
Temperature difference between cold spaces and evaporators (ΔT)	(K)	10
Electrical motor efficiency (η_{em})	(%)	95
Isentropic efficiency (η_{is})	(%)	85
Mechanical efficiency (η_m)	(%)	95

The analysis was performed for the refrigerants R1234yf, R1234ze, R32, R404A, R407C, R410A, R143A, and R502. The thermodynamic analysis of the MRS system based on the following assumptions:

- i. The operation of all components is of steady-state nature,
- ii. Chemical, kinetic and potential energy and exergy of the components are omitted,
- iii. Pressure drops in pipelines are neglected,
- iv. Heat transfers from/to the compressor and expansion valve are neglected,
- v. Expansion of refrigerants in expansion valves is isenthalpic.
- vi. Specific heat capacities (C_p) are assumed to be constant for refrigeration (3 kJ/kg.K) and freezing processes (1.65 kJ/kg.K)
- vii. Refrigerated and frozen fish flow rate is 0.1736 kg/s (15 tons/day).

In addition to this, other factors such as environmental effects, and toxicity and flammability characteristics, were also taken into account. Thermo-physical properties of the refrigerants are given in Table 3.

Tab. 3. Refrigerant Properties [29]

Refrigerant	Boiling Temp. (°C)	Critical Temp. (°C)	Critical Press. (kPa)	Safety Group	ODP
R-32	-52	78.11	5782	A2L	0
R-404A	-46.6/-45.8	72.14	3735	A1	0
R-407C	-43.8/-36.7	86.05	4634	A1	0
R-410A	-51.6/-51.5	70.17	4770	A1	0
R-143a	-47.6	72.89	3776	A2L	0
R-502	-45/19	80.73	4019	A1	0.249
R-1234yf	-29.4	-	-	A2L	0
R-1234ze	-19	-	-	A2L	0

Variations of EPC, COP and ϵ objective functions of MRS for different refrigerants with respect to serial and parallel operation conditions are demonstrated in Fig. 2. We can observe in Fig.2 that R32 gives the maximum EPC, COP and ϵ among all other refrigerants. It can also be seen in Fig. 2 that for all refrigerants the objective functions COP and ϵ take always higher values for parallel working conditions than for serial working conditions, while the objective function EPC is higher for serial working conditions than for parallel working conditions. Variations of Atmospheric lifetime (AL), immediately dangerous to life or health (IDLH), and global warming potential (GWP) values for different refrigerants are shown in Fig. 3. Although the R1234 group refrigerants have the lowest GWP, AL and IDLH, the refrigerant R32 alone is most suitable in terms of performance characteristics. Figure 4 shows the EPC and COP objective functions of MRS versus $T_{Evap,F}$, $T_{Evap,R}$ and T_{Con} for the refrigerant R32. From Fig. 4 one can conclude that the total EPC objective function decreases for increasing $T_{Evap,F}$ and T_{Con} , and increases for increasing $T_{Evap,R}$. The COP value is also decreasing for increasing $T_{Evap,R}$ and T_{Con} while increasing for increasing $T_{Evap,F}$. Variations of EPC with respect to COP as functions of the $T_{Evap,F}$, $T_{Evap,R}$ and T_{Con} can be seen in Fig. 5 altogether. The EPC objective function decreases for increasing COP by changing $T_{Evap,F}$ and $T_{Evap,R}$ and it increases by changing T_{Con} . The effects of $T_{Evap,F}$, $T_{Evap,R}$ and T_{Con} on the total exergy efficiency and the exergy efficiency of system components for the parallel MRS and the refrigerant R32 are presented in Fig. 6. The total exergy efficiency increases for increasing $T_{Evap,F}$ and decreases for increasing $T_{Evap,R}$ and T_{Con} . The exergy efficiencies ordered from highest to lowest are as follows: expansion valve-1, compressor-F, compressor-R and evaporator-R. Variations of the exergetic performance coefficient and exergy destruction ratio of system components for the parallel MRS and R32 with respect to $T_{Evap,F}$, $T_{Evap,R}$ and T_{Con} are pictured in Fig.7 and Fig.8. These figures are important to see the effects of system parameters on exergy destruction ratios and exergetic performance coefficients of particular components for the refrigerant R32. The exergy destruction ratios ordered from

highest to lowest are as follows: compressor-F, condenser, expansion valve-2, and compressor-R. It can also be seen in Fig. 8 and Table 5 that the best component from the viewpoint of EPC is expansion valve-1 followed by evaporator-R, expansion valve-2, and evaporator-F. The calculated thermodynamic properties for each node of R32 refrigeration and the base case exergetic performance of the parallel MRS system and its components are given in Table 4 and 5, respectively. In Table 5, it can be seen that the highest exergy destruction rates in the system occur in the freezer-compressor, then in the condenser and the expansion valve-2, as a result of electrical, mechanical and isentropic efficiencies of the compressor. As the highest irreversibility rate, amounting to much more than half of the total exergy destruction rate, is observed in the compressor, much attention should be given to selecting a freezer compressor for the multipurpose refrigeration system.

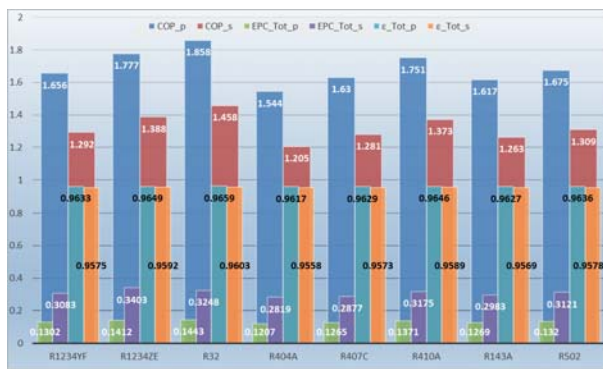


Fig. 2. Variations of COP, EPC & ε objective functions of MRSs and MRSP for different refrigerants

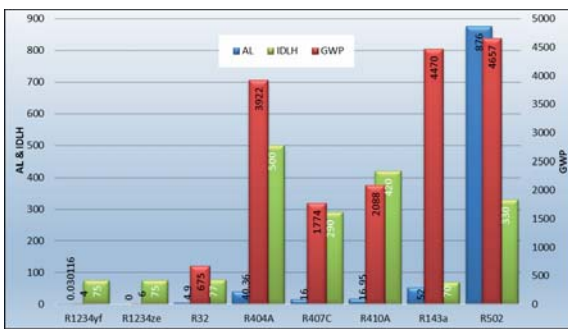


Fig. 3. Variations of AL, IDLH & GWP values of MRSP for different refrigerants

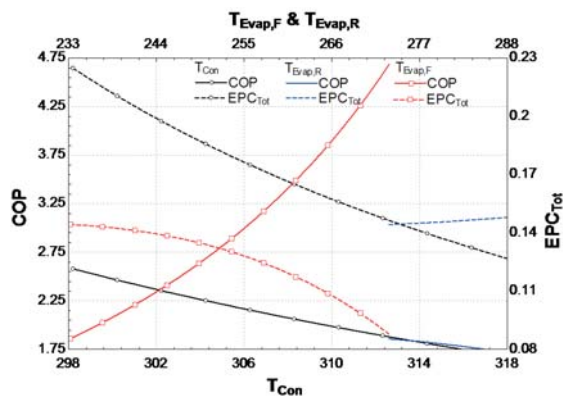


Fig. 4. Variations of COP & EPC objective functions of MRSP for R32 with respect to $T_{Evap,F}$, $T_{Evap,R}$ and T_{Con}

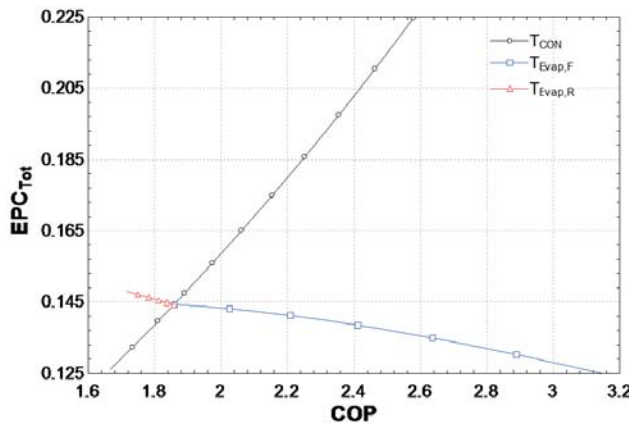


Fig. 5. Variations of EPC with respect to COP as functions of $T_{Evap,F}$, $T_{Evap,R}$ and T_{Con} for R32

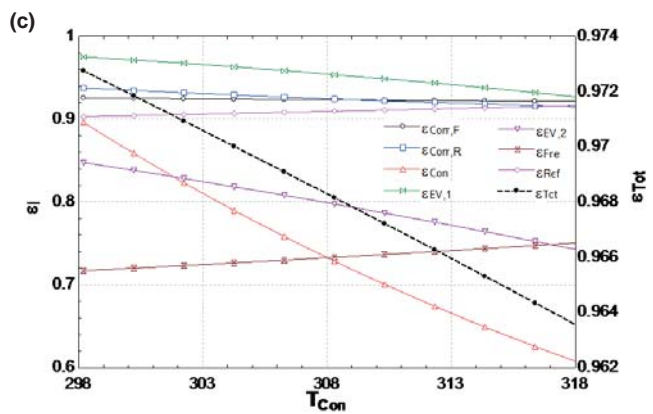
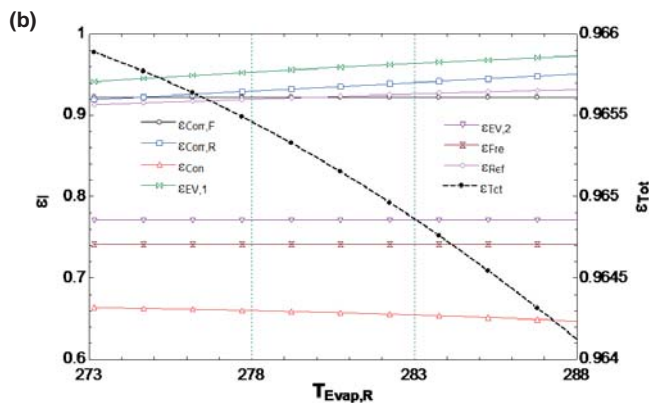
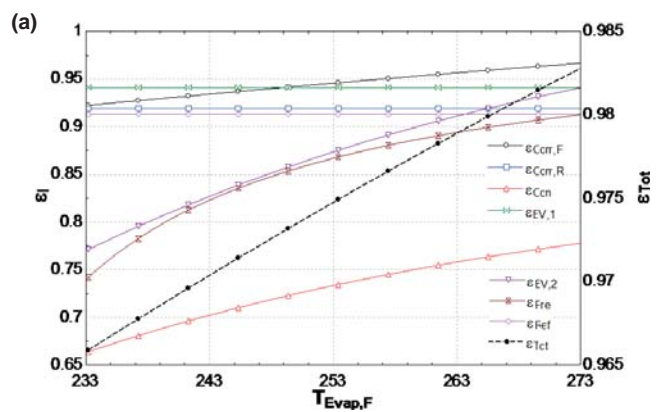


Fig. 6. Variations of exergetic efficiency of MRSP and its components for R32 with respect to a) $T_{Evap,F}$; b) $T_{Evap,R}$; and c) T_{Con}

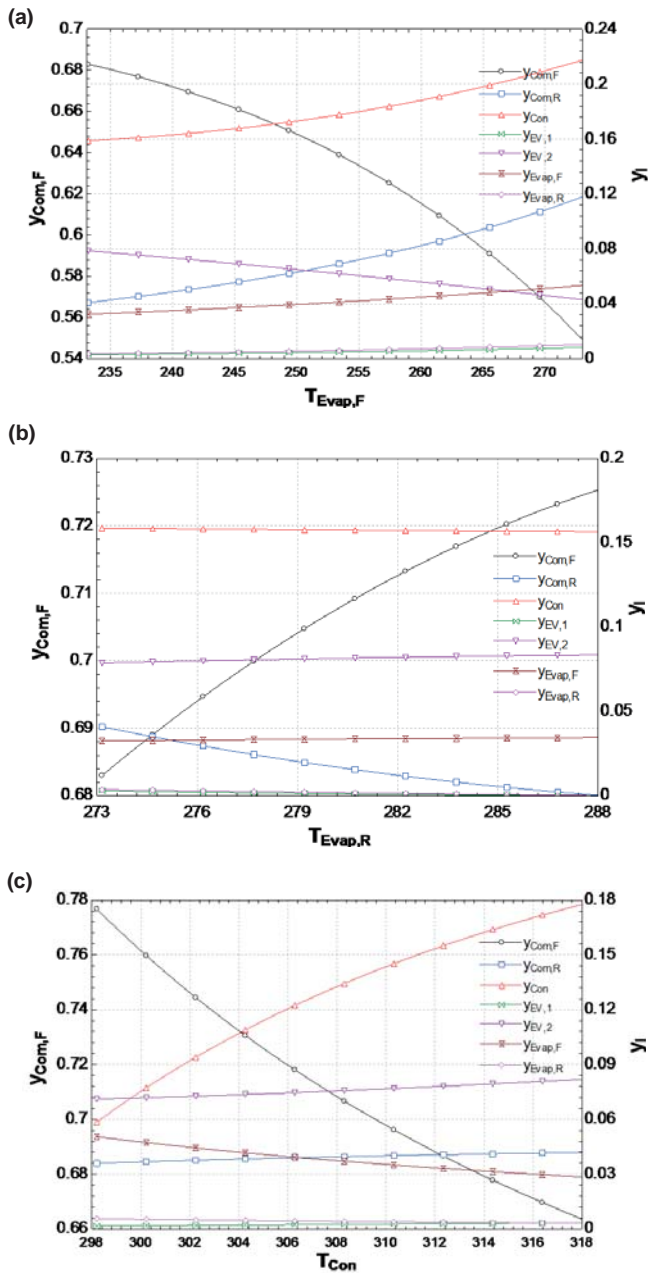


Figure 7. Variations of exergy destruction rate of MRSP components for R32 with respect to a) $T_{Evap,F}$; b) $T_{Evap,R}$; and c) T_{Con}

Table 4- Base case simulation results at each node of MRSP for R32

Node	P (bar)	T (K)	x	h (kJ/kg)	s (kJ/(kg K))	Ex (kW)
1	24.78	393.6		621.1	2.32	41.74
2	24.78	387.9		614.5	2.303	47.25
3	24.78	313.2	0	275.6	1.252	39.31
4	24.78	313.2	0	275.6	1.252	4.936
5	8.132	273.2	0.2398	275.6	1.277	4.646
6	8.132	273.2	1	515.3	2.154	3.788
7	24.78	349.8		568.1	2.177	5.588
8	24.78	313.2		275.6	1.252	34.37
9	1.774	233.2	0.3861	275.6	1.349	26.5
10	1.774	233.2	1	502	2.32	9.307

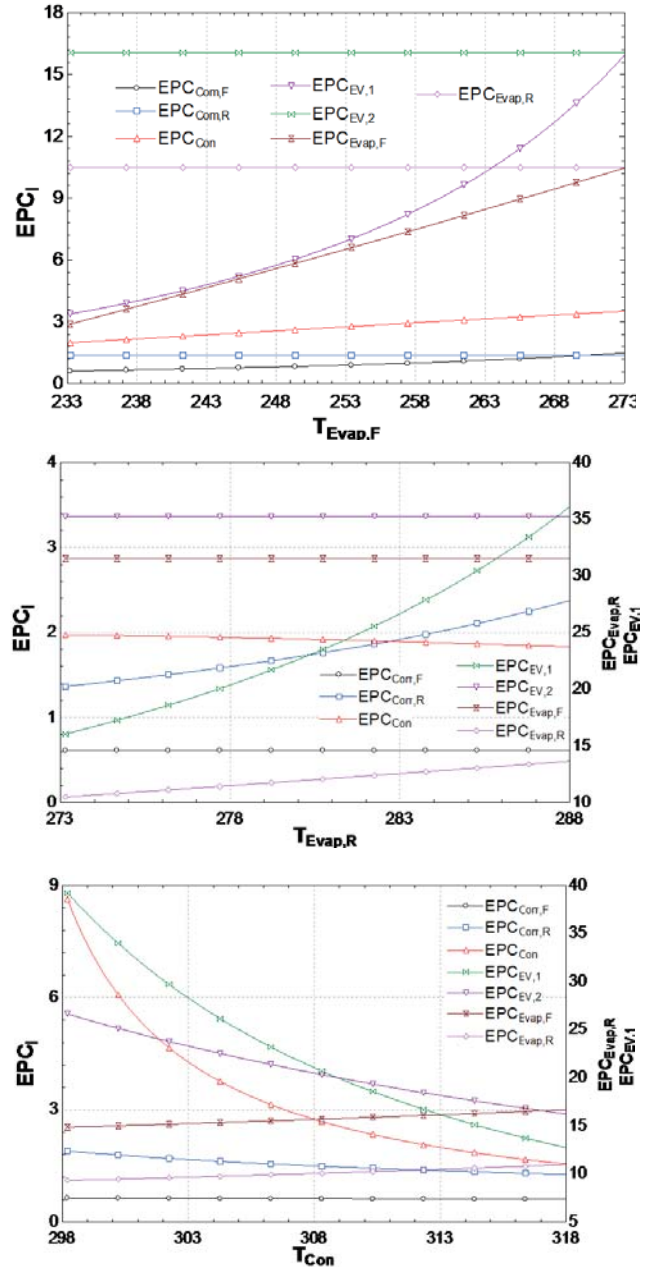


Fig. 8. Variations of EPC of MRSP components for R32 with respect to a) $T_{Evap,F}$; b) $T_{Evap,R}$; and c) T_{Con}

Tab. 5. Base case exergetic performance results of MRSP and its components for R32

System Components	ϵ	EPC	y	ExD (kW)
Compressor_F	0.9226	0.6105	0.683	68.38
Compressor_R	0.9194	1.366	0.04085	4.09
Condenser	0.6639	1.975	0.1586	15.88
Exp. Valve_1	0.9413	16.04	0.00289	0.2896
Exp. Valve_2	0.771	3.367	0.07862	7.871
Evap. Freezer	0.7415	2.869	0.0324	3.244
Evap. Refriger.	0.9129	10.48	0.0036	0.3613
Total	0.9659	0.1443	1	100.1

CONCLUSION

Performance evaluation of the multipurpose refrigeration system by using such parameters as exergetic performance coefficient, exergy efficiency, coefficient of performance, and exergy destruction ratio as performance criteria has been carried out in order to provide guidance for the conceptual design of MRS. From the definition of EPC function, it represents a compromise between exergy output and total exergy destruction rate in view of environmental considerations. This thermodynamic analysis has been carried out using different refrigerants based on given conditions. The main results are outlined as below:

- Although R1234yf and R1234ze have the lowest GWP, AL and IDLH, the refrigerant R32 shows the best performance in terms of EPC, COP and ϵ objective functions.
- Parallel operation of MRS gives better performance in terms of COP and ϵ than serial operation of MRS while EPC performance is opposite for all refrigerants.
- Total exergy efficiency decreases with increasing $T_{\text{Evap,R}}$ and T_{Con} and increases with increasing $T_{\text{Evap,F}}$.
- The best component from the viewpoint of EPC is expansion valve-1 followed by evaporator-R, expansion valve-2, and evaporator-F.
- The exergy efficiencies ordered from highest to lowest are as follows: expansion valve-1, compressor-F, compressor-R and evaporator-R from.
- The exergy destruction ratios ordered from highest to lowest are as follows: compressor-F, condenser, expansion valve-2 and compressor-R.
- The method presented in the paper can also be applied to other refrigerants and working cycles.

REFERENCES

1. Y. A. Çengel, Heat and Mass Transfer: A Practical Approach, 3rd ed. Online: McGraw-Hill Higher Education, 2007.
2. A. I. Gan, S. A. Klein, and D. T. Reindl, "Analysis of Refrigerator / Freezer Appliances Having Dual Refrigeration Cycles," *Ashrae Trans.*, vol. 106, no. 2, pp. 1–7, 2000.
3. W. J. Yoon, H. W. Jung, H. J. Chung, and Y. Kim, "Performance optimization of a two-circuit cycle with parallel evaporators for a domestic refrigerator-freezer," *Int. J. Refrig.*, vol. 34, no. 1, pp. 216–224, Jan. 2011.
4. G. Ding, C. Zhang, and Z. Lu, "Dynamic simulation of natural convection bypass two-circuit cycle refrigerator-freezer and its application: Part I: Component models," *Appl. Therm. Eng.*, vol. 24, no. 10, pp. 1513–1524, Jul. 2004.
5. Z. Lu, G. Ding, and C. Zhang, "Dynamic simulation of natural convection bypass two-circuit cycle refrigerator-freezer and its application: Part II: System simulation and application," *Appl. Therm. Eng.*, vol. 24, no. 10, pp. 1525–1533, Jul. 2004.
6. M. Lavanis, I. Haider, and R. Radermacher, "Experimental investigation of an alternating evaporator duty refrigerator/freezer," presented at the ASHRAE Transactions, Toronto, 1998, vol. 104.
7. S. Won, D. Jung, and R. Radermacher, "An experimental study of the performance of a dual-loop refrigerator freezer system," *Int. J. Refrig.*, vol. 17, no. 6, pp. 411–416, Jul. 1994.
8. W. J. Yoon, K. Seo, H. J. Chung, and Y. Kim, "Performance optimization of dual-loop cycles using R-600a and hydrocarbon mixtures designed for a domestic refrigerator-freezer," *Int. J. Refrig.*, vol. 35, no. 6, pp. 1657–1667, Sep. 2012.
9. J. C. Bare, C. L. Gage, R. R., and J. D.S., "Simulation of nonazeotropic refrigerant mixtures for use in a dual-circuit refrigerator/freezer with countercurrent heat exchanges," 1991.
10. J. C. Bare, "Simulation Results of Single Refrigerants for Use in Dual-Circuit Refrigerator/Freezer," *J. Air Waste Manag. Assoc.*, vol. 42, no. 2, pp. 185–186, 1992.
11. W. J. Yoon, H. W. Jung, H. J. Chung, and Y. Kim, "An Experimental Study on the Performance of a Two Circuit Cycle with Parallel Evaporators for a Domestic Refrigerator-Freezer."
12. K. Kim, B. Kopko, and R. Radermacher, "Application of tandem system to high-efficiency refrigerator/freezer," presented at the ASHRAE Transactions, 1995, vol. 101, p. 2.
13. Y. Joo, Y. Kim, M. Lee, W. Yoon, and Y. Kim, "Performance Characteristics of a Household Refrigerator with Dual Evaporators Using Two-Stage Compression Cycle," *Int. J. Air-Cond. Refrig.*, vol. 17, no. 3, pp. 107–113, 2009.
14. X. Wang and J. Yu, "An experimental investigation on a novel ejector enhanced refrigeration cycle applied in the domestic refrigerator-freezer," *Energy*, vol. 93, Part 1, pp. 202–209, Dec. 2015.
15. M. Yang, C. W. Jung, and Y. T. Kang, "Development of high efficiency cycles for domestic refrigerator-freezer application," *Energy*, vol. 93, Part 2, pp. 2258–2266, Dec. 2015.
16. Z. Lu and G. Ding, "Temperature and time-sharing running combination control strategy of two-circuit cycle refrigerator-freezer with parallel evaporators," *Appl. Therm. Eng.*, vol. 26, no. 11–12, pp. 1208–1217, Aug. 2006.
17. C. J. L. Hermes and C. Melo, "A first-principles simulation model for the start-up and cycling transients of household refrigerators," *Int. J. Refrig.*, vol. 31, no. 8, pp. 1341–1357, Dec. 2008.

18. C. J. L. Hermes, C. Melo, F. T. Knabben, and J. M. Gonçalves, "Prediction of the energy consumption of household refrigerators and freezers via steady-state simulation," *Appl. Energy*, vol. 86, no. 7–8, pp. 1311–1319, Jul. 2009.
19. Y. S. S. Esmail M. A. Mokheimer, "Comparative Analysis of Different Configuration Domestic Refrigerators: A Computational Fluid Dynamics Approach," *J. Energy Resour. Technol.*, vol. 137, no. 6, p. 062002, 2015.
20. J. R. Sand, C. L. Rice, and E. A. Vineyard, "Alternative Refrigerants and Refrigeration Cycles for Domestic Refrigerators," Oak Ridge National Lab., TN (United States), ORNL/M--2270, Dec. 1992.
21. M. VISEK, "Study of innovative techniques aimed at reducing energy consumption in domestic refrigeration system," 05-Mar-2013. Available: <https://www.politesi.polimi.it/handle/10589/74911>.
22. M. Visek, C. M. Joppolo, L. Molinaroli, and A. Olivani, "Advanced sequential dual evaporator domestic refrigerator/freezer: System energy optimization," *Int. J. Refrig.*, vol. 43, pp. 71–79, Jul. 2014.
23. J. M. Gonçalves, C. Melo, and C. J. L. Hermes, "A semi-empirical model for steady-state simulation of household refrigerators," *Appl. Therm. Eng.*, vol. 29, no. 8–9, pp. 1622–1630, Jun. 2009.
24. Y. Üst and A. S. Karakurt, "Analysis of a Cascade Refrigeration System (CRS) by Using Different Refrigerant Couples Based on the Exergetic Performance Coefficient (EPC) Criterion," *Arab. J. Sci. Eng.*, vol. 39, no. 11, pp. 8147–8156, Nov. 2014.
25. Yunus A. Çengel and Michael A. Boles, *Thermodynamics An Engineering Approach*, 5th ed. McGraw-Hill Higher Education, 2006.
26. T. J. Kotas, *The exergy method of thermal plant analysis*. Butterworths, 1985.
27. Y. Ust, A. V. Akkaya, and A. Safa, "Analysis of a vapour compression refrigeration system via exergetic performance coefficient criterion," *J. Energy Inst.*, vol. 84, no. 2, pp. 66–72, May 2011.
28. A. Bejan and M. J. Moran, *Thermal Design and Optimization*. John Wiley & Sons, 1996.
29. "ASHRAE Handbook-Fundamentals," in *Designation and safety classification of refrigerants*, ASHRAE, 2007, pp. 8–12.

CONTACT WITH THE AUTHOR

Yasin Ust
 Department of Naval Architecture
 Yildiz Technical University
 Besiktas 34349
 Istanbul
 Turkey

Tel.: +90-212-383-2980;
 fax: +90-212-383-2989.

E-mail address: yust@yildiz.edu.tr

METHOD OF SUM OF POWER LOSSES AS A WAY FOR DETERMINING THE k_i COEFFICIENTS OF ENERGY LOSSES IN HYDRAULIC MOTOR

A. Maczyszyn, Ph. D.
 Gdańsk University of Technology, Poland

ABSTRACT

This paper shows application of the method of sum of power losses to determining energy losses which occur in hydraulic rotary motor in situation when not all laboratory data are at one's disposal or when no use is made of data contained in catalogue charts. The method makes it possible to determine the coefficients, k_i , of energy losses occurring in the motor. The method of sum of power losses is based on the approach proposed by Z. Paszota, in the papers [3 ÷ 9]. It consists in adding power flow of energy losses occurring in the motor to power flow output and comparing the sum to the power flow input. Application of the method is exemplified by using a A6VM hydraulic motor.

Keywords: hydrostatic drive, power of energy losses, hydraulic rotary motor

INTRODUCTION

Since not long ago a diagram proposed by prof. Paszota[7], which presents a power increase in hydraulic motor opposite to power flow direction in the motor, has been available in the subject –matter literature. The diagram clearly describes dependences of particular power losses occurring in hydraulic motor and relations between them.

According to Fig. 1 the power losses and energy efficiency depends on output parameters of the motor, i.e. its angular velocity ω_M and torque M_M . They are quantities independent on the motor itself and the system within the motor operation field $0 \leq \omega_M < \omega_{Mmax}$, $0 \leq M_M < M_{Mmax}$ [3, 4]. Whereas the motor input parameters, i.e. the motor input flow rate Q_M (motor absorbing capacity) and the pressure decrease ΔP_M in the motor are dependent quantities [7]. The Paszota's approach makes it possible to present the total efficiency η_M of the hydraulic motor, i.e. the ratio of the effective motor shaft power P_{Mu} , demanded from the side of the machine driven by the motor and the power P_{Mc} , consumed by the motor, in function of the motor shaft torque M_M , shaft rotational speed n_M and working liquid viscosity ν :

$$\eta_M = \frac{P_{Mu}}{P_{Mc}} = f(M_M, n_M, \nu)$$

In the publication [2], which initiated the forming of a library of the coefficients k_i of energy losses occurring in various types of pumps and hydraulic motors, it was proposed

the method of sum of power losses, which allows to determine the coefficients k_i on the basis of knowledge of particular power losses occurring in a given machine.

In order to prepare energy balance for a hydraulic motor used in a hydrostatic drive system, power losses should be (acc. Fig.1) added to motor power output because these are power output parameters which decide on power of particular losses [7]. Such approach made it possible to develop the method of sum of powers [2], which allows for determining the coefficients k_i , of energy losses occurring in hydraulic motor.

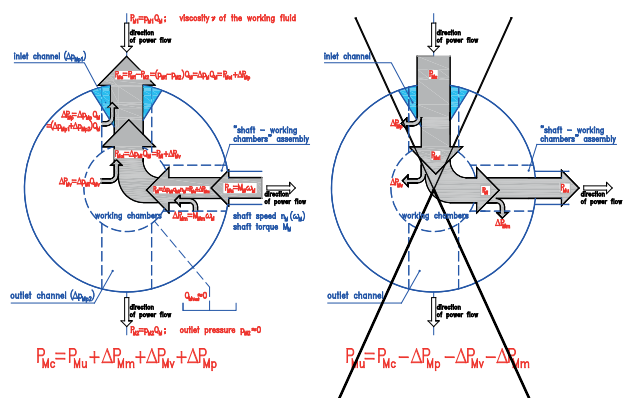


Fig.1 Diagram of power increase in a hydraulic motor opposite to the direction of power flow, replacing the Sankey's diagram of power decrease in the direction of power flow [7]

A6VM HYDRAULIC MOTOR

In the A6VM Bosch Rexroth axial piston motor, shown in Fig. 2, whose basic working parameters are given in Tab. 1, the pistons are placed axially in the rotating cylinder block. Axial piston motors are usually fitted with an uneven number of pistons. During rotation of the cylinder block 6, the pistons 7 located in it, forming - together with the cylinders - the working chamber, connect one by one with the inflow and outflow space of the hydraulic motor through the holes in the face space of the cylinder block 6. At the motion of the plunger to the left the working space increases, connects to the inflow (pressure) space and become filled with liquid. At the motion of the plunger to the right the working space decreases, the liquid is discharged into the outflow (low-pressure) space. During operation of the motor a part of its chambers is filled with the working liquid whereas from the other chambers the liquid is discharged into the outflow conduit. To the motor was applied the spherical distributor 5 in which the spaces are connected to the channels in the motor casing and the inflow and outflow holes. In the motor, mainly in the distributor 5, leakages from the high- pressure leg into the low-pressure leg take place.

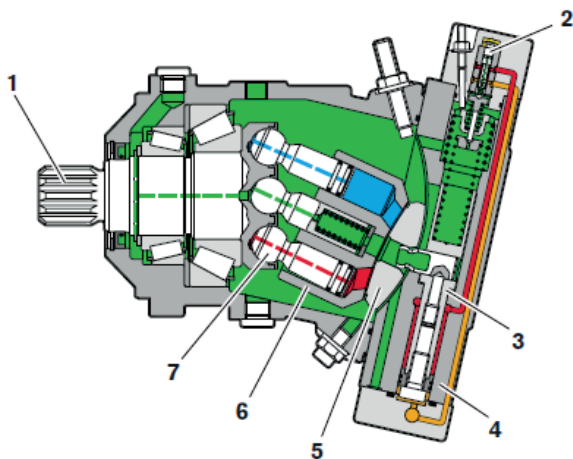


Fig. 2 Overall view [12] and cross-section [9] of the A6VM axial piston motor of a variable absorbing capacity per rotation, fitted with the tilting cylinder block, produced by Bosch Rexroth:

- 1 - driving shaft, 2 - control piston, 3 - piston stroke control unit,
4 - casing in which the control piston is placed, 5 - distributor,
6 - cylinder block, 7 - piston (plunger)

Tab. 1 The basic parameters of A6VM motor [11]

	q_{Mt} [m ³ /rotation]	n_{Mt} [s ⁻¹]	v_n [mm ² s ⁻¹]	p_n [MPa]	M_{Mt} [Nm]	P_{Mc} [kW]
A6VM55	54,8·10 ⁻⁶	70,0	22	40	348,9	153,4

METHOD OF SUM OF POWERS

For determining the coefficients, k_i , of energy losses in the A6VM55 motor the use was made of the tables containing results of the laboratory tests [11] in which the following quantities are given: the pressure decrease Δp_{pM} in the motor; the rotational speed n_M of the motor, defined as the ratio of the current rotational speed n_{Mt} and the theoretical (maximum) rotational speed n_{Mt} ; the absorbing capacity per shaft rotation, q_{Mt} , of the motor as well as the coefficient, b_M , of change of motor absorbing capacity defined as the ratio of the variable absorbing capacity per shaft rotation, q_{Mgv} , and that theoretical per shaft rotation, q_{Mt} , the total efficiency η_{Mt} ; the “mechanical – hydraulic” efficiency η_{mh} ; the volumetric efficiency η_{Mv} . The measurements were carried out at the constant viscosity of the liquid equal to $\nu = 22\text{mm}^2\text{s}^{-1}$.

In compliance with Fig. 1 the working liquid power P_{Mc} consumed by the motor is a sum of the effective power P_{Mu} (demanded on the motor shaft by a device driven by it), the power, ΔP_{Mm} , of mechanical losses in the “shaft – working chambers” constructional unit, the power, ΔP_{Mv} , of volumetric losses in working chambers and the power, ΔP_{Mp} , of pressure losses in the motor channels:

$$P_{Mc} = P_{Mu} + \Delta P_{Mm} + \Delta P_{Mv} + \Delta P_{Mp}$$

The above given equation became the starting point for developing the algorithm presented in the publication [2]. By calculating particular components of power losses within the motor it was possible to determine losses occurring in the machine and, basing on them, to calculate the loss coefficients k_i , precisely.

THE POWER P_{Mc} CONSUMED BY THE MOTOR

The power P_{Mc} absorbed by the hydraulic motor from the liquid, results from the product of the pressure decrease, Δp_M , in the motor and its absorbing capacity Q_M :

$$P_{Mc} = \Delta p_M \cdot Q_M$$

The motor absorbing capacity Q_M demanded by the motor from the side of the liquid driving it, must be greater than the rate equal to the product $q_{Mt} n_M$ (resulting from the theoretical absorbing capacity per shaft rotation, q_{Mt} , and the shaft motor rotational speed n_M , demanded by a device driven by the motor) because of occurrence of volumetric losses in working chambers of the motor. The absorbing capacity Q_M is hence equal to the sum of of the rate $q_{Mt} n_M$ and the volumetric losses rate Q_{Mv} :

$$Q_M = q_{Mt} \cdot n_M + Q_{Mv}$$

In order to know quantity of the absorbing capacity, Q_M , of the motor of the variable absorbing capacity per shaft rotation, q_{Mgv} , can be used the formula representing the quotient of the product of the absorbing capacity per shaft rotation, q_{Mgv} , and the motor shaft rotational speed n_M over the motor volumetric efficiency η_{Mv} :

$$Q_M = \frac{q_{Mgv} n_M}{\eta_{Mv}} = \frac{q_{Mt} b_M n_M}{\eta_{Mv}}$$

Knowing the pressure decrease, Δp_{Mp} , in the motor and its absorbing capacity Q_M one can calculate the power, P_{Mc} , of the working liquid consumed by the motor.

THE EFFECTIVE POWER P_{Mu} OF THE MOTOR

The motor effective power P_{Mu} can be calculated by using the transformed formula for the total efficiency η_M of hydraulic motor, as follows :

$$P_{Mu} = \eta_M P_{Mc}$$

From mathematical point of view the above given relationship is correct though it represents rather Sankey's approach; however it results from the necessity of determining the quantity of the effective power P_{Mu} in which quantity of the motor shaft torque M_M is contained.

THE POWER ΔP_{Mp} OF PRESSURE LOSSES IN THE MOTOR

The power ΔP_{Mp} of pressure losses in hydraulic motor is the sum of the power ΔP_{Mp1} of pressure losses in inflow channel and the power ΔP_{Mp2} of pressure losses in outflow channel of the motor, as follows:

$$\Delta P_{Mp} = \Delta P_{Mp1} + \Delta P_{Mp2}$$

In the general case the power ΔP_{Mp} of pressure losses is equal to the product of the pressure loss Δp_{Mp} and the liquid flow rate Q_M :

$$\Delta P_{Mp} = \Delta p_{Mp} \cdot Q_M$$

According to the above given relation, the formula which describes the power ΔP_{Mp} of pressure losses in hydraulic motor takes the following form:

$$\Delta P_{Mp} = \Delta P_{Mp1} + \Delta P_{Mp2} = \Delta p_{Mp1} Q_M + \Delta p_{Mp2} Q_M$$

In rotary motor the liquid flow rate Q_{M2} in its outflow channel is practically equal to that in its inflow channel (i.e. the motor absorbing capacity Q_M): $Q_{M2} = Q_M$, therefore it is possible to write that the power ΔP_{Mp} of pressure losses in the motor is equal to:

$$\Delta P_{Mp} = (\Delta p_{Mp1} + \Delta p_{Mp2}) Q_M = \Delta p_{Mp} \cdot Q_M$$

In order to determine the pressure losses, Δp_{Mp} , in motor channels (flow drag and losses in distributor) the use was made of the laboratory data given by J. Koralewski in [1], and the quantity of the pressure losses Δp_{Mp} in motor channels was assumed equal to that of the losses occurring in the A7V.58. DR.1.R.P.F.00 pump which is a twin unit for the A6VM motor. It results also from the fact that the publication [11] in which the laboratory data are presented, deals with an entire series of types of the motors whose absorbing capacity per shaft rotation is contained within the interval: $28,1 \cdot 10^{-6} \div 200 \cdot 10^{-6} \text{ m}^3/\text{rotation}$, and their rotational speed changes in the range: $88,33 \div 45,83 \text{ rotation/s}$.

The pressure losses Δp_{pp} in channels of the A7V.58. DR.1.R.P.F.00 pump reached, at the viscosity $\nu = 22 \text{ mm}^2\text{s}^{-1}$ used for testing the hydraulic motor, the following value:

$$\Delta p_{pp} = k_3 p_n \left(\frac{Q_p}{Q_{pt}} \right)^{a_{qp}} \left(\frac{\nu}{\nu_n} \right)^{a_{vp}} = 0,0012 \cdot 32 \cdot 10^6 \cdot \left(\frac{1472,5 \cdot 10^{-6}}{1472,5 \cdot 10^{-6}} \right)^{1,76} \cdot \left(\frac{22}{35} \right)^{0,26}$$

$$\Delta p_{pp|Q_p=Q_{pt};\nu} = 0,034 [\text{MPa}]$$

Therefore the pressure losses Δp_{Mp} in channels of the A6VM55 motor will be in compliance with the following formula:

$$\Delta p_{Mp} = k_8 p_n \left(\frac{Q_M}{Q_{pt}} \right)^{a_{qp}} \left(\frac{\nu}{\nu_n} \right)^{a_{vp}}$$

and, due to the fact that the tests of the A6VM55 motor were carried out at one constant value of the hydraulic oil viscosity $\nu = 22 \text{ mm}^2\text{s}^{-1}$, the expression $\left(\frac{\nu}{\nu_n} \right)^{a_{vp}}$ was assumed equal to 1. The exponent a_{qp} of the influence of the liquid flow rate Q_M in channels on the pressure losses Δp_{Mp} was assumed equal to 1,78; based on the tests [1] which were performed at hydraulic oil viscosity varying in the range from $14,53 \text{ mm}^2\text{s}^{-1}$ to $91,16 \text{ mm}^2\text{s}^{-1}$. With taking into account the change of the motor speed from n_{pt} to n_{Mt} , and the motor absorbing capacity the following was reached:

$$\Delta p_{Mp} = \Delta p_{pp|Q_p=Q_{pt};\nu} \left(\frac{Q_M}{Q_{pt}} \right)^{1,78}$$

$$\Delta p_{Mp} = 0,034 [\text{MPa}] \cdot \left(\frac{54,8 \cdot 10^{-6} [\text{m}^3 / \text{obr}] \cdot 70 [\text{s}^{-1}]}{58 \cdot 10^{-6} [\text{m}^3 / \text{obr}] \cdot 25 [\text{s}^{-1}]} \right)^{1,78} = 0,192 [\text{MPa}]$$

The coefficient, k_8 , of pressure losses in internal channels of the A6VM55 hydraulic motor at the flow rate equal to the theoretical capacity Q_{pt} of the pump, in relation to the nominal pressure p_n of the system, reached the following value:

$$k_8 = \frac{\Delta p_{Mp|Q_M=Q_{pt};\nu}}{p_{Mn}} = \frac{0,192 [\text{MPa}]}{40 [\text{MPa}]} = 0,005$$

Knowing the value of the coefficient k_8 one can determine value of the pressure losses Δp_{Mp} in motor channels by using the formula:

$$\Delta p_{Mp} = k_8 p_n \left(\frac{Q_M}{Q_{Pt}} \right)^{a_{Qp}} \left(\frac{v}{v_n} \right)^{a_{vp}}$$

Values of the pressure losses Δp_{Mp} in A6VM55 motor channels, determined this way, are presented in Fig. 3 in function of the motor absorbing capacity Q_M .

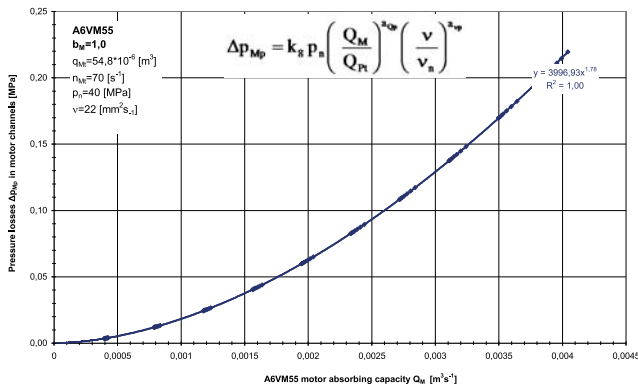


Fig. 3 Pressure losses Δp_{Mp} in A6VM55 motor channels in function of the motor absorbing capacity Q_M

THE POWER ΔP_{MV} OF VOLUMETRIC LOSSES IN THE MOTOR

The power ΔP_{MV} of volumetric losses in the motor are equal to the product of the volumetric losses rate Q_{Mv} (mainly the rate of internal leakages between the working inflow and outflow chambers) and the pressure decrease Δp_{Mi} induced between the pressure p_{Mi} in inflow chambers of the motor and the pressure p_{M2i} in its outflow chambers:

$$\Delta P_{MV} = Q_{Mv} \cdot \Delta p_{Mi} = Q_{Mv} (p_{Mi} - p_{M2i})$$

The pressure decrease Δp_{Mi} induced in motor working chambers together with the pressure losses Δp_{Mp} in motor channels provides the pressure decrease Δp_M in the motor, as follows:

$$\Delta p_M = \Delta p_{Mi} + \Delta p_{Mp}$$

On transformation of the expression, one is able to determine the pressure decrease Δp_{Mi} induced in motor working chambers:

$$\Delta p_{Mi} = \Delta p_M - \Delta p_{Mp}$$

To calculate the volumetric losses rate Q_{Mv} in motor working chambers one can make use of the following relation:

$$Q_{Mv} = Q_M - b_M Q_{Mt} n_{Mt}$$

For determining the coefficient k_9 of the volumetric losses Q_{Mv} in hydraulic motor one can make use of the formula:

$$k_9 = \frac{Q_{Mv} | \Delta p_{Mi} = p_n}{Q_{Pt}}$$

applying appropriate values read from Fig. 4.

$$k_9 = \frac{0,000206 [m^3 s^{-1}]}{0,0038 [m^3 s^{-1}]} = 0,054 [-]$$

Knowing value of the pressure decrease Δp_{Mi} induced in motor working chambers as well as the volumetric losses rate Q_{Mv} in the motor, one can calculate values of the power ΔP_{MV} of volumetric losses which occur in the motor.

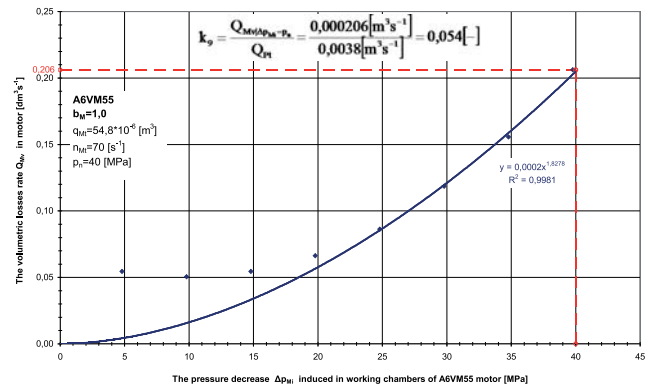
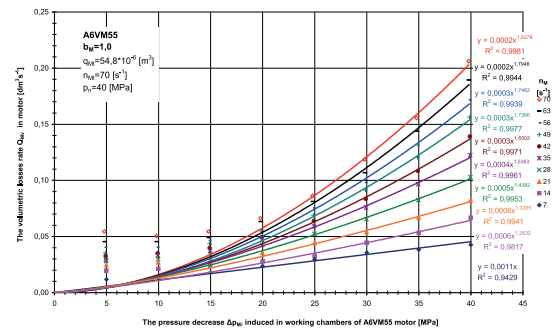


Fig. 4 The volumetric losses rate Q_{Mv} in working chambers of A6VM55 motor in function of the pressure decrease Δp_{Mi} induced in motor working chambers

Drawing the relationship of the volumetric losses rate Q_{Mv} in motor working chambers in function of the pressure decrease Δp_{Mi} in motor working chambers at constant values of the shaft rotational speed n_M (Fig. 5), one obtains the data which allow to determine the exponent a_{pv} as shown in Fig. 6.



THE POWER ΔP_{Mm} OF MECHANICAL LOSSES IN THE "SHAFT-WORKING CHAMBERS" CONSTRUCTIONAL UNIT OF THE MOTOR

In compliance with the equation being the basis for the developed algorithm, the power P_{Mc} of working liquid consumed by motor is equal to the sum of the effective power P_{Mu} and the power of losses which occur in the motor. The power ΔP_{Mm} of mechanical losses in the "shaft-working chambers" constructional unit can be hence calculated, on transformation, as follows:

$$\Delta P_{Mm} = P_{Mc} - P_{Mu} - \Delta P_{Mv} - \Delta P_{Mp}$$

The mechanical losses power ΔP_{Mm} in hydraulic motor is that associated with mechanical friction forces and inertia forces of moving elements in the constructional unit which transmits mechanical power from moving elements in working chambers to rotational motor shaft.

The mechanical losses power ΔP_{Mm} is the product of the mechanical losses torque M_{Mm} and motor shaft angular velocity ω_M :

$$\Delta P_{Mm} = M_{Mm} \cdot \omega_M$$

Therefore the mechanical losses torque M_{Mm} determined from the above given relation, is equal to:

$$M_{Mm} = \frac{\Delta P_{Mm}}{\omega_M}$$

The torque M_{Mi} induced in motor working chambers is equal to the sum of the torque M_M loading the motor shaft and the mechanical losses torque M_{Mm} :

$$M_{Mi} = M_M + M_{Mm}$$

The torque M_{Mi} induced in motor working chambers can be also calculated from the relation:

$$\frac{q_{Mt} \Delta p_{Mi}}{2\pi} = M_{Mi}$$

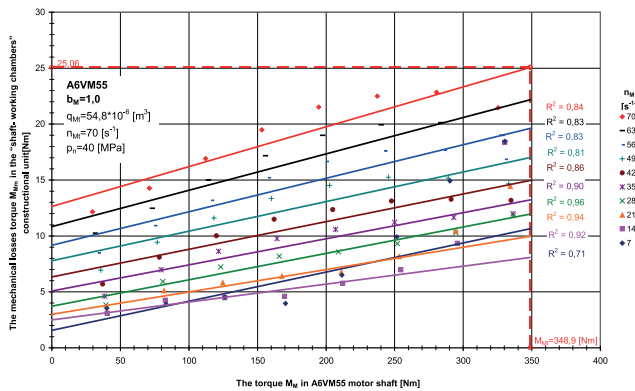


Fig. 7 The mechanical losses torque M_{Mm} in the "shaft-working chambers" constructional unit in function of the torque M_M in A6VM55 motor shaft

Value of the mechanical losses torque M_{Mm} in the motor of the geometrical (changeable) absorbing capacity q_{Mgv} per

shaft rotation was calculated in compliance with the relations given by Paszota Z. in [5]:

$$M_{Mm|M_M, n_M, b_M, v} = \left(k_{7.1.1} + k_{7.1.2} \frac{n_M}{n_{Mt}} b_M \right) M_{Mt} \left(\frac{v}{v_n} \right)^{a_{vm}} + k_{7.2} M_M = \left(k_{7.1.1} + k_{7.1.2} \frac{n_M}{n_{Mt}} b_M \right) \frac{q_{Mt} p_n}{2\pi} \left(\frac{v}{v_n} \right)^{a_{vm}} + k_{7.2} M_M$$

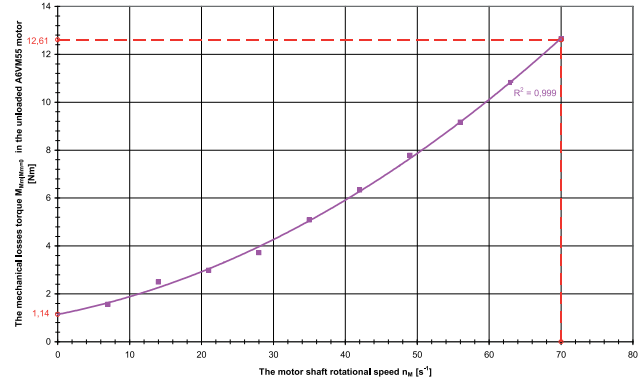


Fig. 8. The mechanical losses torque $M_{Mm|M_M=0}$ in the unloaded motor ($M_M=0$) in function of the rotational speed n_M of A6VM55 motor shaft

With taking into account constant hydraulic oil viscosity, the segment $\left(\frac{v}{v_n}\right)^{a_{vm}}$ was assumed equal to 1; therefore the formula which describes the mechanical losses torque M_{Mm} , takes the following form:

$$M_{Mm|M_M, n_M, b_M, v} = \left(k_{7.1.1} + k_{7.1.2} \frac{n_M}{n_{Mt}} b_M \right) M_{Mt} + k_{7.2} M_M$$

The coefficient $k_{7.1.1}$ was calculated by using the relation:

$$k_{7.1.1} = \frac{M_{Mm|M_M=0, n_M=0, b_M=1, v_n}}{M_{Mt}} = \frac{M_{Mm|M_M=0, n_M=0, b_M=1, v_n}}{\frac{q_{Mt} p_n}{2\pi}}$$

for which an appropriate value of the mechanical losses torque M_{Mm} was read from Fig. 8.

$$k_{7.1.1} = \frac{1,14[\text{Nm}]}{348,9[\text{Nm}]} = 0,003$$

The coefficient $k_{7.1.2}$ was calculated by using the relation:

$$k_{7.1.2} = \frac{M_{Mm|M_M=0, n_M=n_{Mt}, b_M=1, v_n} - M_{Mm|M_M=0, n_M=0, b_M=1, v_n}}{M_{Mt}}$$

for which an appropriate value of the mechanical losses torque M_{Mm} was read from Fig. 8.

$$k_{7.1.2} = \frac{12,61[\text{Nm}] - 1,14[\text{Nm}]}{348,9[\text{Nm}]} = 0,033$$

The coefficient $k_{7.2}$ was calculated by using the relation:

$$k_{7.2} = \frac{M_{Mm|M_M=M_{Mt}, n_M=n_{Mt}, b_M=1, v_n} - M_{Mm|M_M=0, n_M=n_{Mt}, b_M=1, v_n}}{M_{Mt}}$$

for which an appropriate value of the mechanical losses torque $M_{Mm|M_M=M_{Mt}, n_M=n_{Mt}, b_M=1, v_n}$ in the motor loaded by the theoretical torque M_{Mt} was read from Fig. 7, and an appropriate

value of the mechanical losses torque $M_{Mm|M_M=0, n_M=n_{Mn}, b_M=1, v_n}$ in the unloaded motor – from Fig. 8.

$$k_{7.2} = \frac{25,06[\text{Nm}] - 12,61[\text{Nm}]}{348,9[\text{Nm}]} = 0,036$$

The presented method of sum of powers made it possible to calculate the coefficients k_i of energy losses occurring in A6VM motor, whose values are given in Tab. 2.

THE ENERGY LOSSES COEFFICIENTS

Tab. 2 which contains values of the coefficients k_i of energy losses in A6VM55 motor, clearly provides information on quantity and proportion of particular losses occurring in the motor in question. Similar breakdowns of the losses coefficients k_i in the case of other displacement machines would largely contribute in improving work quality and its advance rate of designers dealing with hydrostatic drive systems.

Tab. 2. Breakdown of the coefficients k_i of energy losses which occur in A6VM55 motor

A6VM55		v=22 [mm²s⁻¹]
		q_{Mt} = 54,8·10⁻⁶ [m³]
		b_M≠const.
		n_{Mn} = 70 [s⁻¹]
		p_n = 40 [MPa]
		P_{Mc} = 153,4 [kW]
M_{Mm}	k_{7.1.1}=	0,003
	k_{7.1.2}=	0,033
	a_{vm}=	-
	k_{7.2}=	0,036
Q_{Mv}	k₉=	0,054
	a_{pV}=	1,83
	a_{vV}=	-
	a_{nV}=	-
Δp_{Mp}	k₈=	0,005
	a_{Qp}=	1,78
	a_{vP}=	-

The exponents a_{vm} , a_{vV} and a_{vP} which tell about the impact of the working liquid viscosity v on particular types of losses (m – mechanical; v – volumetric, p – pressure) were omitted because the tests were performed only for one value of working liquid viscosity equal to 22 mm²s⁻¹.

The coefficient $k_{7.1}$ of the mechanical losses torque M_{Mm} which is the sum of the coefficients $k_{7.1.1}$ and $k_{7.1.2}$, provides information on losses due to friction between structural elements (e.g. bearings) as well as on losses between liquid which fills the casing and the cylinder block, friction between the rotating cylinder block and the motionless distributor.

The coefficient $k_{7.2}$ of the mechanical losses torque M_{Mm} tells about quantity of the mechanical losses torque increase ΔM_{Mm} in the motor as a result of increase in load, i.e. the motor shaft torque M_M .

The coefficient k_8 of the pressure losses Δp_{Mp} tells about quantity of losses which occur in the internal channels and distributor of the machine. The losses result mainly from local pressure losses due to changes in direction and velocity of liquid flow.

Value of the exponent a_{Qp} tells about the impact of the liquid flow rate Q_M in channels on the pressure losses Δp_{Mp} .

Value of the exponent a_{vP} tells about the impact of the induced pressure decrease Δp_{Mi} in working chambers on the volumetric losses rate Q_{Mv} . Its value informs both about a character of working liquid flow and the impact of gap changes in the motor.

SUMMARY

In this paper has been presented the method of sum of powers, which can be used for determining the coefficients, k_i , of energy losses occurring in hydraulic motors in the situation when not all laboratory data are given at one's disposal or when no use is made of the data contained in catalogue charts. The energy losses coefficients k_i achieved this way make it possible to assess, from energy point of view, displacement machines by using the approach to losses, proposed by Paszota Z. in [3÷8].

The energy losses coefficients k_i were thought so as to obtain a relative value of particular losses in an element of hydrostatic system (in a pump, hydraulic motor, as well as conduits and a motor speed throttle control unit). They make it possible to assess proportion and quantity of losses and value of element power efficiency (volumetric, pressure and mechanical one) resulting from losses which occur at the nominal working pressure p_n of the system where a considered element is applied. Consequently, knowing the coefficients k_i of particular losses one is able to determine losses and power efficiency (total, volumetric, pressure and mechanical one) of elements operating in a driving system as well as total efficiency of a system with a given motor speed control structure in function of the velocity coefficient $\bar{\omega}_M$ and the hydraulic motor loading coefficient \bar{M}_M as well as the hydraulic oil viscosity v [9].

The library of the coefficients k_i makes it possible, by using a numerical method, to assess power efficiency of a hydrostatic

drive of a given motor speed control structure, in every point of the hydrostatic drive working field determined by motor shaft speed and load coefficients.

BIBLIOGRAPHY

1. Koralewski J.: Impact of viscosity on energy losses in variable- delivery piston pump (in Polish). Scientific report on the research project No. N N504 4684 33,
2. Maczyszyn A.: Analysis , from energy point of view, of construction of displacement rotary machines applied to hydrostatic transmission (in Polish). Doctorate thesis. Gdańsk University of Technology, Faculty of Ocean Engineering and Shipbuilding, Gdańsk 2014
3. Paszota Z.: Parameters of the power efficiency investigations of hydraulic pumps and motors. Operating field of hydrostatic drive system (in Polish). Napędy i sterowanie (Technical scientific monthly) No. 11(127) , XI, November 2009, pp. 124÷ 129
4. Paszota Z.: The operating field of hydrostatic drive system parameters of the energy efficiency investigations of pumps and hydraulic motor. Polish Maritime Research 4 (62) 2009, Vol. 16; pp. 16÷21
5. Paszota Z.: Energy losses in hydraulic rotary motor – definitions and relationships for assessing efficiency of motor and hydrostatic drive (in Polish). A chapter of the monograph on „Research, design , manufacture and operation of hydraulic systems”(in Polish), Editors : Klich A., Kozieł A. and Palczak E., „Cylinder 2010”, Gliwice 2010, pp. 31÷54
6. Paszota Z.: Theoretical and mathematical models of mechanical losses in hydraulic rotary motor applied to hydrostatic drive (in Polish). A chapter of the monograph on „Research, design , manufacture and operation of hydraulic systems” (in Polish), Editors : Klich A., Kozieł A. and Palczak E., „Cylinder 2010”, Gliwice 2010, pp. 123÷137
7. Paszota Z.: Hydrostatic drives as safe and energy saving machines. The drive investigation method compatible with the diagram of power increase opposite to the direction of power flow. Polish Maritime Research 1 (68) 2011, Vol. 18, pp. 3÷9
8. Paszota Z.: Effect of the working liquid compressibility on the picture of volumetric and mechanical losses in a high pressure displacement pump used in a hydrostatic drive. Part I – Energy losses in a drive system, volumetric losses in a pump. Polish Maritime Research 2 (73) 2012, Vol. 19, pp. 3÷10
9. Paszota Z.: The coefficients k_i of energy losses in hydraulic drive elements . A chapter of the monograph on „Research, design , manufacture and operation of hydraulic systems” (in Polish), Editors : Klich A., Kozieł A. and Palczak E., „Cylinder 2010”, Gliwice 2013, pp. 91÷113.
10. Bosch Rexroth : Service manual for A6VM motor , RE 91604-01-B/01.2012
11. Bosch Rexroth : Technical information , API 309-09/92
12. Bosch Rexroth Poland : Technical information: <http://www.boschrexroth.com/mobile-hydraulics-catalog/Vornavigation/Vornavi.cfm?Language=EN&VHist=g54069,g61367&PageID=m3726> , issued 20-12-2013
13. Czyński M.: Laboratory investigations on power efficiency model of hydrostatic gear (in Polish). Doctorate thesis. Technical University of Szczecin, Faculty of Maritime Technology, Szczecin 2005.

CONTACT WITH THE AUTHOR

Agnieszka Maczyszyn
Faculty of Ocean Engineering and Shipbuilding
Gdańsk University of Technology
11/12 Narutowicz St.
80 – 233 Gdańsk
POLAND

Phone: +48-58-347-21-32
e-mail: agnieszka.maczyszyn@pg.gda.pl

THE APPLICATION OF KALMAN FILTERING TO PREDICT VERTICAL RAIL AXIS DISPLACEMENTS OF THE OVERHEAD CRANE BEING A COMPONENT OF SEAPORT TRANSPORT STRUCTURE

Daria FILIPIAK – KOWSZYK¹,

Waldemar KAMIŃSKI^{1,2},

1) Gdansk University of Technology, Poland

2) University of Warmia and Mazury in Olsztyn, Poland

ABSTRACT

As the devices designed to transport materials, the overhead cranes should meet certain geometric requirements for their operation to be safe. The presently available geodetic equipment, in particular total stations, provides opportunities for precise 3D measurements of coordinates of the controlled points. These coordinates make a basis for correcting the height of crane runway axes. The paper presents a method to calculate position corrections for the crane rail axes in both vertical and horizontal direction, and indicates that these results can find much wider application. Among other goals, the observations of this type, along with the Kalman filtration method, can be used to predict vertical displacements of the crane rail axes. The object of practical considerations in the paper is a crane working in the area with unfavourable geotechnical conditions and the settling limits attributed to this crane and location area in the technical design. The sample practical application has confirmed the validity of the use of the proposed solution for evaluating the operational safety of the crane. Although the tests were performed for the gantry crane, the proposed solution is believed to be applicable for other types of overhead cranes.

Keywords: operational safety of the crane, rectification corrections, parametric method with conditions imposed on parameters, prediction, Kalman filtering

INTRODUCTION

Kalman filtering [10] is frequently used in numerical calculations performed in various fields of technology, including land, inland and sea navigation, and geodesy. The use of Kalman filtering for monitoring deformations of engineering objects, such as water dams for instance, is discussed in [9]. The application of the Kalman filter in marine navigation allows the operator, among other aspects, to make decisions which help the watercraft unit to reach safely the target [2, 4, 5, 16, 18, etc.]. The paper which is also worth noticing here is Ref. [15], in which the author describes the ship position estimation procedure making use of the extended Kalman filter with robust adjustment. Besides, Kalman filtering can be applied to track objects, which is discussed in Ref. [17], among other sources. Along with marine applications, Kalman filtering can be used in numerical analyses of the operation of devices composing port infrastructure. A device of this type which is used in maritime industry to transport materials is the overhead crane. The cranes are very frequently installed on quays, in ports, shipyards, etc. They transport materials in both vertical

and horizontal directions. They operate simultaneously with other devices used in maritime industry (for instance: hoists, fork-lift trucks, road transport, etc.), and also with continually moving human teams at work. Those and other aspects are reasons why constant monitoring of runways and rectification of crane rail axes are of utmost importance for ensuring the safety of crane's operation and transport. One of tasks of engineering geodesy is measurement of crane rail axes. Numerous publications have been devoted to the operation of overhead cranes. Some of them, [1, 7, 8, 12, 14] for instance, discuss issues related with the methodology of measurement and control of crane rail axes, while other authors focus their attention on geometric conditions which should be met for the overhead crane to operate faultlessly, [13] for instance. Standard measurements used for this purpose have the form of observations done by integrated total stations. The presently available total stations enable to perform measurements at very high accuracy, which leads to high accuracy of the final estimation of, for instance, point coordinates. Technical reference manuals and standards provide permissible deviations for crane runways, which are used as the limits for correct operation of the overhead

crane. The cranes can be installed in different parts of the quay, even those with very unfavourable geotechnical conditions. Locations of this type can cause displacements of the ground on which the crane rails are laid. This problem refers to field cranes operating on the ground. It can also lead to the displacement of track bed pillars and crane beams. In contrast, it does not refer to suspended travelling cranes or gantry cranes working in closed rooms or at certain heights. The presented situations can disturb the initial, correct geometry of the crane rail axes and, consequently, lead to construction disaster. Horizontal and vertical displacements of the crane pose a threat for people and port infrastructure equipment situated in its vicinity. The measurements intended to estimate these displacements make use of, as a reference, a number of controlled points situated on the ground or on track bed pillars.

In the paper, the authors propose a method which makes use of the observations basically oriented on controlling the crane runway axes to predict and estimate the value of vertical displacements of the crane. The controlled points used for this purpose should be situated on the rail segment fixed to the crane beam lying on the track bed pillar. The estimation method used to solve this task is the Kalman filtering method.

The practical sample cases presented in the paper were analysed using simulated results of measurements. They enabled to verify the assumptions adopted in the theoretical part of the work.

Although the theoretical considerations, the simulated results, and the real case analyses making use of these results refer to only one type of crane, which is the gantry crane, the proposed method can also be used for other types of overhead cranes.

CALCULATING RECTIFICATION CORRECTIONS IN 3D SYSTEM

Calculating rectification corrections plays an important role in correct operation of the overhead crane and, consequently, in the safety of its operation in the vicinity of port infrastructure objects. The calculated correction values enable to rectify the crane rail axes in such a way that the rails meet certain geometric requirements, and that the operation of the crane is not only correct but also most effective. The crane rail axis measurement is possible due to the use of total stations, among other aspects. The observations performed using the polar method and the principles of trigonometric rectification enable to obtain 3D coordinates in the local reference system fixed to the object. An essential stage of the measurement is position estimation of the controlled points situated on the crane rail axes. Tools which are helpful in this task include: the rule, millimetre graduation, scissors type centring tool, and clamp with central point [7]. Figure 1 shows a sample device of this type.

The above quoted literature describes standard principles of measurement and processing of the results of observations performed in order to calculate rectification corrections for crane rail axes. In this paper the authors use the original

method described in [6, 11] to solve the problem in the local 3D reference system. The estimation method used to calculate the rectification corrections for crane rail axes is the parametric method with conditions imposed on parameters (for instance [3, 19, 20]). The quoted references analyse in detail the issue of calculating corrections for crane rail axes in 3D, and include simulated real cases referring to different types of overhead cranes. Since calculating corrections is not the main subject of this paper, only basic assumptions of this method are presented here.



Fig. 1. Clamp with central point and mini prism
Source: photo from own collection

Let us adopt the following system of observation equations for particular crane rails:

$$\begin{aligned} \text{left rail } y &= ax + b \\ \text{right rail } y &= az + b + c \end{aligned} \quad (1)$$

and the corresponding system of correction equations in the form:

$$\begin{aligned} \text{left rail } v_{y_jL} &= ax_j + b - y_j \\ \text{right rail } v_{y_jP} &= ax_j + b + c - y_j \end{aligned} \quad (2)$$

The observation equation for the height of both rails can have the form of the relation

$$z = z^w \quad (3)$$

with the correction equation

$$v_{z_j} = z^w - z_j \quad (4)$$

In relations (1), (2), (3), (4) the following nomenclature is used:

- $v_{y_jL}, v_{y_jP}, v_{z_j}$ - corrections for y and z coordinates, respectively
- a, b, c, z^w - estimated parameters
- x_j, y_j, z_j - coordinates of controlled points
- $j=1, 2, \dots, n$, where n - number of controlled points.

According to the assumptions of the parametric method with conditions imposed on parameters, the problem of calculating rectification corrections for crane rail axes can be given in the form of the following equation system:

$$\left. \begin{aligned} AX + L &= v \\ BX + \Omega &= 0 \end{aligned} \right\} \quad (5)$$

where:

A, B – matrices of known coefficients

X – vector of unknowns (model parameters)

L – vector of measurement results or free terms

v – vector of rectification corrections of crane rail axes

Ω – vector of free terms resulting from geometric conditions of the overhead crane.

The model parameters X and the rectification corrections v can be determined using a simplified approach to the problem (5), discussed for instance in Ref. [19]. We assume that the condition equation (BX+Ω=0) is an additional correction equation with very large weight values, after which we can solve the problem in a way typical for parametric methods. We can write

$$\tilde{A}X + \tilde{L} = \tilde{v} \quad (6)$$

where:

$$\tilde{A} = \begin{bmatrix} A \\ B \end{bmatrix}, \tilde{L} = \begin{bmatrix} L \\ \Omega \end{bmatrix}, \tilde{v} = \begin{bmatrix} v \\ v_\Omega \end{bmatrix}$$

In the calculations we make use of the weight matrix $\tilde{P} = \begin{bmatrix} P & 0 \\ 0 & P_\infty \end{bmatrix}$ in which P is the diagonal matrix of weights related to free terms L, while P_∞ represents the diagonal matrix of weights for the imposed geometric conditions. The latter matrix is defined in such a way that the vector of corrections v_Ω obtained as the final solution is equal to zero ($v_\Omega = 0$).

The model parameters X are determined from the following equation form:

$$X = -(\tilde{A}^T \tilde{P} \tilde{A})^{-1} \tilde{A}^T \tilde{P} \tilde{L} \quad (7)$$

while the control corrections v for the crane rail axes are determined from the relation

$$\tilde{v} = \begin{bmatrix} v \\ v_\Omega \end{bmatrix} = -\tilde{A}(\tilde{A}^T \tilde{P} \tilde{A})^{-1} \tilde{A}^T \tilde{P} \tilde{L} + \tilde{L} \quad (8)$$

Due to limited volume of the paper, the authors do not discuss the subject matter of accuracy represented by the covariance matrices. Relevant derivations can be found in [3, 6, 11, 19].

PREDICTION, KALMAN METHOD FILTRATION

When solving the task with the aid of Kalman filtration, we should take into account not only parameters describing the model position, but also those characteristic for the kinematic model of the examined object. This way we can create the state vector with components representing both object position and kinematic parameters, obtained from other independent measurements. The dynamic model enables to predict the behaviour of the object after a specified time interval. As mentioned above, the basic goal of the paper is to determine vertical displacements of the overhead crane based on the results of measurements performed to correct the rail axes. Consequently, only those basic principles of Kalman filtration are presented in the paper which are essential for correct understanding of the analysed problem. In a broader range

the problem of Kalman filtration and prediction is described in [20], among other references.

The essential stage related to prediction and filtration is building a dynamic model of the object. Here, the following form of the dynamic model is adopted (after [20])

$$\begin{cases} z_i^w = z_{k=0}^w - V_{k=0} \Delta t_i - \frac{1}{2} \bar{a}_{k=0} \Delta t_i^2 + e_1 \\ V_i = V_{k=0} + \Delta t_i \bar{a}_{k=0} + e_2 \\ \bar{a}_i = \bar{a}_{k=0} + e_3 \end{cases} \quad (9)$$

where:

z_i^w, V_i, \bar{a}_i – model parameters (respectively: height, velocity, acceleration) at the prediction time t_i

$z_{k=0}^w, V_{k=0}, \bar{a}_{k=0}$ – model parameters at the starting time of measurements $t_{k=0}$ (starting time, initial measurement)

$\Delta t_i = t_i - t_{k=0}$ – time interval

e_1, e_2, e_3 – random disturbances

The relation (9), which defines prediction of the state vector \bar{X}_i at time t_i , can be written in the following matrix form

$$\begin{bmatrix} z_i^w \\ V_i \\ \bar{a}_i \end{bmatrix} = \begin{bmatrix} 1 & -\Delta t_i & -\frac{1}{2} \Delta t_i^2 \\ 0 & 1 & \Delta t_i \\ 0 & 0 & 1 \end{bmatrix} \begin{bmatrix} z_{k=0}^w \\ V_{k=0} \\ \bar{a}_{k=0} \end{bmatrix} + \begin{bmatrix} e_1 \\ e_2 \\ e_3 \end{bmatrix} \quad (10)$$

$$\bar{X}_i = \Phi_{k|i} \bar{X}_{k=0} + e_i \quad (11)$$

where:

$\bar{X}_{k=0}$ – state vector at time $t_{k=0}$

$\Phi_{k|i}$ – transition matrix between states \bar{X}_i and $\bar{X}_{k=0}$

e_i – vector of random disturbances

The prediction can be determined for an arbitrary time t_i , including the time period t_{k+1} of new geodetic measurements. An important role in making predictions is played by the transition matrix $\Phi_{k|i}$. For the calculated prediction the covariance matrix $C_{\bar{X}_i}$ has the form [20]:

$$C_{\bar{X}_i} = \Phi_{k|i} C_{\bar{X}_{k=0}} \Phi_{k|i}^T + C_{e_i} \quad (12)$$

Here we can assume [20] that the covariance matrix is

$$C_{\bar{X}_{k=0}} = C_{e_i} = \begin{bmatrix} m_{z_i^w}^2 & & \\ & m_{V_i}^2 & \\ & & m_{\bar{a}_i}^2 \end{bmatrix} \quad (13)$$

For prediction purposes we can assume [20] that $E(e_i) = 0$, (E – the expected value operator), hence

$$\bar{X}_i = \Phi_{k|i} \bar{X}_{k=0} \quad (14)$$

As mentioned above, in filtration problems, along with geodetic observations made in the time period $t_{k=0}$ we should know the velocity or acceleration, or both of them, obtained from another independent measurement of the examined object. Kalman filtration enables to take into account

prediction when balancing new observations l_{k+1} made in the time period t_{k+1} (current measurement). The Kalman filtration algorithm which takes into account both prediction and new results of measurement can be presented in the following way:

1. Building the system of observation equations in the form

$$v_{k+1} = A_{k+1}v_{\bar{X},k+1} + L_{k+1} \quad (15)$$

where:

v_{k+1} – vector of corrections for observation l_{k+1} made in time period t_{k+1}

A_{k+1} – matrix of known coefficients at time t_{k+1}

$v_{\bar{X},k+1}$ – vector of corrections for prediction in time period t_{k+1}

L_{k+1} – vector of free terms at time t_{k+1}

2. Building the matrix of weights of the correction prediction vector $P_{v,k+1}$.

$$P_{v,k+1} = (P_{k+1}^{-1} + A_{k+1}P_{\bar{X},k+1}^{-1}A_{k+1}^T)^{-1} \quad (16)$$

where:

P_{k+1} – matrix of weights (given for results of observation, velocity, and acceleration)

$P_{\bar{X},k+1}$ – matrix of weights of the state vector ($P_{\bar{X},k+1} = C_{\bar{X},k+1}^{-1}$)

3. Determining the gain matrices

- gain matrix for corrections: $K_{k+1} = P_{k+1}^{-1}P_{v,k+1}$, (17)

- gain matrix for parameters: $K_{X,k+1} = -P_{\bar{X},k+1}^{-1}A_{k+1}^T P_{v,k+1}$. (18)

4. Calculating corrections for observation v_{k+1} and corrections $v_{\bar{X},k+1}$ for prediction (relations (19) and (20), respectively)

$$v_{k+1} = K_{k+1}L_{k+1} \quad (19)$$

$$v_{\bar{X},k+1} = K_{X,k+1}L_{k+1} \quad (20)$$

5. Calculating the vector of balanced observations \hat{L}_{k+1} (21), the state vector \hat{X}_{k+1} (22), and the variance coefficient estimator $\hat{\sigma}_0^2$ (23)

$$\hat{L}_{k+1} = l_{k+1} + v_{k+1} \quad (21)$$

$$\hat{X}_{k+1} = \bar{X}_{k+1} + v_{\bar{X},k+1} \quad (22)$$

$$\hat{\sigma}_0^2 = m_0^2 = \frac{1}{n_{k+1}}(v_{k+1}^T P_{k+1} v_{k+1} + v_{\bar{X},k+1}^T P_{\bar{X},k+1} v_{\bar{X},k+1}) \quad (23)$$

(n_{k+1} – number of observations made at time t_{k+1}).

The use of prediction and Kalman filtration enables to predict the scale of settlement of the controlled points in the time interval between successive measurements, and to balance the geodetic observation with the aid of prediction. The above procedure can be used to control the crane runway axes, as well as to calculate vertical displacements, indispensable when assessing the operational safety of the overhead crane. It was assumed in the paper that the crane

runway settles due to its unfavourable location, on an unstable quay ground for instance. What is also of high importance is calculating the maximal permissible limit for vertical displacement which will not lead to construction disaster. This task is to be agreed with the designer or construction expert.

SAMPLE PRACTICAL APPLICATION

The measurements done by the total station provide x, y, z coordinates of the controlled points. The presented sample of practical application bases on simulated data. For this purpose the positions of 8 controlled points uniformly distributed along crane rail axes were assumed, see Fig. 2. Moreover, for the purpose of the present analysis an assumption was adopted that settling of the system by up to 30 mm does not threat with construction disaster.

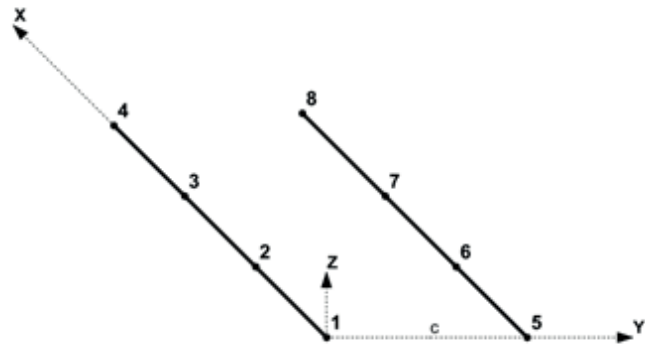


Fig. 2. Distribution of controlled points

In the local 3D reference system the controlled points 1-4 are situated on the left rail axis of the overhead crane, while those numbered 5-8 on the right rail axis. The calculations were performed for a gantry crane. The rails are assumed parallel to each other and distant by $c = 8$ m. Table 1 collates the coordinates simulated for the time $t_{k=0}$. Moreover, the correction equations based on relations (2) and (4) were built.

Tab. 1. Simulated coordinates of controlled points

No of point	x [mm]	y [mm]	z [mm]
1	0	0	0
2	4004	10	-10
3	7996	8	-15
4	11992	-6	-10
5	16	8012	-5
6	3998	7998	-15
7	8010	8006	-20
8	11998	8002	-10

The assumed distance between the rail axes, $c = 8000$ mm, enabled to formulate the condition equation in the form $c - 8000 = 0$

The relations (7) and (8) were used to calculate parameters and corrections needed to adjust the crane rail axes. The results obtained in the time period $t_{k=0}$ are given in Table 2. The calculations were performed assuming unit weights for free terms L and the weight $p = 20000$ for the assumed geometric condition.

Tab. 2. Results calculated at time $t_{k=0}$

Parameters and corrections		[mm]
Parameters	a	0
	b	7
	c	8000
	z	-11
corrections	v_1	7
	v_1	-11
	v_2	-5
	v_2	-1
	v_3	-5
	v_3	4
	v_4	7
	v_4	-1
	v_5	-5
	v_5	-6
	v_6	7
	v_6	4
	v_7	-3
	v_7	9
	v_8	-1
	v_8	-1
v	0	

The calculated results shown in Table 2 make the basis for possible adjustments of crane rail axes in the time period $t_{k=0}$, according to the applicable tolerances.

The results of observations of dynamic parameters, simulated from an independent measurement, are the following:

- settling rate of the points $V_{k=0} = 0,01\text{m/year}$, with the mean error $m_v = 0,002\text{m/year}$
- constant acceleration $a_{k=0} = 0,005\text{ m/year}^2$, with mean error $m_a = 0,001\text{ m/year}^2$.

The height values obtained in the time period $t_{k=0}$ and the simulated kinetic parameters were used to calculate the displacement prediction at times $i = 1/2$ year and $i = 1$ year.

State vector prediction for time $i = 1/2$ year

Here, the transition matrix has the form

$$\Phi_{k|i} = \begin{bmatrix} 1 & -0,5 & -0,125 \\ 0 & 1 & 0,5 \\ 0 & 0 & 1 \end{bmatrix}$$

The state vector $\bar{X}_{k=0}$ can be presented in the form

$$\bar{X}_{k=0} = \begin{bmatrix} z_{k=0}^w = -11 \\ V_{k=0} = 10 \\ \bar{a}_{k=0} = 5 \end{bmatrix} \begin{bmatrix} \text{mm} \\ \text{mm/year} \\ \text{mm/year}^2 \end{bmatrix}$$

Hence, based on relation (14) the state vector $\bar{X}_{i=1/2}$ takes the form

$$\bar{X}_{i=1/2} = \begin{bmatrix} z_{i=1/2}^w \\ V_{i=1/2} \\ \bar{a}_{i=1/2} \end{bmatrix} = \begin{bmatrix} -16,6 \\ 12,5 \\ 5,0 \end{bmatrix} \begin{bmatrix} \text{mm} \\ \text{mm/year} \\ \text{mm/year}^2 \end{bmatrix}$$

A conclusion which can be derived from the performed calculations is that after half a year the observed system will settle by 5,6 mm, reaching the level $z_{i=1/2}^w = -16,6$ mm. This value does not exceed the limit of 30 mm assumed before the beginning of observation.

The relation (12) was used to calculate mean errors of the prediction, shown in Table 3.

Tab.3. Mean prediction errors

m_i	$m_{z_{i=1/2}^w}$	$m_{V_{i=1/2}}$	$m_{\bar{a}_{i=1/2}}$
[mm]	1,4	0,9	1,4

State vector prediction for time $i=1$ year

The transition matrix has the following form

$$\Phi_{k|i} = \begin{bmatrix} 1 & -1 & -0,5 \\ 0 & 1 & 1 \\ 0 & 0 & 1 \end{bmatrix}$$

After determining the state vector $\bar{X}_{i=1\text{year}}$ we get

$$\bar{X}_{i=1\text{year}} = \begin{bmatrix} z_{i=1\text{year}}^w \\ V_{i=1\text{year}} \\ \bar{a}_{i=1\text{year}} \end{bmatrix} = \begin{bmatrix} -23,5 \\ 15,0 \\ 5,0 \end{bmatrix} \begin{bmatrix} \text{mm} \\ \text{mm/year} \\ \text{mm/year}^2 \end{bmatrix}$$

The performed analysis shows that the object will keep settling until it reaches the level of $z_{i=1\text{year}}^w = -23,5$ mm, but it still will not exceed the assumed permissible limit of 30 mm. Table 4 shows mean errors $\bar{X}_{i=1\text{year}}$ of the state vector.

Tab.4. Mean errors of prediction

m_i	$m_{z_{i=1\text{year}}^w}$	$m_{V_{i=1\text{year}}}$	$m_{\bar{a}_{i=1\text{year}}}$
[mm]	1,6	1,2	1,4

In the sample real application it was assumed that after one year (time period t_{k+1}) new measurements were performed, which enabled further calculations of the four following variants:

- variant I: settling of the entire system by 10 mm after one year
- variant II: settling of the entire system by 5 mm after one year

variant III: settling of the left rail by 5 mm, and the right rail by 10 mm after one year

variant IV: points 1, 2, 4, 5, and 8 settled by 10mm, while points 3, 6, 7 by 5mm.

Calculations of all four variants, taking in to account the yearly prediction, were performed using the above presented Kalman filtration algorithm. The obtained results are collated in Table 5. The estimation was done assuming unit weights for free terms L_{k+1} and the weight $p = 20000$ for the assumed geometric condition.

Tab. 5. Results of calculations at time t_{k+1}

Parameters and corrections		Variant I [mm]	Variant II [mm]	Variant III [mm]	Variant IV [mm]
parameters	a	0,0	0,0	0,0	0,0
	b	6,9	6,9	6,9	6,9
	c	8000	8000	8000	8000
	z^w	-24,1	-29,1	-26,6	-26,0
	V	5,0	5,0	5,0	5,0
	\bar{a}	0,0	0,0	0,0	0,0
Corrections	v_{y1}	6,9	6,9	6,9	6,9
	v_{x1}	-10,6	-10,6	-8,1	-12,5
	v_{y2}	-5,2	-5,2	-5,2	-5,2
	v_{x2}	-0,6	-0,6	1,9	-2,5
	v_{y3}	-5,3	-5,3	-5,3	-5,3
	v_{x3}	4,4	4,4	6,9	7,5
	v_{y4}	6,6	6,6	6,6	6,6
	v_{x4}	-0,6	-0,6	1,9	-2,5
	v_{y5}	-5,1	-5,1	-5,1	-5,1
	v_{x5}	-5,6	-5,6	-8,1	-7,5
	v_{y6}	6,8	6,8	6,8	6,8
	v_{x6}	4,4	4,4	1,9	7,5
	v_{y7}	-3,3	-3,3	-3,3	-3,3
	v_{x7}	9,4	9,4	6,9	12,5
	v_{y8}	-1,4	-1,4	-1,4	-1,4
	v_{x8}	-0,6	-0,6	-3,1	-2,5
	v_c	0,0	0,0	0,0	0,0
	v_y	0,0	0,0	0,0	0,0
v_x	0,0	0,0	0,0	0,0	

The obtained results can have the following interpretations:

1. Settling of the entire object.

The largest object settling, which neared the assumed limits, was observed for variant II ($z^w = -29.1$ mm). However, taking into account the fact that the assumed permissible limit for both crane rail heights cannot exceed 30mm, we can conclude that the results obtained for all variants are correct.

2. Crane rail axis rectification corrections obtained in successive variants.

The results of these calculations provided the information about the values of the rectification corrections in both horizontal and vertical plane. They allow to conclude that the values of rectification corrections in the horizontal plane are exactly the same in all analysed variants. The higher values of the rectification corrections for the majority of the controlled points along the vertical axis of the system are observed in variant IV. However, if we assume that the rail level difference in particular cross sections cannot exceed 10 mm and compare corresponding z_i values of the controlled points we can conclude that this deviation is not exceeded, regardless of the variant.

CONCLUSIONS

The above analysis reveals that the operational safety of the overhead crane as a port infrastructure component depends on many factors. Along with geometric conditions which the correctly working crane should meet, these factors also include its location. The method to calculate 3D crane axis rectification corrections which is proposed in [6, 11] offers the possibility to use the results for predicting object settling and calculating vertical displacements. The proposed solution can be used to analyse cases when the overhead crane is located in a place with unfavourable geotechnical conditions. The performed calculations making use of the simulated data confirm the applicability of the Kalman filtration to analysing the presented problem. Moreover, the developed dynamic model enables to predict the behaviour of the object after a certain time period. This piece of information is essential for evaluating the operational safety of the working crane, as well the safety of people and the equipment in its vicinity. Although both the theoretical analysis and the simulated data based practical calculations were performed for the gantry crane, the proposed methodology can also be applied to other types of overhead cranes. Practical application of the here presented theoretical considerations was confirmed using the simulated data. As the next step of the here reported activities, authors are going to perform analyses based on real data.

BIBLIOGRAPHY

1. Anigacz W., Modification of geodetic design methods for overhead crane runway rectification, (in Polish), Opole University of Technology, Studies and Monographs, z.57, Opole, 1992
2. Banachowicz A., Structure of Kalman Filter at an algorithm of Integrated Navigation System, Proceedings of 2nd Symposium on "Integrated Navigation", Maritime University of Szczecin, 2000.
3. Baran L. W., Theoretical principles of processing of geodetic measurement results (in Polish), Wydawnictwo Naukowe PWN, Warsaw, 1999
4. Borkowski P., Data fusion in a navigational decision support system on a sea-going vessel, Polish Maritime Research, No 4(76), Vol. 19, pp. 78-87, 2012, DOI 10.2478/v10012-012-0043-1
5. Borkowski P., Magaj J., Mąka M., Positioning based on multi-sensor Kalman filter (in Polish), Scientific Journals of the Maritime University of Szczecin, 13,(85), pp 5-9, 2008.
6. Filipiak D., Kamiński W., Determination of rectification corrections for semi gantry crane rail axes in the local 3D coordinate system, Reports on Geodesy and Geoinformatics, vol. 97/2014, 71-79, DOI: 10.2478/rgg-2014-0012, 2014

7. Gocał J., Engineering and industrial geodesy. Part III (in Polish), Wydawnictwo AGH, Krakow, 2010
8. Grala M., & Kopiejewski G., Engineering Geodesy. Selected divisions. (in Polish), Wyd. UWM, Olsztyn, 2003
9. Gulal E., Structural deformations analysis by means of Kalman-filtering., Boletim De Ciencias Geodesicas, Volume: 19 Issue: 1 Pages: 98-113 Published: JAN-MAR, 2013, DOI 10.1590/S1982-21702013000100007
10. Kalman, R.E., A new approach to linear filtering and prediction problems. Transactions of the ASME-Journal of Basic Engineering, 82 (D): 35-45, 1960, DOI 10.1115/1.3662552
11. Kamiński W., New method for determination of adjustment corrections for crane rail axes, Reports on Geodesy vol. 94/2013, 47-55, DOI: 10.2478/rgg-2013-0006 , 2013
12. Křemen T., Koska B., Pospíšil J., Kyrinovič P., Haličková J., & Kopáček A., Checking of crane rails by terrestrial laser scanning technology, 13th FIG, 4th IAG, Lnc, Lisbon 12-15 May, 2008
13. Kyrinovič P., & Kopáček A., Automated measurement system for crane rail geometry determination, 27th International Symposium on Automation and Robotics in Construction (ISARC 2010), 294 – 305, 2010
14. Marjetič A., Kregar K., Ambrožič T., & Kogoj D., An Alternative Approach to Control Measurements of Crane Rails, Sensors, 12, 5906-5918, 2012, DOI 10.3390/s120505906
15. Naus K., The effect of measurements burdened with gross error on the accuracy of ship position estimation with the aid of extended Kalman filter and robust geodesic adjustment (in Polish), Logistyka, 3/2014, 4589-4602, 2014
16. Shi. C., Zhao D., Peng J., Shen C., Identification of ship maneuvering model Using extender Kalman filters, TransNav, International Journal on Marine Navigation and Safety of Sea Transportation, Vol.3, No. 1, March 2009, DOI 10.1201/9780203869345.ch59
17. Stateczny A., Kazimierski W., A Concept of Decentralized Fusion of Maritime Radar Targets with Multisensor Kalman Filter, IEEE, Proceedings of IEEE 11-th International Radar Symposium, 16-18 June 2010, pp.1-4
18. Tomera M., Dynamic positioning system for a ship on harbour manoeuvring with different observers. experimental results. Polish Maritime Research Volume: 21 Issue: 3 Pages: 13-24 Published: SEP 2014
19. Wiśniewski Z., Compensatory calculation in geodesy (with examples) (in Polish), Wydawnictwo UWM, Olsztyn, 2005
20. Wiśniewski Z., Advanced methods of geodetic observation processing with examples (in Polish), Wydawnictwo UWM w Olsztynie, Olsztyn, 2013.

CONTACT WITH THE AUTHOR

Daria FILIPIAK – KOWSZYK

FACULTY OF CIVIL AND ENVIRONMENTAL
ENGINEERING
Gdańsk University of Technology
11/12 Narutowicz Street
80 – 233 Gdańsk
POLAND

ANALYSIS OF FATIGUE CRACK GROWTH IN SHIP STRUCTURAL DETAILS

Heba W. Leheta

Ahmed M. H. Elhewy

Helmy A. Younes

Naval Architecture and Marine Engineering Department, Faculty of Engineering,
Alexandria University

ABSTRACT

Fatigue failure avoidance is a goal that can be achieved only if the fatigue design is an integral part of the original design program. The purpose of fatigue design is to ensure that the structure has adequate fatigue life. Calculated fatigue life can form the basis for meaningful and efficient inspection programs during fabrication and throughout the life of the ship. The main objective of this paper is to develop an add-on program for the analysis of fatigue crack growth in ship structural details. The developed program will be an add-on script in a pre-existing package. A crack propagation in a tanker side connection is analyzed by using the developed program based on linear elastic fracture mechanics (LEFM) and finite element method (FEM). The basic idea of the developed application is that a finite element model of this side connection will be first analyzed by using ABAQUS and from the results of this analysis the location of the highest stresses will be revealed. At this location, an initial crack will be introduced to the finite element model and from the results of the new crack model the direction of the crack propagation and the values of the stress intensity factors, will be known. By using the calculated direction of propagation a new segment will be added to the crack and then the model is analyzed again. The last step will be repeated until the calculated stress intensity factors reach the critical value.

Keywords: Fatigue crack, linear elastic fracture mechanics (LEFM), finite element method (FEM)

INTRODUCTION

Although a ship may be designed to withstand the ultimate stresses imposed by heavy storm waves, failure could occur due to apparently low stresses generated by the continuously encountered smaller, although significant, ocean swells, as well as impact loads resulting from the routine loading and manoeuvring of a ship. When assuming that a ship has a life of 20 years and operates at sea for 75% of her life time, and knowing that the medium period of wave encounter is approximately equal to 5 seconds, the ship will experience nearly 100 million loading cycles throughout her life. Structural failure of a ship may result in consequences that range from simple leaks to severe loss of lives. The failure consequences are functions of the ship's age, the damaged component, its location, and the maintenance and repair

history of the ship [1, 2]

In the past, ship structure design often did not incorporate explicitly an analysis of fatigue. However, as stated in the subject-matter literature, the main reasons for interest to studying fatigue cracking is, in the last few years, the introduction of high tensile steels and the development of very large ships (e.g. VLCC, ULCC) which results in increasing the stresses in critical structural details and decreasing its fatigue life. Although the allowable stress methods are used in the design of majority of ship structures, more and more of the new designs incorporate detailed analysis methods. [3,4]

Fatigue failure avoidance is a goal that can be achieved only if the fatigue design is an integral part of the original design program. An improper design may lead to an unacceptable catastrophic fatigue failure resulting in loss of life and damage

to the environment. Non-catastrophic fatigue failures are also unacceptable due to difficulty and cost of repairs as well as the need to increase costly inspection and maintenance intervals. The aim of fatigue design is to ensure that the structure has adequate fatigue life. Calculated fatigue life can also form basis for meaningful and efficient inspection programs during fabrication and throughout the life of the ship [3, 5].

The finite element method is a numerical procedure that can be applied to obtain solutions to a variety of engineering problems e.g. stress analysis, heat transfer, fluid flow, etc. Such problems may be steady, linear, or nonlinear ones. Yet, it was not until 1960 that Clough made the term “finite element” popular [6]. There are many finite element software packages available in the market however, most of them do not have a built- in function for fatigue analysis. The few that have a built -in function for fatigue analysis can be used to study fatigue crack propagation along a predefined path. For example, ABAQUS ver. 14 software package has either static crack analysis or crack propagation analysis but the crack propagation path must be known before the analysis. The case of predefined path crack analysis may be practical for the analysis of lamination cracks, e.g. in fibre glass composites. However, this feature cannot be used for crack in steel ship structural details where the crack path is unknown.

The aim of this paper is to evaluate fatigue analysis by using linear elastic fracture mechanics (LEFM), and to achieve this aim an add-on program is developed to analyze fatigue crack growth in ship structural details. The program will be an add-on script in ABAQUS software. The application was developed by using python programming language which can be incorporated into ABAQUS to extend its features.

The fatigue analysis techniques are presented in the next section, where a summary on cumulative damage approach emphasizing linear cumulative damage approach (Miner’s rule) is discussed. A detailed discussion of fracture mechanics especially linear elastic fracture mechanics, LEFM, is presented in Sec. 4. Also crack stages and stress intensity factors are discussed. The application of LEFM for fatigue analysis is given to show fatigue life calculation by using LEFM (Paris law).

METHODS FOR FATIGUE ANALYSIS

A broad view of the common methods for fatigue analysis is shown in Fig. 1 [7]. Fatigue analysis may be carried out by methods based on fatigue tests (S-N data) and estimation

of cumulative damage (Miner rule). Another approach to fatigue analysis is fracture mechanics which is discussed in details in the following section, separately.

Predicting fatigue damage for structural components subjected to variable loading conditions is a complex issue. The first, simplest, and most widely used damage model is the linear damage. This rule is often referred to as Miner’s rule (1945). However, in many cases the linear rule often leads to non-conservative life predictions. The results from this approach do not take into account the effect of load sequence on the accumulation of damage due to cyclic fatigue loading. Since the introduction of the linear damage rule many different fatigue damage theories have been proposed to improve the accuracy of fatigue life prediction [3, 8, 9].

Ship structure design often did not include explicit treatment of fatigue by means of an analysis. However, with the increasing in using higher strength steels and the increased cyclic stress ranges, fatigue analysis of structures is increasingly required. Although the developed allowable stress methods (which use S-N curves) are applied in the design of majority of ship structures, more and more of the new designs incorporate detailed analysis methods (which use fracture mechanics) [6].

The material resistance to fatigue failure primarily depends on the characteristics of detail/joint geometry, material chemical composition and mechanical properties, and the service environment. The material resistance is typically determined in laboratory tests by the application of constant amplitude stress cycle on various detail/joint geometries until fatigue failure occurs. By carrying out similar tests for different stress amplitudes a relationship between the stress amplitude, S , and the number of cycles, N , is established. The S-N curves developed for simple details (i.e., stiffener, cut-out, etc.) account for the peak stresses and can be directly used with the member nominal stresses [10].

The application of linear elastic fracture mechanics, LEFM, in estimating the life of the structure assumes that cracks has already initiated in the material. The behaviour of the crack can be predicted under anticipated service loading. The estimated behaviour is used to schedule inspection and maintenance in order to assure that defects do not propagate to a catastrophic size [3].

FRACTURE MECHANICS APPROACH

This section provides an introduction to the important

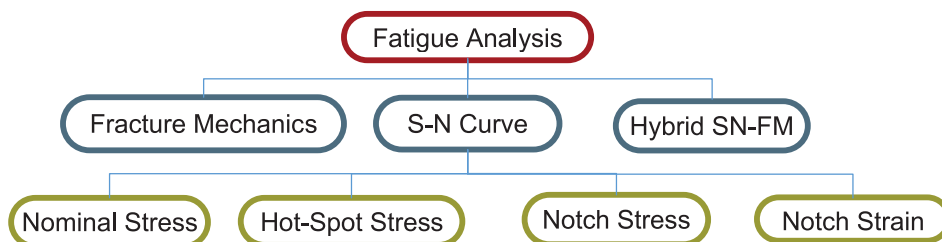


Fig. 1 Fatigue Analysis Techniques

aspects of linear elastic fracture mechanics (LEFM) and shows how it can be used to describe and predict fatigue crack growth rate and fatigue life. It provides a general background for the concepts of fracture mechanics and numerical tools needed for fatigue design involving crack growth and fracture analysis. The basic control factors in fracture mechanics are the stress intensity factor K , the energy release rate G , the crack opening displacement COD , and the J-integral J . These quantities along with their critical or limiting values are the foundation of any fracture analysis [7].

LEFM CONCEPTS

Fracture mechanics is used to evaluate the strength of a structure or component in the presence of a crack or flaw. Its application to fatigue involves the crack growth process, covering the range from a detectable crack or flaw to final fracture. One of the common methods used to analyze this process is LEFM. The method is used to determine crack growth in materials under the basic assumption that material conditions are predominantly linear elastic during the fatigue process. For crack growth or fracture conditions that violate this basic assumption, elastic-plastic fracture mechanics approaches are used to describe the fatigue and fracture process. It is necessary to define the basic crack surface displacement modes by which a crack can extend before using LEFM concepts for the crack growth analysis [11].

MODES OF CRACK EXTENSION

- Fig. 2 shows three modes by which a crack can extend.
- **MODE I** is the opening (tensile) mode where the crack surfaces move directly apart ;
 - **MODE II** is the sliding (in-plane shearing) mode where the crack surfaces slide over one another in the direction perpendicular to the leading edge of the crack;
 - **MODE III** is the tearing (anti-plane shear) mode where the crack surfaces move relative to one another and parallel to the leading edge of the crack.

FATIGUE CRACK GROWTH BASED ON LEFM

The main goal of the application of fracture mechanics in fatigue analysis is to estimate the total number of cycles for the assumed initial crack a_i to reach a final length a_f . The crack

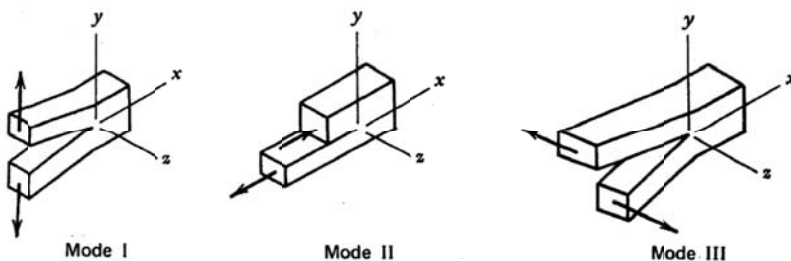


Fig. 2 Modes of crack extension

tip stress intensity factor is an extremely useful parameter to address crack growth behaviour as long as the bulk of the material is elastic and plastic deformation is limited to a small region at the crack tip [12] .

In order to illustrate the basic parameters of the fatigue crack growth, Fig. 3 shows a typical plot of crack propagation where it is noticed that:

- Crack length increases with the increasing number of loading cycles;
- Crack growth rate most often increases with increasing crack length;
- Crack growth rate increases with increasing stress level;
- Crack becomes longer at an increasingly rapid rate;
- Most of the loading cycles involved in the total life of the component are consumed during the early stages of crack extension [10, 13].

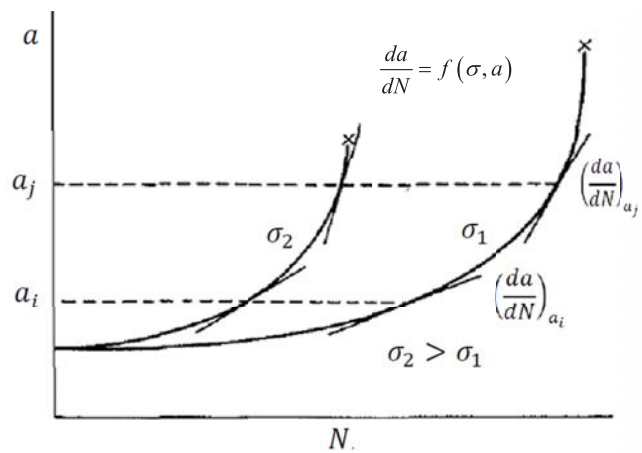


Fig. 3 Effect of crack length and stress level on crack propagation rate

In general, as shown in Fig. 4, Fig. 5 and 6 , it has been observed that the fatigue process involves the following stages:

1. Stage I – Initiation
 - a. Cyclic slip
 - b. Crack nucleation,
 - c. Short (micro) crack growth,
2. Stage II – Stable crack growth
 - a. Long (macro) crack growth, and
3. Stage III – unstable crack growth
 - a. Final fracture.

FATIGUE ANALYSIS OF SHIP STRUCTURES

Fatigue is responsible for a large amount of cracks occurring in welded ship structural details. For many years fatigue - related failure has become a major concern in the maintenance

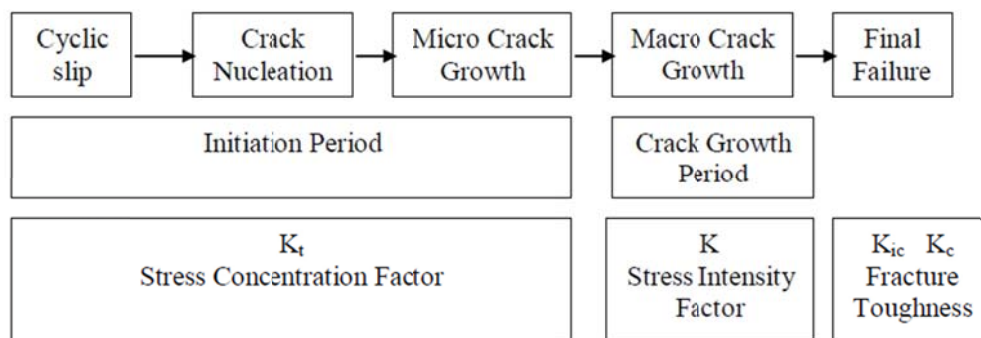


Fig. 4 Phases of fatigue cracking

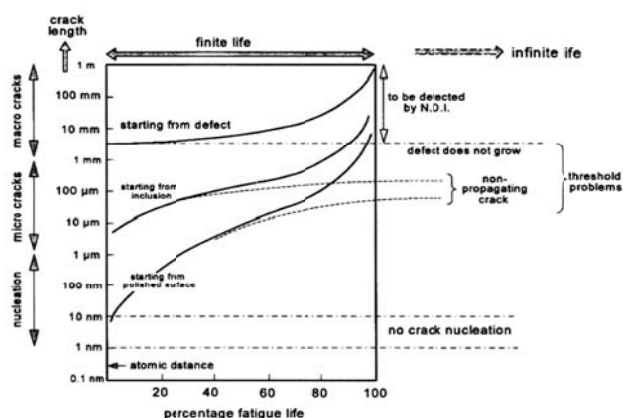


Fig. 5 Different scenarios of fatigue crack growth

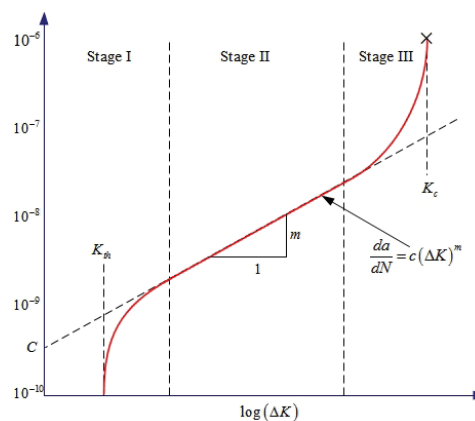


Fig. 6 Fatigue rate curve da/dN versus ΔK

of existing ships and the design of new ships especially after the introduction of high tensile steel (HTS). Numerous cracks were experienced by relatively new oil carriers constructed of HTS materials. The cracks were discovered when the ships were about 3 to 4 years old without any significant corrosion or wastage [1, 14].

The main factors affecting increased number of fatigue cracks in ships may be summarized as follows:

1. The trend of reducing the ship scantlings based on detailed stress analysis and the increased use of HTS, has resulted in the increase of the general stress level. Note that improved detail design which would cause a reduction of the SCF value for ship structural details, has minimized the effect of increased stress level [4, 14].
2. Tankers operate on trade routes (e.g., TAPS trade route from California to Alaska) having severe weather for the majority of their operational time, which causes very severe loading with respect to fatigue damage.
3. The presence of corrosion (general, pitting, and grooving) in ballast and cargo tanks resulting in a reduction of the fatigue life of ship structural details [4].

Due to the growing number of fatigue cracks a more direct control of fatigue is needed. The aim of the fatigue control is to ensure that all parts of the hull structure subjected to fatigue (dynamic) loading have an adequate fatigue life. Calculated fatigue lives, calibrated with the relevant fatigue damage data,

may give the basis for the structural design (steel selection, scantlings and local details). Furthermore, they can form the basis for efficient inspection programs during fabrication and throughout the service life of the structure. [14]

AREAS SUSCEPTIBLE TO FATIGUE DAMAGE

Fatigue damages are known to occur more frequently for some ship types and categories of hull structure elements. The fatigue life is in particular related to the magnitude of the dynamic stress level, the corrosiveness of the environment and the magnitude of notch and stress concentration factors of the structural details, which all vary depending on ship type and structure. The importance of possible fatigue damage is related to the number of potential damage points of a considered type for the ship or structure in question and to its consequences. [14]

In ship structures a major fraction of the total number of fatigue damages occurs in panel stiffeners on the ship side and bottom and on the boundaries of ballast and cargo tanks [14].

Fig. 7 and 8 show a possible distribution of fatigue cracks in a typical ship structural component. In tankers, cracks occur mostly on the side longitudinals at the connections to transverse bulkheads or transverse webs. Other ship types such as bulk carriers also suffer from fatigue cracks. Where in some bulk carriers, cracks were commonly found in the hard corners of the lower hopper tanks connecting to the

side frames, and the lower stools connecting to the double bottom [1].

DNV [14] and other classification societies has published some tables showing the critical areas for different ship types. As an example for tankers Tab. 1 is listed hereunder.

Tab.1 Critical details for a tanker

Structure member	Structural detail	Load type
Side, bottom and deck plating and longitudinals	Butt joints, deck openings and attachment to transverse webs, transverse bulkheads, hopper knuckles and intermediate longitudinal girders	Hull girder bending, stiffener lateral pressure load and support deformation
Transverse girder and stringer structures	Bracket toes, girder flange butt joints, curved girder flanges, knuckle of inner bottom and sloped hopper side and other panel knuckles including intersection with transverse girder webs. Single lug slots for panel stiffeners, access and lightening holes	Sea pressure load combined with cargo or ballast pressure load
Longitudinal girders of deck and bottom structure	Bracket terminations of butting transverse members (girders, stiffeners)	Hull girder bending, and bending / deformation of longitudinal girder and considered abutting member

Also, the following assumptions are used for the analysis of the finite element model:

- Material is isotropic;
- Linear fracture mechanics applies;
- the plastic zone in the crack front is minimal.

ABAQUS built-in features can only be used to analyze a static crack (i.e. in-site crack) or a propagating crack through a predefined path. The case of crack propagation through a predefined path is practical for the analysis of laminations (i.e. fibre glass reinforced composites). However, in case of fatigue crack propagation through ship structural details the path of the crack is unknown. Hence, because of limitation of this software a special script is developed with the purpose of analyzing a propagating crack without having predefined path.

The simplest way to explain this idea is that a static crack will be first analyzed and from the analysis the crack propagation direction is made known and then the crack is propagated in this direction. Another static crack will be analyzed in the new location until the crack is terminated.

MODELLING THE ORIGINAL , NON-CRACKED ELEMENT MODEL

The original model is analyzed by using the finite element method to indicate the critical point, i.e. the point where maximum stresses

occur and where the crack is suspected to start. The modelling technique, meshing and loading of the original model is discussed below.

PROPOSED PROCEDURES APPLICABLE TO CUT-OUTS

A calculation method applied to a cut-out model in a side connection of a crude oil carrier, is proposed. The model encompasses a longitudinal stiffener passing through a side transverse. Due to the cut-out introduced in the side transverse this connection is suspected of fatigue failure [15].

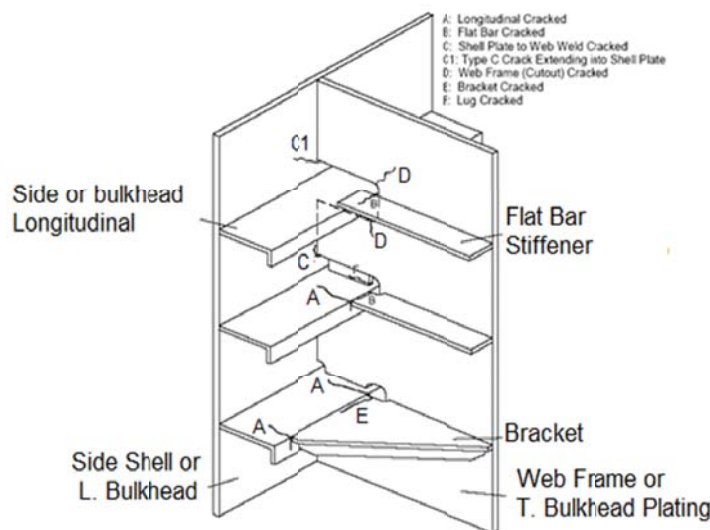


Fig. 7 Distribution of ship's fatigue cracks

MODELLING THE GEOMETRY

The crack analysis can be carried out by using either 2D or 3D models. For each model either shell or solid elements

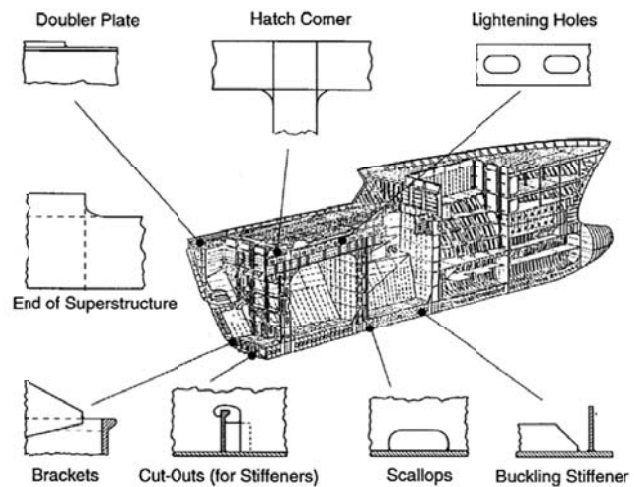


Fig. 8 Critical structural details

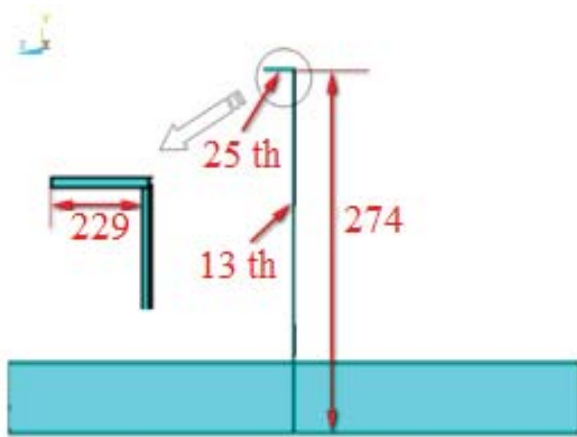


Fig. 9 Model dimensions

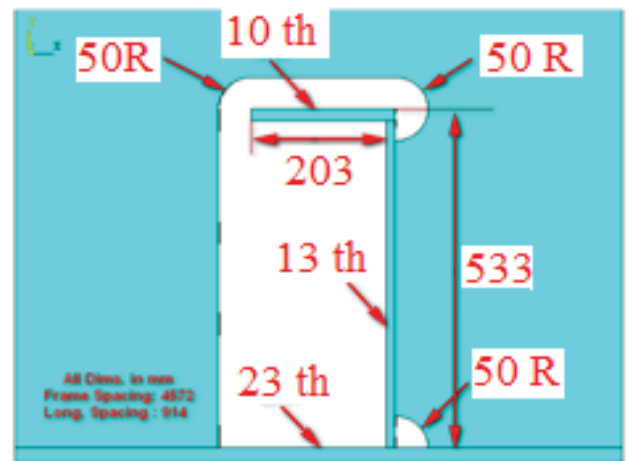


Fig. 10 Model dimensions

can be used. The modelling by using shell and continuum elements can be applied to analyzing fully through cracks, e.g. a cracked plate. However continuum elements cannot be used for 3D modelling. The solid modelling has the advantage of analyzing both fully through cracks and partially through cracks, e.g. penny cracks in shafts [16]. Fig. 9 and 10 show model dimensions in two views.

Since most cracks in the ship structures will be fully through ones, hence the using of shell elements will be much easier than solid elements with no reduction in the quality of the analysis. This also helps reducing the programming used in propagating cracks and reduces the time required for the analysis. The proposed element is that of four nodes, S4, which can be degenerated into a triangle to allow the account of crack tip singularity. The area around the cut-out in the web frame, with estimated high stress concentration, will be meshed by using a finer mesh as shown in Fig. 11 and 12.

After several trials by using both medial axis and advancing front meshing algorithms, the advancing front meshing algorithm was selected for this analysis. The medial axis meshing algorithm is much faster than the advancing front meshing algorithm, especially with the repeated re-meshing. However, due to sensitivity of the mesh around the crack tip, especially in the initiation phase, the mesh has to follow an exact seeding pattern which can only be achieved by using the advancing front meshing technique [17].

BOUNDARY CONDITIONS

Some studies were made to show the effect of boundary conditions on the hot-spot stress. The results showed the insensitivity of the fixation boundary conditions on the hot-spot stress away from the boundary. However, boundary conditions are based on symmetry, continuity and engineering judgment. The boundary conditions applied to this analysis are shown in Fig.13, where, UX, UY and UZ are the translation

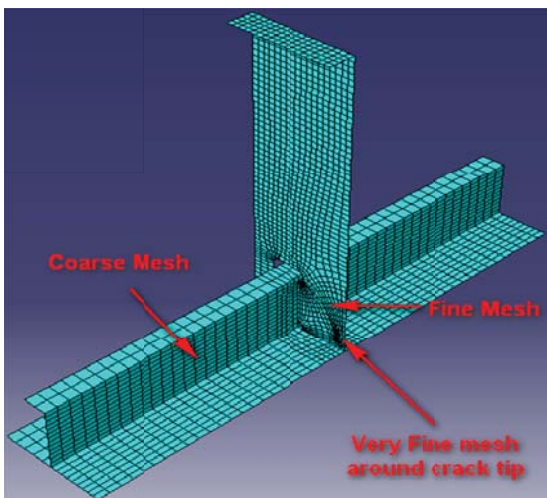


Fig. 11 Different mesh sizes

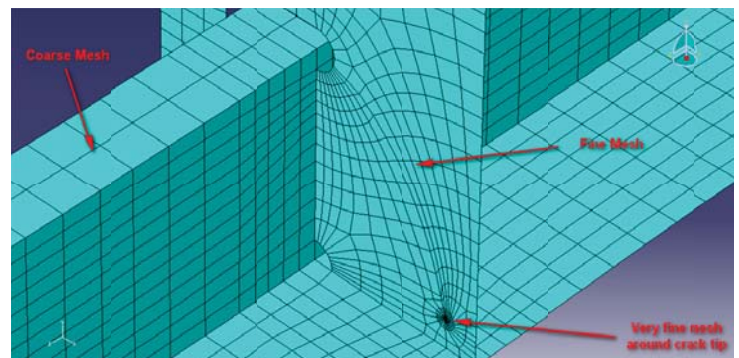


Fig. 12 Different mesh sizes

in X, Y and Z directions, respectively, and ROTX, ROTX and ROTX are the rotation about X, Y and Z axis, respectively, [15, 18].

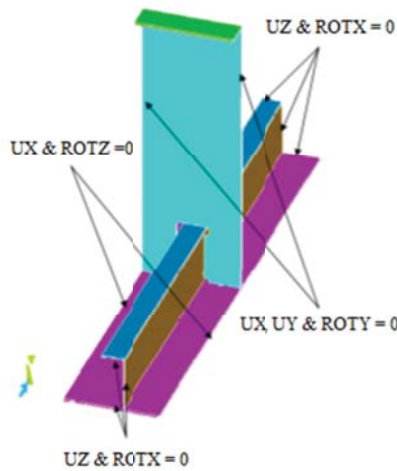


Fig. 13 FEM model boundary conditions

APPLIED LOADS

To analyze the crack propagation by using fracture mechanics the fatigue loading will be simplified as much as possible. This could be done by choosing a detail placed as close to the ship’s neutral axis as possible to eliminate hull girder loads. In addition, the cargo tank will be assumed empty to eliminate internal loads. Hence, for the considered model of oil tanker’s side connection, the fatigue loads playing the major role in this analysis, are those resulting from the varying sea water pressure on the outer shell.

INITIAL CRACK

LOCATION OF INITIAL CRACK

The welded structure in question will be assumed to have only one initial crack. After the analysis of the non-cracked element model the location of the maximum stresses (von Mises stress) is recorded and will represent the location for the start point of the initial crack.

SIZE OF INITIAL CRACK

As discussed before, the initial crack length can be estimated by using different methods, and to keep the estimation practical, the crack length is assumed as that of the smallest crack detectable by using X-ray NDT method; this length is equal to 3.81mm. [7]

RESULTS OF THE INITIAL CRACK ANALYSIS

After the analysis of the initially cracked element model, the values of ΔK_I and ΔK_{II} are obtained directly by applying the finite element model. The fatigue crack growth rate has been expressed by Tanaka [20] who used a Paris type equation

as a function of an effective stress intensity factor:

$$\frac{da}{dN} = C(\Delta K_{eff})^m$$

where the effective stress intensity factor range ΔK_{eff} for combined mode -I -and- II loadings is expressed by:

$$\Delta K_{eff} = (\Delta K_I^4 + 8\Delta K_{II}^4)^{\frac{1}{4}}$$

INTRODUCTION OF A NEW CRACK SEGMENT

After the analysis of the initial crack and determining the value of the crack extension angle θ , a new crack extension segment with the length da is introduced. The da - length is not an essential value for the analysis, however a smaller da value will lead to better numerical integration for the fatigue life. And of course the smaller the value the more calculation processes are needed and hence the time to complete a full analysis.

One major problem that occurs when selecting a relatively large length da is that the meshing becomes impossible sometimes. This is due to the big difference between the seed values of the lines representing the start of the crack, see Fig.14 below.

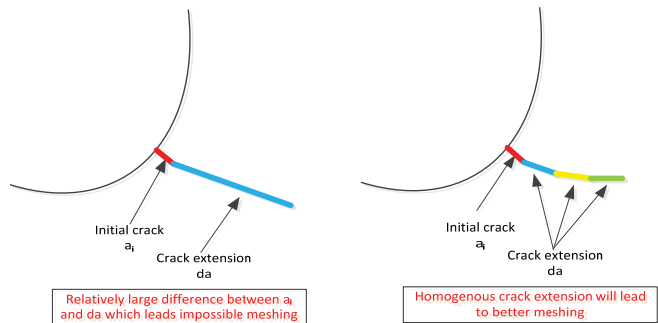


Fig. 14 Different values of the crack extension da

ANALYSIS OF THE CRACKED ELEMENT MODEL AFTER EXTENSION

The analysis of the model after each crack extension is continued and all relevant values are stored for each step of the crack extension. The most important parameters are : a , ΔK_I , ΔK_{II} , ΔK_{eff} , θ . The event of $\Delta K_{eff} > K_C$ means that the crack will continue to propagate under Paris’ law. Hence a new crack segment is introduced and analyzed, as stated previously in 6.4.

This analysis continues until the effective stress intensity

factor ΔK_{eff} reaches its maximum value which is equal to the value of the critical stress intensity factor K_C . The event of $\Delta K_{eff} > K_C$ means that the stage II of stable crack growth have ended and Paris law is no more applicable. The crack size a at this stage, can be considered the critical crack size, a_c .

As discussed before, after reaching this value the crack propagation enters stage III where the crack propagates at very high speed and will not affect the fatigue life calculation. Hence, at this stage the analysis can be ended without any compromise in the calculation of the fatigue life of the model.

Another important check which must be programmed is to check that each time a new crack segment is introduced and the end of this crack segment still remains within the domain of the model. Unless this quite simple check is programmed the program may never terminate if the variable load is small and the model is completely cracked without reaching the condition of $\Delta K_{eff} > K_C$.

FATIGUE LIFE CALCULATION

The fatigue life calculation can be accomplished in two stages. First, the number of fatigue load cycles required to propagate the crack from the initial size a_i to the final size a_f . This can be done by integrating Paris formula, as discussed below. The second step is to estimate the number of fatigue load cycles that occur each year for a ship. This way the calculated number of cycles from the first step can be translated into number of years.

NUMBER OF CYCLES TO FAILURE

At the end of the calculations and after the value of the range of effective stress intensity factor ΔK_{eff} exceeds the value of the critical stress intensity factor K_C , the fatigue life, as number of cycles to failure, can be calculated by using numerical integration of Paris law, as discussed in 6.3.

$$\frac{da}{dN} = C(\Delta K)^m$$

$$\text{Fatigue Life} = \int_0^N dN = \frac{1}{C} \int_{a_i}^{a_f} \frac{da}{(\Delta K)^m}$$

In the discussed analysis method the step at which crack propagates, da , is held constant all over the analysis. Also the material constants C and m are kept constant. Hence the above mentioned integration can be simplified into a very simple summation as follows:

$$N = \frac{d_a}{C} \sum_{a_i}^{a_f} \frac{1}{(\Delta K)^m}$$

The limitation of the Paris law is that it is only capable of describing data in Stage II (see Fig. 6). If the data exhibits a threshold (Stage I) or an accelerated growth (Stage III) Paris law cannot adequately describe these regions. Depending

upon the analysis being undertaken, this approximation may not be adequate. Finally, the Paris law does not consider the effect of stress ratio and it depends upon the used material. For steels tested at various stress ratios, a family of straight lines parallel to each other is produced. This means that the value of m is the same for all stress ratios but the value of C is specific for a particular stress ratio.

FATIGUE LIFE

As indicated in Bureau Veritas rules [19] the number of cycles for the expected ship's life Nt can be estimated by using the following equation:

$$N_t = \frac{\alpha_o T}{4 \log L}$$

where: T is the design life in seconds, L is the length of the ship, α_o is the sailing factor which takes into account the time needed for loading/unloading operations, repairs, etc. As a rule, α_o may be taken equal to 0.85.

Calculating the number of cycles corresponding to a crack length or final failure, knowing the number of cycles by using crack propagation analysis as stated before, the previous relation could be used accordingly, to estimate the time (e.g. number of years) corresponding to each stage of the crack growth.

$$T = \frac{4 \log L}{\alpha_o} N = 4.71 \times \log L \times N \quad \rightarrow \text{T in seconds}$$

$$T = 1.492 \times 10^{-7} \times \log L \times N \quad \rightarrow \text{T in years}$$

Finally, by using the assumptions of number of load cycles per year, the life of the ship can be calculated. Also the following graphs can be plotted:

- Crack profile;
- ΔK_{eq} , ΔK_I and ΔK_{II} versus crack length a ;
- ΔK_{eq} , ΔK_I and ΔK_{II} versus time;
- Crack length a versus time;

RESULTS

After the successful running of the developed program shown in the flow chart of Fig. 15, the results of the analysis could be presented as follows:

A crack will initiate at the scallop of the cut-out in the web frame due to increased stresses at this area. This crack will start propagating towards the side shell plating due to fatigue loading. The total life of the model was calculated to be 7.8 years. The illustration of the crack propagation during the fatigue life of the model is illustrated in the form of graphs and crack profiles for different stages of the crack propagation. Tab. 2 shows the summary of the different phases.

the material.

CRACK LENGTH VERSUS TIME

Fig. 25 shows that the crack starts propagating at a relatively very low rate. As an example, 25% of the fatigue life is consumed to propagate the crack for only 6% of its final length. However the rate increases rapidly after reaching about 50% of the fatigue life. Also, it shows that the last 50% of the crack length is consumed rapidly in less than 7% of the total life.

EQUIVALENT STRESS INTENSITY FACTOR VERSUS CRACK LENGTH AND TIME

Fig. 26 shows that the equivalent stress intensity factor ΔK_{eq} increases steadily during the crack propagation phase while increases rapidly at the final stages. This shows that the ΔK_{eq} follows Paris law during stage II of the propagation phase.

In combination with Fig. 26, Fig. 27 shows that during stage II of the propagation phase, where the ΔK_{eq} follows Paris law, the ΔK_{eq} increases by the increasing of the crack size. However, at the final stages it decreases with the increase of crack size. This shows that the analysis is only valid for the propagation period because the developed programs is only applicable to the area following Paris law and does not include formulas for stage III of the crack propagation.

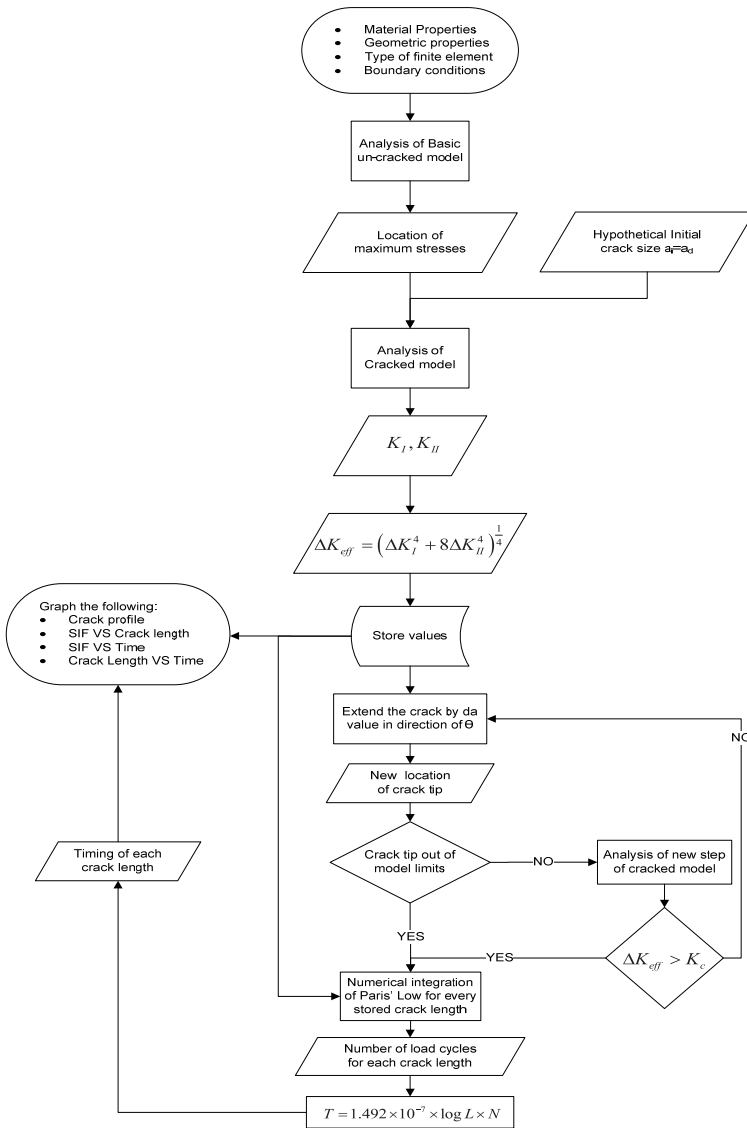


Fig. 15 Flow chart of the developed program

Tab. 2 Summary of crack propagation

Figure	Crack length		Time	
	a (mm)	$\% a_f$	T (years)	% Life
Fig. 16	3.81	0%	0	0%
Fig. 17	39.81	6%	1.9	25%
Fig. 18	99.81	15%	3.9	50%
Fig. 19	163.81	25%	5.5	70%
Fig. 20	183.81	28%	5.8	75%
Fig. 21	323.81	50%	7.3	93%
Fig. 22	487.81	75%	7.7	98%
Fig. 23	647.81	100%	7.8	100%

CRACK PROFILE AND STRESS FIELD

The stress field shown in Fig. 24 illustrates the distribution of the stresses around the crack tip. The red area in the region indicates where the stress is higher than the yield stress of

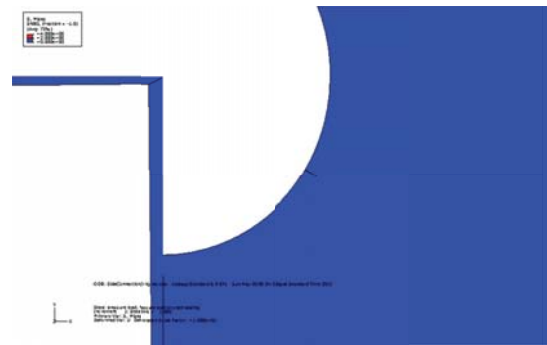


Fig. 16 Initial crack profile

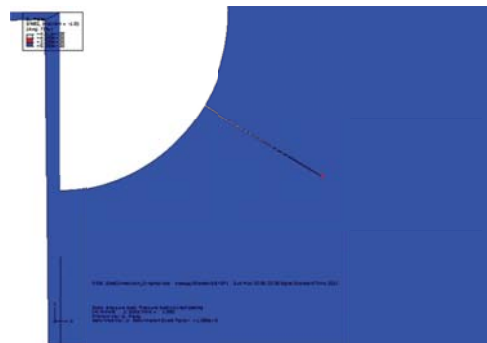


Fig. 17 Crack profile

$a=39.81$ mm= $6\% a_f$ $t = 1.9$ Years = 25% Life

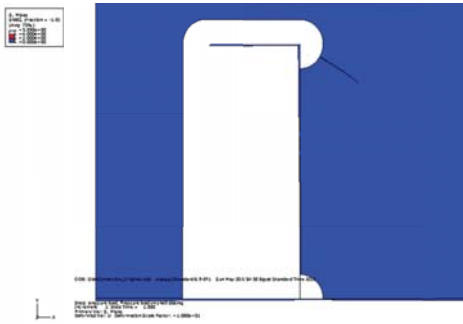


Figure 18 – Crack Profile
 $a = 99.81\text{mm} = 15\%a_f$; $t = 3.9\text{Years} = 50\% \text{ Life}$)

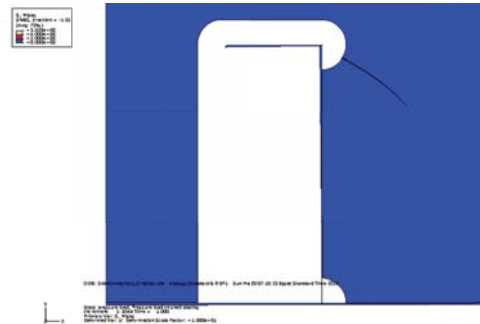


Figure 19 – Crack Profile
 $a = 163.81\text{mm} = 25\%a_f$; $t = 5.5\text{Years} = 70\% \text{ Life}$)

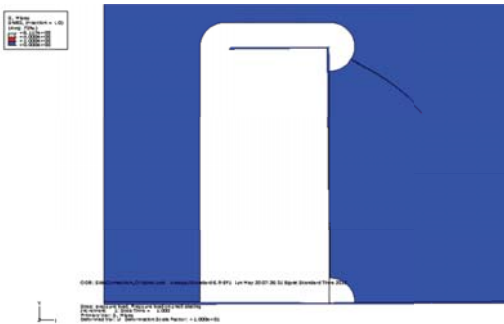


Figure 20– Crack Profile
 $(a = 183.81\text{mm} = 28\%a_f$; $t = 5.8\text{Years} = 75\% \text{ Life}$)

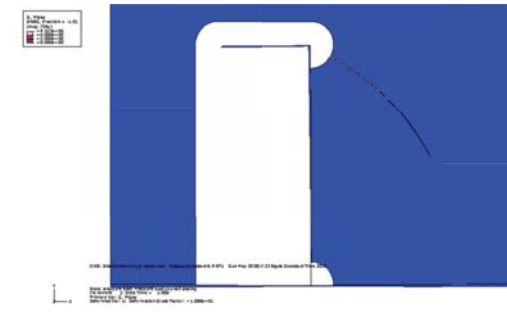


Figure 21 – Crack Profile
 $(a = 323.81\text{mm} = 50\%a_f$; $t = 7.3\text{Years} = 93\% \text{ Life}$)

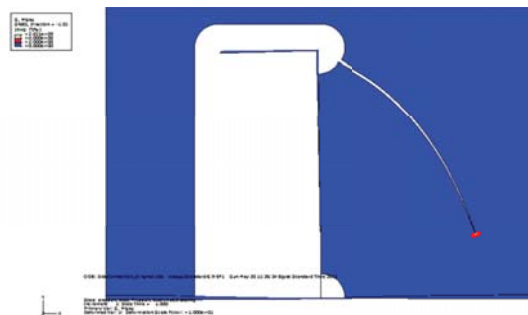


Figure 22 – Crack Profile
 $a = 487.81\text{mm} = 75\%a_f$; $t = 7.7\text{Years} = 98\% \text{ Life}$)

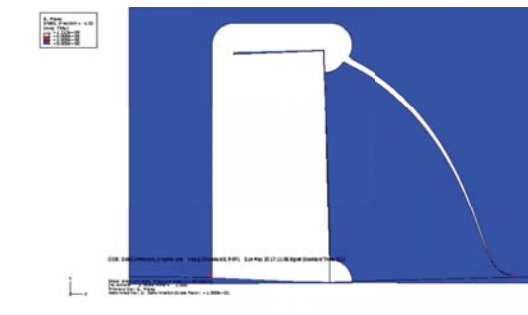


Figure 23 – Final Crack Profile
 $a = 647.81\text{mm} = 100\%a_f$; $t = 7.8\text{Years} = 100\% \text{ Life}$)

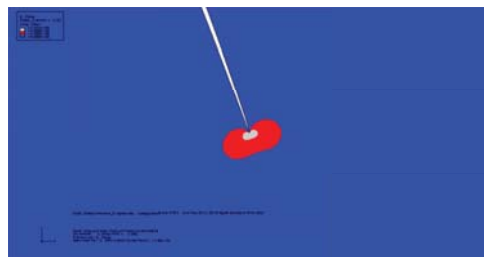


Figure 24 - Crack tip stress field

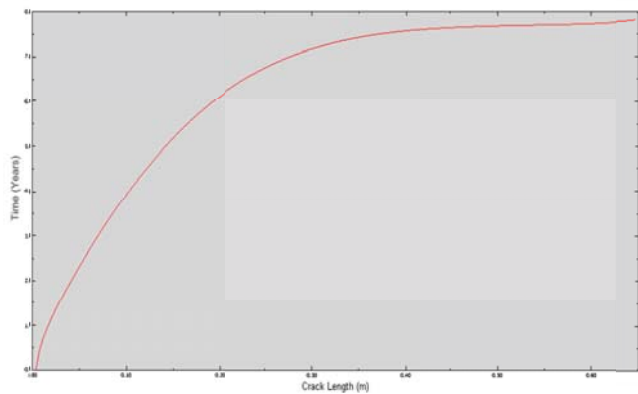


Figure 25 - Time VS Crack Length

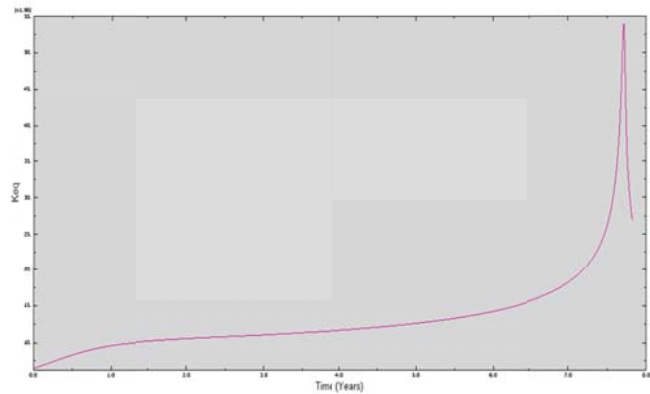


Figure 26 - K_{eq} VS Time

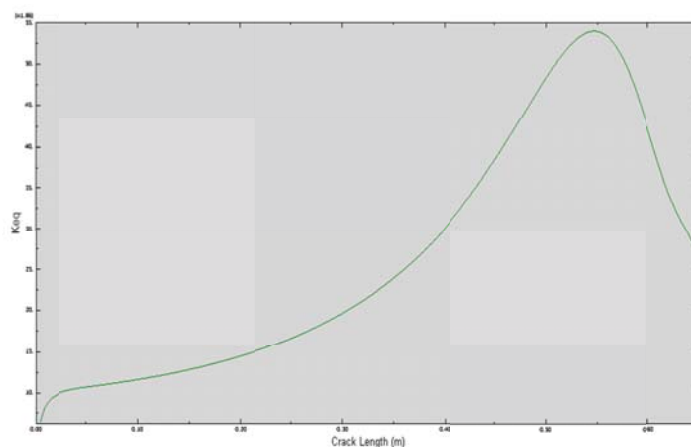


Figure 27 - K_{eq} VS Crack length

CONCLUSIONS

1. The fatigue durability of ship structural details is achieved not only by careful initial design but also by a proper construction and an effective inspection, maintenance and repair program.
2. FEM is a very cost- effective tool for structural analysis which saves a lot compared to physical model testing. However, FEM cannot substitute physical testing since the results from FEA should be verified by using physical models. However application of FEM reduces the number of physical models to be tested hence also the cost of the analysis.
3. The developed program is used for the fatigue analysis of a side connection of a tanker. It uses basic programming and features of ABAQUS software package. A more complicated and generic programs can be derived by applying the same methodology for the analysis of other models.
4. Crack propagation analysis for ship structural details helps scheduling the inspection programs (locations and period) for such parts of the ship, e.g. close-up survey for tankers.
5. Fatigue analysis of the ship connections and details is very important because designing a ship that would not suffer fatigue, i.e. in the case of $\Delta K \leq \Delta K_{th}$, is highly impractical. The lightweight of the ship will be then increased exponentially, reducing her deadweight. In addition, the added material will increase the initial cost of building the ship.
6. All of the above mentioned side effects could be avoided by carefully designing the ship structural details vulnerable to fatigue damage.
7. Immediate repair and docking delay the delivery of cargo and decrease the profit from this ship.
8. The ships that usually encounter fatigue problem are large tankers and bulk carriers. Hence, in the most extreme cases where the cracks are left without inspection or repair, the situation may lead to leakage of oil or hazardous fluids into the sea causing environmental problems.
9. Finally, the most effective way is to conduct an overall fatigue analysis for any new design of tankers or bulk carriers. As a result of such analysis the schedule of inspection of critical details can be determined. In this case, the high initial cost and loss of deadweight can be avoided, moreover the critical parts where fatigue cracks may occur are in advance determined

before their growing into catastrophic cracks. On the contrary, if fatigue analysis was not conducted, this may lead to cracks in different high - stressed spots. If the cracks are not repaired in a satisfactory manner, they may lead to damage of ship members

BIBLIOGRAPHY

1. B. Ayyub, et al. : Risk-informed inspection of marine vessels. Ship Structures Committee, SSC-421, 2002.
2. R. Bea: Maintenance of marine structures: A state of the art summary. DTIC Document1993.
3. C. C. Capanoglu: Fatigue Technology Assessment and Strategies for Fatigue Avoidance in Marine Structures. Ship Structure Committee (SSC), 1993.
4. T. Xu : Fatigue of ship structural details – Technical Development and Problems. Journal of Ship Research, vol. 41, pp. 318-331, 1997.
5. S. Moaveni: Finite element analysis: theory and application with ANSYS. Upper Saddle River, N.J.: Prentice Hall, 1999.
6. Y.-L. Lee: Fatigue testing and analysis: theory and practice. Amsterdam; Boston: Elsevier Butterworth-Heinemann, 2005.
7. J. Schijve: Fatigue of structures and materials. New York: Springer, 2008.
8. International Association of Classification Societies Ltd. (IACS) : Standard Wave Data . Recommendation 34, 2001.
9. Det Norske Veritas : Fatigue Strength Analysis of Offshore Steel Structures. (DNV) RP-C203 Recommended Practice-C203, 2001.
10. B. Farahmand, et al., Fatigue and fracture mechanics of high risk parts: application of LEFM & FMDM theory. New York: Chapman & Hall, 1997.
11. B. Farahmand : Fracture mechanics of metals, composites, welds, and bolted joints: application of LEFM, EPFM, and FMDM theory. Boston: Kluwer Academic Publishers, 2001.
12. S. Beden, et al.: Review of Fatigue Crack Propagation Models for Metallic Components. European Journal of Scientific Research, vol. 28, pp. 364-397, 2009.
13. H. A. Rothbart and T. H. Brown: Mechanical design handbook: measurement, analysis, and control of dynamic systems. 2nd Ed. New York: McGraw-Hill, 2006.
14. Det Norske Veritas : Fatigue Assessment of Ship Structures. (DNV) CN 30.7, 2010.
15. Dassault Systèmes Simulia Corp.: ABAQUS Analysis User's Manual. Dassault Systèmes Simulia Corp., 2008.
16. K. Ma and R. G. Bea: A Repair Management System for Fatigue Cracks in Ships. SNAME Transactions, vol. 103, pp. 343-369, 1995.
17. M. R. Andersen: Fatigue crack initiation and growth in ship structures. Ph. D Thesis, Department of Naval Architecture and Offshore Engineering, Technical University of Denmark, Lyngby, 1998.
18. Dassault Systèmes Simulia Corp.: ABAQUS Theory Manual. Dassault Systèmes Simulia Corp., 2008.
19. Registro Italiano Navale : Rules for the checking of the fatigue strength of ship hull structures. 1995.
20. A. Miranda, et al.: Path and life predictions under mixed mode I-Mode II complex loading. Paper presented at the International Symposium on Solid Mechanics, University of São Paulo, São Paulo, Brazil, 2007.

CONTACT WITH THE AUTHOR

Ahmed M H Elhewy

Naval Architecture and Marine Engineering Department
Faculty of Engineering
Alexandria University

e-mail: ahmed.elhewy@gmail.com

EGYPT

A METHOD FOR RELIABILITY ASSESSMENT OF STRUCTURAL COMPONENTS OF AIRCRAFT AND SEA-GOING SHIPS WITH TAKING INTO ACCOUNT A GIVEN FAILURE GENERATION MODEL

Henryk Tomaszek, Prof.

Mariusz Zieja, Ph. D.

Mariusz Ważny, Ph. D.

Air Force Institute of Technology, Poland

ABSTRACT

This paper presents a method for reliability assessment of structural components on the basis of diagnostic parameters recorded during operation of aircraft and sea going ships. It was assumed that a potential failure may simultaneously concerns surface wear process and fracture of an arbitrary structural component. In order to develop a reliability assessment model some elements of random walk theory were applied. This work covers surface wear density functions of a component. In the case of surface wear the model is based on a difference equation from which, after transformation, a Fokker-Planck partial differential equation was obtained. By solving the equation component's surface wear density function is achieved.

In the second part of the work a generalization of the model was made by introducing to it probability of disastrous fracture of a component. As a result, a generalized Fokker-Planck's equation was obtained. By making use of the equation, was obtained a relationship for assessment of reliability of a structural component in case when failure occurs due to surface wear with taking into account possible fracture of the component. In the end a numerical example which shows practical application of the developed method, is attached.

Keywords: bearing capacity factor, displacement, compression, tension, depth factor

INTRODUCTION

Assessment of reliability of structural components during operation of sea-going ships and aircraft is associated with prediction of their technical state. Such assessment is usually described by diagnostic parameters. A change in technical state is connected with change in values of diagnostic parameters [4,6,12,22]. Character of the loading of the structural components in the form of destructive processes causes changes in values of diagnostic parameters.

Wear, fatigue, corrosion, erosion and ageing processes have a decisive impact on changes in values of diagnostic parameters of mechanical components. The processes lead to changing the characteristics of structural components: geometrical, physical, strength etc [10,18,19,21]. Recognition of physics and analytical description of consequences of action of destructive processes is connected with many difficulties due to complexity of the problems associated with the considered issue. To ease description of consequences of action of destructive processes many different simplified mathematical models are often used [2,5,7,8,9,16,17].

This work is aimed at assessing reliability of a structural component subjected to wear processes in the form of loss in mass and changes in geometrical dimensions of the component which is additionally subjected to structural loads.

To assess reliability of structural component some elements of random walk theory were used.

The following assumptions are taken into account:

- Technical state of a structural component is determined by a single dominating diagnostic parameter „z” in the form of the deviation from its nominal value :

$$z = | X - X^{nom} | \quad (1)$$

where:

X - current value of diagnostic parameter,

X^{nom} - nominal value of diagnostic parameter.

- Load upon the component is of a pulse mode. Load impulses acting onto ship propulsion shafts or components of aircraft landing gear during landing operation, may serve as its example.

- Change in diagnostic parameter value takes place first of all during operation of sea-going ship or aircraft.
- The parameter „z” is non-decreasing.
- Value of deviation of the diagnostic parameter „z” determines a state of structural component reliability. If it is contained within the range $z \in [0, z_d]$ then it will be taken as fit for use. Otherwise it will be considered unfit for use.
- Measuring the diagnostic parameter deviation is made in a discrete system with the step h, where:

$$h = \frac{X_{nom}}{\hat{k}} \quad (2)$$

and, \hat{k} is appropriately selected.

- Deviation of the diagnostic parameter takes discrete values in the form:

$$z_k = k h, \quad (3)$$

where $k = 0, 1, 2, \dots$

- Schematic diagram of changes in values of the diagnostic parameter deviation along the time is presented in Fig. 1.

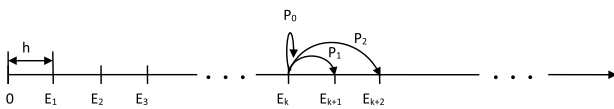


Fig.1 Schematic diagram of changes in the diagnostic parameter deviation

where:

E_k - component's state ($k = 0, 1, 2, \dots$),

P_i - occurrence probability of a change in component's state.

DETERMINATION OF WEAR DENSITY FUNCTION FOR STRUCTURAL COMPONENT OF SEA-GOING SHIP OR AIRCRAFT

As assumed in this work, the wearing of a mechanical device component is manifested by a loss in its mass and change in its linear dimensions. It was also assumed that the component is loaded, during operation, by random short-term impulses whose number, depending on time, is described by a process with the rate λ :

$$\lambda = \frac{P}{\Delta t} \quad (4)$$

where:

P - probability of using the component within the time interval Δt ,

Δt - time interval in which a load impulse occurs.

The impulse rate may be considered to be intensity of aircraft flights or sea-going ship voyages.

It can be assumed that:

$$(1 - \lambda \Delta t) + \lambda \Delta t \approx 1 \quad (5)$$

As a result of action of load impulses a discrete increase in values of wear takes place (it randomly occurs after the states $E_0, E_1, E_2, \dots, E_k, \dots$).

It is assumed that a single impulse can cause an increase of wear with an appropriate probability of occurrence, as follows:

0 - with the probability P_0 ;

h - with the probability P_1 ;

2h - with the probability P_2 .

If other possibilities are very low probable, then:

$$P_0 + P_1 + P_2 \approx 1 \quad (6)$$

Let $U_{k,t}$ means probability of the event that in the instant t deviation of diagnostic parameter reaches the state k. On the basis of these assumptions a difference equation which characterizes a way of growing the parameter deviation can be written [15] as follows :

$$U_{k,t+\Delta t} = (1 - \lambda \Delta t) U_{k,t} + \lambda \Delta t P_0 U_{k,t} + \lambda \Delta t P_1 U_{k-1,t} + \lambda \Delta t P_2 U_{k-2,t} \quad (7)$$

where:

$$(1 - \lambda \Delta t) + \lambda \Delta t P_0 + \lambda \Delta t P_1 + \lambda \Delta t P_2 \approx 1 \quad (8)$$

In functional description Eq. (7) takes the following form :

$$u(z, t + \Delta t) = (1 - \lambda \Delta t) u(z, t) + \lambda \Delta t P_0 u(z, t) + \lambda \Delta t P_1 u(z - h, t) + \lambda \Delta t P_2 u(z - 2h, t) \quad (9)$$

The difference equation (9) can be transformed into a partial differential equation by using the following approximation [14]:

$$\left. \begin{aligned} u(z, t + \Delta t) &\cong u(z, t) + \frac{\partial u(z, t)}{\partial t} \Delta t; \\ u(z - h, t) &\cong u(z, t) - \frac{\partial u(z, t)}{\partial z} h + \frac{1}{2} \frac{\partial^2 u(z, t)}{\partial z^2} h^2; \\ u(z - 2h, t) &\cong u(z, t) - \frac{\partial u(z, t)}{\partial z} 2h + \frac{1}{2} (2h)^2 \frac{\partial^2 u(z, t)}{\partial z^2}; \end{aligned} \right\} \quad (10)$$

On substitution of the approximation (10) into Eq. (9) the following is obtained:

$$\frac{\partial u(z, t)}{\partial t} = -\lambda(P_1 h + P_2 2h) \frac{\partial u(z, t)}{\partial z} + \frac{1}{2} \lambda(P_1 h^2 + P_2 (2h)^2) \frac{\partial^2 u(z, t)}{\partial z^2} \quad (11)$$

On taking the notation:

$$\begin{aligned} b &= P_1 h + P_2 2h \\ a &= P_1 h^2 + P_2 (2h)^2 \end{aligned} \quad (12)$$

the following can be written :

$$\frac{\partial u(z,t)}{\partial t} = -\lambda b \frac{\partial u(z,t)}{\partial z} + \frac{1}{2} \lambda a \frac{\partial^2 u(z,t)}{\partial z^2} \quad (13)$$

Eq. (7) has the form of Fokker-Planck equation.

A particular solution of Eq. (13) is searched, namely such one that fulfils the following conditions: when $t \rightarrow 0$, the solution converges to Dirac function, i.e. $u(z,t) \rightarrow 0$ for $z \neq 0$ and $u(0,t) \rightarrow +\infty$, but in the way that integral of the function u is equal to one for all the instants $t > 0$.

The solution of Eq. (13) with the above given condition is of the following form [20]:

$$u(z,t) = \frac{1}{\sqrt{2\pi a \lambda t}} e^{-\frac{(z-b\lambda t)^2}{2a\lambda t}} \quad (14)$$

The relationship (8) is the searched probability density function of structural component wearing due to action of randomly occurring damaging impulses.

As the number of impulses (aircraft landings) is described by the relation:

$$N = \lambda t \quad (15)$$

then the wear density function of structural component can be written in the form:

$$L = u(N_0, z_0; b, a) \prod_{k=0}^{n-1} u(N_k, z_k, N_{k+1}, z_{k+1}; b, a) \quad (16)$$

where:

bN - expected value of diagnostic parameter deviation in the instant t when the number of impulses equals N ;

aN - variance value of diagnostic parameter deviation up to the instant t when the number of impulses equals N .

In order to be able to make use of the density function (16) the parameters b and a should be first estimated. Data necessary to use Eqs. (12) not always are available. Another way to estimate the parameters is to apply the likelihood function which is represented by the following product [3,14]:

$$L = u(N_0, z_0; b, a) \prod_{k=0}^{n-1} u(N_k, z_k, N_{k+1}, z_{k+1}; b, a) \quad (17)$$

where:

$(z_0, z_1, z_2, \dots, z_n)$ stand for observed values of diagnostic parameter deviation from nominal value, for the numbers of load cycles $(N_0, N_1, N_2, \dots, N_n)$, respectively.

Estimation of the unknown parameters b and a is obtained by solving the following set of equations:

$$\left. \begin{aligned} \frac{\partial \log L}{\partial b} &= 0 \\ \frac{\partial \log L}{\partial a} &= 0 \end{aligned} \right\} \quad (18)$$

The appropriate calculation formulae achieve the following form:

$$b^* = \frac{z_n}{N_n} \quad (19)$$

$$a^* = \frac{1}{n} \sum_{k=0}^{n-1} \frac{[(z_{k+1} - z_k) - b^*(N_{k+1} - N_k)]^2}{(N_{k+1} - N_k)} \quad (20)$$

Having estimated the parameters b^* and a^* one can write the formula for device component reliability:

$$R(N) = \int_{-\infty}^{z_d} u(z, N) dz \quad (21)$$

where:

$u(z, N)$ - determined from Eq. (16)

z_d - permissible value of diagnostic parameter deviation.

A MODEL OF THE WEARING OF STRUCTURAL COMPONENT OF SEA-GOING SHIP OR AIRCRAFT WITH TAKING INTO ACCOUNT POSSIBILITY OF ITS SUDDEN DAMAGE (FRACTURE)

It is assumed that load applied to structural component produces its surface wear and simultaneously reaches such value that the component may suffer sudden damage (fracture occurs). Such possibility may be illustrated by the case of work of tyre of airplane during its hard landing.

Let:

Σ - stand for random variable of immediate strength of structural component, of the density function $g_1(\sigma)$,

W - stand for random variable of stress resulting from load impulse of the density function (Fig. 2).

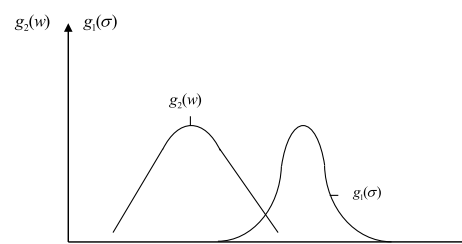


Fig. 2. Schematic diagram of load applied to the structural component of sea-going ship or aircraft

Immediate damage will take place when :

$$w - \sigma > 0 \quad (22)$$

where:

w and σ are realizations of the random variables W and Σ .

Therefore :

$$\aleph = W - \Sigma \quad (23)$$

The density function of the random variable \aleph can be determined from the relation:

$$f(\aleph) = \int_{C_1}^{C_2} g_1(w - \aleph) g_2(w) dw \quad (24)$$

where:

C_1, C_2 - limit values of stresses due to action of load impulse.

Occurrence probability of damage of structural component is as follows :

$$P_w = \lambda \Delta t Q \quad (25)$$

where:

$$Q = P\{W - \Sigma > 0\} = \int_0^{\infty} f(\aleph) d\aleph \quad (26)$$

The events which occur during wearing process and sudden damage, sum up to one.

Therefore,

$$(1 - \lambda \Delta t) + \lambda \Delta t P_0(1 - Q) + \lambda \Delta t P_1(1 - Q) + \lambda \Delta t P_2(1 - Q) + \lambda \Delta t Q \cong 1 \quad (27)$$

Let $U_{z,t}$ stand for probability of the event that in the instant „t” the component wear deviation is equal to „z”. By making use of Eq. (27) the following difference equation can be written:

$$U_{z,t+\Delta t} = (1 - \lambda \Delta t)U_{z,t} + \lambda \Delta t P_0(1 - Q)U_{z,t} + \lambda \Delta t P_1(1 - Q)U_{z-h,t} + \lambda \Delta t P_2(1 - Q)U_{z-2h,t} \quad (28)$$

In functional description Eq. (28) takes the following form:

$$u(z,t + \Delta t) = (1 - \lambda \Delta t)u(z,t) + \lambda \Delta t P_0(1 - Q)u(z,t) + \lambda \Delta t P_1(1 - Q)u(z-h,t) + \lambda \Delta t P_2(1 - Q)u(z-2h,t) \quad (29)$$

By taking into account the relations (10) Eq. (29) can be transformed to the form :

$$u(z,t) + \frac{\partial u(z,t)}{\partial t} \Delta t = (1 - \lambda \Delta t)u(z,t) + \lambda \Delta t P_0(1 - Q)u(z,t) + \lambda \Delta t P_1(1 - Q)\left(u(z,t) - h \frac{\partial u(z,t)}{\partial z} + \frac{1}{2} h^2 \frac{\partial^2 u(z,t)}{\partial z^2}\right) + \lambda \Delta t P_2(1 - Q)\left(u(z,t) - 2h \frac{\partial u(z,t)}{\partial z} + \frac{1}{2} (2h)^2 \frac{\partial^2 u(z,t)}{\partial z^2}\right) \quad (30)$$

Therefore:

$$u(z,t) + \frac{\partial u(z,t)}{\partial t} \Delta t = [(1 - \lambda \Delta t) + \lambda \Delta t P_0(1 - Q) + \lambda \Delta t P_1(1 - Q) + \lambda \Delta t P_2(1 - Q)]u(z,t) + [\lambda \Delta t P_1(1 - Q)h + \lambda \Delta t P_2(1 - Q)2h] \frac{\partial u(z,t)}{\partial z} + \frac{1}{2} [\lambda \Delta t P_1(1 - Q)h^2 + \lambda \Delta t P_2(1 - Q)(2h)^2] \frac{\partial^2 u(z,t)}{\partial z^2} \quad (31)$$

Now, $u(z,t)$ is added to and distracted from the right hand side of Eq. (31). Instead of one at $(-u(z,t))$, the relation (27) is substituted. On simplification the following is obtained :

$$\frac{\partial u(z,t)}{\partial t} \Delta t = -\lambda \Delta t Q u(z,t) - [\lambda \Delta t P_1(1 - Q)h + \lambda \Delta t P_2(1 - Q)2h] \frac{\partial u(z,t)}{\partial z} + \frac{1}{2} [\lambda \Delta t P_1(1 - Q)h^2 + \lambda \Delta t P_2(1 - Q)(2h)^2] \frac{\partial^2 u(z,t)}{\partial z^2} \quad (32)$$

Dividing by Δt one obtains:

$$\frac{\partial u(z,t)}{\partial t} = -\lambda Q u(z,t) - (\lambda P_1(1 - Q)h + \lambda P_2(1 - Q)2h) \frac{\partial u(z,t)}{\partial z} + \frac{1}{2} (\lambda P_1(1 - Q)h^2 + \lambda P_2(1 - Q)(2h)^2) \frac{\partial^2 u(z,t)}{\partial z^2} \quad (33)$$

By substituting the notations:

$$c = \lambda Q \\ \hat{b} = \lambda(1 - Q)(P_1 h + P_2 \cdot 2h) = \lambda(1 - Q)b \\ \hat{a} = \lambda(1 - Q)(P_1 h^2 + P_2 (2h)^2) = \lambda(1 - Q)a \quad (34)$$

the following equation is finally achieved:

$$\frac{\partial u(z,t)}{\partial z} = -cu(z,t) - \hat{b} \frac{\partial u(z,t)}{\partial z} + \frac{1}{2} \hat{a} \frac{\partial^2 u(z,t)}{\partial z^2} \quad (35)$$

Eq. (35) is more general than Fokker-Planck equation. Like in the case of Fokker-Planck equation, is searched a particular solution which fulfils the following conditions:

when $t \rightarrow 0$ the solution converges to Dirac's function, i.e. $u(z,t) \rightarrow 0$ for $z \neq 0$ and $u(0,t) \rightarrow +\infty$, but in such way that integral of the term of the function which contains z is equal to one for all $t > 0$.

The solution of Fokker-Planck equation (i.e. that without the term „-cu(z,t)”), for the above specified condition, has the following form [15]:

$$\bar{u}(z,t) = \frac{1}{\sqrt{2\pi\lambda(1-Q)at}} e^{-\frac{(z-\lambda(1-Q)bt)^2}{2\lambda(1-Q)at}} \quad (36)$$

or

$$\bar{u}(z,N) = \frac{1}{\sqrt{2\pi(1-Q)aN}} e^{-\frac{(z-(1-Q)bN)^2}{2(1-Q)aN}} \quad (37)$$

Hence the solution of Eq. (35) will achieve the following form [15]:

$$u(z,t) = e^{-ct} \bar{u}(z,t) \quad (38)$$

In order to prove that the above given relation is just the searched solution of Eq. (35) the following transformation can be offered:

$$\begin{aligned} \frac{\partial u(z,t)}{\partial t} &= -c e^{-ct} \bar{u}(z,t) + e^{-ct} \frac{\partial \bar{u}(z,t)}{\partial t} = \\ &= -c u(z,t) + e^{-ct} \left(-\hat{b} \frac{\partial \bar{u}(z,t)}{\partial z} + \frac{1}{2} \hat{a} \frac{\partial^2 \bar{u}(z,t)}{\partial z^2} \right) = \\ &= -c u(z,t) - \hat{b} \frac{\partial u(z,t)}{\partial z} + \frac{1}{2} \hat{a} \frac{\partial^2 u(z,t)}{\partial z^2} \end{aligned} \quad (39)$$

The following density function is the solution of Eq. (35):

$$u(z,t) = \lambda e^{-\lambda t} \bar{u}(z,t) \quad (40)$$

where:

$$\int_0^{\infty} \int_{-\infty}^{\infty} \lambda e^{-\lambda t} \bar{u}(z,t) dz dt = 1$$

The presented transformation (39) is also valid in case it is applied to the relation (40).

ASSESSMENT OF STRUCTURAL COMPONENT RELIABILITY IN THE ASPECT OF WEAR WITH SIMULTANEOUSLY POSSIBLE SUDDEN DAMAGE

Causes of structural component failures in the form of wear and disastrous fracture, in the sense of reliability, form a series structure. It can be assumed that a structural component is built from "two components". One is subjected to wear and the other is put under structural load. The system is in serviceable state when all its components are in serviceable state, and the system is in non-serviceable state when at least one of its components is damaged.

Hence the reliability of structural component of sea-going ship or aircraft is described by the relation as follows [1,11,13]:

$$R(t) = R_1(t)R_2(t) \quad (41)$$

where:

$$\begin{aligned} R_1(t) &= e^{-ct} \\ R_2(t) &= \int_{-\infty}^{z_d} \bar{u}(z,t) dz \end{aligned}$$

z_d - value of diagnostic parameter deviation permissible for safety reasons,

$\bar{u}(z,t)$ - density function of the deviation, determined by the relation (36) or (37).

Eq. (41) can be written in the form:

$$R(t) = e^{-ct} \int_{-\infty}^{z_d} \bar{u}(z,t) dz \quad (42)$$

where:

$$\bar{u}(z,t) = \frac{1}{\sqrt{2\pi \lambda(1-Q)\Delta t}} e^{-\frac{(z-(1-Q)b\lambda t)^2}{2(1-Q)a\lambda t}}$$

And, unavailability of an component is:

$$\hat{Q}(t) = 1 - e^{-ct} \int_{-\infty}^{z_d} \bar{u}(z,t) dz \quad (43)$$

Density function of failures can be determined in the following way:

$$f(t) = \frac{\partial}{\partial t} \hat{Q}(t) \quad (44)$$

Hence:

$$\begin{aligned} f(t) &= -[(-c e^{-ct} \int_{-\infty}^{z_d} \bar{u}(z,t) dz) + e^{-ct} \frac{d}{dt} \int_{-\infty}^{z_d} \bar{u}(z,t) dz] \\ f(t) &= c e^{-ct} \int_{-\infty}^{z_d} \bar{u}(z,t) dz - e^{-ct} \frac{d}{dt} \left(1 - \int_{z_d}^{\infty} \bar{u}(z,t) dz \right) \\ f(t) &= c e^{-ct} \int_{-\infty}^{z_d} \bar{u}(z,t) dz + e^{-ct} \frac{d}{dt} \int_{z_d}^{\infty} \bar{u}(z,t) dz \end{aligned} \quad (45)$$

Making use of the work [20] one can write the following:

$$\frac{d}{dt} \int_{z_d}^{\infty} \bar{u}(z,t) dz = \frac{z_d + (1-Q)b\lambda t}{2t} \frac{1}{\sqrt{2\pi(1-Q)a\lambda t}} e^{-\frac{(z_d - (1-Q)b\lambda t)^2}{2(1-Q)a\lambda t}} \quad (46)$$

Therefore it can be written :

$$f(t) = c e^{-ct} \int_{-\infty}^{z_d} \bar{u}(z,t) dz + e^{-ct} \cdot \frac{z_d + (1-Q)b\lambda t}{2t} \cdot \frac{1}{\sqrt{2\pi(1-Q)a\lambda t}} e^{-\frac{(z_d - (1-Q)b\lambda t)^2}{2(1-Q)a\lambda t}} \quad (47)$$

On the basis of the determined reliability and density function for structural component its failure rate can be determined as follows:

$$\chi(t) = \frac{f(t)}{R(t)} \quad (48)$$

where: $f(t)$ - as described by Eq. (45) and $R(t)$ - as described by Eq. (42).

Making use of the failure rate according to Eq. (48) one can write the following formula for the reliability of a structural component of aircraft or sea going ship in the assumed failure generation conditions , as follows:

$$R(t) = e^{-\int_0^t \chi(w) dw} \quad (49)$$

A NUMERICAL EXAMPLE OF RELIABILITY ASSESSMENT

In the below presented example a fragment of an aircraft tyre (Fig. 3) was taken into consideration. In the process of operation wear of tyre tread takes place during starts and landings of airplane. Aircraft tyre is also subjected to structural loads and during hard landing it may undergo sudden damage.

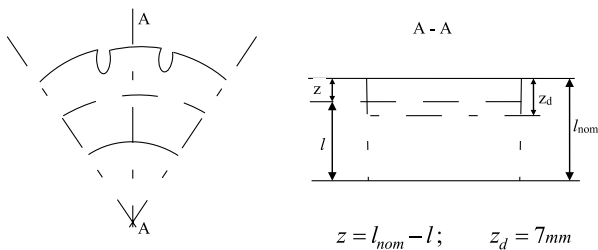


Fig. 3. Cross-section of a tyre fragment

- l_{nom} - nominal thickness of tyre tread,
- l - current thickness of tyre tread,
- z - current wear of tyre tread,
- z_d - permissible wear of tyre tread.

For the assessment of aircraft tyre reliability Eq. (42) was applied:

$$R(N) \cong e^{-QN} \int_{-\infty}^{z_d} \frac{1}{\sqrt{2\pi(1-Q)aN}} e^{-\frac{(z-(1-Q)bN)^2}{2(1-Q)aN}} dz$$

Hence, after normalization :

$$R(N) = e^{-QN} \cdot \frac{1}{\sqrt{2\pi}} \int_{-\infty}^{\frac{(z_d-(1-Q)bN)}{\sqrt{(1-Q)aN}}} e^{-\frac{\chi^2}{2}} dx \quad (50)$$

For the reliability assessment in accordance with Eq. (50) the following data were selected [20]:

- $b = 0,0166$
- $a = 0,00051$
- $Q = 0,00001$
- $z_d = 7 \text{ mm}$

Tab. 1 and Fig. 4. present results of the calculations performed with the use of the following relations:

$$\beta(N) = \frac{z_d - (1-Q)bN}{\sqrt{(1-Q)aN}} \quad (51)$$

$$R_1(N) = e^{-QN} \quad (52)$$

$$R_2(N) = \frac{1}{\sqrt{2\pi}} \int_{-\infty}^{\beta(N)} e^{-\frac{\chi^2}{2}} dx \quad (53)$$

Tab. 1. Reliability of the considered aircraft tyre

N	20	50	100	150	200	250	300	350	400	450	500
$\beta(N)$	66,023	38,638	23,646	16,306	11,523	7,982	5,164	2,817	0,797	-0,981	-2,574
$R_1(N)$	1	1	1	1	1	1	1	0,998	0,787	0,163	0,005
$R_2(N)$	1	1	0,999	0,999	0,998	0,998	0,997	0,997	0,996	0,996	0,995
$R(N)$	1	1	0,999	0,999	0,998	0,998	0,997	0,995	0,784	0,162	0,005

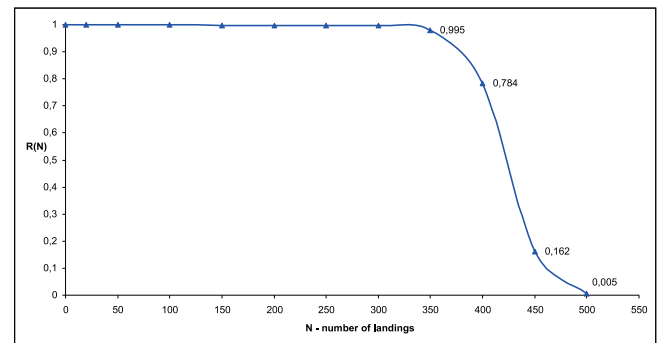


Fig. 4. Reliability of the considered aircraft tyre

FINAL REMARKS

The modelling of wear of structural components which are subjected to different modes of failure generation, requires to make use of test results acquired from operational processes of sea-going ships and aircraft. The more accurate and complete the results of tests of structural components in operation, the more precise and complex the developed formulae for assessment of their reliability. In this work relatively simple assumptions as to operational conditions of structural component, were accepted. It was assumed that wear and fatigue processes may take place simultaneously. Mechanisms of wear and destruction of structural components of sea-going ships and aircraft are complex as a result of complicated environment in which they operate. From the scientific point of view , are very interesting models which take additionally into account fatigue fracture processes occurring in structural components. The presented reliability assessment method with the use of random walk theory should be further perfected by taking into account more accurate models of wear and fatigue processes occurring in structural components.

BIBLIOGRAPHY

1. Baranowski P., Małachowski J.: Numerical study of selected military vehicle chassis subjected to blast loading in terms of tyre strength improving. *Bulletin of The Polish Academy of Sciences: Technical Sciences*. Vol. 63, No 4, 2015, pp. 867 – 878.
2. Casciati F., Roberts B.: *Mathematical Models for Structural Reliability Analysis*. Boca Raton/New York/London/Tokyo: CRC Press, 1996.
3. DeLurgio SA.: *Forecasting principles and applications*. University of Missouri-Kansas City. Irwin/McGraw-Hill, 1998.
4. Dhillon BS.: *Design Reliability. Fundamentals and Applications*. Ottawa: Boca Raton/New York/London/Washington: CRC Press 1999.
5. Girtler J., Ślęzak M.: Four-state stochastic model of changes in the reliability states of a motor vehicle. *Eksploatacja i Niezawodność – Maintenance and Reliability*. Vol. 15, No 2, 2013, pp. 156 – 160.
6. Girtler J.: Identification of damages of tribological associations in crankshaft and piston systems of two-stroke internal combustion engines used as main propulsion in sea-going vessels and proposal of probabilistic description of loads as causes of these damages. *Polish Maritime Research*. Vol. 22, No 2, 2015, pp. 44 – 54.
7. Girtler J.: The semi-Markov model of the process of appearance of sea-going ship propulsion system ability and inability states in application to determining the reliability of these systems. *Polish Maritime Research*. Vol. 20, No 4(80), 2013, pp. 18 – 24.
8. Grabski F.: Semi-Markov failure rates processes. *Applied mathematics and computation*. Vol. 217, No 24, 2011, pp. 9956-9965.
9. Gucma S., Slaczka W.: Methods for optimization of sea waterway systems and their application. *Polish Maritime Research*. Vol. 22, No 3, 2015, pp. 14 – 19.
10. Idziaszek Z., Grzesik N.: Object characteristics deterioration effect on task realizability – outline method of estimation and prognosis. *Eksploatacja i Niezawodność - Maintenance and Reliability*. Vol. 16, No 3, 2014, pp. 433-440.
11. Jodejko-Pietruczuk A., Werbinska-Wojciechowska S.: Analysis of maintenance models' parameters estimation for technical systems with delay time. *Eksploatacja i Niezawodność - Maintenance and Reliability*. Vol. 16, No 2, 2014, pp. 288-294.
12. Korczewski Z.: Analysing the potential for application of the phase shift method in endoscopic examination of marine engines. *Polish Maritime Research*. Vol. 20, No 1, 2013, pp. 23 – 30.
13. Nowakowski T., Tubis A., Werbinska-Wojciechowska S.: *Maintenance Decision Making Process - A Case Study of Passenger Transportation Company. Theory and engineering of complex systems and dependability. Advances in Intelligent Systems and Computing. Proceedings of the Tenth International Conference on Dependability and Complex Systems DepCoS-RELCOMEX*. Vol. 365, 2015, pp. 305-318.
14. Pham H.: *Handbook of Engineering Statistics*. London: Springer-Verlag 2006.
15. Risken H.: *The Fokker-Planck Equation. Methods of Solution and Applications*. Springer Verlag, 1984.
16. Rudnicki J.: Application issues of the semi-markov reliability model. *Polish Maritime Research*. Vol. 22, No 1, 2015, pp. 55 – 64.
17. Rudnicki J.: The time of the first transition of the semi-Markov process in the evaluation of diesel engine operation. *Combustion Engines*. Vol. 145, No 2, 2011 (145), pp. 89-98.
18. Tomaszek H., Jaształ M., Zieja M.: A simplified method to assess fatigue life of selected structural components of an aircraft for a variable load spectrum. *Eksploatacja i Niezawodność - Maintenance and Reliability* 2011; 4: 29-34.
19. Tomaszek H., Jaształ M., Zieja M.: Application of the Paris formula with $m=2$ and the variable load spectrum to a simplified method for evaluation of reliability and fatigue life demonstrated by aircraft components. *Eksploatacja i Niezawodność - Maintenance and Reliability* 2013; 15(4): 297-304.
20. Tomaszek H., Żurek J., Jaształ M.: Prediction of failures endangering safety of aircraft operation (in Polish). *Wydawnictwo Naukowe Instytutu Technologii Eksploatacji, Warszawa* 2008.
21. Woch M., Kurdelski M., Matyjewski M.: Reliability at the checkpoints of an aircraft supporting structure. *Eksploatacja i Niezawodność – Maintenance and Reliability*. Vol. 17, No 3, 2015, pp. 457 – 462.
22. Żurek J., Tomaszek H., Zieja M.: Analysis of structural component's lifetime distribution considered from the aspect of the wearing with the characteristic function applied. *Safety, Reliability and Risk Analysis: Beyond the Horizon*. CRC Press/Balkema, Taylor & Francis Group, 2014: p. 2597-2602.

CONTACT WITH THE AUTHORS:

Henryk Tomaszek
Instytut Techniczny Wojsk Lotniczych
ul. Księcia Bolesława 6
01-494 Warszawa
Polska

e-mail: poczta@itwl.pl

Mariusz Zieja
Instytut Techniczny Wojsk Lotniczych
ul. Księcia Bolesława 6
01-494 Warszawa
Polska

e-mail: mariusz.zieja@itwl.pl

Mariusz Ważny
Instytut Techniki Lotniczej
Wojskowa Akademia Techniczna
ul. Kaliskiego 2
00-908 Warszawa
Polska

e-mail: mwazny@wat.edu.pl

DEPTH IMAGES FILTERING IN DISTRIBUTED STREAMING

Tomasz Dziubich, Assoc. Prof.

Julian Szymański, Assoc. Prof.

Adam Brzeski, M. Sc.

Jan Cychnerski, M. Sc.

Waldemar Korłub, M. Sc.

Gdańsk University of Technology, Poland

ABSTRACT

In this paper, we propose a distributed system for point cloud processing and transferring them via computer network regarding to effectiveness-related requirements. We discuss the comparison of point cloud filters focusing on their usage for streaming optimization. For the filtering step of the stream pipeline processing we evaluate four filters: Voxel Grid, Radial Outliner Remover, Statistical Outlier Removal and Pass Through. For each of the filters we perform a series of tests for evaluating the impact on the point cloud size and transmitting frequency (analysed for various fps ratio). We present results of the optimization process used for point cloud consolidation in a distributed environment. We describe the processing of the point clouds before and after the transmission. Pre- and post-processing allow the user to send the cloud via network without any delays. The proposed pre-processing compression of the cloud and the post-processing reconstruction of it are focused on assuring that the end-user application obtains the cloud with a given precision.

Keywords: point cloud processing, distributed system, parallel processing, depth image filtering

INTRODUCTION

Underwater (UW) imagery presents several challenging problems for automated remote target recognition. One of them is the development of real-time data processing methods. We can divide these methods into two groups. The first of them includes methods running in a local execution environment (located on an autonomous device/object/vehicle) and the second group include techniques that operate in a remote processing centre on locally acquired data (so called client-server model). In both cases, the researchers focus on providing real-time services for underwater facilities products and delivering an efficient and high-performance parallel computation platform.

Nowadays LIDAR sensors in autonomous inspection of UW activities are becoming increasingly popular. This technique often supports acoustic signals analysis which is still a dominant technique in the UW solutions. The combination of both methods is called a multi-modal approach. It assures better measurement precision, reduction in risks, economic benefits and superior data products compared to conventional means.

An example of such a solution is an underwater camera system with a laser line source to measure seafloor features at a millimetre scale [1]. The quality of underwater photography is limited by the visibility of the water column. In real underwater environments there are always floating particles that scatter

the light. As a result, photographic images taken under such conditions tend to be blurred. Consequently, series of image filters and transformation need to be applied in order to achieve better quality. Measurements show, that the error rate of this solution is less than 1.5 mm when the target is scanned from a distance of 1 m. One of the disadvantages of the described method is low computation efficiency (ca. 5 fps). System performance decreases if we apply additional image filters.

Another example is the DP2TM 3D LiDAR built-in the Marlin Autonomous Underwater Vehicle for detection and localization of structural changes vs. reference model [8]. This device has better parameters than the solution mentioned above (performance of 3D imaging ca. 10 fps, higher resolution > 0.040 Mpx, and different range > 3Km). It can also operate in degraded visual environments and requires dual scans for 100% data validation. This solution was deployed in water depths of 50 - 3,000 meters with measurements distances varying from 6 - 90 meters.

3D LiDAR can not only distinguish between shapes and objects, but detects moving objects as well. This means that it is possible to acquire data of moving seafloor hydrothermal plumes or oil spills. 10fps real-time detection enables even measurement of the space between a number of objects and their speed. Another characteristic of the 3D measurement is the ability to see data in a 3D environment, from a head-on perspective, the bird's eye view or any other.

In [11] authors present a methodology that utilizes visual cues in multi-modal optical and sonar images, namely, the occluding contours of various scene objects that can be detected and matched more robustly than point features. Unfortunately, the use of this method in AUV is possible in very limited range due to computing power.

Data obtained from LIDARs can be stored using data structures referred to as Point Clouds, which allows storing points along with additional information. It can also store colour or size, depending on the implementation of the structure. The points stored in the Point Clouds can be very often considered as not connected voxels (three-dimensional pixels) and they can be used for objects visualization.

Rusu and Cousins [10] have called point cloud a high quality representation of the world. Generally, this statement referred to clouds obtained from LIDAR scanners, but it can be used to describe any point cloud received from a depth sensor, which is able to acquire data of the observed world. Obviously, the scale of the represented view of the world may differ. One of listed in [10] cloud advantages is the fact, that space robots will “see” the world in 3D in the future. Theoretically, it is already possible with PCL. In [3, 14] authors managed to represent an entire city using a single point cloud. For example, an aerial scan with a spatial resolution of 7 cm of the city of Munich, roughly containing 200.000 individual buildings and being spread over about 300 km². In this case the total raw data size consists of 61*10⁹ points (approx. 180 TB) [14]. In the case of point-cloud shape detection for city-modelling, the large dataset needs to be processed in parallel. It can be assumed, that each building consists of only 6 individual faces with a total surface area of approximately 1000 m², resulting in about 32000 points per primitive shape. One of the problems of the merging process for providing the point cloud data (PCD) is to assure high performance of the system, especially in parallel and distributed environments.

To process huge amount of data we need to ensure high computing power with a stable level of energy consumption. We can achieve this aim using a pipeline model in a parallel computer system. In real-time 3D data acquisition systems with motion detection and recognition feature an efficient processing pipeline has to be tailored to used hardware. Currently, using a multi-core and many-core computer architectures as NVidia CUDA and Intel Xeon Phi real-time data processing is most common. However software for these architecture has to be very sophisticated.

In this paper we propose a distributed pipeline used for point cloud processing and transferring them using computer network that fulfil requirements related to their effectiveness.

PCD DATA FLOW

Point cloud processing pipeline can be divided into the following steps shown in Fig. 1:

- Cloud acquisition (depth image obtaining, point cloud building).
- Pre-processing (filtering – cutting off, reducing the noise and the point cloud size, compression).
- Network transmission.

After that, the second node also has to process the frame. The second part of the pipeline is the same as on the first (input) machine, but the acquisition is different:

- Depth image obtaining – getting a depth image from local sensor and from remote sensor via network,
- Point cloud building – depth image to point cloud conversion (optional).

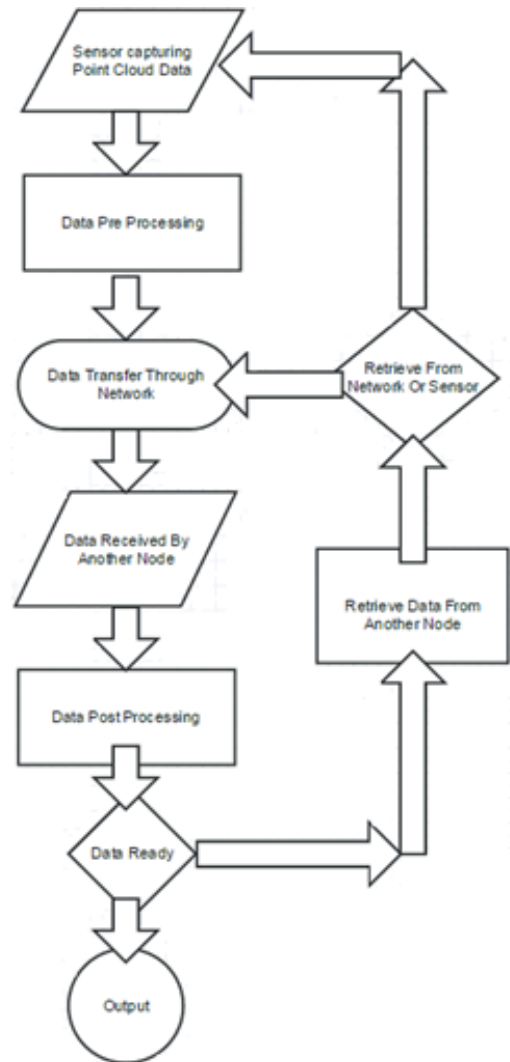


Fig. 1. Dataflow in parallel point clouds processing

Existing systems often focus on a part of the actual problem, instead of all of the sub-problems related to the processing. In this paper we divide those problems into several parts. These groups can be considered as potential stages mapped from processing pipeline: the cloud is grabbed and then pre-processed – filtered so that only interesting points can be found in the cloud. Then, such cloud should be optionally compressed, if the first stage is insufficient. Next the cloud is sent via network.

The last stage – the reconstruction is the opposite stage to the filtering and compression. The networking stage should be transparent for the end user, the cloud should be visually (almost) identical with the data received from the sensor (it does not apply to e.g. background subtraction filters).

Hence, if during pre-processing any significant or necessary points were removed, reconstruction is required. Otherwise, this step may be skipped.

Generally, filtering is needed almost in all applications that employ depth cameras. In our experiments we used the Kinect sensor as a depth camera. The error of information provided by Kinect increases with an object distance from the sensor. What is more, the factor of this growth is square [13].

For some projects the accuracy of depth image data may be crucial. For the expected solution described in this paper the accuracy is not so important, since it can be assumed, that the end-user (e.g. application that gets point clouds provided by the system) may use their own filters in order to increase accuracy. A comparison of depth sensors were provided e.g. in [4].

Thumbunpeng et al. [12] were trying to use depth camera to measure the proportion between burn area of human body and the body surface. They wanted to provide an alternative method for eye estimation, since the quality of the estimation highly influences the treatment efficiency (patients need to get the proper doses of water depending on calculated area). They decided to use spatial filters in order to reduce camera error and distortions, and proved, that the proposed solution increases the quality of cloud surface significantly.

In literature, some authors also design dedicated filtering and compression algorithms. E.g. in [2], authors proposed Enhanced Vector Quantization (EVQ) algorithm, an enhanced version of standard EQ algorithm. EVQ reduces disadvantages of similar approaches and is easy to use, requiring only to set the compression level. The goal of this work was to create an appropriate model for building a mesh.

In [9] authors focus on point cloud filtering as a pre-processing stage in robotics learning. They decided to use Growing Neural Gas network, and to prove that this method can be more effective than e.g. Voxel Grid filter.

Wenming et al. proposed their own algorithm for point cloud processing [15], dedicated for cloud de-noising. As in many algorithms, they proposed to divide the cloud into a grid and then de-noise it using neighbourhood distance calculations. As they report this algorithm is very simple and easy to implement. In comparison to bilateral mesh de-noising algorithm, the proposed one seems to be much more promising.

In [5] authors propose an algorithm for filtering LiDAR point clouds. Their main goal was to remove any objects like buildings, leaving territory malformations intact. Interestingly, the algorithm works also on mountainous territories – all buildings are removed while the territory remains intact. That would allow to create e.g. physical maps. Despite this algorithm was invented for LiDAR point clouds to filter territory surfaces, that would be used also in other fields – e.g. in de-noising of general surfaces of observed objects, but this idea would require further research.

In [7] a different approach to surface de-noising has been shown. Since the goal of a large number of algorithms is to make surfaces smooth, the authors attempt to preserve features of the cloud. This may be important for creating e.g. point clouds of some historical objects with carved details, like inscriptions. In order to achieve this, they create

smooth surfaces using standard algorithms, additionally preserving extra data like high vectors – distance between old and smoothed position. Then, vectors of neighbouring points are compared and new positions are calculated. Despite some limitations of the algorithm, the authors achieved the expected result. Nevertheless, this approach may not be relevant in the presented work, since probably the smallest details will be lost in order to perform optimization.

FILTERS IN POINT CLOUD PROCESSING

There exists a wide range of filters. The most popular are listed below:

- Pass Through – enables cutting off point cloud parts,
- Voxel Grid – allows to replace a set points with a mean point,
- Points projecting – allows to project points onto e.g. plane,
- Indices extracting – uses segmentation algorithm to extract inliers,
- Conditional removal – removes points which does not meet given conditions,
- Statistical Outlier Removal – deletes outliers,
- Radius Outlier Removal – deletes outliers,
- Spatial filter – performs a cloud smoothing,
- Growing Neural Gas network (GNG) – allows to down sample the cloud (similarly to Voxel Grid),
- Enhanced Vector Quantization (EVQ) – allows to down sample the cloud.

Technically, the filters that do not perform down sampling or removing points should be rejected, since they do not resolve the problem addressed in the paper. Moreover, filters should be widely available and allow to process clouds in real-time. The first condition makes indices extracting and spatial filters not useful. GNG and EVQ algorithms seem to be promising, but they are not widely available, since they are novel procedures. It makes them hard to use and to implement in an optimized version. What is more, the results they produce are very similar to Voxel Grid filter. Considering the fact that they may need some kind of initialization [5] (which depreciates their use in changing environment) and that the better results may influence the computational time [9], only Voxel Grid algorithm will be considered from this group. Another group of filters are Outlier Removal filters. They can increase the quality of the cloud reducing their size, so they have to be taken into consideration. What's more, they are well known and easy to use, so they set up good baseline for evaluation. They do not require any kind of initialization (but may need one additional iteration for calculating e.g. some mean values). The last group enables removal points under given conditions, and here Conditional Removal filter seems be very promising. However, Conditional Removal is a general concept and typically it is based on a Pass Through filter (which may be considered a special case of Conditional Removal). Thus we select from this group the Pass Through filter for testing. Some of the filters are not useful for optimization purposes, while alternative ones have other disadvantages.

Our review allows us to select four most important, popular and promising filters that have been chosen for evaluation, namely: Pass Through, Voxel Grid, Statistical and Radial Outlier Removal.

Voxel, which is a group of cube units distributed in the centre of the orthogonal grid, can be understood as the extension of two-dimensional pixel into three-dimensional space. The point cloud data generated by a computer vision method is usually density-uneven. It samples by the voxel grid method and creates 3D voxel grid for the input point cloud data, with centroid of all the points in voxel to approximate the other points, all of which can not only reduce the point cloud data, but also maintain the shape characteristics of point cloud and more accurate approximation of the surface. All points in the voxel are expressed with a centroid, then:

$$\bar{x} = \frac{1}{S} \sum_{x,y,z \in V} x, \quad \bar{y} = \frac{1}{S} \sum_{x,y,z \in V} y, \quad \bar{z} = \frac{1}{S} \sum_{x,y,z \in V} z$$

where S is the total number of discrete points in voxel V, x, y, z are dimensions of voxel (referred to as leaf).

The PassThrough filter removes points that lie outside a given range for the specified user-given dimension. For example, if all points laying farther than 3 m away have to be discarded, the filter would have to be run on the Z coordinate with a range of [0; 3 m]. This filter can be useful to discard unneeded objects from the cloud, but a different reference frame may have to be adapted if the default one (relative to the sensor) is inappropriate. For example, filtering on the Y value to remove all points not laying on a given surface will yield unwanted results if the camera is at an odd angle. So we define visibility range as $R = \langle 0; z_{\max} \rangle$, where z_{\max} is the maximal depth of voxel from the camera plan.

Outliers are single points that are spread through the cloud. They are the product of the sensor's inaccuracy, which inappropriately registers measurements from empty space. Outliers are considered undesired noise, because they may introduce calculation errors, e.g. in normal estimation. Hence, removing the points from the cloud will not only make the computations faster, but also more precise. The radius-based outlier removal is the simplest method of this type. First, search radius r must be specified as well as the minimum number of neighbours K that a point should have to avoid being labelled as outlier. The algorithm will then iterate through all of the points (which can be extremely slow in if the cloud is big) and perform the check: if less than that the given number of the points are found within the radius, the point is removed.

The statistical outlier removal process is a more advanced method. First, for every point the mean distance to its K neighbours is computed. Then, assuming that the result is a Gaussian distribution with a mean μ and a standard deviation σ , all points with mean distances falling out of the global mean plus deviation are removed. It performs statistical analysis of the distances between neighbouring points, and trims all which are not considered "normal" (which is a parameter of

the algorithm). In further part of paper we assign symbol K to the number of neighbours to analyse for each point and m to the standard deviation multiplier.

TESTS

The test system was implemented in a way that the results could be kept as accurate as possible, relative, and insensitive to environment changes.

The application takes as input the data from Kinect cameras (up to 8) - RGB video stream with a monochrome depth video stream [6]. The stream specification is as follows:

- each point is represented on 9 bytes, 6 which describe coordinates in 3D space and 3 represent RGB colour. Every frame contains 640x480 points (the VGA normal resolution), resulting in 2 764 800 bytes of data. Multiplied by 30 frames per second, the result is 82 944 000 bytes/sec, which is equal to 79.1 megabytes per second,
- frame output of the camera is 640x480 (VGA),
- frame output can be imposed, in our research 30 frames per second was assumed.

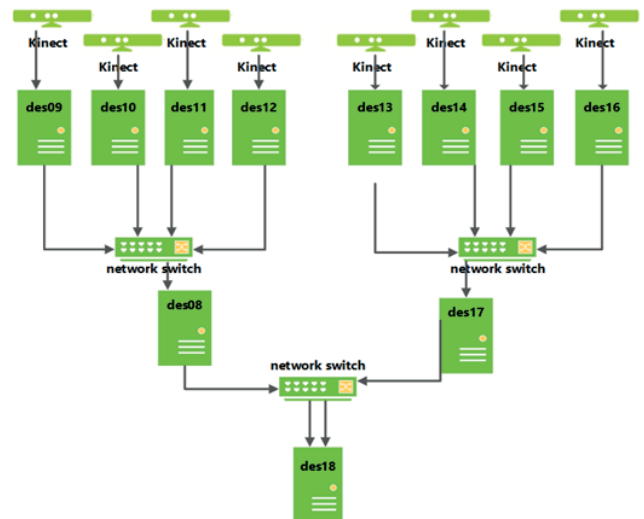


Fig. 2. The schematic of the test environment

The output of the application is a merged point cloud. It is released only after the input from every camera was fully delivered to the final node.

The tests were run for different numbers of cameras (2-8), for one point cloud resolution (see Fig. 2). We were able to observe the delay that was caused both by cloud processing and sending it to next node. The limitation of the system is implied by the largest number of cameras that can be handled by the network. It allows to choose the best configuration for a concrete system, and to decide which configuration is most scalable. The perfect configuration would enable adding as many cameras as possible, without any visible impact on the system delay. Since it is not possible to provide such configuration, we aim at finding the best possible solution.

Obviously, the tests results should not depend on the changes in the input frames, assuming that all of them are similar. For that reason, for each test tens of thousands of

point clouds were sent. For each point on the x-axis (see charts below) there were sent up to three thousands of point clouds.

The test results are given as percentages – we assume, that 100% of frequency is an ideal frequency, equal to the frequency of capturing data from the sensor (30 Hz). The 100% of point cloud size is the size of unfiltered cloud. Because of the possible occurrence of changes in the environment (and consequently the relative results inaccuracy), the unfiltered clouds are sent during the test along the filtered ones. For each single test (for each single x-axis point) the same number of filtered and unfiltered cloud sequences were sent. Between these sequences also delay periods were introduced in order to avoid possible overlays. Finally, for each single test arithmetic means were computed. Tests were performed for each of the algorithms described above. All filters were tested in terms of changes of the point cloud size and the transmitting frequency.

All presented charts are two-dimensional, where the axes represent respectively:

- Changes of the considered parameter of filter – this can be understood as test range of different values of attributes,
- Values – point cloud size, differential growth or frequency. The measures are described in more detail below.

For each of the filters two charts are presented:

1. Mean size – size of the cloud, which should be reduced by the filter. Note, that the cloud cannot be too small, because it would become useless for the user. On the other hand, if the cloud is too big, then the filter is not helpful at all, and superfluously wastes resources.
2. Frequency – the rate of the cloud processing on the server. By default, the cloud is captured 30 times per second. If the filtering is too slow, the frequency is smaller than 30 frames per second, and this should be avoided, i.e. if frequency is no longer effective, then the last effective point was probably the most effective configuration. This means, that probably the best parameters were just passed, i.e. this is the smallest cloud which can be effectively achieved using this filter. Although, if the system had no requirement of real-time operation, then this issue would not be as important as in the considered system.

RESULTS

VOXEL GRID FILTER

The Voxel Grid test was performed by changing the leaf size. Generally, the leaf size is composed of three dimensional variables (X, Y and Z). All of them were manipulated in the same way and the same time. Manipulating the components independently is probably useful only in specific applications. Generally, the Voxel Grid “boxes” shape is a cube, ensuring that the point dispersion is balanced. Note, that changing the box size for each dimension simultaneously causes rapid change of cube volume. Pre-processing using filters allows to

modify the image: extract particular features and hide others. To give general impression about capabilities of the filtering in Fig. 3 we present the effect of pre-processing using a Voxel Grid applied for a three single frames.



Fig. 3. Effect of pre-processing using a vortex grid on a single frame (leaf= 0.01)

The results shown in the Fig. 4a show, that there is a rapid change of point cloud size in the first test, but the size very quickly reaches to 0 value. This means, obviously, that the filter is very effective, but sending nearly empty point cloud is useless. When observing point cloud size changes, only the first values of the leaf size should be considered as useful. The frequency chart (Fig. 4b) shows, that the frames per second factor is very stable (with some fluctuations). Fortunately, the frequency is stable at 100% and changes to about 80% when the size of leaf is close to 0.50. 80% is not an acceptable value in terms of real-time system requirements, but for some systems it would be considered as acceptable too, even for real-time in specific cases. The last chart shows, that as a results of very high frequency rates, only the first chart (size) should be considered in the majority of cases, as it has higher impact on the effects of the working system. The differential changes are not very useful for this test, because the size of the cloud very rapidly reaches values close to zero.

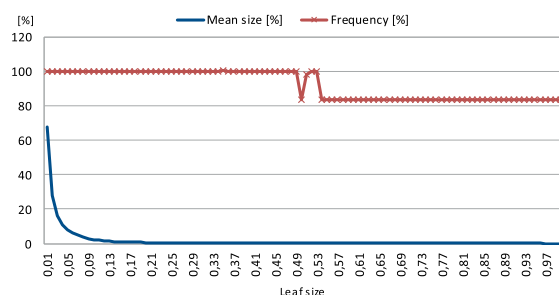


Fig. 4. (a) Changes of the point cloud size and (b) frequency of cloud transmitting

PASS THROUGH FILTER

The Pass Through filter is very characteristic because of its irregularity and difficulties in estimation of usability. This is because the efficiency of the filter strictly depends on the shape of the cloud. What is more, it is possible, that the filter can remove some important point concentration when used improperly. Generally, the charts may help to properly rate the filter, but its configuration (attribute choice) should depend also on the visual observation.

The test was performed in such a way, that the range of filtered area changes in one dimension. However, in practise, it would be worth performing it for each axis independently. The range was changed bilaterally. The changes of the size (Fig. 5a) are irregular, as expected, but the size never grows. The zero value at the end is also expected, because the range of the filter was configured to finally filter out the entire cloud. Looking at the chart, the size reduction is useful for range attribute value lower than 5. However, as it was mentioned before, it is important to make sure, that significant points were not deleted, because the filter may give different results for different clouds (i.e. acquired in different environments).

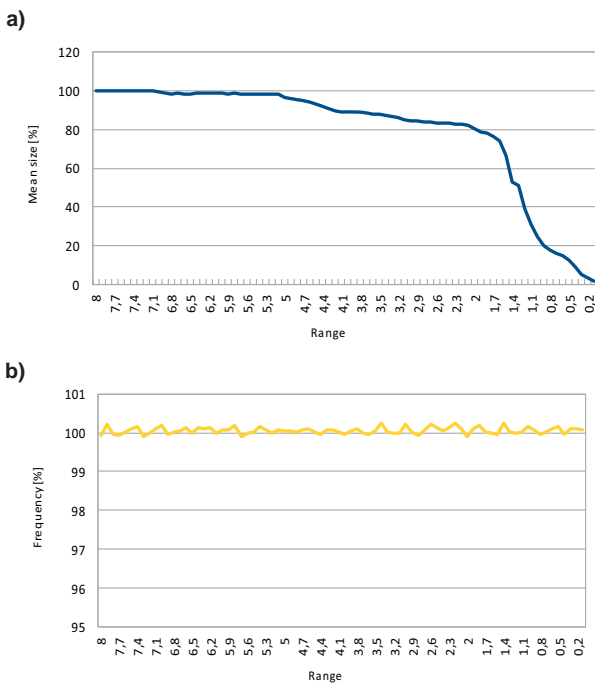


Fig. 5. (a) Changes of the point cloud size and (b) frequency of cloud transmitting

The frequency chart (Fig. 5b) shows, that Pass Through filter works very fast for any values of the range attribute. Again, this means, that the filter should be rated using size changes only, including the differential chart.

FILTERING WITH STATISTICAL OUTLIER REMOVAL

For Statistical Outlier Removal filter we performed two different tests because there are two different factors of the filter (K and m - number of neighbours and multiplier

quantity). It turned out, that the number of neighbours was not very significant, so we skipped them. The multiplier tests were performed using number 10 for the neighbours.

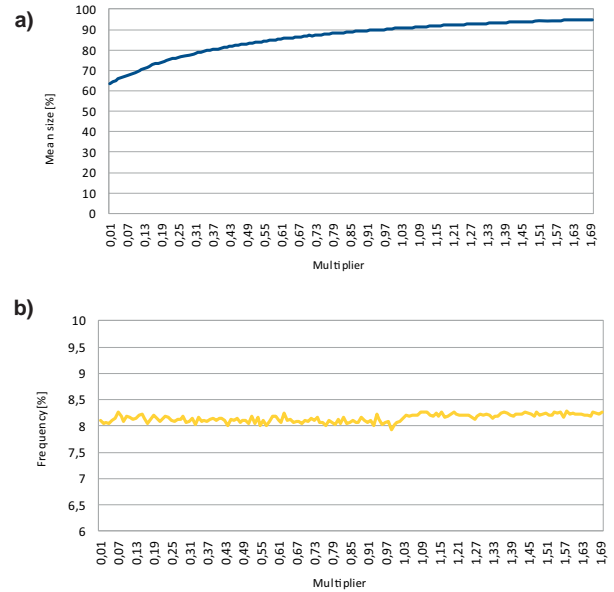


Fig. 6. (a) Size of cloud filtered (b) frequency of cloud transmitting using Statistical Outlier Removal filter ($K=10$)

The point cloud size (Fig. 6a) dropped along with the value of the multiplier. High values of the multiplier result in the higher number of points accepted by the filter. Because the minimal size of the cloud for this filter corresponds to most cases, the tests for smaller values were not necessary. Changing the multiplier is mostly useful for small values, as no significant change was observed for high values. Unfortunately, the frequency chart (Fig. 6b) shows, that the filter does not apply for real-time systems. What is more, the frequency seems to be the biggest for larger values of the multiplier.

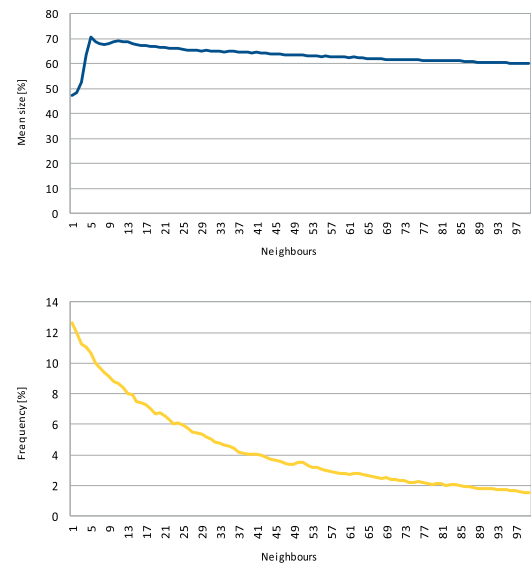


Fig. 7. (a) Size of the cloud filtered (b) frequency of cloud transmitting using Statistical Outlier Removal filter ($m=0.10$)

The size chart (Fig. 7) might indicate, that additional tests for bigger number of neighbours should be performed, but the frequency chart shows, that the frequency of cloud transmitting would be too low. The filter definitely does not meet the requirements, As the performed tests exclude the filter from real-time use. However, the filter may still be useful for some calculations that can be performed after the process of grabbing the clouds, e.g. if all clouds are stored at the server, then such filter could be used to reduce the size of clouds, discarding the useless points.

FILTERING WITH RADIAL OUTLIER REMOVAL

The Radius Outlier Removal test, similarly to Statistical Outlier Removal, was performed for two factors separately: neighbours K and radius r (instead of multiplier for Statistical Outlier Removal). Note, that the neighbours test was performed twice because the results were different for two different values of radius ($r=0.1$ and 0.05). The radius test was performed using the number of neighbours $K=25$.

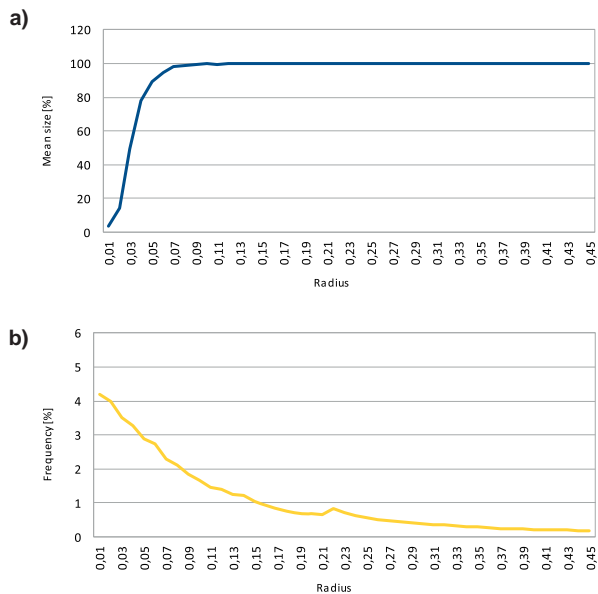


Fig. 8. (a) Size of the cloud filtered (b) frequency of cloud transmitting using Radial Outlier Removal filter ($K=25$)

In the radius test, the size (Fig. 8a) changes for only small radius values. For high radius values, more and more points are accepted so the cloud is actually not filtered. This means, that the filter is useful only for values of radius up to 0.07 assuming, that the number of neighbours is 25. Note, that the result may be slightly different for different kinds of point cloud. For stable cloud size equal to 100% of the original (not filtered) cloud, the differential value is zero as well. The differential chart shows the points, where the size grows in a higher or lower degree. Interestingly, it can be used to find the point of inflection (the extreme of the differential). This information can be useful for the deep analysis of the filter efficiency. Similarly to Statistical Outlier Removal, the analysed filter is not appropriate for real-time systems. The frequency rate (Fig. 8b) is too small. Of course, it may be useful

for some processing performed on the last node, which does not require real-time operation.

The tests of Radius Outlier Removal with changing neighbours number were performed twice, because of two different results for two similar radius values. Obviously, the higher value of neighbours' condition, the smaller the point cloud (Fig. 9a). This is because a higher number of neighbours is required for a point in order to not be deleted. Interestingly however, the change of the size is not rapid. The further experiments were not performed (for higher numbers of neighbours), because of the frequency results (see Fig. 9b), and because of much more satisfactory results acquired in the tests performed with radius 0.05.

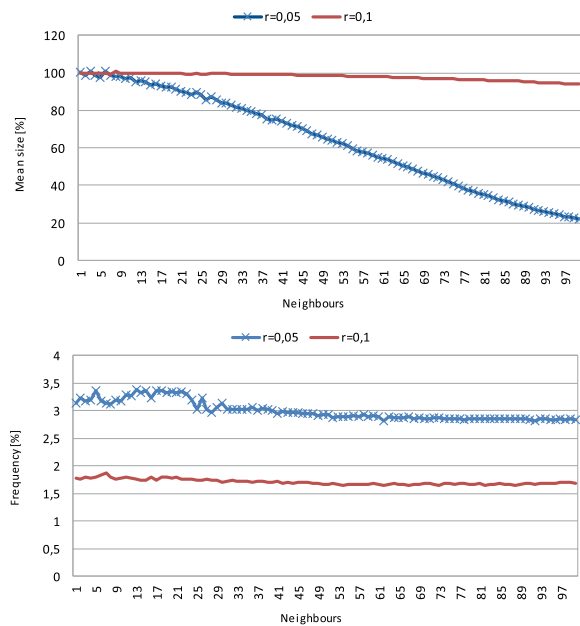


Fig. 9. (a) Size of the cloud filtered (b) frequency of cloud transmitting using Radial Outlier Removal filter ($r=0.1$ and 0.05)

Fig. 9b shows again, that the Outlier Removal filters are not useful for real-time systems. It shows that very small change of radius parameter (from 0.1 to 0.05) causes dynamic changes in frequency. For the same number of neighbours, the cloud size changes much faster and makes the filter much more useful. Interestingly, not only the size results were better, but also frequency.

SUMMARY AND FUTURE WORK

The paper compares four filters with various parameters choice. We performed time-consuming and precise tests to get the best and most accurate results. The results were averaged and collected in diversified, coherent and legible charts. Tests prove, that both Voxel Grid and Pass Through filters can be used mostly in any appropriate parameters configuration. Of course they should be used with caution, to be able to perform cloud reconstruction and not to lose important or relevant points, since all of them carry some information.

The Outlier Removal filters do not meet real-time requirements, so it is not recommended to use them in such

systems. However, they can be used in non-real-time systems. What is more, they can be possibly applied in real-time systems with less strict requirements. As optimization is a large area to investigate, the research can be continued in many ways. As mentioned in the beginning of the paper, there are many approaches for optimising point cloud transmission and consolidation. What is more, Point Cloud processing, even if performed in distributed environment, can be optimized in more than one way and does not have to be focused only on networking. Each of the steps of PCD data flow (described in Section 2) can be more or less optimized. This paper was mostly focused on the pre-processing strictly connected with networking. However, other parts were also partially covered. A sort of optimization was also tried from physical layer perspective. In General, all of these stages can be optimised. First of all, the main topic of the paper – optimization of pre-processing can be performed in other ways. There are some other filters which can be tested instead of the presented ones. Moreover, there are also other ways of point cloud reduction (i.e. compression). Also networking can be optimised (e.g. the choice of the protocol). Additionally, post-processing is a good area to optimize. It is also worth to find a more real-time adjusted solution. Filters should be used with caution, in order to keep the possibility of performing cloud reconstruction or not to lose important or relevant points.

Voxel Grid and Pass Through filters turned to be applicable in any appropriate configuration. Outlier Removal do not meet real-time requirements, and are not recommended for use in such systems. They can be still used in non-real-time systems.

REFERENCE

1. W. Chau-Chang, C. Min-Shine: Nonmetric Camera Calibration for Underwater Laser Scanning System. *IEEE Journal of Oceanic Engineering*, vol. 05, 32(2), (2007), 383-399.
2. S. Ferrari, I Frosio, V. Piuri, N.A Borghese: Enhanced vector quantization for data reduction and filtering. *Proceedings of 2nd International Symposium on 3D Data Processing, Visualization and Transmission, 3DPVT*, (2004), 470–477.
3. S. Gernhardt, X. Cong, M. Eineder, S. Hinz, R. Bamler: Geometrical fusion of multitrack ps point clouds, *IEEE Geoscience and Remote Sensing Letters*, vol. 9(1), (2012), 38–42.
4. H. Haggag, M. Hossny, D. Filippidis, D. Creighton, S. Nahavandi, V. Puri: Measuring depth accuracy in rgb-d cameras. *7th International Conference on Signal Processing and Communication Systems (ICSPCS)*, (2013), 1–7.
5. L. Hong Xie, Z. Zhao: A new method of cylinder reconstruction based on unorganized point cloud, *18th International Conference on Geoinformatics*, (2010), 1–5.
6. P. Kiljański, Optimization of PCD consolidation process in distributed system, Master Thesis, Gdansk University of Technology, 2014
7. P. Li, H. Wang, Z. Liu: A morphological LIDAR point cloud filtering method based on fake scan lines, *International Conference on Electronics, Communications and Control (ICECC)*, (2011), 1228–1231.
8. D. McLeod, J. Jacobson, M. Hardy, C. Embry: Autonomous inspection using an underwater 3D LiDAR. *2013 OCEANS*, San Diego, (2013), 1-8.
9. S. Orts-Escolano, V. Morell, J. Garcia-Rodriguez, M. Cazorla: Point cloud data filtering and downsampling using growing neural gas. *International Joint Conference on Neural Networks(IJCNN)*, (2013), 1–8.
10. R. Rusu, S. Cousins: 3D is here: Point cloud library (PCL). *Proc. of International Conference in Robotics and Automation (ICRA)*, (2011), 1-4.
11. K. Santilli, K. Bemis, D. Silver, J. Dastur, P. Rona: Generating realistic images from hydrothermal plume data. *Visualization*, 2004. *IEEE*, (2004), 91-98
12. P. Thumbunpeng, M. Ruchanurucks, A Khongm: Surface area calculation using Kinect's filtered point cloud with an application of burn care. *International Conference on Robotics and Biomimetics (ROBIO)*, (2013), 2166–2169.
13. Y. Wan, Z. Miao, Z. Tang: Reconstruction of dense point cloud from uncalibrated widebaseline images. *IEEE International Conference on Acoustics Speech and Signal Processing (ICASSP)*, (2010), 1230–1233.
14. Y. Wang, X. Xiang Zhu, R. Bamler, S. Gernhardt: Towards terrasax street view: Creating city point cloud from multi-aspect data stacks. *Proc. of Joint Urban Remote Sensing Event (JURSE)*, (2013), 198–201.
15. H. Wenming, L. Yuanwang, W. Peizhi, W. Xiaojun: Algorithm for 3d point cloud denoising. *3rd International Conference on Genetic and Evolutionary Computing WGEC '09*, (2009), 574–577

CONTACT WITH THE AUTHOR

Tomasz Dziubich

Gdańsk University of Technology
G. Narutowicza 11/12 street
80-233 Gdańsk
Poland,

e-mail: dziubich@eti.pg.gda.pl